Mario Mugitsch, BSc

Investigation of Coating and Drying of Cardboard Substrates

MASTERARBEIT

zur Erlangung des akademischen Grades

Diplom-Ingenieur (Dipl.-Ing.)

Masterstudium Chemical and Pharmaceutical Engineering

eingereicht an der

Technischen Universität Graz

Betreuer

Univ.-Prof. Dr.-Ing. habil. Günter Brenn

Institut für Strömungslehre und Wärmeübertragung

Graz, Mai 2018

Danksagung

Mein Dank gilt allen Personen die mich während meiner Arbeit unterstützt haben.

Im Speziellen möchte ich mich bei Herrn Prof. Brenn für unzählige fachliche Ratschläge bzw. Beiträge und die sehr gute Betreuung bedanken. Während meiner Arbeit konnte ich dadurch sehr viel Neues im Bereich der Strömungsmechanik lernen und auch scheinbar aussichtslose Herausforderungen meistern.

Großer Dank gebührt auch Herrn Dr. Zischka, der das Projekt ins Leben gerufen und durch Anregungen und Koordination einen wesentlichen Beitrag geleistet hat. Das Vertrauen, das mir bei der Bearbeitung der Problemstellungen entgegengebracht wurde bildet den Grundstein für die erreichten Erfolge und die ausgetauschten Erfahrungen waren stets ein wichtiger Bestandteil im Lösungsfindungsprozess.

Verschiedenste Herausforderungen wurden durch Diskussionen mit Herrn Dr. Reischl und Frau Dr. Peters gelöst, die stets ihr Fachwissen und ihre Erfahrungen mit mir geteilt haben. Auch hierfür vielen Dank.

Die Planung bzw. der Bau des Konvektionstrockners wäre ohne wichtige Beiträge von Herrn ao. Prof. Steiner und Herrn Dipl.-Ing. Hinterbichler vom Institut für Strömungslehre und Wärmeübertragung der TU Graz nicht möglich gewesen. Sowohl der finale Designvorschlag für den Konvektionstrockner als auch die CFD Simulation sind das Produkt dieser Zusammenarbeit. Vielen Dank für diese Unterstützung.

Die technische Umsetzung und der Bau des Konvektionstrockners wurde maßgeblich durch Herrn Ing. Paar und Herrn Ing. Stadlhofer von der Technischen Abteilung Mayr-Melnhof Karton Frohnleiten verwirklicht. Änderungen, Verbesserungen und die optimale Umsetzung wurden mit viel Engagement und Offenheit angegangen. Ein sehr großes Dankeschön hierfür.

Für jegliche Problemstellung die eine pragmatische, technische Lösung bedurfte, war Herr Beingrübel ein wichtiger Ansprechpartner. Oft war eine passende Konstruktion innerhalb kürzester Zeit auch schon einsatzbereit. Vielen Dank dafür.

Für die gute Zusammenarbeit und die Hilfestellung in verschiedensten Bereichen bedanke ich mich weiters bei Christopher, Dominik, Ivana, Melanie, Mona, Sonja und Stefan. Im Besonderen sind hier die vielen Stunden an der Labor Curtain Coating Einheit mit Christopher zu erwähnen, die alleine kaum zu bewältigen gewesen wären.

Zu guter Letzt bedarf es auch noch eines besonderen Danks an meine Familie und Freunde, die mich während des Studiums in unterschiedlichster Weise unterstützt haben. Vielen Dank!

EIDESSTATTLICHE ERKLÄRUNG

Ich erkläre an Eides statt, dass ich die vorliegende Arbeit selbstständig verfasst, andere als die angegebenen Quellen/Hilfsmittel nicht benutzt, und die den benutzten Quellen wörtlich und inhaltlich entnommenen Stellen als solche kenntlich gemacht habe.

…… ……

Datum Unterschrift

Abstract

Coating and drying steps are highly important in the production of recycled cardboard for packaging purposes. Major properties can be influenced by adequately deposited and dried coating suspensions. To investigate the behavior of newly designed coating suspensions, it is advantageous to run tests on laboratory-scale coating units and dryers with well-known conditions.

A discontinuous laboratory-scale Curtain Coating unit of the slide-fed type owned by the Research and Development Department of Mayr-Melnhof Karton GmbH is the focus of interest in this study. The device is used before going to full-scale experiments, but both, the coating process as well as the drying step, show potential for optimization in efficiency and reproducibility.

The Curtain Coating unit of the slide-fed type is investigated and the central design problems are mentioned. Modifications are done which lead to enhancements in curtain stability and coatability. The new process is investigated, and a standard characterization procedure based on dimensionless numbers is modified to describe the process correctly. A self-designed convection drying stage is integrated in the Curtain Coating unit. The drying process of a frequently used cardboard type, coated with pure water, is simulated. The results are validated and used to extract specific drying energies from drying experiments of the same type of cardboard with two different coatings.

Kurzfassung

Beschichtungs- und Trocknungsprozesse sind essentielle Schritte in der Herstellung von rezyklierten Kartonsubstraten für die Verpackungsindustrie. Wichtige Eigenschaften werden maßgeblich durch die Qualität des Beschichtungs- und Trocknungsprozesses beeinflusst. Um diese Prozesse zu untersuchen, ist die Verwendung von Beschichtungsanlagen im Labormaßstab und Trocknern mit bekannten Bedingungen hilfreich.

Eine diskontinuierlich betriebene Vorhanggießanlage im Labormaßstab der Forschungsabteilung von Mayr-Melnhof Karton GmbH ist von zentralem Interesse in dieser Arbeit. An dieser Anlage werden Untersuchungen von neuen Beschichtungsflüssigkeiten durchgeführt, bevor sie an der Großanlage getestet werden. Sowohl der Beschichtungsprozess, als auch der Trocknungsprozess weisen jedoch Optimierungspotential in den Bereichen Effizienz und Reproduzierbarkeit auf.

Die Vorhanggießanlage wird untersucht, und Probleme durch die verwendete Geometrie werden aufgezeigt. Modifizierungen der Anlage führten zu Verbesserungen der Vorhangstabilität sowie der Beschichtungseffizienz. Es wird gezeigt, dass eine Charakterisierung des Prozesses gemäß einer Standardprozedur basierend auf dimensionslosen Größen nicht anwendbar ist und diese modifiziert um die Anwendbarkeit auf den gegebenen Prozess zu garantieren. Ein Konvektionstrockner wird geplant und in die Beschichtungseinheit integriert. Der Trocknungsvorgang eines häufig verwendeten Kartonsubstrates, beschichtet mit reinem Wasser, wird simuliert. Die Ergebnisse werden validiert und zur Berechnung der spezifischen Trocknungsenergie eines Substrates mit zwei verschiedenen Beschichtungen herangezogen.

Table of Contents

Symbols

Latin Letters

A	Area;	[m^2];
	Apparatus function;	[-];
	Constant;	
a	Thermal diffusivity;	[m^2/s];
	Activity;	[-];
	Constant;	
b	Distance;	[m];
	Constant;	
B	Magnetic field;	[T];
	Constant;	
C	Constant	
c	Specific heat capacity;	[J/(kgK)];
	Constant;	
d	Thickness;	[m];
	Differential;	[-];
D	Diameter;	[m];
	Diffusion coefficient;	[m^2/s];
f	Force	[N]
F	Correction factor	[-]
g	Gravitational acceleration	[m/s^2]
G	Grammage;	[g/m^2];
	Constant;	
h	Position;	[m];
	Height;	[m];
	Specific enthalpy;	[J/kg];
H	Enthalpy	[J]
I	Identity tensor	[-]
i	Unit vector in x-position	[-]
j	Unit vector in y-position	[-]
k	Constant	
K	Constant	
L	Length	[m]
m	Mass;	[kg];
	Counter;	[-];
M	Momentum	[Ns]
Mw	Molecular weight	[kg/mol]
n	Unit normal vector	[-]
N	Constant	
n	Counter	[-]
p	Pressure	[Pa]
q	Heat flux	[$W/(m^2)$]
Q	Volume flow per width;	[m^2/s];
	Total sorption energy;	[J/mol];
R	Radius;	[m];
	Gas constant;	[J/(Kmol)];
r	Mass source	[kg/m^3]
s	Surface/Interface position	[m]
	Vector	

s	Distance along interface; Constant;	[m];
T	Temperature	[K]
t	Time	[s]
t	Tangential position vector	[m]
T	Stress tensor	[Pa]
U	Constant velocity;	[m/s];
	Perimeter;	[m];
	Voltage;	[V];
u	Velocity	[m/s]
u	Velocity vector	[m/s]
V	Volume	[m^3]
v	Velocity	[m/s]
w	Mass fraction	[kg/kg]
W	Width;	[m];
	Mass load;	[kg/kg pure substrate];
x	Molar fraction	[mol/mol]
x,y,z	Position coordinate	[m]

Dimensionless Numbers

B	Spalding transfer number	[-]
Bi	Biot number	[-]
Bo	Bond number	[-]
Ca	Capillary number	[-]
Fo	Fourier number	[-]
Le	Lewis number	[-]
Nu	Nusselt number	[-]
Pr	Prandtl number	[-]
Re	Reynolds number	[-]
Sc	Schmidt number	[-]
Sh	Sherwood number	[-]
St	Stokes number	[-]
We	Weber number	[-]

Greek Letters

α	Heat transfer coefficient;	[W/(m^2K)];
	Angle;	[°];
β	Mass transfer coefficient	[m/s]
Γ	Adsorption	[mol/m^2]
Δ	Difference operator	[-]
δ	Boundary layer thickness	[m]
ε	Characteristic Lennard-Jones energy	[J/mol]
ζ	Resistance coefficient	[-]
η	Dynamic viscosity	[Pas]

$\boldsymbol{\theta}$	Contact angle;	[°];
	Dimensionless Temperature difference;	[-];
$\boldsymbol{\kappa}$	Association factor	[-]
$\boldsymbol{\lambda}$	Dimensionless friction factor;	[-];
	Thermal conductivity;	[W/(mK)];
	Apparatus constant; Constant;	[-];
$\boldsymbol{\mu}$	Dynamic viscosity;	[Pas];
	Dipole moment;	[D];
$\boldsymbol{\nu}$	Kinematic viscosity	[m^2/s]
$\boldsymbol{\pi}$	Constant	[-]
$\boldsymbol{\rho}$	Density	[kg/m^3]
$\boldsymbol{\sigma}$	Surface tension;	[N/m];
	Characteristic Lennard-Jones length;	[m];
$\boldsymbol{\tau}$	Shear stress	[Pa]
$\boldsymbol{\tau}$	Viscous stress tensor	[Pa]
$\boldsymbol{\varphi}$	Isotherm;	[-];
	Relative humidity;	[kg/kg];
$\boldsymbol{\Phi}$	Dissipation loss	[J/s]
∅	Porosity;	[m^3/m^3];
	Exponent for Spalding transfer number;	[-];
	Mixing parameter;	[-];
ψ	Volume fraction of water	[m^3/m^3]
$\boldsymbol{\Omega}$	Collision integral	
$\boldsymbol{\omega}$	Acentric factor;	[-];
	Rotation velocity;	[1/s];

Others

$\boldsymbol{\nabla}$	Nabla-Operator	[1/m]
$\dot{\boldsymbol{X}}$	Time Derivative of X	unit of X per s
$\boldsymbol{X}^*$	Dimensionless X;	[-];
	Modified X;	

Sub-/Superscripts

0	initial;
	standard;
1,2	of substance one/two;
	counter;
∞	after long time
age	nominal age
air	of air
amb	at ambient conditions
aw	air with water
B	relates to body;

	Boltzmann;
b	at boiling point;
bubble	of bubble pressure tensiometer
bulk	of bulk phase
BW	backside wall of dryer
c	at/relates to critical conditions
change	relative change
channel	of/in channel
char	characteristic
coat	of coating
coated	with coating
cond	conductive
conv	convective
crit	at critical flow conditions
cross	of cross section
curtain	of/in curtain
d	distance
D	relates to diffusion
DF1	at very upstream position of substrate at upper dryer wall
DF2	at mid position of substrate along main flow direction at upper dryer wall
DF3	at very downstream position of substrate at upper dryer wall
diff	diffusive
down	at downstream position
dry	in dry state
dryer	of dryer
drying	of drying process
E	of entrance
e	extern
eq	in equilibrium
exp	experimental
F	of fluid
film	in/of film/boundary layer
fit	fitted
g	in gas/vapor phase
GAB	Guggenheim-Anderson-DeBoer sorption model
grid	of grid
h	hydraulic
H_2O	of water
i	of substance; at position; counter; inner;
imp	at impingement
in	of inlet/incoming
inf	outside of boundary layer
l	in liquid phase
low	at lower position
m	mean of
M	mass based
max	maximum
min	minimum
mon	of monolayer
Nu	related to Nusselt number
O	Ostwald-De Waele
p	at constant pressure

par	parallel
pdiff	planar diffusion
pe	at pouring edge
pipe	of/in pipe
Q	relates to heat flow
r	reduced quantity
s,l	at solid/liquid interface
s,a	at solid/air interface
safe	safety
sat	at saturation
ser	serial
sig	related to sigmoidal model
slide	in/of slide
slit	in/of slit
solid	dissolved solid
sorp	sorption
sub	of/in substrate
surf	at surface
SW	at side walls of dryer
T	thermal
t	of time step
u	universally applicable
uncoated	without coating
up	at upper position; at upstream position;
v	for viscosity
vap	of vapor; for vaporization;
W	at wall
wa	water with air
x	in x-direction
y	in y-direction
$\boldsymbol{\gamma}$	relates to dynamic surface tension.
$\boldsymbol{\mu}$	relates to viscosity

Abbreviations

A/D	Analog/Digital
CFD	Computational Fluid Dynamics
COST	European Cooperation in Science and Technology
CPU	Central Processing Unit
DTAB	Dodecyltrimethylammonium bromide
MM Karton	Mayr-Melnhof Karton GmbH
MTME	Mobile Temperature Measuring Element
PEEK	Polyetheretherketone
PTFE	Poly(tetrafluoroethylene)
SBS	Solid Bleached Sulphate
SDS	Sodium Dodecyl Sulphate
SSE	Sum of Square Errors
TRR	Trust-Reflective-Region

1 Introduction

This thesis was prepared with the Research and Development Department of Mayr-Melnhof Karton GmbH in Frohnleiten, Styria under the guidance of Dr. Michael Zischka, in corporation with the Institute of Fluid Mechanics and Heat Transfer of Graz University of Technology with the supervisor of this study and head of the institute Prof. Dr.-Ing. Günter Brenn.

1.1 Coating Technologies

Over 40.000 years, is the age of the earliest known man-made cave paintings. The simple drawings made from Iron-Oxide were found in the El Castillo cave, Spain. This could also define the starting point of the history of coating technology. While in the Upper Palaeolithic the technology was mainly used to express information or belief on stone walls, the Ancient Egyptians took the next step forward. Besides the investigation of novel pigments and binders, they also applied protective coatings as finish. Waxes and resins may be the reasons why some paintings could withstand nearly 5000 years of environmental impact [2]. However, if one talks about coating technology, normally the mass production of diverse products relates to it. It was the Industrial Revolution in the 18th and 19th century which gave rise to a variety of new production processes and machineries. Since more and more metal products were manufactured, there was also the need of anti-corrosive primers and processes to assure continuous layer deposition on diverse surface geometries [3]. A variety of coating techniques had been developed during these times to meet the vast amount of engineering requirements. Even though the development was ongoing, it was mainly product oriented, and a lack of communication between producers prevented the formation of a coating society until the mid of the 20th century [4]. As a first scientific contribution to the field of coating technology one should mention the article by Landau and Levich (1942) [5]. They derived a simple relationship between liquid properties, coating speed and the resulting film thickness under conditions of low capillary numbers for the dragging of liquid by a moved plate. The results were used, among others, in the Dip Coating process. Since then, things have changed drastically. Indeed, the society has grown substantially, as has the market. The World Paint & Coating Association estimates the global market at $ 149 billion in 2016, with stable compound annual growth rates of about 5.5 % in the past years. Especially the Asia-Pacific region is the driving force of growth with 8.3 % and contributes 55 % of the overall market, whereas the European market could only add 1.8 % in 2016 [6]. At first sight, these numbers seem to be stunningly high, but one should keep in mind the widespread applications of coating technology. Coatings are used in paper and pulp production as well as for computer discs, it is important in the field of microelectronics as well as for textiles. There is hardly any industrial field without impact on

it. As diverse as the coated products, so are the techniques for implementation of the coating material. From simple Dip- to Electrochemical Coating, Physical Vapor Deposition, Spraying or Spin Coating, all these techniques lie within the spectrum of this field. If wet film thicknesses of 1 to 100 microns are in consideration, it can basically be distinguished between self-metered and pre-metered coating technologies [4]. In self-metered coating technologies, the wet film thickness is determined by the interaction of the fluid flow with the coating applicator. Examples for this strategy are the well-known Dip Coating and Roll Coating, which had their origins in the 1930s [7]. In pre-metered techniques, the wet film thickness is given by the amount of liquid transported to the substrate. A main advantage of this group is the applicability to non-uniform surfaces, and a representative of it is Curtain Coating, which is also the central coating technique in this thesis. In Curtain Coating, free liquid surface is produced by the formation of a freely falling liquid sheet before impinging onto the moving substrate. Due to the high impingement pressure on the area of contact between liquid and the solid substrate, the present air layer is pushed aside, and high coating speed without air entrainment can be realized [8]. The first known Curtain Coating device was mentioned in a German patent publication by Taylor (1903) with the purpose of candy production covered by a uniform layer of chocolate [9]. The use of Curtain Coating for continuous webs made it accessible for the pulp and paper industry in the 1960s. Modern devices apply several liquid layers simultaneously, leading to advantages in the drying process [8]. The first multilayer Curtain Coater was published by Hughes (1968) [10]. The better part of our current knowledge was, however, developed by the photographic industry in the years after this prior milestone. In 2010, the first in-board Curtain Coater in the pulp and paper industry was installed at Mayr-Melnhof Karton GmbH Frohnleiten which finally led to the interest of planning the current thesis. The packaging or, more specific, the food packaging industry is confronted with several challenges. On the one hand, the containment must be cheap, which implies high production speed and low material use, but, on the other hand, food safety must be guaranteed in any case. Food contact materials must additionally comply with specifications given in Article 3 (European Commission 2004) as stated in EU Regulation No. 1935/2004. This restricts the materials to be used drastically, and highly innovative strategies must be developed. The primary function of the package is always to provide optimal conditions for the packed good. Besides the protection from external threats, migration of packaging materials into the food is a prevailing topic. This is shown by the 'ITX affair' in 2005. A packaging layer of a beverage carton of the major enterprise Tetrapak® was contaminated with the photo initiator ITX (2-isopropyl thioxanthone) that migrated into the packaged food. For this reason, concentrations of 250 ppb could be found in baby milk [11]. Although no health concern was assessed from EFSA (European Food Safety Authority), this underlines the importance of good barrier properties in the food packaging industry. Recycled cardboard products are often affected by

this topic, since low amounts of organic compounds are always found in the recycled raw material. Coating technology is used to add powerful barriers to avoid any contamination of the packed good, and at the same time to preserve the advantage of cost efficiency and sustainability of the containment. Thus, the circle closes and one again ends up at the importance of coating technology. It is vital to understand the coating step, as well as the most important downstream step, the drying, for reliable production of high-quality products. However, since both steps involve plenty of complex processes, a thorough understanding is hard to accomplish. Of course, a full understanding of the processes should always be the aim, where adequately designed coating and drying experiments can confirm or refute the chosen strategies in coating development.

1.2 Aims of this Thesis

A laboratory-scale Curtain Coating Unit at Mayr-Melnhof Karton Frohnleiten for cardboard coating was the object of this thesis (Figure 1). The coating unit was analyzed and optimized in a first step. Subsequently, coating experiments were performed to find optimal settings and check the validity of literature methods to characterize the process, based on dimensionless numbers. In the second part of the thesis, a convection dryer was integrated in the coating unit. A paper drying process was simulated, and a mean heat transfer coefficient for the dryer was found. Thereby drying experiments could be performed, where the specific drying energy for two differently coated substrates was investigated.

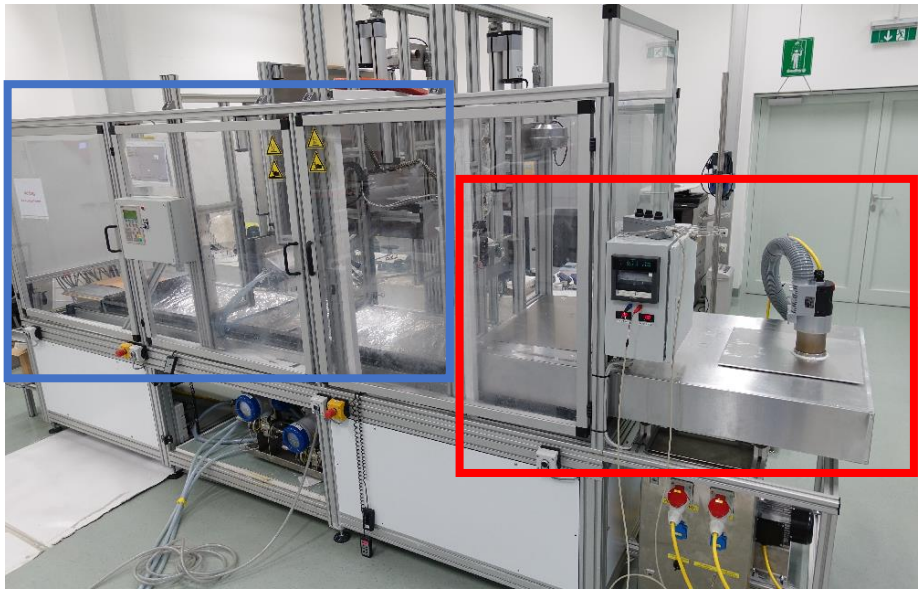

Figure 1 - Curtain Coating unit with convection dryer. The blue frame shows the coating section, the red frame the drying section.

2 Theoretical Background

2.1 Curtain Coating

2.1.1 Basics of Coating

2.1.1.1 Conservation of Mass

To understand physical processes in fluid motion, one must know about the conservation laws in fluid mechanics, namely the conservation of mass and linear momentum. These laws can be derived from balancing masses and forces, respectively. Conservation of mass, in the stated local form also called the 'continuity equation', for a continuous fluid is given by [12]:

$$\frac{\partial \rho}{\partial t} + \boldsymbol{\nabla} \cdot \rho \boldsymbol{u} = 0 \tag{1}$$

This reveals that for fluids with variable density, there must be a difference between in- and outflow. For coating liquids, the density is constant, and equation (1) can be simplified to [12]:

$$\boldsymbol{\nabla} \cdot \boldsymbol{u} = 0 \tag{2}$$

This equation applies to unsteady as well as to steady flow.

2.1.1.2 Conservation of Linear Momentum

From Newton's second law of motion it is known that the net force on a body gives the time dependent change of momentum. The local form of conservation of momentum for some continuous fluid reads [12]:

$$\frac{\partial \rho \boldsymbol{u}}{\partial t} + \boldsymbol{\nabla} \cdot \rho \boldsymbol{u}\boldsymbol{u} = \boldsymbol{\nabla} \cdot \boldsymbol{T} + \rho \boldsymbol{g} \tag{3}$$

The left-hand side of this equation describes the rate of change of momentum within the body in consideration, which represents its inertia. The right-hand side sums all the relevant surface and body forces, with the gravitational force as a single body force. The surface forces, combined in the stress tensor $\boldsymbol{T}$, are the pressure and the deformation-induced stresses which can be found by constitutive relations. Generally, the stress tensor can be written in the following form [12]:

$$\boldsymbol{T} = -p\boldsymbol{I} + \boldsymbol{\tau} \tag{4}$$

This means that the stress tensor $\boldsymbol{T}$ is the sum of pressure p and viscous forces, with the viscous stress tensor $\boldsymbol{\tau}$ and the identity tensor $\boldsymbol{I}$. The constitutive relation for the viscous stress tensor $\boldsymbol{\tau}$ of Newtonian fluids with the simplification of constant density reads [12]:

$$\boldsymbol{\tau} = \mu[\boldsymbol{\nabla}\mathbf{u} + (\boldsymbol{\nabla}\mathbf{u})^T] \tag{5}$$

with the expression in brackets as the strain rate for three-dimensional flow and the superscript 'T' for the transpose of the quantity. Using this relation leads to the important Navier-Stokes equations [12]:

$$\frac{\partial \rho \boldsymbol{u}}{\partial t} + \boldsymbol{\nabla} \cdot \rho \boldsymbol{u}\boldsymbol{u} = -\boldsymbol{\nabla}\mathrm{p} + \mu \boldsymbol{\nabla^2 u} + \rho \boldsymbol{g} \tag{6}$$

These equations are valid for constant density and viscosity only. Because many coating liquids show a dependency of viscosity on the shear rate, the existence of various models to include this dependency into the equation must be mentioned.

2.1.1.3 Power Law Model

The shear stress subjected to an incompressible Newtonian fluid under laminar flow can be computed by the product of shear rate and (the substance property) viscosity [13]:

$$\tau = \mu \frac{du}{dy} = \mu \dot{\gamma} \tag{7}$$

herein the shear stress is applied in flow direction and the velocity gradient $\frac{du}{dy}$ is the one perpendicular to the shear surface. This relation is valid for simple, one-directional shear flow. The important difference to the case of non-Newtonian fluids is that viscosity of the latter can depend on shear rate and time. Since viscosity can vary substantially, at least the dominant dependency must be considered in the conducted calculations. The observation that a double-logarithmic plot of shear rate and shear stress often leads to a straight line within a certain shear rate range for time-independent fluids, led to the 'Power Law'- or Ostwald-De Waele model. Consequently, the 'effective' or 'apparent' viscosity can be expressed in the following way [13]:

$$\mu = K_O(\dot{\gamma})^{n_O - 1} \tag{8}$$

with consistency index K_O and flow behaviour index n_O taken from curve fitting of experimental data. The cases of n_O<1, n_O>1 and n_O=1 stand for shear thinning, shear thickening and Newtonian behavior, respectively.

2.1.1.4 Dimensionless numbers

Dimensionless parameters are extensively used in the field of fluid mechanics as well as in heat and mass transfer. Elimination of dimensions and analyzing the ratio of relevant quantities, provides often the basics for upscaling and comparison procedures. An example from the book 'Liquid Film Coating' shall provide an understanding of the procedure and the origin of these numbers [12]:

The routine of elimination of the dimensions starts with appropriate scaling of the variables involved. For this purpose, a sketch of the problem statement is often a helpful tool (Figure 2) [12].

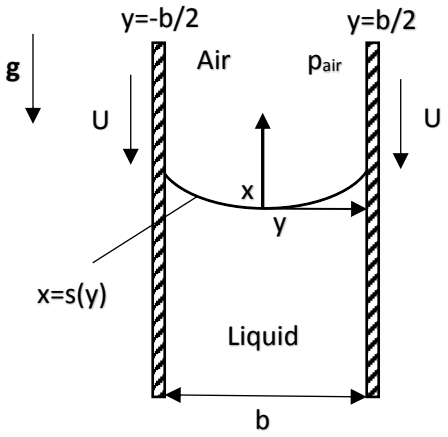

Figure 2 – Constant-shape meniscus between moving plates [12].

The problem consists of a moving meniscus between air and a Newtonian liquid bounded by two parallel plates of distance b. The meniscus moves upward with steady speed U and a constant shape. The plates are infinitely long in z-direction (into the plane of the page), and gravity acts in the negative x-direction. The coordinate system is fixed on the interface, and therefore the plates move in the negative x-direction. Viscous effects of air on the film are negligible ($\boldsymbol{\tau_{air}}$=0), and the air pressure p_{air} is constant. For problems involving interfaces, a boundary condition to describe a potential stress jump across the interface, e.g. because of surface tension, must be included. This is done with the 'Dynamic Boundary Condition' for the normal stress. For the current problem, the normal condition reads [12]:

$$-p + [\boldsymbol{n} \cdot \boldsymbol{\tau}] \cdot \boldsymbol{n} = -p_{air} - \frac{\sigma}{R_m} \; at \; x = s(y) \tag{9}$$

with the pressure in the liquid p, the pressure in the air p_{air}, the outward normal unit vector of the liquid $\boldsymbol{n}$, the viscous stress tensor from the liquid $\boldsymbol{\tau}$, the surface tension σ and the mean radius of curvature of the interface R_m. Since there is a static-looking interface involved, the

pressure is scaled by σ/b, in conjunction to the Young-Laplace equation. The following scales were chosen for the involved variables [12]:

$$p^* = \frac{pb}{\sigma}, \qquad {p_{air}}^* = \frac{p_{air}b}{\sigma}, \qquad {R_m}^* = \frac{R_m}{b}, \qquad \boldsymbol{\tau}^* = \frac{\boldsymbol{\tau}b}{\mu U}, \qquad \boldsymbol{\nabla}^* = b\boldsymbol{\nabla}, \qquad t^* = \frac{tU}{b},$$

$$\boldsymbol{u}^* = \frac{\boldsymbol{u}}{U}, \quad x^* = \frac{x}{b}, \qquad y^* = \frac{y}{b}, \qquad \mathrm{s(y)}^* = \frac{\mathrm{s}(y)}{b}$$

with the plate distance b, the dynamic viscosity μ, the Nabla-operator $\boldsymbol{\nabla}$, the time t, the velocity of the moving plates U, the velocity vector **u** and the coordinate positions x and y as well as the interface position s. Insertion into the Navier-Stokes equation (6) and the Dynamic Boundary Condition for the normal stress (10) gives the following results [12]:

$$ReCa\left[\frac{\partial \boldsymbol{u}^*}{\partial t^*} + \boldsymbol{u}^* \cdot \boldsymbol{\nabla}^* \boldsymbol{u}^*\right] = -\boldsymbol{\nabla}^* \mathbf{p}^* + Ca\boldsymbol{\nabla}^{*\mathbf{2}}\boldsymbol{u}^* - (Bo)\boldsymbol{i} \tag{10}$$

$$-p^* + Ca[\boldsymbol{n} \cdot \tau^*] \cdot \boldsymbol{n} = -{p_{air}}^* - \frac{1}{{R_m}^*} \; at \; x = s^*(y) \tag{11}$$

$$Re = \frac{\rho U b}{\mu} \tag{12}$$

$$Ca = \frac{\mu U}{\sigma} \tag{13}$$

$$Bo = \frac{\rho g b^2}{\sigma} \tag{14}$$

Here, the gravity vector was written as $\boldsymbol{g} = -g\boldsymbol{i}$ (with unit vector in x-direction $\boldsymbol{i}$). With the Reynolds number Re, the capillary number Ca and the Bond number Bo as the corresponding dimensionless numbers to describe the problem**.** The Reynolds number stands for the importance of inertial forces compared to viscous forces, the capillary number compares viscous to surface tension forces and the Bond number is the ratio between gravitational and surface tension forces. Many of these dimensionless groups appear in the different fields of fluid mechanics as well as in heat and mass transfer. Another dimensionless number of interest in the Curtain Coating process is the Weber number We that compares inertial to surface tension forces [12]:

$$We = ReCa = \frac{\rho U^2 b}{\sigma} \tag{15}$$

As can be seen in (15) the Weber number depends on Reynolds and capillary number for the considered problem. An obvious advantage of these dimensionless numbers is that possible

simplifications of the balance equations can be identified. For example, viscous stresses can be neglected in the Dynamic Boundary Condition (11) if the capillary number is small.

2.1.1.5 Contact Lines

At well-defined conditions, liquid contact with a solid involves a certain contact angle. This is the static angle θ_{eq} which is a measure of wettability and is defined between the outward normal of the liquid and the normal of the solid (Figure 3) [12].

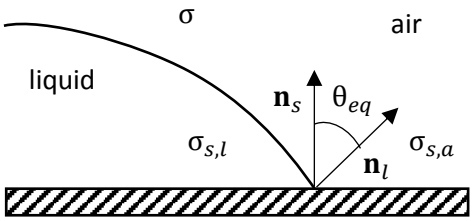

Figure 3 – Liquid/Solid Wetting. Symbols are explained in the text [12].

If the free surface energy of the solid/air interface $\sigma_{s,a}$ exceeds the surface tension of the solid/liquid interface $\sigma_{s,l}$, spontaneous spreading of the liquid occurs. For the mentioned conditions, Young's equation shows the relation [12]:

$$\sigma\cos(\theta_{eq}) = \sigma_{s,a} - \sigma_{s,l} \tag{16}$$

In coating technology, liquid displaces air from a solid substrate in flow direction. The contact line then moves relative to the solid. Such contact lines are called dynamic contact lines and are less well understood than their static counterparts.

2.1.2 Curtain Coating Process

In a Curtain Coating device of the slide-fed type, the coating fluid enters a homogenization chamber of the die. From this location, the fluid is forced through an exit slot, which generally sets the maximum coating width of the device. Along a slide, the liquid film flows towards the lip. Before reaching the lip, the slide inclination increases to accelerate the fluid at the slide elongation. At the lip, a freely falling liquid sheet forms, which is kept in shape by edge guides. This so-called 'curtain' is the most distinguishing feature to other coating methods. After a certain free-fall distance, the liquid impinges onto the substrate. Air shields are installed to drag away the air tagged along with the moving substrate. The Curtain Coating set-up in use is shown in Figure 4.

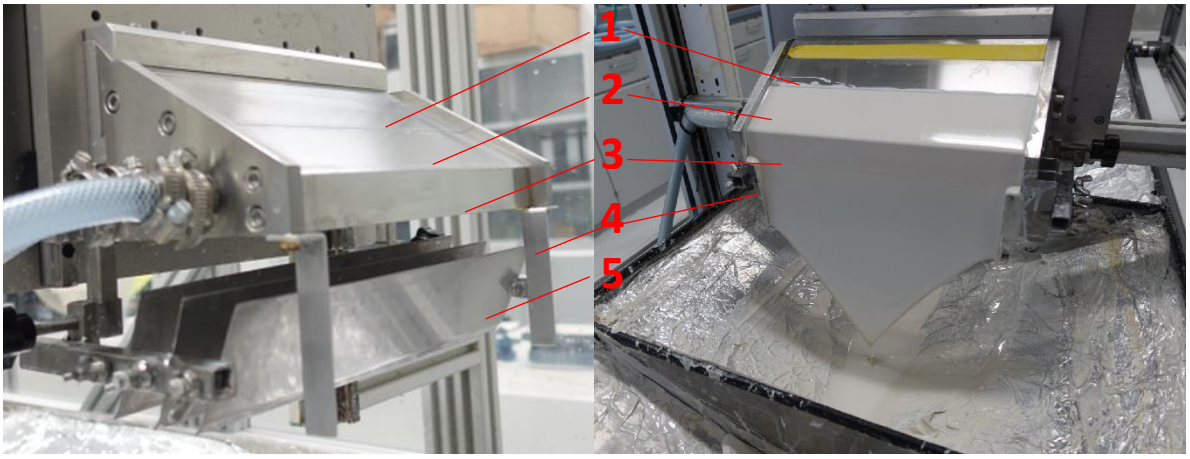

Figure 4 – Coating device with slot exit (1), slide with increased inclination before the lip (= slide elongation) (2), lip (3), edge guide (4) and air shield (5).

The flow at slide-fed Curtain Coating devices is generally divided into five different flow zones, namely a film forming zone after the slot exit, a falling film zone along the slide, a sheet forming zone at the lip, a curtain flow zone, and finally an impingement zone (Figure 5) [8].

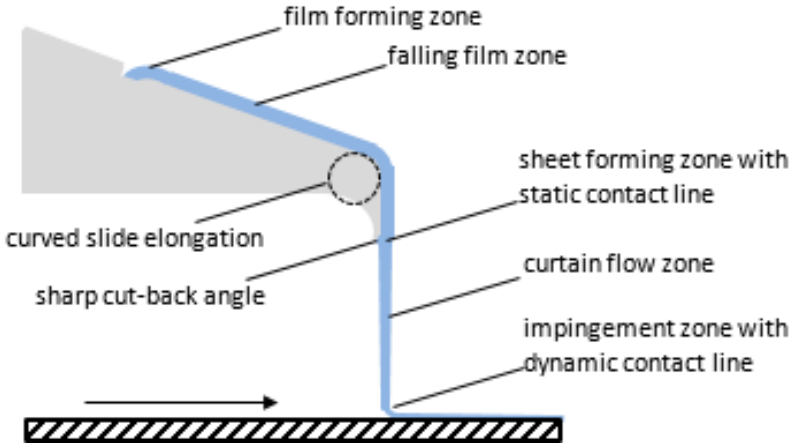

Figure 5 – Different flow zones at slide-fed Curtain Coating devices and important design characteristics.

The slot exit design is crucial for optimal flow conditions in the film forming zone. Backflow upstream the slide surface, or vortex formation adjacent to the downstream end of the slot, can be observed for poorly designed slot exits [8]. Consequently, this leads to the risk of streak lines on the coated substrate due to particle deposition. At a well-designed slot exit, the wall at the upstream side is slightly higher than the downstream end, and the downstream edge is skewed as stated by Ade (1976) [14]. The slot exit design of the device in use, however, is quite simple and therefore possesses none of those features. The difference between the ideal and the present slot exit designs is illustrated in Figure 6 [8].

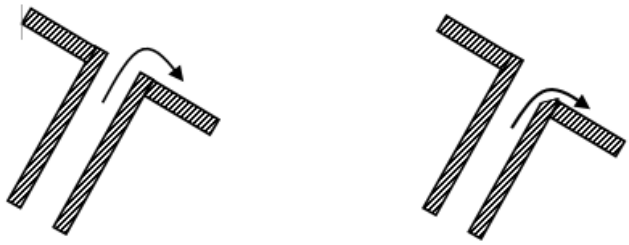

Figure 6 – Present slot exit design (left) and ideal slot exit design (right). The arrow indicates the resulting flow, which is more attached in the ideal design [8].

Other vital design aspects which show to differ from optimum in the device are the slide elongation and the lip design (Figure 5). Acceleration of the liquid before reaching the lip to form a falling liquid sheet is the task of the slide elongation. This acceleration leads to the reduction of surfactant concentration on the upper surface, which is a free surface directly in contact with the surrounding air. The elongation supports the stability of the curtain because the difference in surface tension between the upper liquid surface and the newly formed free surface is reduced [8]. A slide elongation of 20 to 40 mm radius of curvature is stated by Fahrni et al. (1978) to give the best results [15]. The lip design is recommended to include a sharp cut-back angle at the pouring edge to avoid wetting of the underside of the slide and coating non-uniformities related to an uneven and irregular wetting line at the position of liquid detachment [8,15]. As can be seen in Figure 4, these recommendations are violated in the used coating tool. The slide elongation abruptly changes the inclination of the slide to 90° to the horizontal, and the lip does not include the sharp cut-back angle. Other parts of the present set-up are, however, in good agreement with guidelines in literature, as for example the slide-inclination angle of 30° to the horizontal and the principal use of edge guides [8]. It has to be mentioned, however, that the original edge guide geometry was altered intentionally during this thesis. Without use of edge guides, the curtain contracts to ultimately form a cylindrical jet after a certain distance downstream. This can also be seen in Figure 4 on the right picture at the very downstream position. Investigations of Nishida and Katagiri (1994) revealed the growth of a Blasius-type boundary layer along the edge guides (Figure 7) [16]. Surface formation due to acceleration is faster in the region outside of the boundary layer. This leads to different adsorption times for surfactants in the center of the curtain and at positions within the boundary layer and, consequently, to a difference in surface tension. A Marangoni flow towards the center develops, which, together with capillary forces due to the wetting of the solid material, is responsible for thinning of the curtain near the edge guides [8,16].

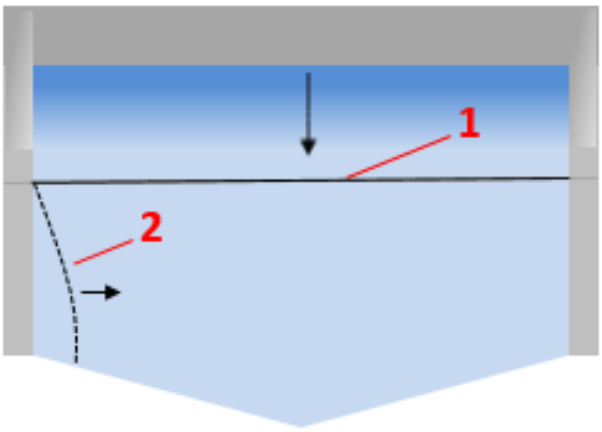

Figure 7 - Sketch of the front view of a Curtain Coating device of the slide-fed type with the main flow direction along the long arrow, the pouring edge (1) and a dynamic boundary layer that develops near the edge guides (2), which leads to liquid flow towards the center of the curtain (short arrow).

Rod-shaped stainless-steel guides became the standard since their introduction by Greiller (1975) [8,17]. Different solutions were proposed to maintain a stable curtain of constant width. The use of a low-viscosity lubricating liquid is a common strategy to prevent liquid separation from the edge guides and can be implemented in several ways [18,19]. If principal stability of the curtain can be maintained, the most important position for a successful coating process is the impingement zone. Protection from the air tagged along with the moving substrate is essential to avoid disturbance of the dynamic contact line and prevent air entrainment [8,20]. For this reason, an air shield based on the patent of Hughes (1968) was installed during this thesis (Figure 4) [10].

Besides all the design and process aspects discussed above, it turned out that the most influential difference of the present Curtain Coating device to standard devices is the discontinuous operation procedure. Instead of a continuously coated web, which is installed in standard devices, a substrate transporter with the substrate fixed on the upper surface is driven through the falling liquid sheet. As will be discussed in section 6.1.2 below, the process is therefore not in steady-state during the liquid deposition, which makes the standard operability window not applicable.

2.1.3 Modeling of the Impingement Zone

The central point of interest for describing successful Curtain Coating is the impingement zone. Based on the analysis of Kistler and Scriven (1984), the impingement zone can be modelled in the following way (Figure 8) [20]:

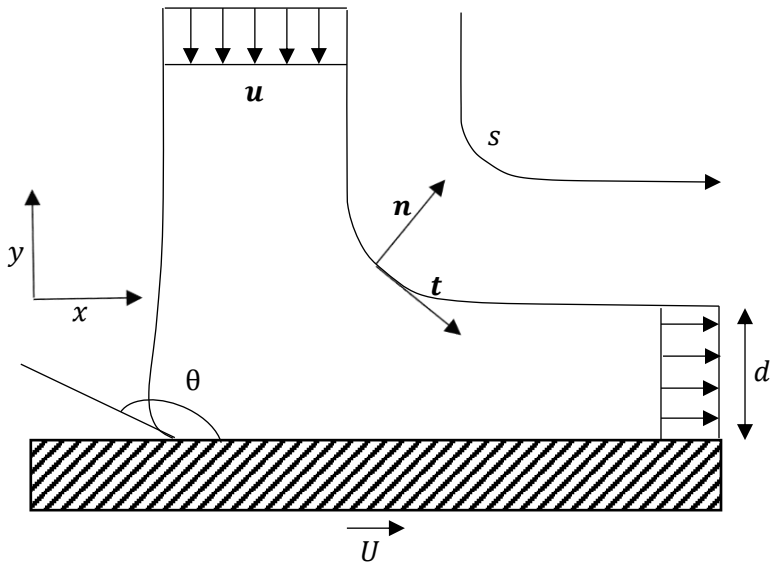

Figure 8 - The impingement zone in a Curtain Coating process [20]. Symbols are explained in the text.

The domain possesses an inflow boundary of known position and velocity (= impingement velocity). The flow is described by the continuity and Navier-Stokes equations, for a steady-state process ($\frac{\partial}{\partial t} = 0$) and incompressible fluids [20]:

$$\boldsymbol{\nabla} \cdot \boldsymbol{u} = 0$$

$$\boldsymbol{\nabla} \cdot \rho \boldsymbol{u}\boldsymbol{u} = \boldsymbol{\nabla} \cdot \boldsymbol{T} + \rho g \boldsymbol{j}$$

Kistler and Scriven (1984) introduced the following scales for the parameters in the equations [20]:

$$\boldsymbol{u}^* = \frac{\boldsymbol{u}}{U}, \qquad \boldsymbol{\nabla}^* = d\boldsymbol{\nabla}, \qquad \boldsymbol{T}^* = \left(\frac{d}{\mu U}\right)\boldsymbol{T}$$

This gives the non-dimensional form of the Navier-Stokes equations [20]:

$$Re\boldsymbol{u}^* \cdot \boldsymbol{\nabla}^* \boldsymbol{u}^* = \boldsymbol{\nabla}^* \cdot \boldsymbol{T}^* + St\boldsymbol{j} \tag{17}$$

with the unit vector in y-direction $\boldsymbol{j}$, Reynolds number defined as $Re = \rho U d/\mu$ and the Stokes number defined as $St = g\rho d^2/\mu U$. Note that the definition of the Reynolds number is essentially the same as the one proposed by Miyamoto and Katagiri (1997) to describe the coating process, which reads $Re = \rho Q/\mu$ with the volume flow of coating liquid divided by the slot width Q [8]. Along the free surface s, a unit tangent vector $\boldsymbol{t}$ exists, and the normal-stress boundary condition requires that the viscous normal stress ($[\boldsymbol{n} \cdot \boldsymbol{T}] \cdot \boldsymbol{n}$, with the unit outward normal $\boldsymbol{n}$) in the liquid relative to air pressure, balances any capillary pressure [20]. This was

already mentioned in 2.1.1.4.The ratio of the viscous and capillary stresses is given by the capillary number $Ca = \mu U/\sigma$ and the Dynamic Boundary Condition at this free surface is given by [20]:

$$\boldsymbol{n} \cdot \mathbf{T} = \frac{1}{Ca}\frac{d\boldsymbol{t}}{ds} \tag{18}$$

Since the free surface is material, there can be no flow across the surface, which gives [20]:

$$\boldsymbol{n} \cdot \mathbf{u} = 0 \tag{19}$$

At a position far enough downstream, the flow is fully developed and mass as well as momentum flux are known, which gives the outflow boundary conditions. The liquid in contact with the solid normally fulfills the no-slip condition. However, this is not the case in the region near to the dynamic wetting line. Here some slip conditions can be implemented, which is further discussed in the article by Kistler and Scriven (1984) [20].

2.1.4 Operability

As mentioned above, especially two aspects must be considered for successful Curtain Coating:

- Sufficient stability of the falling liquid sheet
- Appropriate conditions at the impingement zone

The first aspect is important to avoid disintegration of the sheet during the process. A force balance between inertial and surface tension forces on the free edge between a moving liquid and air gives the widely used stability criterion (Figure 9) [21]:

$$We = \frac{\rho_l Q_l v_{imp}}{\sigma} > 2 \tag{20}$$

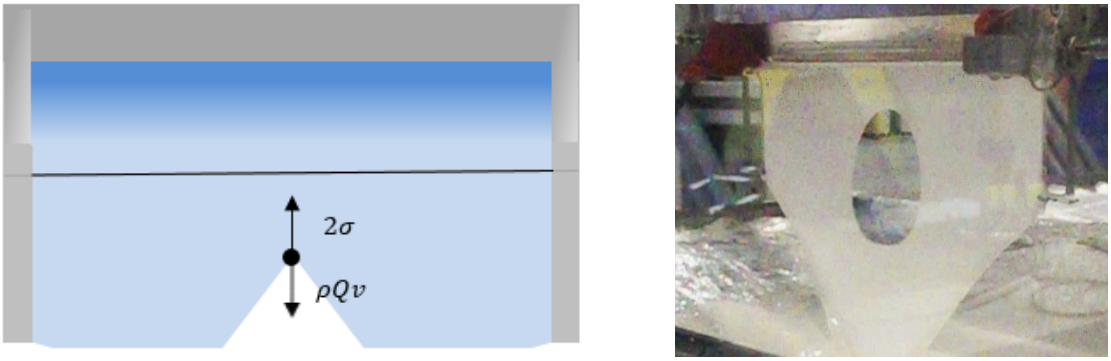

Figure 9 - Disintegrating curtain. Force balance that shows: Inertia of falling liquid sheet must balance surface tension of both free surfaces (left). Growing hole in a curtain (right).

Brown (1961) suggests that (20) must hold at the position of the severest disturbance, directly above the impingement zone [21]. This results in the use of v_{imp} for the velocity in the Weber number. Although there are reports of stable curtains below this value, it can give a good indication for daily problems and was therefore used in this thesis. Brown furthermore mentioned the importance of a high impingement velocity for successful Curtain Coating, which can be controlled mostly by the curtain falling height [21]. The curtain falling height is, in contrary, limited by thinning along the edge guides. Moderate heights often lead to satisfactory results [8,16]. In any case, the process is negatively affected by air transported along with the moving substrate [8,21]. Introduced disturbances can limit the applicability of the standard operability criteria, as will be further discussed in section 6.1.4.

The second aspect can be investigated by means of a coating window. The coating window proposed in [8] holds true for high values of the capillary number defined in equation (21). A critical value is not given in the discussion, but in some further description of limiting phenomena of coatability, capillary numbers as low as 0.25 appear. Since in the present study the capillary numbers are one to two orders of magnitude higher, the applicability was supposed. The coating window shows a region inside which successful operation is possible, together with the limiting phenomena. Two parameters are used to describe this area, namely the Reynolds number defined in (22) and the ratio of substrate velocity to impingement velocity (Figure 10).

$$Ca = \frac{\mu_l v_{imp}}{\sigma} \tag{21}$$

$$Re = \frac{\rho_l Q_l}{\mu_l} \tag{22}$$

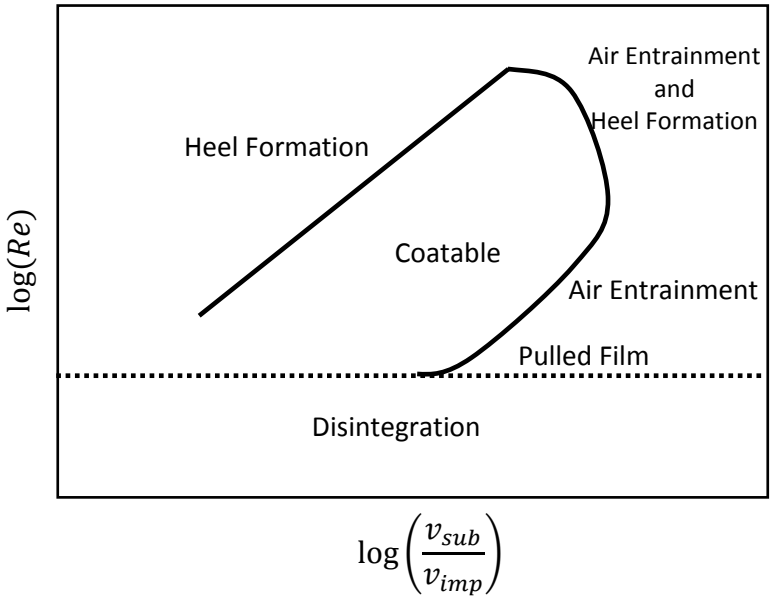

Figure 10 - Operability window with limiting phenomena [8].

The high Reynolds number regime is reached if flow rates are high. The dynamic contact line migrates upstream, and a heel is formed. Often bubbles or other particles are trapped within the heel [8]. The high Reynolds number regime is not of central interest in this thesis, because the focus was set on the successful deposition of low amounts of coating liquid. On the other side of the coating window, the low Reynolds number regime, disintegration of the curtain occurs. Exceeding a certain minimum flow rate, the falling liquid sheet becomes stable and coating can be performed. If the purpose lies on thin film coating, the velocity of the substrate can be increased. By increasing the substrate velocity at low Reynolds numbers, a pulled film effect can eventually be observed. This phenomenon is characterized by a lack of free-fall region and a highly bent curtain (Figure 11) [8]. The appropriate dimensionless parameter is the Weber number, since capillary pressure dominates over inertia in this region. The pulled film region can be avoided by increasing the curtain height or decreasing the surface tension [8].

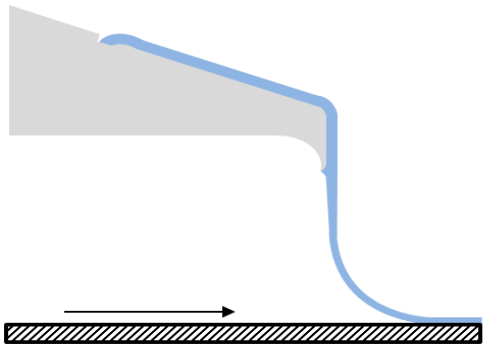

Figure 11 – Pulled Film Effect

Air entrainment can be seen for moderate to high flow rates (or rather Reynolds numbers) und high substrate speed (Figure 12). Although the large pressure at the impingement position delays air entrainment in Curtain Coating compared to other methods, it is still a limit at high substrate speed. It is assumed that air entrainment sets in if the dynamic contact angle reaches 180° [8]. Countermeasures against air entrainment include increasing the impingement velocity (via increasing the curtain falling height) and lowering viscosity [8].

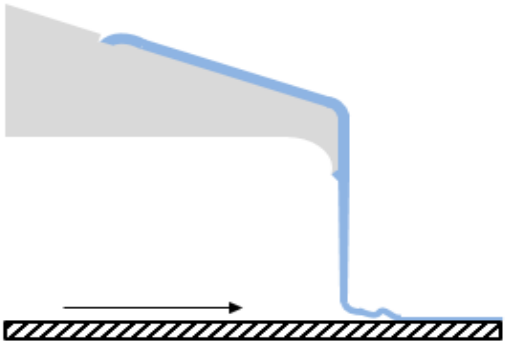

Figure 12 - Air Entrainment

2.2 Drying of Coatings

2.2.1 Basics

Drying of coatings can be done in several ways. In the paper and pulp industry, drying energy for dehumidification of fibers is mainly delivered via the contact with heated drying cylinders. The drying of coatings, however, is handled differently. Coatings are dried using convection and radiation dryers. For the sake of simplicity, only one energy source to investigate the drying process, namely heat transfer under the influence of convection, was used in this thesis. The drying air flow in a convection dryer functions as energy source and carries away the evaporated water. To achieve a minimum influence of the ambient conditions and by considering the geometry of the coating unit, a channel flow was planned. A further discussion on the dryer geometry can be found in 4.2.2.

2.2.2 Channel Flow

Channel flow is the flow of a fluid between two parallel plates at distance h. The appropriate coordinate system is rectangular and for infinitely long, parallel plates in the z-direction (into the plane of the page), the flow is two-dimensional, as illustrated in Figure 13 with the main flow in the positive x-direction.

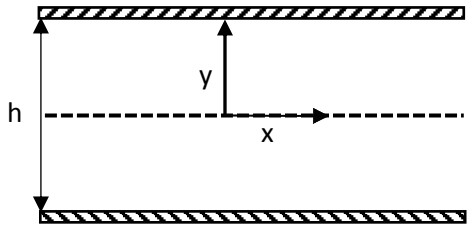

Figure 13 – Geometry for two-dimensional channel flow.

The analysis of flow problems generally starts with balance of mass and linear momentum, as already discussed in section 2.1.1. For two-dimensional, laminar and incompressible flow in rectangular coordinates, conservation of mass can be written in the form [22]:

$$\frac{\partial u}{\partial x}+\frac{\partial v}{\partial y}=0 \tag{23}$$

which is the same as (2), but in two dimensions. Conservation of linear momentum in the x- and y-directions for the flow of a Newtonian fluid reads [22]:

$$x-direction\text{:}\ \frac{\partial u}{\partial t}+u\frac{\partial u}{\partial x}+v\frac{\partial u}{\partial y}=-\frac{1}{\rho}\frac{\partial p}{\partial x}+\nu\left(\frac{\partial^2 u}{\partial x^2}+\frac{\partial^2 u}{\partial y^2}\right)+f_x^B \tag{24}$$

$$y-direction: \frac{\partial v}{\partial t}+u\frac{\partial v}{\partial x}+v\frac{\partial v}{\partial y}=-\frac{1}{\rho}\frac{\partial p}{\partial y}+\nu\left(\frac{\partial^2 v}{\partial x^2}+\frac{\partial^2 v}{\partial y^2}\right)+f_y^B \quad (25)$$

with the fluid velocity in x-direction u, fluid velocity in y-direction v, time t, kinematic viscosity ν and the body forces in the corresponding directions f^B. Simplifications can be made for channel flow based on the following assumptions [22]:

- the flow is fully developed
- the flow is steady
- body forces are negligible
- the fluid cannot penetrate through the walls

Since the flow is fully developed, velocity does not depend on the x-coordinate, and all velocity derivatives in the main flow direction are identically zero ($\frac{\partial u}{\partial x}=0, \frac{\partial v}{\partial x}=0$). The flow is steady and hence the time derivative is also zero ($\frac{\partial}{\partial t}=0$). Body forces are neglected ($f^B=0$). The first point dictates that the continuity equation simplifies to $\frac{\partial v}{\partial y}=0$. This means that the velocity in the y-direction does not depend on the y-coordinate. From the assumption of impenetrable walls, it follows that the velocity in the y-direction is zero at the walls, which implicates that it is zero everywhere. The momentum equations simplify to [22]:

$$x-direction: \frac{\partial p}{\partial x}=\mu\frac{\partial^2 u}{\partial y^2} \quad (26)$$

$$y-direction: \frac{\partial p}{\partial y}=0 \quad (27)$$

There is no pressure gradient in the y-direction as stated by (27). From the fact that in the equation for the x-momentum no dependency of x appears at the right-hand side, it is instantly known that the pressure gradient in the x-direction is a constant, and (26) can be rewritten to [22]:

$$\frac{\partial^2 u}{\partial y^2}=\frac{1}{\mu}\frac{dp}{dx} \quad (28)$$

After integration, it is found that

$$u(y)=\frac{1}{\mu}\frac{dp}{dx}\frac{y^2}{2}+C_1 y+C_2 \quad (29)$$

With the no-slip condition, which states that the fluid velocity at a wall equals the wall velocity, and realizing that the walls are stagnant, the following boundary conditions appear [22]:

$$u\left(y=\frac{h}{2}\right)=0 \tag{30}$$

$$u\left(y=-\frac{h}{2}\right)=0 \tag{31}$$

Equation (29) becomes [22]:

$$u(y)=\frac{1}{2\mu}\frac{dp}{dx}\left(y^2-\left(\frac{h}{2}\right)^2\right) \tag{32}$$

Since the term in brackets is negative for all y smaller than $h/2$, the pressure must decrease in the positive x-direction. Therefore, it can be called a 'pressure drop', which is often written simply as Δp. This pressure is necessary to sustain the flow in the channel. From the engineering perspective, effort is taken to minimize the pressure drop in all flows and hence minimize the power requirement of pumps or blowers to drive the flow. From the analysis above, it is known that the velocity profile in the channel is parabolic in shape (Figure 14).

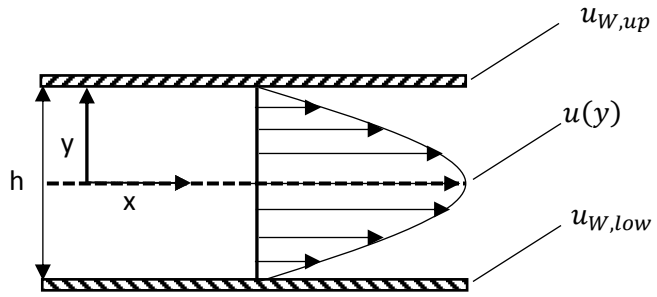

Figure 14 – Fully developed laminar velocity profile in a channel flow.

As mentioned above, fully developed flow is considered, which means that dynamic boundary layers, which develop along the channel walls, have merged. Near the inlet position, this is not the case, and a certain distance must be provided, the dynamic entrance length L_E (Figure 15).

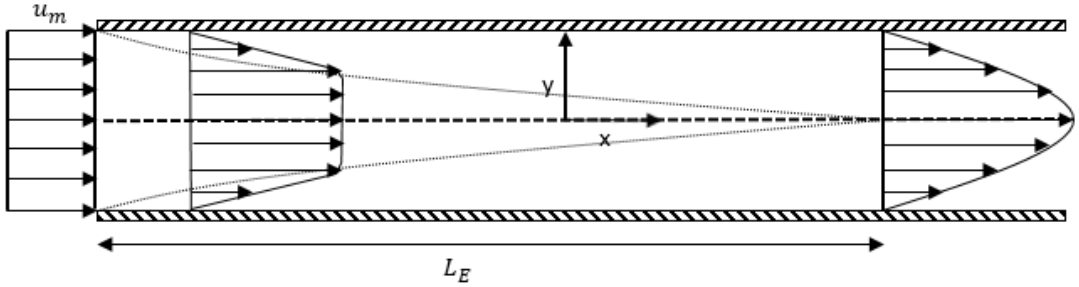

Figure 15 – Developing channel flow. The dotted lines illustrate the growing boundary layers at the channel walls.

The entrance length depends on the flow situation and can be estimated for laminar flow with the well-known relation [23]:

$$\frac{L_E}{h} = 0.056Re \tag{33}$$

with the Reynolds number defined as [23]:

$$Re = \frac{u_m h}{\nu} \tag{34}$$

Here, the mean velocity in the channel u_m, the kinematic viscosity of the fluid ν and the distance between the plates h as the characteristic length were used.

2.2.3 Pressure Drop in Internal Flow

As mentioned above, according to the flow situation, a certain pressure drop occurs, which has to be overcome to drive the flow. In the case of laminar channel flow along smooth walls, the Darcy-Weisbach equation describes the pressure drop [24]:

$$\Delta p = \lambda \frac{\rho u_m^2}{2} L_{channel}/D_h \tag{35}$$

with the hydraulic diameter defined as $D_h = 4A_{cross}/U_{channel}$ with the cross sectional area of the channel A_{cross} and the perimeter of the channel $U_{channel}$, the channel length $L_{channel}$ and the friction factor λ calculated from [24]:

$$\lambda = k\frac{64}{Re} \tag{36}$$

The constant k accounts for the ratio between channel width and channel height. For ducts in which the upper and lower plates are much closer together than the side walls, Idel'chik (1966) suggests using $k = 1.5$ [24].

For some applications, pressure loss can be used to accomplish required conditions. For example, uniformly distributing a fluid over a cross-sectional area by installation of internals, a sudden change of flow direction, or a combination of both. The situation occurs, for instance, when a pipe of small cross-sectional area enters a channel of much larger cross-section or different geometry. If only a small entrance length can be provided, and uniform distribution along the larger cross section is necessary, introducing a pressure drop is inevitable. Consider the following example (Figure 16):

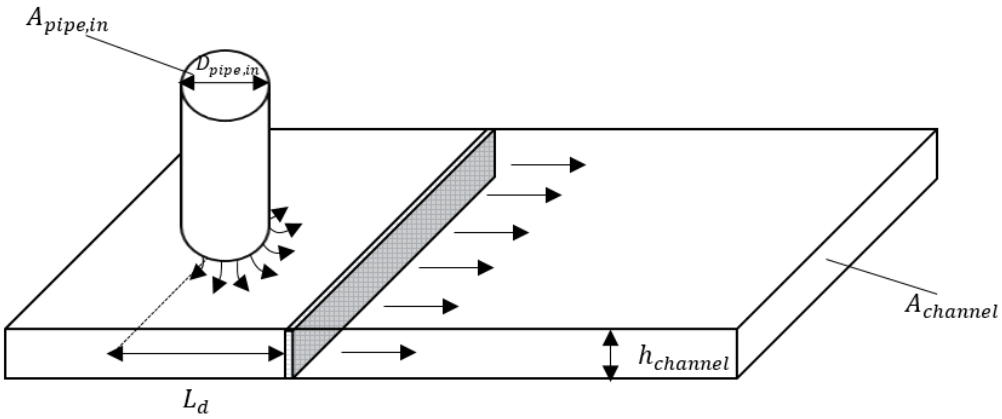

Figure 16 – Flow from a thin pipe enters a channel of larger cross section, with installed grid across the channel width.

According to Idel'chik (1966), the resistance coefficient due to the inlet situation can be estimated as [25]:

$$\zeta = N_0 + 0.7\zeta_{grid}\left(\frac{A_{pipe,in}}{A_{channel}}\right)^2 + 0.1 + \left(2 - 20\frac{L_d}{h_{channel}}\right) \tag{37}$$

with the constant N_0 to describe the inlet flow, which for a straight inlet pipe is 1.06, and ζ_{grid} as the resistance coefficient of the grid. The second term goes to zero for increasing porosity of the grid. The last term can be neglected for $L_d/h_{channel} < 0.1$. If no grid is installed at all, the resistance coefficient assumes the constant value of 1.16. Like before, the pressure drop is estimated by [25]:

$$\Delta p = \zeta\frac{\rho u_{m,in}^2}{2} \tag{38}$$

2.2.4 Heat Transfer

2.2.4.1 Basics

Heat transport is due to three mechanisms:

1. Heat Conduction
2. Heat Convection
3. Thermal Radiation

Especially points one and two are of interest for this thesis and are discussed in the following sections. As before, the discussion starts from an equation of change, namely the thermal energy equation in terms of enthalpy [26]:

$$\rho \frac{dh}{dt} = \frac{dp}{dt} + \Phi_\mu - (\mathbf{\nabla} \cdot \mathbf{q}) + \dot{q}_Q \tag{39}$$

By knowing that the enthalpy of an ideal gas can be rewritten as [26]:

$$h = c_p T \tag{40}$$

and introducing Fourier's law of heat conduction [26]:

$$\mathbf{q} = -\lambda \mathbf{\nabla} \mathrm{T} \tag{41}$$

the equation for a two-dimensional problem with constant specific heat capacity c_p reads [26]:

$$\rho c_p \left(\frac{\partial T}{\partial t} + u\frac{\partial T}{\partial x} + v\frac{\partial T}{\partial y}\right) = \left(\frac{\partial p}{\partial t} + u\frac{\partial p}{\partial x} + v\frac{\partial p}{\partial y}\right) + \Phi_\mu + \lambda\left(\frac{\partial^2 T}{\partial x^2} + \frac{\partial^2 T}{\partial y^2}\right) + \dot{q}_Q \tag{42}$$

The left-hand side tells about the time dependency of temperature and involves the convective transport part. The first term on the right-hand side tells about reversible consumption or production of enthalpy via expansion or compression. The second term is the gain of thermal energy via dissipation of mechanical energy. The third term gives information about heat conduction, and the last term is the rate of heat input due to internal sources, e.g. by chemical reactions. The following simplifications are made for the air flow in the drying process in consideration:

- incompressible flow
- no viscous dissipation

Via these simplifications, the thermal energy equation is given by:

$$\rho c_p \left(\frac{\partial T}{\partial t} + u\frac{\partial T}{\partial x} + v\frac{\partial T}{\partial y}\right) = \lambda\left(\frac{\partial^2 T}{\partial x^2} + \frac{\partial^2 T}{\partial y^2}\right) + \dot{q}_Q \tag{43}$$

2.2.4.2 Heat Conduction

For fluids at rest and solids, the velocity is zero, and equation (43) simplifies to [26]:

$$\frac{\partial T}{\partial t} = \frac{\lambda}{\rho c_p}\left(\frac{\partial^2 T}{\partial x^2} + \frac{\partial^2 T}{\partial y^2}\right) + \frac{1}{\rho c_p}\dot{q}_Q \tag{44}$$

Transient problems of heat conduction are described with this equation, as, for example, the substrate temperature of a drying sheet of cardboard. For the case of a solid sheet within a drying channel, which is insulated on all walls except the contact area with the drying fluid, the heat is transferred from the drying gas across this contact area only. Further information for this specific problem statement are given in chapter 2.3.

2.2.4.3 Heat Convection

For fluids in motion, the velocity is non-zero, and convection has therefore to be included in the thermal energy balance. For a steady-state process without internal energy sources, the thermal energy equation (43) reduces to [26]:

$$\rho c_p \left(u \frac{\partial T}{\partial x} + v \frac{\partial T}{\partial y} \right) = \lambda \left(\frac{\partial^2 T}{\partial x^2} + \frac{\partial^2 T}{\partial y^2} \right) \tag{45}$$

For flow past bodies or within ducts, the temperature is affected mainly within a layer near the solid surface. As before for velocity, internal flow can be divided into thermal entrance and developed regions since boundary layer growth is limited by the distance of the plates. For the case that the upper channel plate is perfectly insulated, where the lower plate has a constant temperature below the fluid temperature, and the entering fluid temperature is uniform at T_{in}, a sketch is given in Figure 17 [27]:

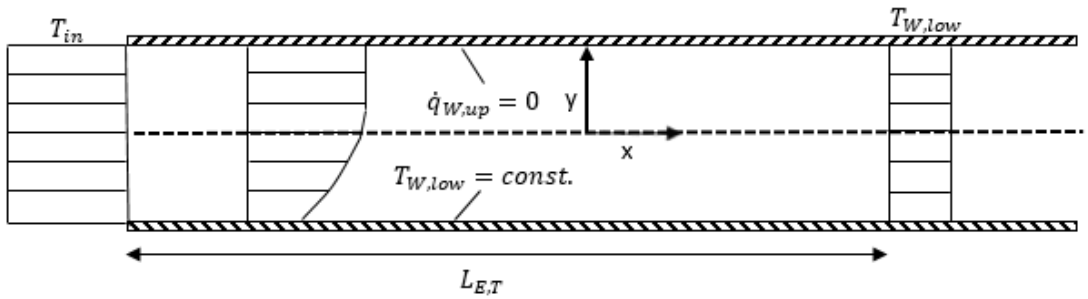

Figure 17 – Thermal entrance region in channel flow for the case explained in the text [27].

The corresponding thermal entrance length can be estimated by the following equation [27]:

$$\frac{L_{E,T}}{h} = 0.056 RePr \tag{46}$$

with the Prandtl number defined as [27]:

$$Pr = \frac{\mu c_p}{\lambda} \tag{47}$$

with the dynamic viscosity μ, the specific heat capacity c_p and the thermal conductivity λ of the fluid. For most gases at moderate temperatures, it is around 0.7. The Prandtl number can be understood as the ratio of kinematic viscosity to thermal diffusivity and hence compares the thicknesses of the dynamic boundary layer and the thermal boundary layer. To quantify heat transferred under the influence of convection, the so-called heat transfer coefficient is used. It appears in Newton's cooling law and relates the heat flux to a temperature difference [26]. More specific for the entrance region as shown in Figure 17, the temperature difference

between the undisturbed fluid (outside the boundary layer) and the lower channel wall temperature is used.

$$\dot{q} = \alpha(T_{W,low} - T_{in}) \tag{48}$$

with the heat flux $\dot{q}$, the heat transfer coefficient α, the lower channel wall temperature $T_{W,low}$ and the fluid temperature outside the boundary layer T_{in}. From the no-slip condition mentioned in chapter 2.2.2 it is known that the velocity at the wall is exactly the wall velocity, which is zero for the considered case. This means the heat transfer to the wall is solely due to conduction, which can be written by Fourier's law [26] as

$$\dot{q} = -\lambda \frac{\partial T}{\partial y}\bigg|_{y=0} \tag{49}$$

Combining (48) and (49), and non-dimensionalizing by using the following scales [26]:

$$y^* = \frac{y}{L},\ \Theta^* = \frac{T - T_{in}}{T_{W,low} - T_{in}} \text{ and } \Theta_0 = T_{W,low} - T_{in}$$

enables the Nusselt number to be identified as [26]:

$$Nu = \frac{\alpha L}{\lambda} = -\frac{\partial \Theta^*}{\partial y^*}\bigg|_{y^*=0} \tag{50}$$

The Nusselt number gives the ratio between heat transferred under convective influence compared to heat transported purely by conduction. Another interpretation is the temperature gradient in the y-direction directly at the wall. The Nusselt number depends on the flow situation, which is characterized for the present case by the Reynolds number. For fully developed flow, the characteristic length is the channel height h. The heat transfer coefficient, and consequently the Nusselt number, within the entrance region depends on the x-position, which is not the case for fully developed flow. The Nusselt number is highest directly after the start of boundary layer growth, since the temperature gradient in the y-direction is highest at minimum boundary layer thickness. This explains the more intensive heat transfer in this region.

2.2.4.4 Lumped Capacitance Method

To familiarize the important method of lumped capacitance, consider a one-dimensional problem of unsteady heat conduction in a solid which is perfectly insulated at $x = 0$ and in contact with a fluid of temperature T_F at $x = d$. The initial temperature of the solid is T_0 (Figure 18).

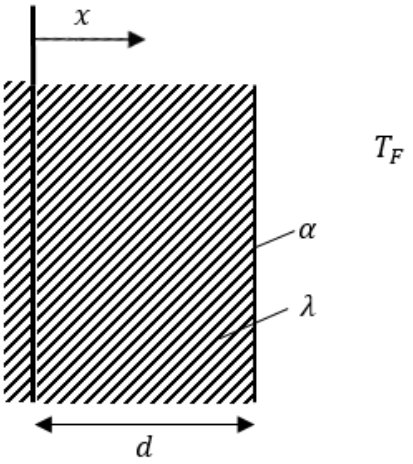

Figure 18 – Solid that is insulated at x=0 and in contact with fluid at the other side x=d.

The corresponding thermal energy equation for this problem reads [26]:

$$\frac{\partial T}{\partial t} = \frac{\lambda}{\rho c_p}\frac{\partial^2 T}{\partial x^2} \tag{51}$$

Non-dimensionalization is done to obtain the following quantities [26]:

$$x^* = \frac{x}{d},\ \Theta^* = \frac{T-T_F}{T_0-T_F} \text{ or } T^* = \frac{T}{T_0}$$

and leads to the following form of the equation with $a = \lambda/(\rho c_p)$ [26]:

$$\frac{\partial T^*}{\partial\left(\frac{at}{d^2}\right)} = \frac{\partial^2 T^*}{\partial x^{*2}} \tag{52}$$

The non-dimensional time on the left-hand side is called the Fourier number [26]:

$$Fo = \frac{at}{d^2} \tag{53}$$

To solve equation (52), boundary conditions have to be applied which state that all the heat transferred under the influence of convection from the fluid has to be transported in the solid via conduction at the solid surface [26]:

$$-\lambda \frac{\partial T}{\partial x}\Big|_{x=d} = \alpha(T(x=d) - T_F) \tag{54}$$

Insulation at x=0 is accounted for by:

$$\frac{\partial T}{\partial x}\Big|_{x=0} = 0 \tag{55}$$

After non-dimensionalization of (54), another characteristic number appears, the Biot number [26]:

$$Bi = \frac{\alpha d}{\lambda} \tag{56}$$

which looks similar to the Nusselt number, but here λ is the thermal conductivity of the solid. It characterizes the intensity of convective heat transfer from the fluid compared to the ability to transport the heat within the solid. A large Biot number means that substantial temperature gradients within the solid appear. After sufficiently long time, a uniform temperature within the solid is reached. Small Biot numbers, on the other hand, correspond to a small temperature gradient within the solid throughout the heat transfer process. Figure 19 depicts the case $T_F > T_0$ after a short duration of the heat transfer process [26]:

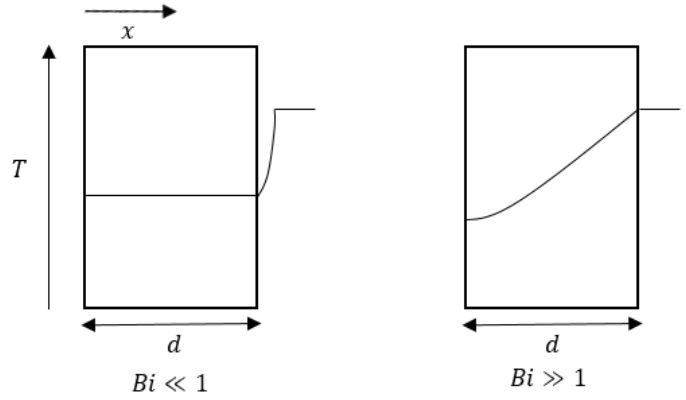

Figure 19 - Temperature profiles in a solid in contact with fluid of higher temperature at low (left) and high (right) Biot numbers.

It is obvious from Figure 19 that even for short duration of the heat transfer process, the temperature is nearly constant within the solid for small Biot numbers. This leads to the important simplification that, for small Biot numbers, the solid temperature depends on time only, but not on position in the thickness direction. The geometry is seen as lumped. Evidently, this is the case for highly conductive solids compared to the transferred heat, and if the characteristic length is very small. Mostly the critical value for validity is set to $Bi = 0.1$ for errors in temperature smaller than 5 % [26]. The energy equation then can be written as [26]:

$$-\rho c_p V \frac{dT}{dt} = \alpha A (T - T_F) \tag{57}$$

with the surface of contact between solid and fluid A and the solid volume V.

2.2.5 Mass Transfer

2.2.5.1 Basics

Similar to the considerations in the heat transfer section, one can write a differential equation for two-dimensional mass balance in laminar flow [26]:

$$\rho\left(\frac{\partial w_1}{\partial t}+u\frac{\partial w_1}{\partial x}+v\frac{\partial w_1}{\partial y}\right)=\rho D\left(\frac{\partial^2 w_1}{\partial x^2}+\frac{\partial^2 w_1}{\partial y^2}\right)+\dot{r} \tag{58}$$

with the density ρ, the mass fraction of substance one w_1, the time t, the position coordinates x, y, the velocity in x-direction u, the velocity in y-direction v, the diffusion coefficient D and the mass source or sink $\dot{r}$. The first term on the left-hand side gives the rate of change of the mass concentration of substance one in the considered region. The rest stands for convective transport of substance one. The first term on the right-hand side describes diffusion of substance one, and the second term gives the production or consumption of substance one, e.g. due to chemical reactions.

2.2.5.2 Mass Diffusion

For fluids at rest in equimolar diffusion and in solids, the velocity is zero and the above equation simplifies to [26]:

$$\rho\frac{\partial w_1}{\partial t}=\rho D\left(\frac{\partial^2 w_1}{\partial x^2}+\frac{\partial^2 w_1}{\partial y^2}\right)+\dot{r} \tag{59}$$

2.2.5.3 Mass Convection

In moving fluids, the velocity is non-zero and has therefore to be included in the mass transport equation. For a steady-state process ($\frac{\partial w_1}{\partial t}=0$) without internal mass sources ($\dot{r}=0$), the mass balance equation reduces to:

$$\rho\left(u\frac{\partial w_1}{\partial x}+v\frac{\partial w_1}{\partial y}\right)=\rho D\left(\frac{\partial^2 w_1}{\partial x^2}+\frac{\partial^2 w_1}{\partial y^2}\right) \tag{60}$$

For flow past objects or within ducts, the mass concentration is affected mainly within a layer near the solid surface. As before for velocity and temperature, internal flow can be divided into entrance and developed regions since boundary layer growth is limited by the distance of the plates. For the case that the upper channel plate is perfectly insulated against mass transfer, the mass concentration of substance one directly at the surface of the lower channel plate is higher than the mass concentration of substance one in the entering fluid and the entering fluid mass concentration is uniform at $w_{1,in}$ a sketch is given in Figure 20.

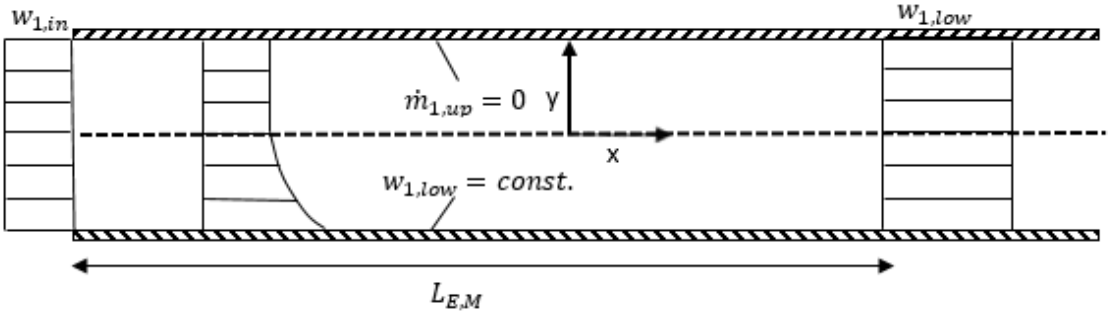

Figure 20– Mass transfer entrance region for channel flow for the case explained in the text [27].

The corresponding mass transfer entrance length can be estimated by the following equation [26]:

$$\frac{L_{E,M}}{h} = 0.056 ReSc \tag{61}$$

with the Schmidt number defined as [26]:

$$Sc = \frac{\nu}{D} \tag{62}$$

with the binary diffusion coefficient D. The Schmidt number is the ratio of kinematic viscosity to mass diffusivities. From the relation above it is clearly seen that the Schmidt number compares the thickness of the dynamic boundary layer and the concentration boundary layer. Analogously to heat transfer, a law can be found to relate the difference in mass concentration of substance one with the mass flux of the substance [26]:

$$\dot{m} = \beta\rho(w_{1,low} - w_{1,in}) \tag{63}$$

The mass transfer coefficient β appears in this equation. Like the Nusselt number, one can identify the Sherwood number as a dimensionless gradient of the mass concentration directly at the wall, where the definition $\rho_1 = \rho w_1$ was applied [26]:

$$Sh = \frac{\beta L}{D} = \left.\frac{\partial \rho_1^*}{\partial y^*}\right|_{y^*=0} \tag{64}$$

with $\rho_1^* = (\rho_1 - \rho_{1,in})/(\rho_{1,low} - \rho_{1,in})$. Another interpretation of the Sherwood number is the ratio of convective to diffusive mass flux at the wall. Again, it depends on the flow situation, which is characterized by Re. For fully developed flow, the characteristic length is the channel height h. The mass transfer coefficient and, consequently, the Sherwood number in the entrance region, depends on the x-position, which is not the case for fully developed flow. The Sherwood number is highest directly after the start of boundary layer growth, since the mass concentration gradient in the y-direction is highest at minimum boundary layer thickness.

2.2.6 Analogy Between Heat and Mass Transfer

Two processes are said to be analogous if they are governed by dimensionless equations of the same form [28]. This can clearly be the case for heat and mass transfer as can be seen by the similar balance equations and dimensionless numbers that appeared in the foregoing chapters. If, moreover, the boundary conditions are similar, for example if the same geometry is considered, one can find mass transfer parameters from heat transfer experiments or vice versa. The central point of interest in a convective transport process is to find the transfer coefficients. Consider a process in which the Nusselt number is given and fluid properties are known. The Sherwood number can then be estimated by [28]:

$$Sh = Nu\left(\frac{Sc}{Pr}\right)^{\frac{1}{3}} \tag{65}$$

2.2.7 One-Sided Diffusion – Stefan Diffusion

Consider a one-dimensional mass transport problem of a binary mixture, as given in Figure 21 [26].

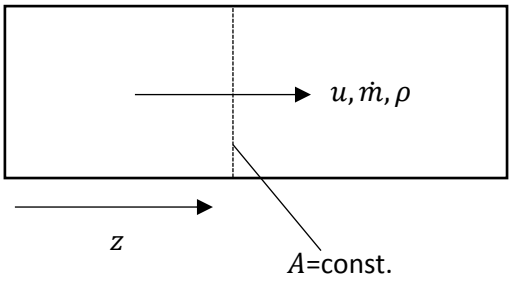

Figure 21 - One-dimensional mass transport

The fluid moves with the velocity u and the mixture density ρ, which leads to the overall mass flux $\dot{m}$. The overall mass flux is given by [26]:

$$\dot{m} = \rho u \tag{66}$$

and the mass flux of substance one reads [26]:

$$\dot{m}_1 = \rho w_1 u - \rho D \frac{dw_1}{dz} \tag{67}$$

with the first term to consider convective mass transport and the second term to consider diffusive mass transport. In one-sided diffusion, which means that $\dot{m} = \dot{m}_1$ and $\dot{m}_2 = 0$, the following relation is found [26]:

$$\rho u = \rho w_1 u - \rho D \frac{dw_1}{dz} \tag{68}$$

After separation of variables one finds the following equation which can be integrated if the integration boundaries are known. Validity is given for the case of constant mass flux, diffusion coefficient and mixture density:

$$\int \frac{dw_1}{1 - w_1} = -\frac{\dot{m}}{\rho D} \int dz + K \tag{69}$$

Stefan diffusion occurs, e.g. in the drying of wet paper sheets. If the wet substrate is saturated with air, there is just one flow that is the evaporated water into the drying air. Air flow into the wet substrate is neglected. This strategy is often used to describe the paper drying process [29,30].

2.2.8 Drying of Paper Materials

The main component of paper is cellulose, which is also the most abundant polymer on the planet. The chemical structure of cellulose is given in Figure 22.

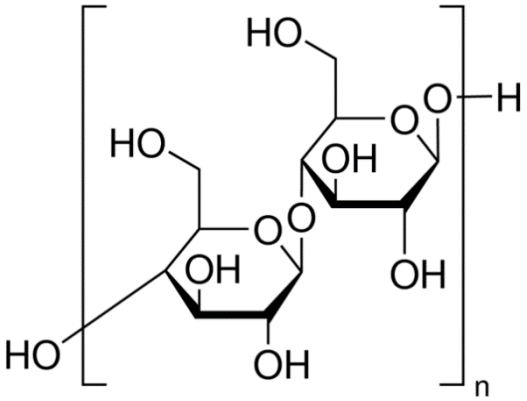

Figure 22 - Molecular structure of Cellulose

The hydrophilic character of cellulose and the porous nature of paper materials may be two reasons for the hygroscopic behavior during the drying process. A substrate is called hygroscopic if, besides the free water, also bound water is present. All processes which support the binding are summarized in the term 'sorption' [31]. Hygroscopic materials show a decline of vapor pressure of the present liquid as compared to saturation pressure below a certain moisture load. Within this region, the vapor pressure is not only a function of temperature, but also a function of the moisture load of the material. The reduced vapor pressure is consequently described by a sorption isotherm [29]:

$$p_{vap} = \varphi_{sorp} p_{sat} \tag{70}$$

At a high moisture load of the porous solid, the removed water is explicitly free water, and the required energy is virtually the heat of vaporization of water. However, in the hygroscopic region, the fraction of bound water on the overall water removed rises with decreasing moisture load of the substrate. This leads to a decrease of vapor pressure, which is accounted for by a decreasing value of φ_{sorp} in equation (70) with decreasing moisture load. Bound water requires an additional amount of energy, called the net isosteric heat of sorption, which in turn depends on the moisture load of the substrate, since water can be bound in several ways [29]. The individual states of bound water differ in binding energy, and relative amounts of the states in the substrate vary with total moisture content of the solid. Strongly bound water tends to be removed at last. These effects lead to a substantial increase of drying effort, in terms of time and energy, to reach low water contents.

2.3 Modeling of Cardboard Drying

2.3.1 Governing Equations

The first step in modeling the drying of cardboard is the formulation of the transport equations. The transport processes were assumed to be constant along the substrate width (into the plane of the page in Figure 23 and Figure 24). This is justified in section 4.2.2.2 due to the special dryer design, which ensures uniform flow over the substrate width. From precalculations it is known that the Lumped Capacitance method for heat transfer is valid since $Bi < 0.1$ during the entire process. This means that heat conduction in thickness direction of the substrate can be neglected, which is mainly due to the low thickness of the sheets. Figure 23 was set up to evaluate the energy balance.

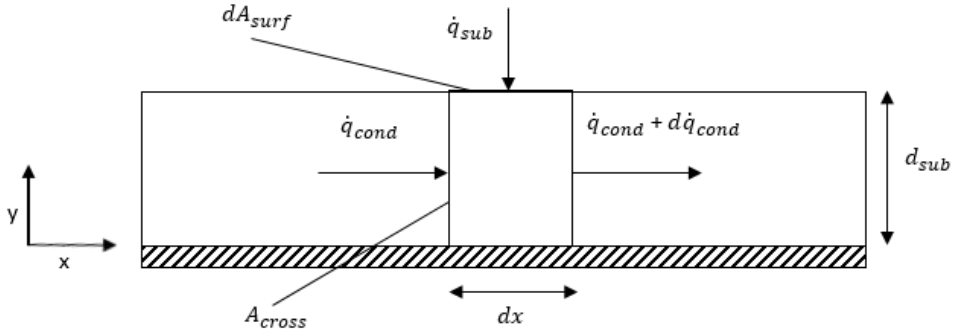

Figure 23 – Differential control volume of cardboard to formulate the energy balance. The dashed line at the bottom indicates the insulated transport plate at which the substrate lies.

The sketch shows a differential control volume of the cardboard of the cross-sectional area A_{cross}, the length dx and the cardboard thickness d_{sub}. The differential surface area between the cardboard and the drying air is dA_{surf}. In the solid, a conductive heat flux $\dot{q}_{cond}$ and through the surface area a net convective heat flux from the drying air into the substrate $\dot{q}_{sub}$ are

accounted for. The underside of the cardboard is insulated; therefore, no heat loss or gain is seen at this position. Consequently, the thermal energy balance reads:

$$\rho_{sub} c_{p,sub} \frac{\partial T_{sub}}{\partial t} = \lambda_{sub} \frac{\partial^2 T_{sub}}{\partial x^2} + \frac{1}{d_{sub}} \dot{q}_{sub} \tag{71}$$

with the density of the wet substrate ρ_{sub}, the isobaric specific heat capacity of the wet substrate $c_{p,sub}$, the substrate temperature T_{sub} and the thermal conductivity of the wet substrate λ_{sub}. For mass transport, the applicability of the Lumped Capacitance method was assumed, since an untreated cardboard of high porosity and low thickness was used. A sketch of the process is given in Figure 24.

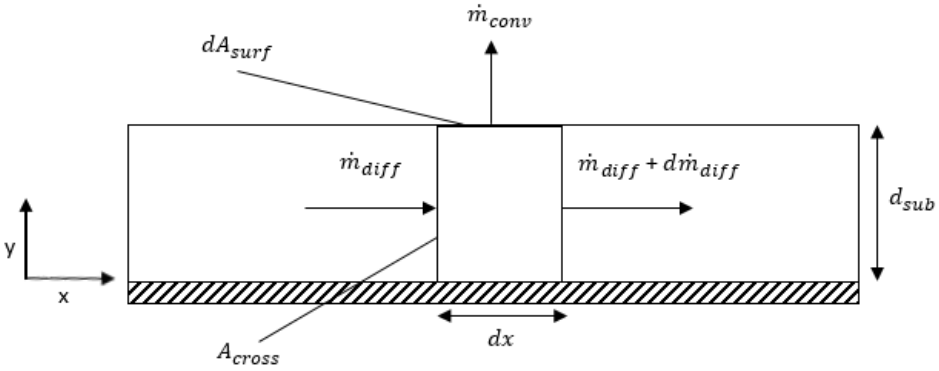

Figure 24 – Differential control volume of cardboard to formulate the mass balance. The dashed line at the bottom indicates the insulated transport plate at which the substrate lies.

The geometrical parameters have the same meanings as in Figure 23. A diffusive flux within the substrate $\dot{m}_{diff}$ and a convection mass flux away from the substrate into the drying air $\dot{m}_{conv}$ are accounted for. Again, the underside of the sheet is perfectly isolated against mass transport. The mass transport balance reads:

$$\frac{\partial \rho_{sub,H2O}}{\partial t} = D_{sub,H2O} \frac{\partial^2 \rho_{sub,H2O}}{\partial x^2} + \frac{1}{d_{sub}} \dot{m}_{conv} \tag{72}$$

with the mass concentration of water in the substrate $\rho_{sub,H2O}$ and the binary diffusion coefficient of water in the plane of the sheet $D_{sub,H2O}$.

2.3.2 Modeling of Transient Drying of a Plane Geometry

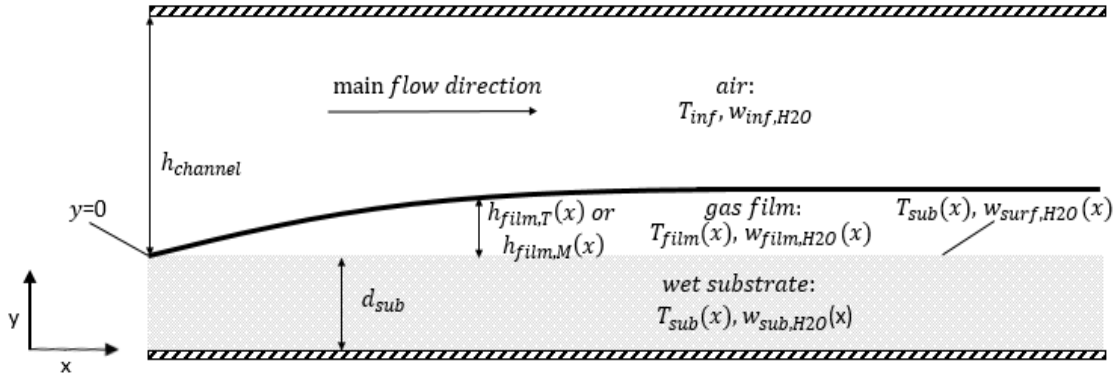

Figure 25 – Transient drying of the plane substrate in channel flow. Flow is dynamically developed, but within thermal and mass transfer entrance region.

Based on the work of Abramzon and Sirignano (1989) that discussed the vaporization of liquid droplets, a model was derived to describe the drying of wet substrates of plane geometry in a drying channel [32]. This model is presented in the current section, starting with the process sketch in Figure 25.

2.3.2.1 Gas Phase Analysis

Abramzon and Sirignano used the already discussed film theory to describe the vaporization of liquid droplets. As a consequence of the no-slip condition, all the energy transfer to the substrate must be due to conduction:

$$\dot{q}_{conv} = -\lambda_{film} \frac{dT}{dy}\bigg|_{y=0} = \alpha(T_{sub} - T_{inf}) \tag{73}$$

By using the heat conduction equation of a steady process (74):

$$\frac{d^2T}{dy^2} = 0 \tag{74}$$

the temperature distribution can be found by integrating the equation twice, to obtain:

$$T(y) = C_1 y + C_2 \tag{75}$$

Using the boundary conditions of the problem sketch in Figure 25 leads to the temperature distribution:

$$T(y = 0) = T_{sub} \tag{76}$$

$$T\left(y = h_{film,T_0}\right) = T_{inf} \tag{77}$$

$$T_{sub} = C_2$$

$$T_{inf} = C_1 h_{film,T_0} + T_{sub} \rightarrow C_1 = \frac{T_{inf} - T_{sub}}{h_{film,T_0}}$$

$$T(y) = T_{sub} + (T_{inf} - T_{sub}) \frac{y}{h_{film,T_0}} \tag{78}$$

The first derivative in y-direction gives the temperature gradient, which is constant within the gas film and reads:

$$\frac{dT}{dy} = \frac{(T_{inf} - T_{sub})}{h_{film,T_0}} \tag{79}$$

Insertion in (73) gives:

$$\dot{q}_{conv} = -\lambda_{film} \frac{(T_{inf} - T_{sub})}{h_{film,T_0}} = \alpha(T_{sub} - T_{inf}) \tag{80}$$

The Nusselt number for a fully developed channel flow is defined by:

$$Nu_0 = \frac{h_{channel}\alpha}{\lambda_{film}} \tag{81}$$

Combining equations (80) and (81) leads to a statement of thermal film thickness based on the Nusselt number, which reads:

$$h_{film,T_0} = \frac{h_{channel}}{Nu_0} \tag{82}$$

Analogously the film thickness for mass transfer can be derived by using the Sherwood number and is given by:

$$h_{film,M_0} = \frac{h_{channel}}{Sh_0} \tag{83}$$

This means that it is necessary to estimate the Nusselt number via adequate correlations to find information about heat transfer from the gas phase. The whole drying chamber lies in the thermal entrance region of the channel flow, but the dynamic boundary layer is fully developed. Solutions for the considered case exist for different boundary conditions [27]:

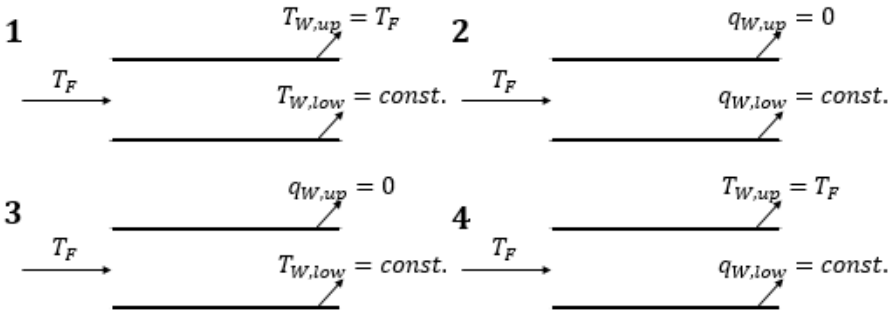

Figure 26 - Fundamental boundary conditions for channel flow defined by Shah and London (1978) [27].

As discussed in section 4.2.2, the upper channel plate is insulated. The lower plate is the substrate with constant initial temperature. For sure, the uniform substrate temperature is not held during the whole process, but experience showed that the boundary conditions number three in Figure 26 provided satisfactory results. Shah and London (1978) referred to these boundary conditions as 'boundary conditions of the third kind'. The corresponding Nusselt number correlation is given by [27]:

$$Nu_0 = \frac{1}{4x^*}\log\left(\frac{1}{\theta_m}\right) \tag{84}$$

with $\theta_m = (T_{m,x*} - T_{W,low,x*})/(T_{W,up,x*} - T_{m,x*}) = 3\sum_{i=0}^{n}\left(G_i/{\lambda_i}^2\right)e^{-(32/3){\lambda_i}^2 x^*}$ as dimensionless mean temperature difference and the position scaled by the thermal entrance length $x^* = x/L_{E,T}$. The first ten numerical values of the eigenvalue λ_i and the eigenfunction G_i were used ($n = 10$). The values were taken from Shah and London (1978) [27]. The trend of the Nusselt number for typical conditions is shown in Figure 27.

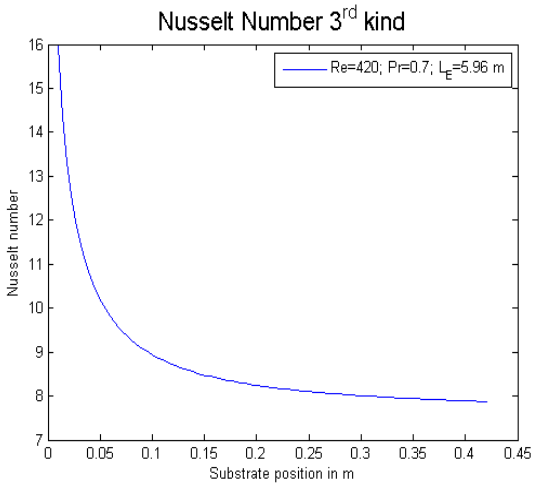

Figure 27 - Typical trend for Nusselt number with boundary conditions of the third kind based on equation (84).

The applicability of the analogy between heat and mass transfer was assumed and the Sherwood number was calculated according to equation (65). However, Abramzon and Sirignano pointed out that the thickness of both boundary layers and hence the dimensionless parameters are influenced by the flow of water vapor out of the substrate. They introduced modified dimensionless numbers, which were adapted for the present situation as shown below:

$$h_{film,T} = \frac{h_{channel}}{Nu^*} \tag{85}$$

$$h_{film,M} = \frac{h_{channel}}{Sh^*} \tag{86}$$

2.3.2.2 Mass Transfer During Drying

The approach of Stefan is often used to describe the drying process as discussed in 2.2.7. The integrated form of (69) with the corresponding boundaries reads:

$$\frac{h_{film,M}}{\rho_{film} D_{film,H2O}} \dot{m}_{conv} = ln\left(\frac{1 - w_{inf,H2O}}{1 - w_{surf,H2O}}\right) \tag{87}$$

The definition of the Spalding mass transfer number is given by [32]:

$$B_M = \left(\frac{w_{surf,H2O} - w_{inf,H2O}}{1 - w_{surf,H2O}}\right) \tag{88}$$

Combining (87) and (88) and introducing the relation of the film thickness including the modified Sherwood number (86) leads to:

$$\dot{m}_{conv} = \frac{\rho_{film} D_{film,H2O}}{h_{channel}} Sh^* \ln(1 + B_M) \tag{89}$$

Since the modified Sherwood number is unknown, a correction factor to relate the modified to the standard relation, which is given by Abramzon and Sirignano (1989), has to be applied [32]:

$$F_M = \frac{h_{film,M}}{h_{film,M_0}} = \frac{Sh_0}{Sh^*} = (1 + B_M)^{0.7} \frac{\ln(1 + B_M)}{B_M} \tag{90}$$

and finally, the equation for the mass flux reads:

$$\dot{m}_{conv} = \frac{\rho_{film} D_{film,H2O}}{h_{channel}} Sh_0 \frac{B_M}{(1 + B_M)^{0.7}} \tag{91}$$

2.3.2.3 Heat Transfer During Drying

The overall heat input into the substrate is given by:

$$\dot{q}_{conv} = -\lambda_{film}\frac{dT}{dy} + \dot{m}_{conv}[h_{H2O,g}(T_{sub}) + c_{p,H2O,g}(T - T_{sub})] \quad (92)$$

$$\dot{q}_{conv} = \dot{m}_{conv}h_{H2O,l}(T_{sub}) - \dot{q}_{sub} \quad (93)$$

Subtraction of equation (93) from (92) gives the net heat input into the substrate. From the Lumped Capacitance assumption, it is known that temperature gradients in the thickness direction of the substrate can be neglected, which simplifies the last term in (92):

$$\dot{q}_{sub} = \lambda_{film}\frac{dT}{dy}\Big|_{y=0} - \dot{m}_{conv}[\Delta h_{H2O,vap}(T_{sub}) + c_{p,H2O,g}(T_{sub} - T_{sub})] \quad (94)$$

By using the result of the temperature gradient (79) it is found:

$$\dot{q}_{sub} = \lambda_{film}\frac{(T_{inf} - T_{sub})}{h_{film,T}} - \dot{m}_{conv}\Delta h_{H2O,vap}(T_{sub}) \quad (95)$$

which is the heat to increase the substrate temperature. The real thermal film thickness is unknown and a correction factor must be introduced. For this purpose, the Spalding heat transfer number is defined as [32]:

$$B_T = (1 + B_M)^{\emptyset} - 1 \quad (96)$$

with the exponent $\emptyset = \frac{c_{p,H2O,g}}{c_{p,film}}\left(\frac{Sh^*}{Nu^*}\right)\left(\frac{1}{Le}\right)$ that includes another dimensionless number, the Lewis number $Le = \lambda_{film}/\left(\rho_{film}D_{film,H2O}c_{p,film}\right)$. The influence of the Stefan flow on the thermal boundary layer can be written analogously to the mass transfer considerations as [32]:

$$F_T = \frac{h_{film,T}}{h_{film,T_0}} = \frac{Nu_0}{Nu^*} = (1 + B_T)^{0.7}\frac{\ln(1 + B_T)}{B_T} \quad (97)$$

The equation for net heat flux into the substrate becomes:

$$\dot{q}_{sub} = \lambda_{film}\frac{(T_{inf} - T_{sub})}{h_{channel}}Nu^* - \dot{m}_{conv}\Delta h_{H2O,vap}(T_{sub}) \quad (98)$$

The important difference to the relation of Abramzon and Sirignano is that for vanishing mass flux, the heat flux approaches an undisturbed heat flux. The relation of Abramzon and Sirignano rather gives a vanishing heat flux for this case. This is true only for drying of pure liquids, but not for the case of a wet substrate. Equation (98) holds only for non-hygroscopic substances. Paper, however, is not at all a non-hygroscopic substance, and therefore sorption

energy must be introduced in this equation. The final equation for the net heat flux into the substrate is given by:

$$\dot{q}_{sub} = \lambda_{film} \frac{(T_{inf} - T_{sub})}{h_{channel}} Nu^* - \dot{m}_{conv}[\Delta h_{H2O,vap}(T_{sub}) + \Delta h_{sorp}(T_{sub})] \quad (99)$$

As recommended by Abramzon and Sirignano the one-third rule was used to calculate the reference temperature and concentration in the gas film that reads [32]:

$$T_{film} = T_{sub} + \frac{(T_{inf} - T_{sub})}{3} \quad (100)$$

$$w_{film,H2O} = w_{surf,H2O} + \frac{(w_{inf,H2O} - w_{surf,H2O})}{3} \quad (101)$$

2.3.3 Initial and Boundary Conditions

The solution of the differential equations for heat and mass transport in the substrate is subject to initial and boundary conditions. As initial conditions, the substrate temperature and the mass concentration of water in the substrate are set and assumed to be constant. This is formulated by:

$$T_{sub} = const., \rho_{sub,H2O} = const. \text{ at } t = 0 \quad (102)$$

The substrate is spatially discretized into n difference volumes along the substrate length. The position of the difference volumes is characterized by an index i which runs from one to n along the main flow direction. Further details to the discretization procedure are given in 2.3.4. The upstream edge of the substrate is not in direct contact with the lower plate of the dryer channel. A stagnant air film is positioned between the lower dryer plate and the upstream edge of the substrate. The air at the surface of the lower dryer plate has the constant temperature T_{inf} and the moisture content $w_{H2O,inf}$. The air at the surface of the substrate has the local substrate temperature $T_1 = T_{sub,1}$ and the moisture content $w_{H2O,1}$, which is determined as explained in 2.2.8 by using the local substrate temperature and the local water fraction of the substrate. The distance between the lower dryer plate and the substrate $x_0 = 1\ mm$. A sketch of the substrate in the dryer with focus on the boundary conditions is shown in Figure 28.

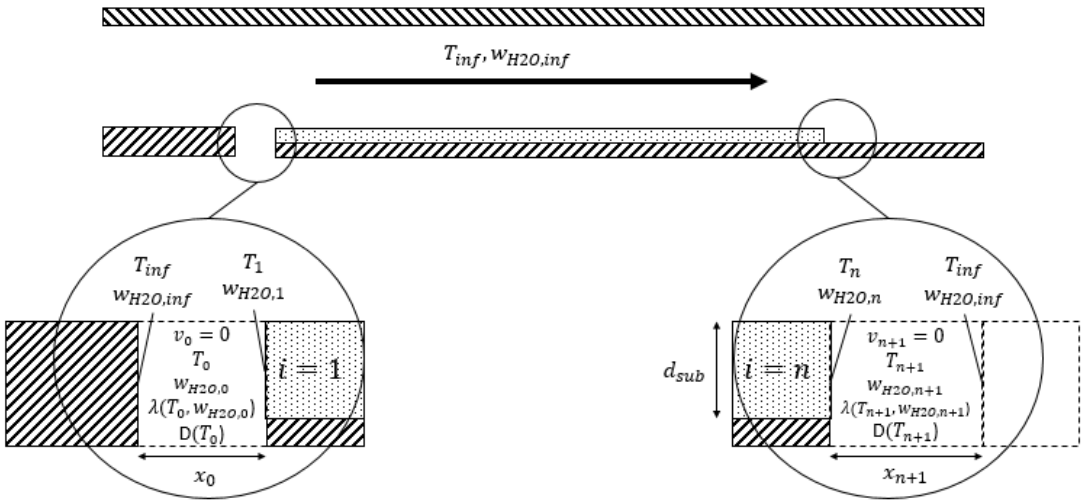

Figure 28 - The substrate at the drying position. The situation on the boundaries is outlined in the circles. The arrow indicates the flow of the drying air.

Since the considered air film is stagnant, the temperature and moisture content profiles are linear along x_0. The mean temperature T_0 and the mean moisture content $w_{H2O,0}$ in the stagnant air film are determined by:

$$T_0 = \frac{T_{inf} + T_1}{2}, w_{H2O,0} = \frac{w_{H2O,inf} + w_{H2O,1}}{2} \tag{103}$$

A similar situation is assumed at the downstream substrate edge. A stagnant air film of the length $x_{n+1} = 5d_{sub}$ is assumed. Upstream to the considered air film, the substrate, at the local temperature $T_n = T_{sub,n}$ and the local moisture content of the air at the substrate surface $w_{H2O,n}$, is located. At the downstream end of the considered air film, drying air at the constant temperature T_{inf} and the constant moisture content $w_{H2O,inf}$ is assumed. The situation is shown in Figure 28. The mean temperature T_{n+1} and the mean moisture content $w_{H2O,n+1}$ in the stagnant air film are calculated according to equation (103) with the adapted temperatures and moisture contents as explained above. The transported heat and mass across the upstream edge of the substrate is consequently calculated by:

$$\dot{q}_0 = \lambda \frac{T_{inf} - T_1}{x_0}, \dot{m}_0 = D \frac{\rho_{H2O,inf} - \rho_{H2O,1}}{x_0} \tag{104}$$

with $\rho_{H2O,1} = w_{H2O,1}\ \rho_1$. The transported heat and mass across the downstream edge of the substrate is calculated by:

$$\dot{q}_{n+1} = \lambda \frac{T_{inf} - T_n}{x_{n+1}}, \dot{m}_{n+1} = D \frac{\rho_{H2O,inf} - \rho_{H2O,n}}{x_{n+1}} \tag{105}$$

with $\rho_{H2O,n} = w_{H2O,n}\ \rho_1$.

2.3.4 Discretization

For the bulk of the substrate, a uniform mesh with a step size of Δx was used. At the substrate edges, the step size was reduced to $\Delta x/2$, which is shown in Figure 29.

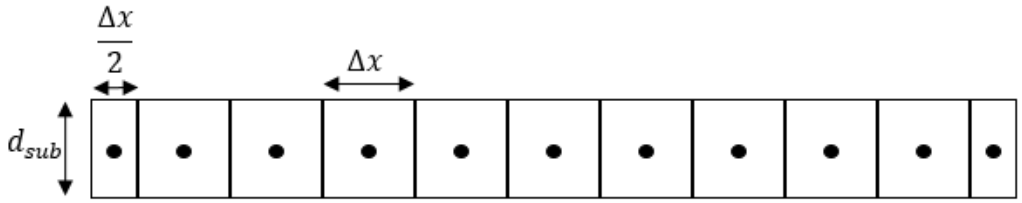

Figure 29 - The discretized substrate with the nodes that mark the substrate positions for the evaluation of parameters to calculate temperature and water concentration.

The second order derivatives in space were discretized in the following way, with subscript i as the position index (the procedure is only shown for the derivatives in the thermal energy balance and was done analogously for the derivatives in the mass balance) [33]:

$$\frac{\partial^2 T_{sub}}{\partial x^2} \approx \frac{\left.\frac{\partial T_{sub}}{\partial x}\right|_{i+1/2} - \left.\frac{\partial T_{sub}}{\partial x}\right|_{i-1/2}}{\Delta x} \tag{106}$$

$$\left.\frac{\partial T_{sub}}{\partial x}\right|_{i+1/2} \approx \frac{T_{sub,\,i+1} - T_{sub,i}}{\Delta x} \tag{107}$$

$$\left.\frac{\partial T_{sub}}{\partial x}\right|_{i-1/2} \approx \frac{T_{sub,i} - T_{sub,i-1}}{\Delta x} \tag{108}$$

with the results:

$$\frac{\partial^2 T_{sub}}{\partial x^2} \approx \frac{T_{sub,i+1} - 2T_{sub,i} + T_{sub,i-1}}{(\Delta x)^2} \tag{109}$$

$$\frac{\partial^2 \rho_{sub,H2O}}{\partial x^2} \approx \frac{\rho_{sub,\,H2O,i+1} - 2\rho_{sub,H2O,i} + \rho_{sub,H2O,i-1}}{(\Delta x)^2} \tag{110}$$

For time discretization, the implicit difference method was used. In this method, the unknown parameters are evaluated at the conditions of the following time step. Figure 30 illustrates, which nodes that are used (orange fields) to update the values of the considered node (green field). The superscript t relates to the current time step, and $t+1$ to the following time step, which is evaluated [33].

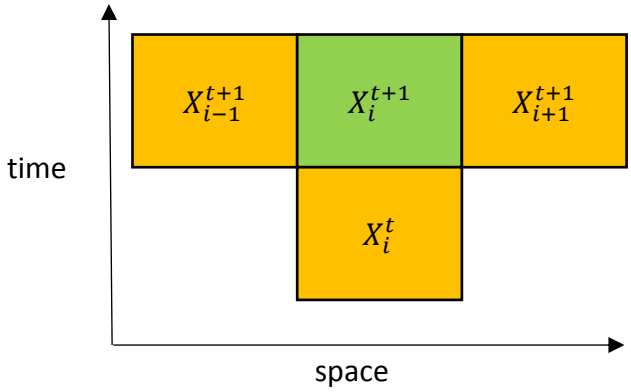

Figure 30 - Implicit difference method update scheme

Time discretization led to the following results:

$$\frac{\partial T_{sub}}{\partial t} \approx \frac{T_{sub,i}^{t+1} - T_{sub,i}^{t}}{\Delta t} \tag{111}$$

$$\frac{\partial \rho_{sub,H2O}}{\partial t} \approx \frac{\rho_{sub,H2O,i}^{t+1} - \rho_{sub,H2O,i}^{t}}{\Delta t} \tag{112}$$

An algebraic set of equations was obtained by the discretization of the differential equations. All constants were summarized in dimensionless numbers, the unknown terms were positioned on the left-hand side, and the known terms on the right-hand side. For the bulk of the substrate, the following equations were found:

$$(1 + 2Fo)T_{sub,i}^{t+1} - FoT_{sub,i+1}^{t+1} - FoT_{sub,i-1}^{t+1} = \frac{\dot{q}_{sub}\Delta t}{d_{sub}\rho_{sub}c_{p,sub}} + T_{sub,i}^{t} \tag{113}$$

$$(1 + 2Fo_m)\rho_{sub,\,H2O,i}^{t+1} - Fo_m\rho_{sub,H2O,i+1}^{t+1} - Fo_m\rho_{sub,H2O,i-1}^{t+1} = \frac{\dot{m}_{conv}\Delta t}{d_{sub}} + \rho_{sub,H2O,i}^{t} \tag{114}$$

with $Fo = \frac{\lambda_{sub}}{\rho_{sub}c_{p,sub}}\frac{\Delta t}{\Delta x^2}$ and $Fo_m = D_{sub,H2O}\frac{\Delta t}{\Delta x^2}$. The situation at the upstream and downstream edge of the substrate is explained in 2.3.3, and a sketch to determine the algebraic equations for heat transport by balancing energy flows at these positions is given in Figure 31 and Figure 32, respectively. Analogy between heat and mass transport was assumed and the algebraic mass transport equations at the boundaries were determined analogously.

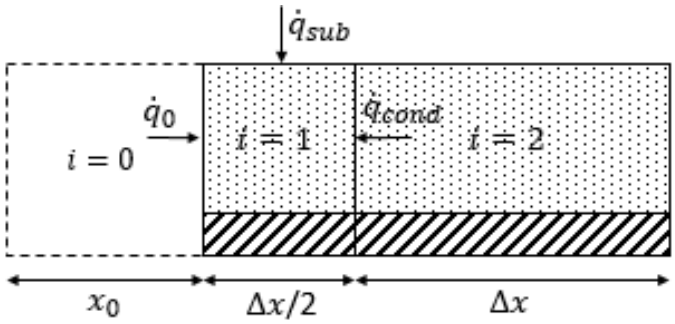

Figure 31 – Sketch of the energy balance at the upstream edge of the substrate.

The algebraic equations at the upstream edge of the substrate read:

$$\left(1+\frac{8}{3}Fo\right)T_{sub,1}^{t+1}-\frac{8}{3}FoT_{sub,2}^{t+1}=T_{sub,1}^{t}+\frac{\Delta t}{\rho_{sub}c_{p,sub}\,\Delta x/2}\dot{q}_0+\frac{\Delta t}{\rho_{sub}c_{p,sub}d_{sub}}\dot{q}_{sub} \quad (115)$$

$$\left(1+\frac{8}{3}Fo_m\right)\rho_{sub,\,H2O,1}^{t+1}-\frac{8}{3}Fo_m\rho_{sub,\,H2O,2}^{t+1}=\rho_{sub,H2O,1}^{t}+\frac{\Delta t}{\Delta x/2}\dot{m}_0+\frac{\Delta t}{d_{sub}}\dot{m}_{conv} \quad (116)$$

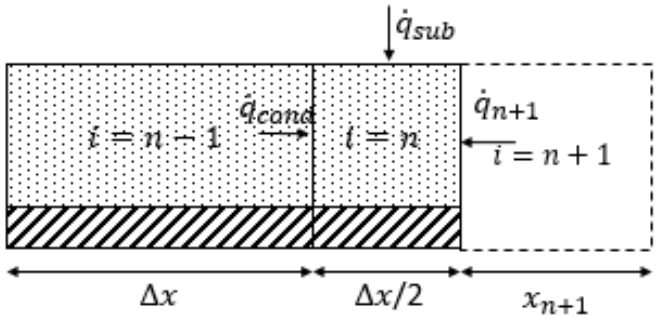

Figure 32 - Sketch of the energy balance at the downstream edge of the substrate.

and the algebraic equations for the downstream edge of the substrate are given by:

$$\left(1+\frac{8}{3}Fo\right)T_{sub,n}^{t+1}-\frac{8}{3}FoT_{sub,n-1}^{t+1}=T_{sub,n}^{t}+\frac{\Delta t}{\rho_{sub}c_{p,sub}\,\Delta x/2}\dot{q}_{n+1}+\frac{\Delta t}{\rho_{sub}c_{p,sub}d_{sub}}\dot{q}_{sub} \quad (117)$$

$$\left(1+\frac{8}{3}Fo_m\right)\rho_{sub,\,H2O,n}^{t+1}-\frac{8}{3}Fo_m\rho_{sub,\,H2O,n-1}^{t+1}=\rho_{sub,H2O,n}^{t}+\frac{\Delta t}{\Delta x/2}\dot{m}_{n+1}+\frac{\Delta t}{d_{sub}}\dot{m}_{conv} \quad (118)$$

According to the position on the substrate, a sparse matrix A was set up with the coefficients of the left-hand side. The unknown parameters were put into the vector X. The right-hand side was summarized in a vector B. Via matrix inversion method, the system of equations was solved to find the desired quantities (temperature or mass concentration of water) in X [33]:

$$[X]=[B][A]^{-1} \quad (119)$$

2.3.5 Simulation Strategy

The simulation program was written in Matlab®. Reasonable accuracy is guaranteed at resolutions as low as $\Delta t = 0.5\ s$ and $\Delta x = 0.0144\ m$, which means for a drying process of drying time $t_{drying} = 80\ s$, a calculation time of about $40\ s$ on an HP Pavilion with Intel i5-4200U processor (2.3 GHz) and 8 GB RAM. An estimate of the resolution influence that means simulation results for coarse to fine grids of space and time discretization, is given in appendix Figure 101 and Figure 102. A simplified flowchart of the simulation program is given in Figure 33. The flowchart does not include details for the calculation of the convective fluxes. This calculation procedure was done as explained in the article of Abramzon and Sirignano with the manipulated relations from the previous chapter [32]. The Spalding heat transfer number was calculated in an iterative way with the stopping criteria of less than 0.1 % deviation from the results of the previous iteration step. Material properties were calculated as stated in the Materials section.

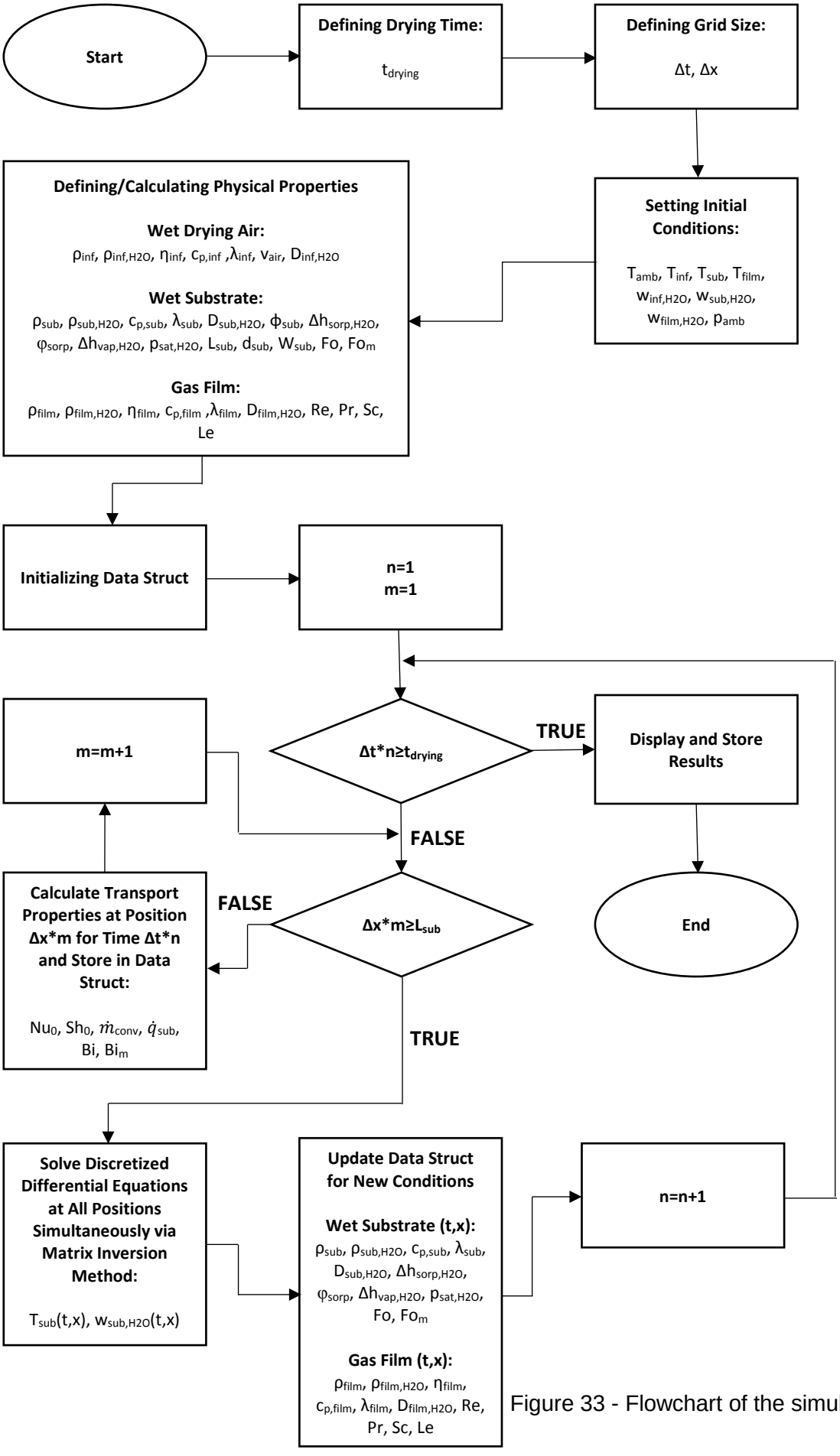

Figure 33 - Flowchart of the simulation.

3 Materials

3.1 Curtain Coating

3.1.1 Coating Liquid - RS2 Std.

3.1.1.1 General Information

The coating suspension is an aqueous based mixture that includes undissolved mineral components, dissolved polymeric components and low molecular substances. This suspension possesses barrier properties at a sufficiently dried state.

3.1.1.2 Rheological Behavior

3.1.1.2.1 Ostwald-De Waele Parameter

The rheological behavior was quantified using the Ostwald-De Waele model (8). The flow curves of three batches of the coating liquid were analyzed in the shear rate range between 10 and 1000 s^{-1} to give the result (for more details see appendix, Table 27):

Table 1 – Ostwald-de Waele Parameter of RS2 Std.

Ostwald-De Waele Parameter	
$\boldsymbol{n_O}$	0.97 ±0.01
$\boldsymbol{K_O}$	0.51 ±0.07

The parameters indicate that the suspension behaves like a pseudo-plastic (i.e., a shear thinning liquid) since the flow index n_O is smaller than one. The absolute difference from one is rather small. This means that nearly Newtonian behavior was observed.

3.1.1.2.2 Influence of High Shear Step

If fluid is forced through the slit of the coating device, it is exposed to a high shear rate for a short period (typically in the orders of 1000 s^{-1} for 100 ms). The influence of this shear rate step on the viscosity downstream was investigated (Figure 34). The change of the viscosity was calculated from the viscosity downstream of the high shear step (at 40 s^{-1}) divided by the viscosity upstream (at 100 s^{-1}) minus one as given by:

$$\eta_{change} = \frac{\eta_{down}}{\eta_{up}} - 1 \qquad (120)$$

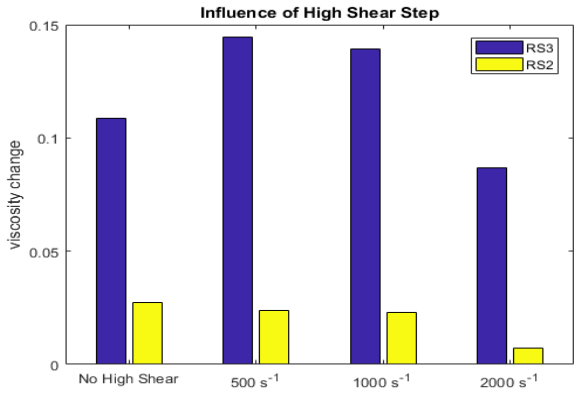

Figure 34 - Influence of high shear step on downstream viscosity

The downstream viscosity was evaluated 2 s from the high shear step for RS2 Std., since this is a typical residence time on the inclined plate of the coating device. For comparison, one experiment did not include the high shear step. All bars of shear rates below 2000 s^{-1} of RS2 Std. in Figure 34 have similar heights. This means literally no influence of the high shear step below 2000 s^{-1} on RS2 Std. Although different shear rates were set up- and downstream, the viscosity is equal within three percent. This supports the calculated flow index near one. Further details are given in the appendix, Table 29.

3.1.1.3 RS2 Std. for Limiting Coating Phenomena

Table 2 - RS2 Std. properties for investigation of coating phenomena

RS2 Std. Properties	
Density [kg/m³]	1097
Solid Content [kg/kg]	0.266
Dynamic Viscosity [mPas]	535
Surface Tension [mN/m]	33

3.1.1.4 RS2 Std. for Impingement Velocity

Table 3 - RS2 Std. properties for investigation of impingement velocity effect

RS2 Std. Properties	
Density [kg/m³]	1097
Solid Content [kg/kg]	0.269
Dynamic Viscosity [mPas]	620
Surface Tension [mN/m]	33

3.1.1.5 RS2 Std. for Operability Window

Table 4 - RS2 Std. properties for investigation of the operability window

	RS2 Std. 1	RS2 Std. 2	RS2 Std. 3
Storage Time [d]	1	20	20
Density [kg/m^3]	1100	1100	1070
Solid Content [kg/kg]	0.270	0.266	0.212
Surface Tension [mN/m]	32	32	32
Dynamic Viscosity [mPas]	353	600	166

3.1.2 Coating Liquid - RS3 Std.

3.1.2.1 General Information

The coating suspension is an aqueous based mixture that includes mainly undissolved mineral components, small amounts of dissolved polymeric components and low molecular substances. This suspension possesses no barrier properties.

3.1.2.2 Rheological Behavior

3.1.2.2.1 Ostwald-De Waele Parameter

The rheological behavior was quantified using the Ostwald-De Waele model (8). The flow curves of three batches of the coating liquid were analyzed in the shear rate range between 10 and 1000 s^{-1} to give the result (for more details see appendix, Table 28):

Table 5 - Ostwald-De Waele parameter of RS3 Std.

Ostwald-De Waele Parameter	
n_0	0.75 ±0.02
K_0	0.48 ±0.15

The parameters indicate that the suspension behaves like a pseudo-plastic (i.e., a shear thinning liquid) since the flow index is smaller than one. The absolute difference from one is rather large, this means that the behavior substantially deviates from Newtonian.

3.1.2.2.2 Influence of High Shear Step

If fluid is forced through the slit of the coating device, it is exposed to a high shear rate for a short period (typically in the orders of 1000 s^{-1} for 100 ms). The influence of this shear rate

step on the viscosity downstream was investigated (Figure 34). The change of viscosity was calculated from the viscosity downstream (at 70 s^{-1}) divided by the viscosity upstream (at 100 s^{-1}) minus one as given in equation (120). The downstream viscosity was evaluated at 1.5 s from the high shear step for RS3 Std. since this is a typical residence time on the inclined plate of the coating device. For comparison, one dataset did not include the high shear step. For RS3 Std., the high shear step shows slightly higher influence than for RS2 Std., but the viscosity changes less than 5 %, which is negligible for the purpose of this thesis. The difference of the shear rates before and after the high shear step is influential for RS3 Std. with changes as high as 15 %. Further details are given in the appendix, Table 30.

3.1.2.3 RS3 Std. for Limiting Coating Phenomena

Table 6 – RS3 Std. properties for investigation of limiting coating phenomena

RS3 Std. Properties	
Density [kg/m³]	1270
Solid Content [kg/kg]	0.397
Dynamic Viscosity [mPas]	97
Surface Tension [mN/m]	36

3.1.2.4 RS3 Std. for Impingement Velocity

Table 7 – RS3 Std. properties for investigation of impingement velocity effect

RS3 Std. Properties	
Density [kg/m³]	1270
Solid Content [kg/kg]	0.397
Dynamic Viscosity [mPas]	97
Surface Tension [mN/m]	34

3.1.2.5 RS3 Std. for Operability Window

Table 8 – RS3 Std. properties for investigation of the operability window

	RS3 Std. 1	RS3 Std. 2	RS3 Std. 3
Storage Time [d]	1	20	1
Density [kg/m³]	1285	1260	1270
Solid Content [kg/kg]	0.414	0.400	0.435
Surface Tension [mN/m]	31	32	34
Dynamic Viscosity [mPas]	92	47	127

3.2 Drying of Coatings

3.2.1 Humid Air

3.2.1.1 General Information

Humid air in the drying chamber functions as energy source and takes up vapor from the substrate. Properties depend on temperature and water content. Formulas are shown for conditions outside the thermal and concentration boundary layers. The properties within the boundary layers are calculated analogously by replacing T_{inf} by T_{film} or T_{sub} and using the corresponding water concentrations.

3.2.1.2 Density

Relative humidity φ_{amb} was measured at room temperature near the blower entrance. By assuming an ideal gas and constant pressure, the density in the drying chamber is calculated in the following way (for calculating the saturation pressure at room temperature, the Antoine equation (121) was used) [34]:

$$p_{sat,amb,H2O} = 10^{A-\frac{B}{C+T_{amb}}} \tag{121}$$

$$p_{amb,H2O} = p_{sat,amb,H2O}\varphi_{amb} \tag{122}$$

$$\rho_{inf,H2O} = \frac{(p_{amb} - p_{amb,H2O})}{RT_{inf}} Mw_{air} + \frac{p_{amb,H2O}}{RT_{inf}} Mw_{H2O} \tag{123}$$

The Antoine parameters were taken from [35], the molecular weights from [36] and the ambient pressure was assumed to be constant at 101.3 kPa.

3.2.1.3 Viscosity

The kinematic viscosity of dry air was fitted from reference [36] in the range of 20 to 400 °C (Figure 35). The dynamic viscosity of water vapor was calculated by the method of Chung et al. This method is recommended for gases at low pressure and is based on the Chapman-Enskog theory as given by [35]:

$$\eta_{inf,H2O,g} = 40.785 \frac{F_{c,H2O}(Mw_{H2O}T_{inf})^{1/2}}{{V_{c,H2O}}^{2/3}\Omega_{v,H2O}} \tag{124}$$

with $F_{c,H2O} = 1 - 0.2756\omega_{H2O} + 0.059035{\mu_{r,H2O}}^4 + \kappa_{H2O}$ that considers the acentric factor ω_{H2O}, the reduced dipole moment $\mu_{r,H2O} = 131.3\frac{\mu_{H2O}}{(V_{c,H2O}T_{c,H2O})^{1/2}}$ and the association factor κ_{H2O}. The viscosity-collision-integral $\Omega_{v,H2O} = [A_v(T^*)^{-B_v}] + C_v[\exp(-D_vT^*)]E_v[\exp(-F_vT^*)]$,

consists, besides the constants, of $T^* = 1.2593 T_{r,H2O}$ with the reduced temperature of water at drying temperature $T_{r,H2O}$.

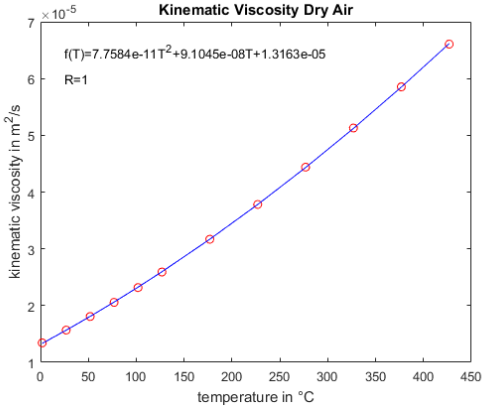

Figure 35 - Fit of temperature dependency of dry air viscosity from data of [36].

Tsilingiris (2008) recommends to use the mixing rule of Reid with an enhancement factor (=correction to saturation pressure) and a compressibility factor of one, which reads [34]:

$$\eta_{inf} = \frac{(1 - x_{inf,H2O,g})\eta_{inf,air}}{(1 - x_{inf,H2O,g}) + x_{inf,H2O,g}\phi_{aw}} + \frac{x_{inf,H2O,g}\eta_{inf,H2O,g}}{x_{inf,H2O,g} + (1 - x_{inf,H2O,g})\phi_{wa}} \tag{125}$$

with the interaction parameters given by [34]:

$$\phi_{aw} = \frac{\sqrt{2}}{4}\left(1 + \frac{Mw_{air}}{MW_{H2O}}\right)^{-\frac{1}{2}}\left[1 + \left(\frac{\eta_{inf,air}}{\eta_{inf,H2O,g}}\right)^{\frac{1}{2}}\left(\frac{MW_{H2O}}{Mw_{air}}\right)^{\frac{1}{4}}\right]^2 \tag{126}$$

$$\phi_{wa} = \frac{\sqrt{2}}{4}\left(1 + \frac{Mw_{H2O}}{MW_{air}}\right)^{-\frac{1}{2}}\left[1 + \left(\frac{\eta_{inf,H2O,g}}{\eta_{inf,air}}\right)^{\frac{1}{2}}\left(\frac{MW_{air}}{Mw_{H2O}}\right)^{\frac{1}{4}}\right]^2 \tag{127}$$

3.2.1.4 Specific Heat Capacity

The specific heat capacity of humid air was calculated with the ideal mixture assumption [34]. The specific heat capacity of dry air and water vapor were assumed to be constant at 1022 and 1926 J/(kgK), respectively, and the mixture data was evaluated by:

$$c_{p,inf} = c_{p,inf,\,H20,g} w_{inf,H2O,g} + c_{p.air}(1 - w_{inf,H2O,g}) \tag{128}$$

Property data of reference [36] was used.

3.2.1.5 Thermal Conductivity

The thermal conductivity of water vapor was assumed to be constant at 0.0184 W/(mK) [36]. The thermal conductivity of dry air was fitted from data of reference [36] in the range of 0 to 400 °C (Figure 36).

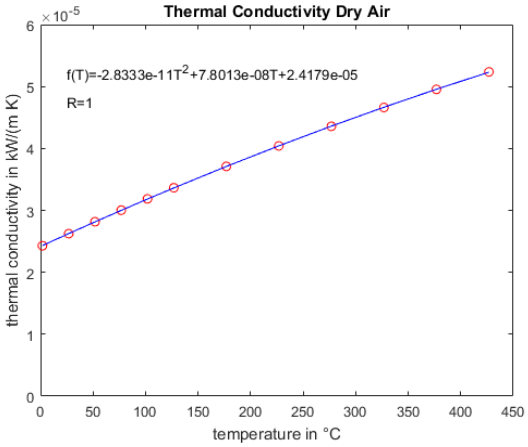

Figure 36 - Fit of temperature dependency of dry air thermal conductivity from [36]

Again, the mixing rule of Reid was used to calculate the thermal conductivity of humid air by [34]:

$$\lambda_{inf} = \frac{\left(1 - x_{inf,H2O,g}\right)\lambda_{inf,air}}{\left(1 - x_{inf,H2O,g}\right) + x_{inf,H2O,g}\phi_{aw}} + \frac{x_{inf,H2O,g}\lambda_{inf,H2O,g}}{x_{inf,H2O,g} + \left(1 - x_{inf,H2O,g}\right)\phi_{wa}} \tag{129}$$

3.2.1.6 Diffusion Coefficient of Water Vapor in Air

The diffusion coefficient of water vapor in air was calculated according to the method of Wilke and Lee for binary gas mixtures and low pressure as given by the following relation [35]:

$$D_{inf,H2O,g} = \frac{\left[3.03 - \left(\frac{0.98}{Mw_{H2O,g,air}^{\frac{1}{2}}}\right)\right] 10^{-3} {T_{inf}}^{3/2}}{p_{amb} Mw_{H2O,air}^{\frac{1}{2}} {\sigma_{H2O,g,air}}^{2} \Omega_D} \tag{130}$$

with $Mw_{H2O,air} = \frac{2}{\frac{1}{Mw_{H2O}} + \frac{1}{Mw_{air}}}$ and the diffusion-collision-integral $\Omega_D = \frac{A_D}{(T^*_{WL})^{B_D}} + \frac{C_D}{\exp(D_D T^*_{WL})} + \frac{E_D}{\exp(F_D T^*_{WL})} + \frac{G_D}{\exp(H_D T^*_{WL})}$. This includes $T^*_{WL} = \frac{k_B T_{inf}}{\varepsilon_{H2O,g,air}}$ with $\frac{\varepsilon_{H2O,g,air}}{k_B} = \left(\frac{\varepsilon_{H2O,g}}{k_B}\frac{\varepsilon_{air}}{k_B}\right)^{1/2}$ with $\frac{\varepsilon}{k_B} = 1.15 T_b$. The characteristic length is $\sigma_{H2O,g,air} = (\sigma_{H2O,g}\sigma_{air})^{1/2}$ with $\sigma = 1.18 {V_b}^{1/3}$.

The molar liquid volume at boiling temperature was calculated according to Tyn and Calus by [35]:

$$V_b = 0.285 {V_c}^{1.048} \tag{131}$$

3.2.2 Wet Cardboard

3.2.2.1 General Information

Cardboard absorbs thermal energy and releases water vapor and is generally named 'substrate' in this thesis. Again, properties depend on moisture content and temperature. For all but the drying experiments with coating liquids (RS2 Std. and RS3_C), untreated ACK 350 cardboard produced by MM Karton GmbH Frohnleiten was used. For the other experiments ACK 350 cardboard with standard coating was used. The porosity of both types is 40 %, sheet thickness is 490 µm and the grammage after storing at standard ambient conditions is around 350 g/m^2. The cardboards are partly based on recycled raw materials.

3.2.2.2 Density

It is assumed that only the fraction of coating water which exceeds the pore volume leads to an increase of substrate volume compared to the uncoated cardboard. The density is given as follows:

$$m_{sub} = G_{sub} A_{sub} + m_{coat} \tag{132}$$

$$if\colon V_{sub,H2O} < \phi_{sub} A_{sub} d_{sub} \rightarrow V_{sub} = A_{sub} d_{sub} \tag{133}$$

$$else\colon V_{sub} = A_{sub} d_{sub} + (V_{sub,H2O} - \phi_{sub} A_{sub} d_{sub}) \tag{134}$$

$$\rho_{sub} = \frac{m_{sub}}{V_{sub}} \tag{135}$$

Here, the grammage G_{sub} is a constant substance property for a certain type of cardboard and the coated mass m_{coat} is given by the coating adjustments, as explained in 4.1.7.4 below.

3.2.2.3 Specific Heat Capacity

The specific heat capacities of pulp fibers and liquid water were assumed to be constant at 1450 and 4190 J/(kgK), respectively. The mixture was assumed to be ideal and was calculated by:

$$c_{p,sub} = c_{p,H20,l} w_{sub,H2O} + c_{p,sub,dry}\left(1 - w_{sub,H2O}\right) \tag{136}$$

The specific heat capacity of pulp fibers was taken from [29] that of liquid water from [36].

3.2.2.4 Thermal Conductivity

The thermal conductivity of the porous, wet substrate is divided into four contributions by the model of Krischer and Kast (1979) [37]. The thermal conductivity of the solid (=0.60 W/(mK) from [29]), of liquid water (=0.58 W/(mK) from [36]), of air and of a vaporization/condensation mechanism is considered in the model. Besides substrate properties like porosity ϕ_{sub}, two model parameters must be known a, b. The parameter a was evaluated by Palosaari for paper materials and was taken from reference [29] to be 0.46. Parameter b is not known to the author for paper materials and was therefore fitted from data of reference [37] for porous mineral substances. The parameter gives the relation between wetted pore walls and volume fraction of moisture in the substance. The fit is shown in Figure 37.

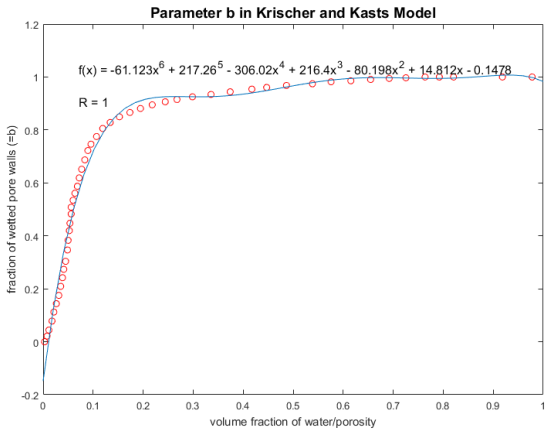

Figure 37 – Parameter b of Krischer and Kast's model for mineral substrates [37].

The contribution of the vaporization/condensation mechanism is given by [37]:

$$\lambda_{diff} = \frac{D_{H2O,g,air}\, Mw_{H2O}}{R} \frac{p_{amb}}{p_{amb} - p_{sat,H2O}} \frac{dp_{sat,H2O}}{dT} \tag{137}$$

Here, $dp_{sat,H2O}/dT$ is given by the Antoine equation near the substrate temperature. The model of Krischer and Kast combines the four contributions in a serial and parallel way. The relative portions of the serial and parallel contributions are given by the model parameter a. The thermal conductivity of the wet substrate is found via the following relations [37]:

$$\lambda_{par} = \lambda_{sub,dry}(1-\phi_{sub}) + \lambda_{H2O,l}\psi_{sub} + b(\lambda_{air} + \lambda_{diff})(\phi_{sub} - \psi_{sub}) + (1-b)\lambda_{air}(\phi_{sub} - \psi_{sub}) \tag{138}$$

$$\lambda_{ser} = \frac{1}{\frac{(1-\phi_{sub})}{\lambda_{sub,dry}} + \frac{\psi_{sub}}{\lambda_{H2O,l}} + \frac{b(\phi_{sub} - \psi_{sub})}{(\lambda_{air} + \lambda_{diff})} + \frac{(1-b)(\phi_{sub} - \psi_{sub})}{\lambda_{air}}} \tag{139}$$

$$\lambda_{sub} = \frac{1}{\frac{1-a}{\lambda_{par}} + \frac{a}{\lambda_{ser}}} \tag{140}$$

with the volume fraction of water in the substrate ψ_{sub}. A characteristic trend of high thermal conductivity for medium moisture contents and high temperatures was reproduced with the current model (Figure 38). This trend originates from the contribution of the vaporization/condensation mechanism, which is highest for fully wetted but not fully filled pores [37].

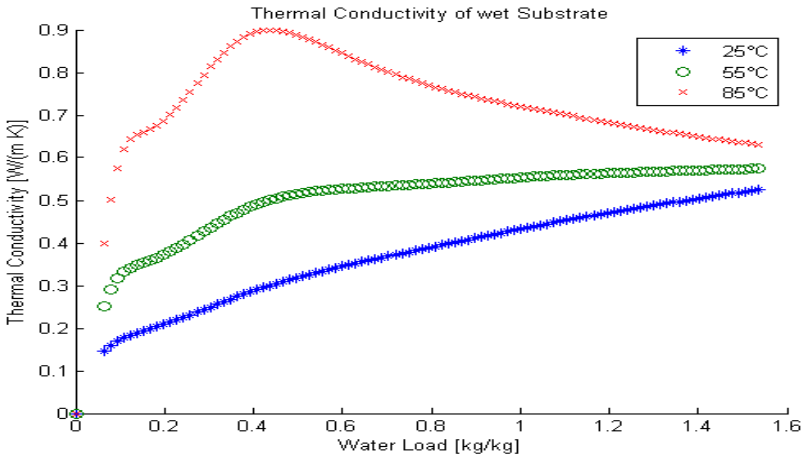

Figure 38 - Thermal conductivity of wet cardboard.

3.2.2.5 In-Plane Diffusion Coefficient of Liquid Water in Substrate

Paper materials exhibit strongly anisotropic diffusion characteristics [38]. The in-plane diffusion coefficient is poorly investigated and the used model from Hashemi et al. (1997) was set up for Kraft paper [38]. However, investigations of the influence of the absolute value of in-plane diffusion coefficients showed a weak influence on simulation results, as seen in the appendix (Figure 104). The following equation was applied to find the in-plane diffusion coefficient [38]:

$$D_{sub,H2O} = A_{pdiff} e^{-B_{pdiff}/w_{sub,H2O}} \tag{141}$$

with $w_{sub,H2O} = \max(0.08, w_{sub,H2O})$.

3.2.2.6 Heat of Vaporization of Pure Water

The heat of vaporization of pure water is calculated by the integrated form of the Clausius Clapeyron equation with saturation pressures calculated for ±1 °C of the substrate temperature by the Antoine equation. The Clausius Clapeyron equation reads:

$$\Delta h_{vap,surf,H2O} = \frac{R}{Mw_{H2O}} \frac{\ln\left(\frac{p_{sat,H2O}(Tsub-1)}{p_{sat,H2O}(Tsub+1)}\right)}{\left(\frac{1}{T_{sub+1}} - \frac{1}{T_{sub-1}}\right)} \quad (142)$$

3.2.2.7 Net Isosteric Heat of Sorption and Desorption Isotherm

Type-2-shaped desorption isotherms were found from desorption experiments on the wet substrate (Figure 39) [39]. The shape is in agreement with isotherm-shapes of similar substrates [40-42].

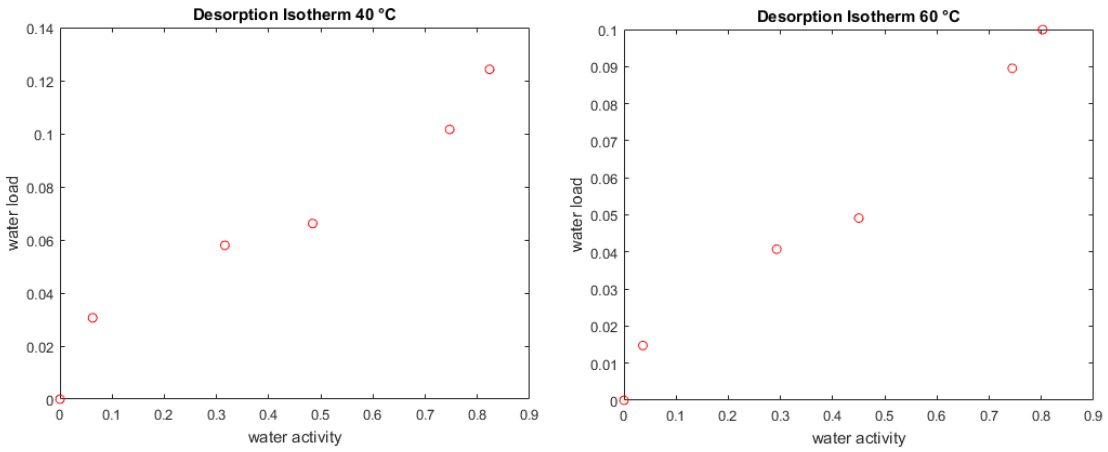

Figure 39– Experimentally determined desorption isotherms for untreated ACK 350 at 40 °C (left) and 60°C (right).

Based on the data sets given in the appendix (Table 33 and Table 34), five fitting models for sorption isotherm data were tested (Modified Chung-Pfost, Modified Henderson, Modified Oswin and Modified Halsley from the work of Menkov (2000) in [43] and a modified GAB-version from the work of Staudt et al. (2009) in [44]). The modified GAB-version gave best results, although the experimentally evident temperature dependency is fairly reproduced as can be seen in Figure 41. The recommended SISH-method (=Single Isotherm Single Heat) was used to analyze the data as follows:

The standard GAB-equation reads [44]:

$$W_{sub,H2O} = \frac{k_{GAB} W_{mon,sub,H2O} C_{GAB} a_{H2O}}{(1 - k_{GAB} a_{H2O})(1 + k_{GAB} a_{H2O}(C_{GAB} - 1))} \quad (143)$$

with the moisture content on dry basis (=mass load) $W_{sub,H2O}$, the mass load of the first moisture layer $W_{mon,sub,H2O}$, the Guggenheim constant C_{GAB}, the water activity in the gas phase a_{H2O} and a constant to distinguish between first- and multilayers k_{GAB}. Data was fitted at a reference temperature to extract $k_{GAB}, W_{mon,sub,H2O}, C^0_{GAB}$ by [44]:

$$W^0_{sub,H2O} = \frac{\mathrm{k}_{GAB}\mathrm{W}_{mon,\mathrm{sub},H2O}C^0_{GAB}a^0_{H2O}}{(1-\mathrm{k}_{GAB}a^0_{H2O})(1+\mathrm{k}_{GAB}a^0_{H2O}(C^0_{GAB}-1))} \tag{144}$$

The Guggenheim constant is used to account for the temperature dependency and can be written in Arrhenius form as [44]:

$$\mathrm{C}_{GAB} = C^0_{GAB}\exp\left[\frac{Q}{R}\left(\frac{1}{T_{sub}}-\frac{1}{T^0_{sub}}\right)\right] \tag{145}$$

with the overall sorption energy Q, the Guggenheim constant at the reference temperature C^0_{GAB}, the gas constant R, the reference temperature T^0_{sub} and the current temperature T_{sub}. The net isosteric heat of sorption Δh_{sorp} can be found if isotherms of at least two different temperatures are known by the Clausius Clapeyron equation given by [44]:

$$\ln a_{H2O} = -\frac{\Delta h_{sorp}}{R}\frac{1}{T_{sub}} \tag{146}$$

The plot of $\ln(a_{H2O})$ versus $-1/T_{sub}$ for the two reference temperatures leads to lines of slope $\Delta h_{sorp}/R$. Here, the widely used assumption of independence of isosteric heat of sorption from temperature was assumed [44]. Figure 40 gives the result for the net isosteric heat of sorption. The shape of the curve can be explained as stated by Quirijns et al. (2005) [45].

During drying of hygroscopic materials, it is seen experimentally that more and more energy is consumed to reduce moisture content for decreasing moisture loads. At high moisture load, the consumed energy is literally the heat of vaporization of the pure liquid. At lower moisture load an extra amount of energy, the net isosteric heat of sorption, is needed, which increases with decreasing moisture load. This is because more and more water from active sites instead of free water has to be removed. The maximum at low, but not zero, water loads is explained by cooperative effects of water molecules, which vanishes at too low water loads.

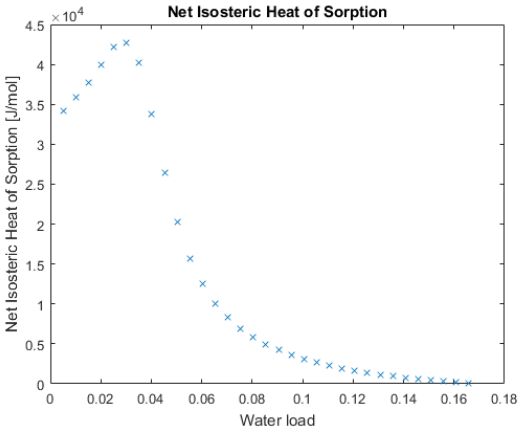

Figure 40 - Net isosteric heat of sorption calculated from experimental data for untreated ACK 350.

The received maximum value (44 kJ/mol H_2O) is higher than values of similar substrates like Kraft paper (27.4 kJ/mol H_2O) or SBS (=Solid Bleached Sulphate) cardboard (26.8 kJ/mol H_2O) given by Rhim and Lee (2009) [42]. The overall sorption energy Q is found by applying the following relation, which was derived by Staudt et al. (2009) via inserting the temperature dependency of the Guggenheim constant in the original GAB equation, integration and some further manipulations. The result reads [44]:

$$\Delta h_{sorp}(W_{sub,H2O}) = \frac{\mathrm{k}_{GAB}{}^2 Q a_{H2O}^0{}^2 - 2\mathrm{k}_{GAB} Q a_{H2O}^0 + Q}{(\mathrm{C}_{GAB} - 1)\mathrm{k}_{GAB} a_{H2O}^0{}^2 + 1} \tag{147}$$

The temperature dependency of the desorption isotherm can hence be included in the conducted calculations. However, as can be seen in Figure 41 the prediction fairly reproduces experimental data.

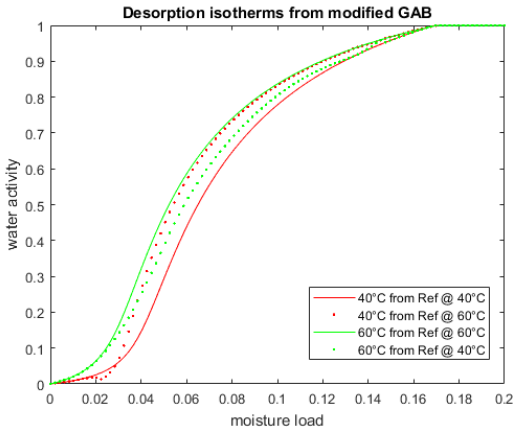

Figure 41 - Fitted isotherms from experiment (full lines) and predictions from model of other reference temperatures (dotted lines).

3.2.3 Coating Liquids

The coating liquids were investigated with the methods explained in the Curtain Coating section. The results are given in Table 9. For the drying section, a slightly modified version of RS3 Std. was used. It is here referred to as RS3_C.

Table 9 - Properties of coating liquids for drying experiments

Properties	RS2 Std.	RS3_C
Density [kg/m³]	1094	1330
Solid Content [-]	0.267	0.448
Dynamic Viscosity [mPas]	515	162
Surface Tension [mN/m]	30	33.5
Grammage of Coating [g/m²]	8.5	18.5

4 Analytical and Processing Methods

4.1 Curtain Coating

4.1.1 Production of Coating Liquids

Coating liquids for the use on the considered coating unit were produced directly at the corresponding facilities of the production division of Mayr-Melnhof Karton GmbH Frohnleiten, or in a laboratory-scale batch reactor. The IKA® Standard Production Plant 50 laboratory batch-reactor can be used up to 200 °C, under vacuum or up to 8 bar overpressure. The reactor volume is 50 L. For mixing, a Turbotron RFG-02-A stirrer and a Process-Pilot UTL 2000/4 disperser are integrated. A dosing system, driven by a peristaltic pump, different manual inlets and a weighing system are included. Furthermore, a temperature-control system (SPP 50), a vacuum system (MP 25/50 (50 Hz)) as well as a real time pH (CPS71D Memosens) and a viscosity (MIVI) measurement system are built in [46].

4.1.2 Mass Measurement

High precision mass determination was performed with a Mettler Toledo XS204 balance. The sensitivity is 0.1 mg with a maximum sample mass of 220 g and a minimum recommended sample mass of 82 mg [47]. If less sensitivity was needed, a Kern 572 scale was used with a sensitivity of 1 mg and a recommended sample mass range between 3010 and 0.1 g [48].

4.1.3 Dynamic Viscosity of Liquids

4.1.3.1 Set-Up

Viscosity measurements were performed on Anton Paar MCR 301 and Anton Paar MCR 302 rheometers. Both rheometers can perform rotational as well as oscillational tests. As a measuring system, a concentric cylinder equipment with high clearance was used, which is recommended especially for highly viscous liquids [49]. The operation method is the Searle-method in which the cup is kept still while the cylinder is rotated. A sketch of the measurement system and the equation to extract viscosity data is given below [49].

$$\eta = \frac{\tau(R_i)}{\dot{\gamma}(R_i)} = \frac{(R_e^2 - R_i^2)}{4\pi L R_e^2 R_i^2} \frac{M}{\omega} \tag{148}$$

With the dynamic viscosity η, the shear stress τ, the shear rate $\dot{\gamma}$, the cylinder radius R_i, the cup radius R_e, the length of the cylindrical part L, the torque M and the rotational velocity ω.

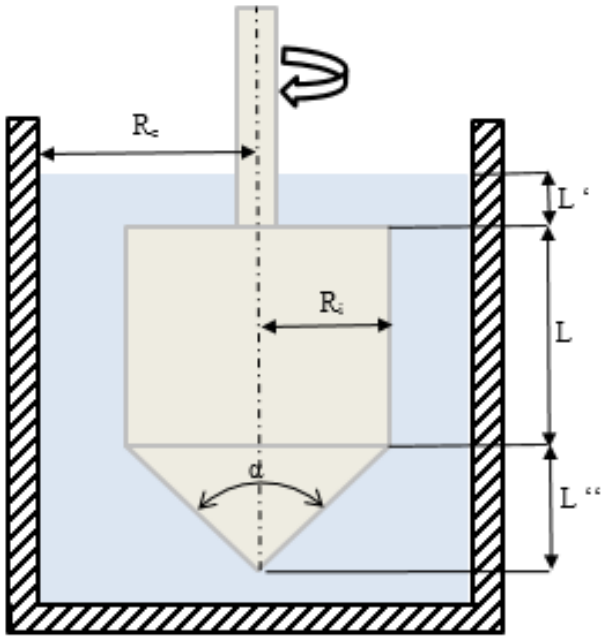

Figure 42 - Rheometer measurement system [49].

4.1.3.2 Apparent Viscosity for Curtain Coating Experiments

Finding the adequate viscosity for the Curtain Coating process is important. High viscosity, on the one hand, helps to dampen small disturbances and hence has positive effects on the stability of the liquid sheet. On the other hand, it promotes the growth of the mentioned boundary layer along the edge guides, which eventually leads to curtain break-up. This means there is an optimum range for viscosity. All coating liquids investigated, are aqueous based suspensions and exhibit non-Newtonian behavior to different extents. The viscosity not only depends on the shear rate, but also on the shear history. To find an apparent viscosity in the curtain, the coating set-up was analyzed by means of two parameters (Figure 43):

- characteristic shear rates for the individual flow situations
- residence times in these flow situations

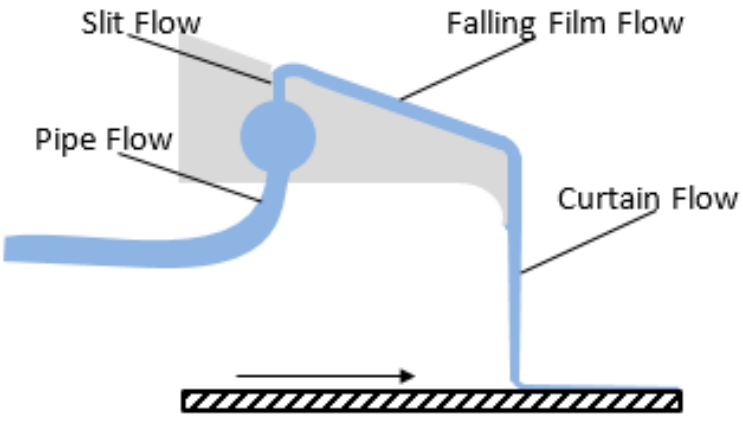

Figure 43 - Investigated flow situations during Curtain Coating.

As a first step, the dependency of the viscosity of the coating suspensions on shear rate must be quantified. This was done by the Ostwald-De Waele model:

$$\tau = K_O \dot{\gamma}^{n_O} \tag{149}$$

A double logarithmic plot of the shear stress τ against the shear rate $\dot{\gamma}$ gives a linear curve with slope as the flow index n_O and intercept as the consistency index K_O. A flow index smaller than one indicates shear thinning behavior and larger than one shear thickening behavior. The amount of deviation from Newtonian fluids is quantified by the absolute difference of the flow index from one. For the bulk shear rate in the pipe flow region, the following relation was used [50]:

$$\dot{\gamma}_{bulk,pipe} = \frac{8v_{m,pipe}}{D_{pipe}} \tag{150}$$

The bulk shear rate in the slit flow region is given by [50]:

$$\dot{\gamma}_{bulk,slit} = \frac{8v_{m,slit}}{D_{h,slit}} \tag{151}$$

where the hydraulic diameter is given by the well-known formula $D_h = 4A_{cross}/U_{slit}$. The bulk shear rate in the falling film region can be estimated by [51]:

$$\dot{\gamma}_{bulk,slide} = \frac{3v_{m,slide}}{h_{film}} \tag{152}$$

The well-known formula for film thickness of a liquid flowing down an inclined plane of angle α to the horizontal reads [52]:

$$h_{film} = \left(\frac{3\mu_l \dot{V}_l}{\rho_l W_{slide} g sin(\alpha)} \right)^{1/3} \tag{153}$$

This means that the film thickness depends on the apparent viscosity μ_l but the effective shear rate (which is connected to the apparent viscosity by (154)) depends on the film thickness. The effective viscosity of an Ostwald-De Waele liquid can be expressed as:

$$\mu_l = K_O \dot{\gamma}_{bulk,slide}^{n_O - 1} \tag{154}$$

and the mean fluid velocity is given by:

$$v_{m,slide} = \frac{\dot{V}_l}{h_{film} W_{slide}} \tag{155}$$

Combining (153), (154) and (155), the film thickness reads:

$$h_{film} = \left(\frac{3^{n_O} K_O \dot{V}_l^{n_O}}{\rho_l W_{slide}^{n_O} g \sin(\alpha)} \right)^{1/(1+2n_O)} \quad (156)$$

An example for the use of these relations is given for understanding. Consider a coating liquid with consistency index $K_O = 0.48$ and flow index $n_O = 0.75$ for a flow rate of 1 L/min and the following set-up:

Table 10 - Set-up for calculation of apparent viscosity.

Flow situation	Length [m]	Cross Sectional Area [m^2]
Pipe Flow	3	11 x10^{-5}
Slit Flow	0.01	15 x10^{-5}
Falling Film Flow	0.08	44 x10^{-5} *

* the film thickness is $h_{film} = 1.7\ mm$, the slide width is 0.25 m.

The shear rates and residence times can be calculated according to the above equations. Based on these parameters, a stress jump experiment can be set up.

Table 11 - Calculated parameters to evaluate apparent viscosity from measurement.

Flow situation	Residence Time [s]	Bulk Shear Rate [s^{-1}]
Pipe Flow	21	96
Slit Flow	0.09	743
Falling Film Flow	2.1	64

4.1.3.3 Viscosity Measurements

4.1.3.3.1 Rheometer Inertia

The minimum time after a stress jump to extract meaningful viscosity data from rheological measurements was investigated. Apparatus inertia is known to interfere with signals, especially for stress jump experiments as planned in this thesis. The influence time was investigated by using a Newtonian oil. The oil was stressed at a high shear rate, and suddenly the shear rate was set to the minimum of the device to extract data [53]. As a result, the shear stress should suddenly drop to zero, which is not the case in real experiments. Apparatus inertia leads to the so-called 'inertia ringing', which limits the minimum time after the high shear step to extract meaningful data (Figure 44) [54]. The experiment was conducted as follows:

20 mL of a Newtonian oil (OMV 200) with dynamic viscosity of 144 mPas at 25 °C was injected into the rheometer cup at RT. The oil was stressed with the following settings, and the shear stress against time was recorded.

Table 12 - Settings for investigation of the rheometer inertia.

Anton Paar MCR 302		
Method	visco-elastic	
Temperature	25 °C	
Duration	201 s	20 s
Shear Rate	2000 s^{-1}	min. (=0.1 s^{-1})
Data Recording	1 s	10 ms

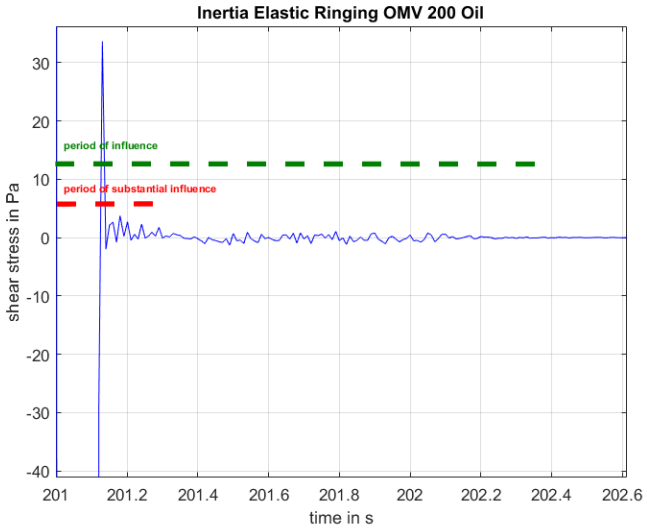

Figure 44 – Results of rheometer inertia measurement.

The experiments revealed that substantial influence from the rheometer can be seen up to 300 ms after the stress jump. Up to 1400 ms the signal is influenced. Data recorded closer than 300 ms to the stress jump were therefore neglected in any case.

4.1.3.3.2 Flow Curve

20 mL of a coating liquid at 40 °C was injected into the tempered rheometer cup. The liquid was stressed with the following settings:

Table 13 - Settings of the rheometer for the flow curve measurement of coating liquids.

Anton Paar MCR 301/302	
Method	visco-elastic
Temperature	40 °C
Number of Points	100
Shear Rate	0.1-2500 s^{-1}
Point Distribution	logarithmic

4.1.3.3.3 Influence of High Shear Step

20 mL of a coating liquid at 40 °C was injected into the tempered rheometer cup. The liquid was stressed with the following settings:

Table 14 - Settings of rheometer for investigation of influence of high shear step.

Anton Paar MCR 301/302			
Method	visco-elastic		
Temperature	40 °C		
Duration	30 s	1 s	30 s
Data Recording	10 ms	100 ms	10 ms
Shear Rate RS2 Std.	100 s^{-1}	0/500/1000/2000 s^{-1}	40 s^{-1}
Shear Rate RS3 Std.	100 s^{-1}	0/500/1000/2000 s^{-1}	70 s^{-1}

4.1.3.3.4 Stress Jump

20 mL of a coating liquid at 40 °C was injected into the tempered rheometer cup. The liquid was stressed with the following settings (each result is the mean of two measurements):

Table 15 – Settings of rheometer for stress jump measurement.

Anton Paar MCR 302			
Method	visco-elastic		
Temperature	40 °C		
Duration	30 s	1 s	30 s
Data Recording	10 ms	100 ms	10 ms
Shear Rate RS2 Std.	100 s^{-1}	1000 s^{-1}	40 s^{-1}
Shear Rate RS3 Std.	100 s^{-1}	1000 s^{-1}	70 s^{-1}

4.1.4 Dynamic Surface Tension

4.1.4.1 Set-Up

The dynamic surface tension was measured with a SITA pro line t15 bubble pressure tensiometer. Single-use PTFE capillaries with an inner diameter of 800 µm were used at the air exit. In this device, air is pumped into a liquid at different pumping speeds and the pressure is measured. A bubble forms at the tip of the capillary. At the point when the bubble radius equals the capillary radius, maximum pressure is reached (maximum of curvature) [55]. The surface tension is measured for different bubble ages using the Young-Laplace equation. A process sketch and the working equation, Young-Laplace equation for spherical bubbles, are given below [55],

$$\gamma = (p_{max} - p_{min})R/2 \tag{157}$$

with the surface tension of the corresponding bubble age γ, the maximum pressure p_{max}, the hydrostatic pressure p_{min} and the bubble radius R.

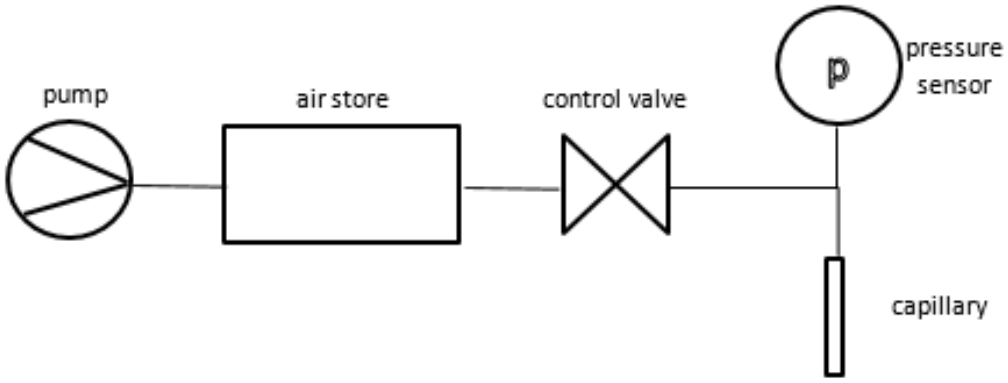

Figure 45 - Set-up of the bubble pressure tensiometer [55].

4.1.4.2 Dynamic Surface Tension for Curtain Coating Experiments

High Weber number enhances stability of the falling liquid sheet. High Weber numbers can be caused by low surface tension. For reducing surface tension, surface-active substances are essential for aqueous coating solutions in the field of coating technology. Surfactants adsorb on the interface of the coating solutions and thus, lower the surface tension. The surface concentration can be orders of magnitude higher than in the bulk liquid. However, if new surface is generated in accelerating flows, or the surface is disturbed by stirring, this strongly influences the surface concentration of these substances. A certain period of time elapses before the new equilibrium is formed. Molecules balance concentration gradients on the interface and diffuse from the bulk to establish the new equilibrium. If surface tension is measured during this period, a dependency on the surface age or the time elapsed after the

disturbance is the result. After a long enough period, the equilibrium value is reached. In the sheet forming zone, a new, free interface forms, and in the Curtain Flow Zone fresh interface is generated by acceleration. This obviously suggests to use the dynamic instead of the static (or rather equilibrium) surface tension. Choosing the proper surface age for the process is an important step to connect the evaluated parameter with the problem in consideration. For the considered process, the difference of the curtain velocity in main flow direction was used to find a characteristic strain rate. This strain rate was inverted to finally get a mean surface age in the curtain [56]. As an example, consider a curtain of a falling height $h_{curtain} = 0.095\ m$ and a velocity at the pouring edge of $v_{pe} = 0.02\ m/s$. The liquid has the following properties: $\mu_l = 0.35$ Pas, $\rho_l = 1100$ kg/m^3. A sketch is given in Figure 46.

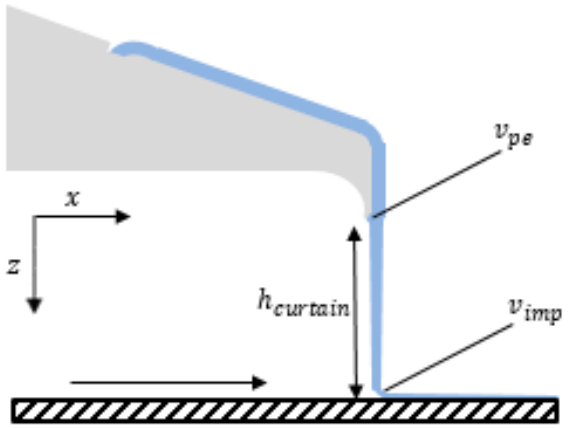

Figure 46 - Sketch for calculation of the surface age in the curtain.

From Brown (1961) it is known that the impingement velocity can be calculated by [21]:

$$v_{imp} = \left\{ v_{pe}^2 + 2g \left[h_{curtain} - 2 \left(\frac{4\mu_l}{\rho_l} \right)^{\frac{2}{3}} g^{-\frac{1}{3}} \right] \right\}^{1/2} \tag{158}$$

Which presently gives $v_{imp} = 1.28\ m/s$. The difference in velocity is therefore $\Delta v = v_{imp} - v_{pe} = 1.26\ m/s$ and the difference in height Δz is essentially the curtain falling height. This gives for the mean strain rate the following result:

$$\dot{\gamma}_{curtain} = \frac{\Delta v}{\Delta z} = 13.52\ s^{-1}$$

and after inversion one finds:

$$t_{curtain} = 74\ ms$$

The order of magnitude of $t_{curtain}$ is confirmed in the book of Kistler and Schweizer (1997), where 10-100 ms is given as the range of characteristic surface ages in Curtain Coating [57].

4.1.4.3 Preperation of Capillaries

The bubble pressure tensiometer was operated with single-use PTFE capillaries of an inner diameter of 800 µm. For economic reasons it is advantageous to order tubes of several meters length and trim them to the required length. Production of smooth and straight cuts without squeezing the tube and a minimum in length difference between final capillaries is essential during this step. At the same time, production speed should be high enough to make it economical. For this reason, a simple device was built where the PTFE tube enters a narrow channel, slightly larger than itself, and is gently pushed against a bordering wall. Using a Stanley knife, the tube can be cut smoothly (Figure 47).

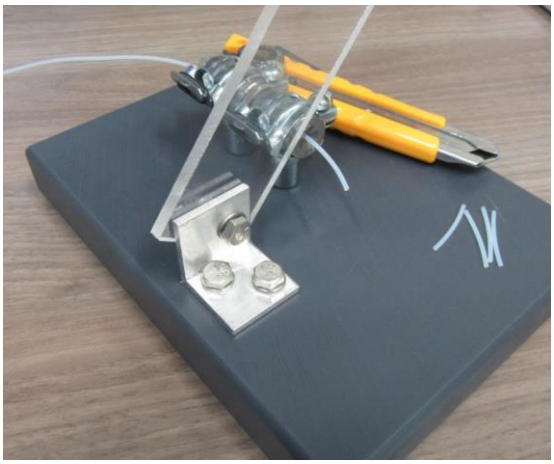

Figure 47 – Capillary cutting tool.

4.1.4.4 Calibration of the Bubble Pressure Tensiometer

4.1.4.4.1 Basics

Measuring the dynamic surface tension via the maximum bubble pressure method is found to give different curves by using different apparatuses or capillaries. The reason lies in varying dependencies of the bubble surface area on time $A_{bubble}(t)$. Without knowing about this dependency for the used set-up, it is impossible to convert the nominal surface age to a surface age of universal validity. Christov et al. developed a new approach for quantitative data interpretation using the mentioned apparatus function $A_{bubble}(t)$ as well as an apparatus constant λ_{bubble} which characterizes the deviation of the nominal bubble age from the universal bubble age [58]. Both are stated to be independent from surfactant type and concentration [58]. For the case of high numbers of λ_{bubble} a calibration procedure is presented by Christov et al.

[58]. They recommend using hydrophobic capillaries to produce results of best quality. The calibration procedure is explained hereafter:

1. A set of reference solutions has to be chosen.
2. The dynamic surface tension curves for the solutions are recorded in dependency of the nominal surface age $\gamma(t_{age})$.
3. The data is fitted by means of the following equation [58]:

$$\gamma = \gamma_{eq} + \frac{s_\gamma}{a_\gamma + t_{age}^{1/2}} \tag{159}$$

with the three fitting parameters γ_{eq} as the surface tension in equilibrium, s_γ as the slope of the plot γ against $t_{age}^{-1/2}$ measured by the maximum bubble pressure method, and a_γ as the ratio of the slope of the plot of adsorption Γ against $t_{age}^{-1/2}$ and the difference between adsorption at maximum surface tension Γ_∞ and at equilibrium surface tension Γ_{eq}. From the result, the apparatus constant can be found by [58]:

$$\lambda_{bubble} = \frac{s_\gamma}{s_{\gamma,0}} \tag{160}$$

Here, the parameter $s_{\gamma,0}$ is the slope of the plot γ against $t_{age}^{-1/2}$ measured with the immobile bubble method. This method gives a universal surface age because the surface area of the bubble is fixed during the measurement and there is no hydrodynamic and convective transport of surfactant. For sufficiently large apparatus constants of the maximum bubble pressure tensiometer, Christov et al. showed that the bubble age t_{age} at maximum pressure is equivalent to the surface age of an immobile and initially clean surface of the age given by [58]:

$$t_u = t_{age}/\lambda_{bubble}^2 \tag{161}$$

with the universal surface age t_u. This surface age has universal validity and therefore can be compared with the mean surface age in the curtain.

4.1.4.4.2 Experiments

Production of Salt Solutions

In a flask (1000 mL) with 1000 mL deionized water and magnetic stir bar, the appropriate quantity of salt was added. The solution was stirred for 1 h at RT. Quantities of the salts are given in Table 31 in the appendix.

Production of Surfactant Solutions

The appropriate quantitiy of surfactant was added into an empty vial (200 mL) with screw cap. The mass was determined using a high precision scale. 100 mL of the corresponding salt solution were added, the vial was closed and shaken for 1 min. The same reference solutions as in the article of Christov et al. were chosen to extract the given parameter $s_{\gamma,0}$ [58]. Two different surfactants were used, namely, Sodium dodecyl sulfate (SDS) and Dodecyltrimethylammonium bromide (DTAB). Quantities of surfactants are given in Table 32 in the appendix.

Measurement of Surfactant Solutions

The bubble pressure tensiometer was operated with single-use PTFE or PEEK capillaries of an inner diameter of 800 μm. Calibration with deionized water was performed using the calibration program of the device. A control measurement of deionized water was done. For deviations of maximum 2 mN/m from the reference values given in the handbook, the surfactant solution was analyzed [55]. Otherwise, the capillary was changed and water-calibration and control measurement were repeated. The capillary was submerged in the surfactant solution, the cleaning program was run once and the surfactant solution was measured with the following settings:

Table 16 - Settings of bubble pressure tensiometer for surfactant solution measurements

SITA proLine t15	
Start Bubble Age	15 ms
End Bubble Age	20 s
Number for Mean	3
Resolution	High
Tolerance	5 %
Refusal	First

The DTAB solutions were measured three times, twice with PTFE capillaries and once with PEEK capillaries, because of data scattering. The SDS solutions were measured twice, once with PTFE and once with PEEK capillaries.

4.1.4.4.3 Data Processing

The surface tension curves were fitted with the Trust-Reflective-Region (TTR) and the Levenberg-Marquardt method in Matlab® by using equation (159). Since substantial data scattering was observed, especially for the DTAB-dataset, the quality of the data was analyzed

statistically, and the most reliable results were extracted. Only data that fulfills the following specifications was used for determination of the apparatus constant:

- confidence interval width ≤ 20 % of fitted value
- no trend in residual analysis
- correlation coefficient >0.98

A 95 % confidence interval was evaluated for the fit in Matlab®. The confidence interval gives a region where the true value of a parameter lies with a certain probability for infinitely many repetitions of the measurement. A narrow confidence interval identifies a good quality of the fit (Figure 48). Residuals can be evaluated by subtraction of the modelled and experimental data. If descending or ascending trends are identified, this can give a hint on poor performance of the model (Figure 49).

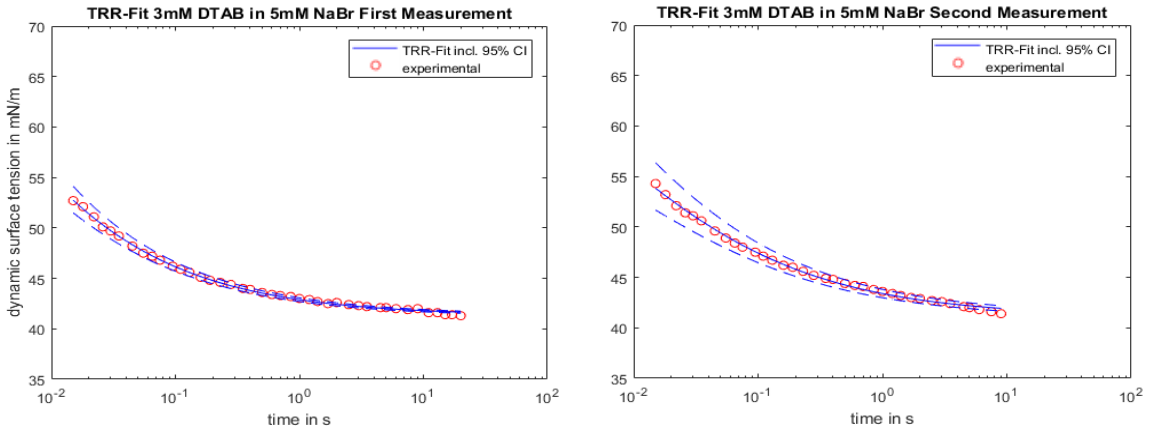

Figure 48 - Confidence intervals of the dynamic surface tension fit of two different 3 mM DTAB in 5 mM NaBr solutions. The narrower confidence interval (left) indicates better data.

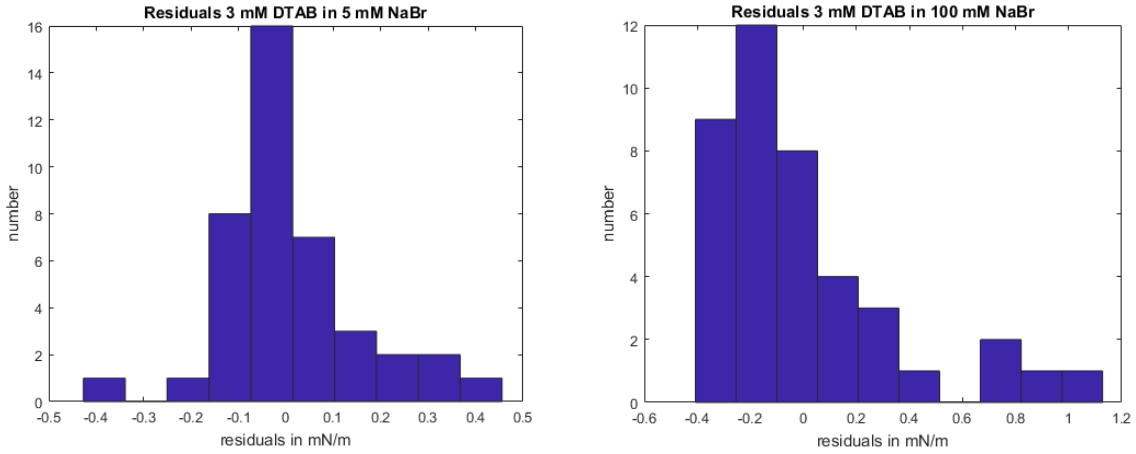

Figure 49 - Residuals of the dynamic surface tension fit of 3mM DTAB in different salt solutions. The left residuals are nearly normal-distributed, while the right show an almost descending trend.

The correlation coefficient shows the linear relation between modelled and measured data. A number close to one shows best agreement. If more than one curve was available for a given surfactant solution, the decision was made according to the absolute values of confidence interval, residuals and correlation coefficient. Values extracted from measurement with PEEK capillaries were only considered if no PTFE capillary data was available. The apparatus constant was calculated by equation (160) from the 14 remaining surface tension curves that fulfilled all criteria. The dataset included all SDS solutions, except the lowest concentration, and all DTAB solutions with high salt concentration. Most measurement problems occurred for the DTAB solutions with 5 mM NaBr and high surfactant concentration, where also two PEEK-capillary measurements were considered. Further data is given in the appendix, Figure 103. Results of the apparatus constants are shown in Figure 50. From analyzing Figure 50 it seems that the SDS solutions with 10 mM of NaCl gave lowest apparatus constants. The arithmetic mean of all apparatus constants is determined as:

$$\lambda_{bubble} = 5.4 \pm 0.9$$

Christov et al. determined an apparatus constant for the Krüss BP 2 device with the same procedure of 6.07 ± 0.01 [58]. As expected, the absolute values of the results are similar. The central difference is the standard deviation, which is nearly two orders of magnitude larger for the current study. It is very likely that the reason for this lies in the used capillaries. Although fabrication of these components was done carefully, minor differences cannot be avoided. Furthermore, the glass capillaries used by Christov et al. were additionally hydrophobized before use to get a hydrophobic capillary with hydrophilic tip. In reference [58] it is mentioned that SITA tensiometers tend to give lower surface tension for the same nominal bubble age compared to the Krüss BP 2. This tendency is supported by the lower apparatus constant for the current SITA device, compared to the bubble pressure tensiometer of Krüss that was used in the article. The higher standard deviation found in this study implies that the determined apparatus constant can only give an approximation and not a sharp value, which is exactly valid in any case.

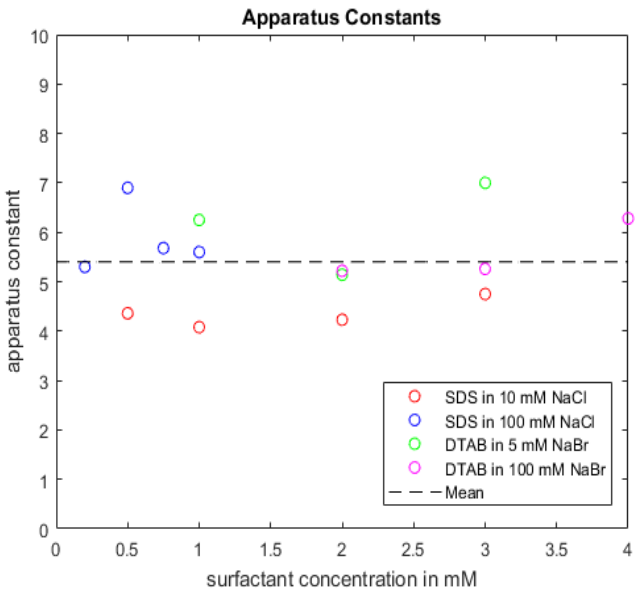

Figure 50 - Calculated apparatus constants.

4.1.4.5 Dynamic Surface Tension Measurement of Coating Liquids

The measurement was performed analogously to the procedure explained in 4.1.4.4.2 that describes the measurement of surfactant solutions. Only PTFE capillaries were used for measuring the dynamic surface tension of coating liquids. Settings are given in Table 17.

Table 17 - Settings of the bubble pressure tensiometer for coating liquid measurement.

SITA proLine t15	
Start Bubble Age	1000 ms
End Bubble Age	3000 ms
Number for Mean	3
Resolution	High
Tolerance	5 %
Refusal	First

Each result is the mean of two measurements. The universal surface age can be found using equation (161). It is known that for both coating liquids, the surface age in the curtain is around 70 ms. This dictates to use a nominal surface age of $t_{age} = t_u \lambda_{bubble}^2 = 70 * 5.4^2 \approx 2000\, ms$ to connect measured data with experiments. An example of a dynamic surface tension curve is given in Figure 51. The corresponding surface tension at a nominal bubble age of 2000 ms is extracted.

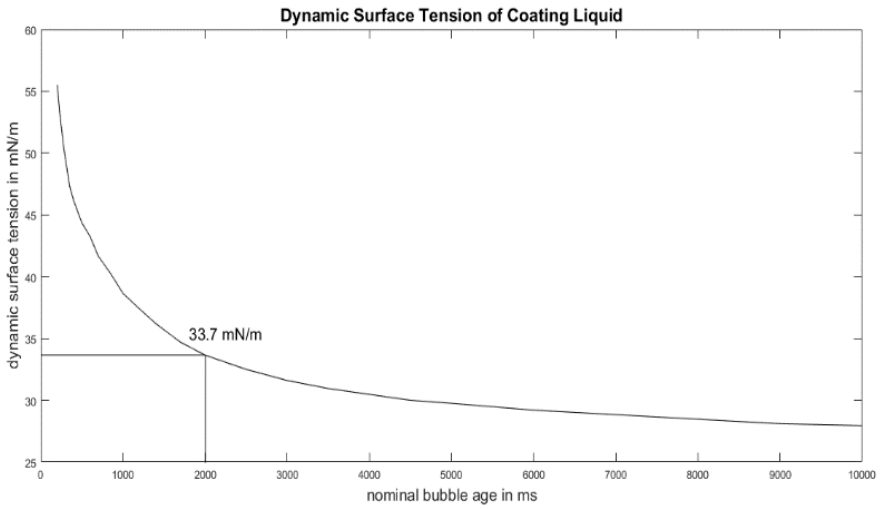

Figure 51 - Example for the use of the calculated universal surface age on measured data.

4.1.5 Liquid Density

The density was measured using a 50 cm^3 pycnometer density cup of BYK Additives & Instruments. The density cup was completely filled with the coating liquid at RT and closed with the cap. Overflow could exit the cup via an exit hole at the center of the cap. The outer shell of the cup was cleaned with water, dried, and the mass was recorded at a laboratory scale.

4.1.6 Solid Content

Solid content of coating liquids was determined with Mettler Toledo Halogen Moisture Analyzer HB43-S. The temperature setting was 140 °C with the stop criterion of a drying rate smaller than 1 mg per 50 s, which is recommended for most samples [59]. The sensitivity of the scale is 1 mg, and the permissible mass range of the sample is 0.5 to 54 g [59]. The heat is delivered by an omnidirectional halogen radiator. A process sketch is given in Figure 52.

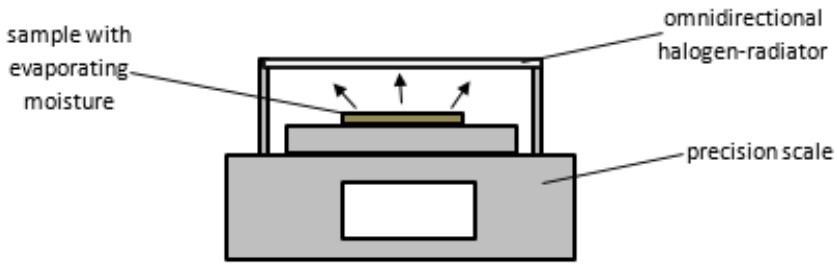

Figure 52 - Sketch of Moisture Analyzer.

4.1.7 Curtain Coating Process

A detailed discussion of the Curtain Coating device in use is given in chapter 2.1.2 and is not repeated in this section. Other devices necessary for the process and optimizations of the device are discussed hereafter.

4.1.7.1 Edge Guide Geometry

Observations on the Curtain Coating process led to the conclusion that the geometry of the edge guides restricts the curtain stability. On the original design, the flow tends to split into two distinct streams. This deteriorates the mentioned thinning at the edge guides, and detachment from the guides can be seen frequently. Coating of substrates at low flow rates was hence not possible with this edge geometry. The left picture in Figure 53 indicates the flow of the coating liquid along the original edge guide geometry. Simple geometries were tested without kinks or edges, which are prone to split the flow. Best results were seen for a flat plate, which reduces the coating width around 1 cm at both sides directly after the pouring edge (see mid picture in Figure 53). The geometry was designed in a purely intuitive way, since no detailed design information for simple edge guides could be found. At the start of the Curtain Flow Zone, coating liquid is collected via the reduction of coating width on the upper end of the proposed edge guides. This leads to a considerable increase of coating liquid flowing along the guides and therefore reduces the risk of detachment. The impact was satisfactory since the minimum flow rate to form a stable curtain was reduced to about one third of the original process. The only evident drawback is the reduction of the coating width from 25 to 23 cm. In the right picture of Figure 53, the new edge design during a coating procedure is shown. The collected liquid pool at the upper plateau and the thinning along the guide is obvious.

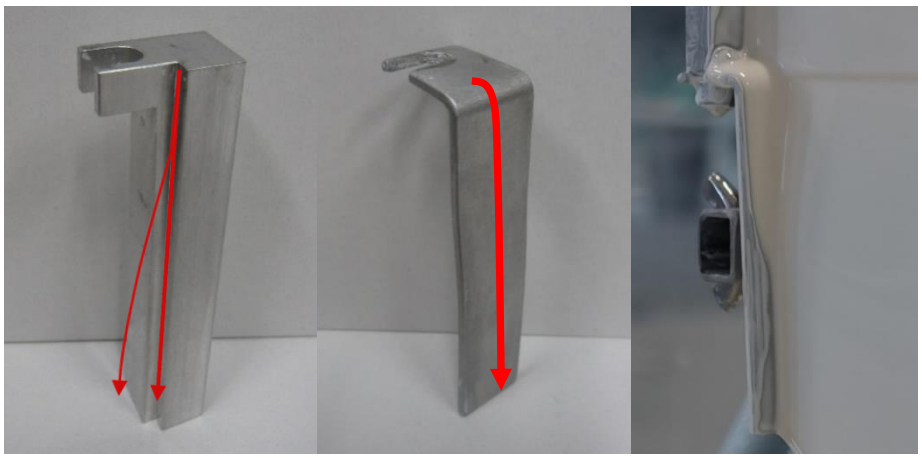

Figure 53 - Edge guide designs with original edge guide geometry (left), proposed edge guide geometry (mid) and proposed edge guide geometry during the process (right). The arrows indicate liquid flow.

4.1.7.2 Air Flow Protection

Air flow dragged along with the moving substrate, or pushed along the transport plate, is minimized by an air shield below the coating device and a sharp-edged front of the transport plate. The air shield was designed analogously to the patent of Hughes (1968) [10]. The invention presented three air shields with scoop-shaped ends mounted in tandem. The shields should be positioned close to the moving web to efficiently remove air from the surface. Figure 54 shows the air shields installed on the coating apparatus at a potential working position. The sharp edge at the front of the transport plate was installed during reconstruction work for the convection dryer. Prior to this, a sharp-edged extension of cardboard was mounted at the front of the transport plate.

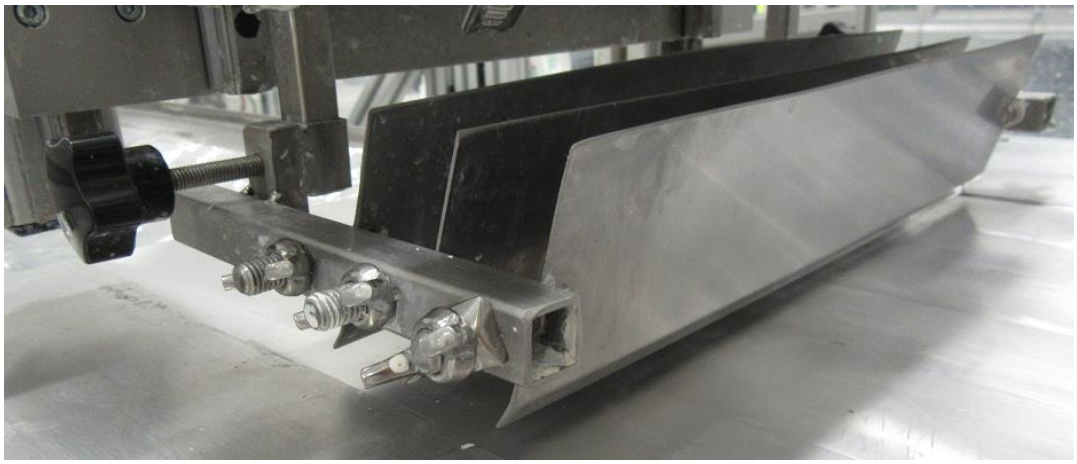

Figure 54 - Installed air shields at potential working position directly above the transport plate.

4.1.7.3 Other devices

Coating liquids had to be stirred in the reservoir during the coating process. Closed Visco-Jet® stirrers of conical geometry were used. Due to the specially designed stirring geometry, coalescence of small air bubbles in the liquid occurs, and deaeration can be performed while mixing. To the feed of the coating device, liquid was transported by a Netzsch NM021BY02S12B progressive cavity pump. The maximum volume flow rate is 7.5 L/min at a revolution speed of 352 min^{-1} [60]. The specified temperature range is 10 to 35 °C [60]. A magnetically coupled Scherzinger gear pump type 4030-710-B-DM-75-2 was used for discharge of the liquid collected in the coating pan. The pump is specified for liquids in the viscosity range of 0.5-3000 mPas and temperatures between -20 and 130 °C [61]. The maximum volume flow rate is 24.85 L/min at the maximum revolution speed of 3500 min^{-1} [61]. Volumetric flow rate of coating suspensions was measured in the range of 0 to 5 L/min with an accuracy of 0.1 L/min by the electromagnetic flow sensor KROHNE OPTIFLUX 4000 and the appropriate signal converter KROHNE IFC 300. The tools were installed according to the

manual description by the Electrical Bureau of MM Karton Frohnleiten. The calibration was done by KROHNE. The measuring principle is as follows [62]: An electrically conducting fluid enters an electrically insulating pipe of known cross section. A magnetic field, perpendicular to the flow direction, is induced by a pair of field coils. This leads to an induced voltage, which can be measured by electrodes. The signal converter intensifies, filters and ultimately converts the signal to a flow quantity. A set-up sketch and the working equation are given in Figure 55 and equation (162), respectively [62].

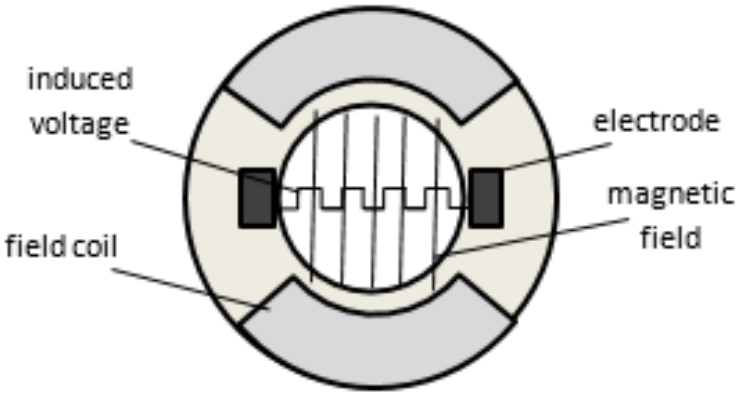

Figure 55 - Magnetic inductive flowmeter set-up [62].

$$U = v * k * B * D \tag{162}$$

With the induced voltage U, the flow velocity v, the geometric correction factor k, the magnetic field B and the inner diameter of the pipe D.

The substrate is transported by two synchronous linear actuators of FMP Technology type FMP LBA CCM SD250 1712 on a self-designed carrying plate. The overall transport distance is 3.4 m, with the coating position 1.5 m from start. The velocity can be varied between 0 and 300 m/min. Two emergency power-off switches are installed, and movement is only possible if the security lock system is activated. Visualization and identification of malfeatures during the Curtain Coating process were done with the compact camera Sony RX100 M4. Since the interesting timescale of the coating process is in the order of 100 ms, the recording tool must produce videos with high frame rates. The camera records videos with frame rates as high as 960 fps for approximately 4 s at time priority and approximately 2 s at quality priority mode [63]. All videos were recorded in the time priority mode with a resolution of 1920x1080.

4.1.7.4 Coated Mass

The amount of solid deposited on the substrate by Curtain Coating can be calculated by:

$$m_{coat} = \frac{\dot{V}_l \rho_l w_{solid}}{\left(\frac{v_{sub}}{L_{sub}}\right)} \tag{163}$$

Here, the numerator accounts for the mass of solid transported per unit time via the coating flow, and the denominator for the time of the substrate in the impingement zone (Figure 56).

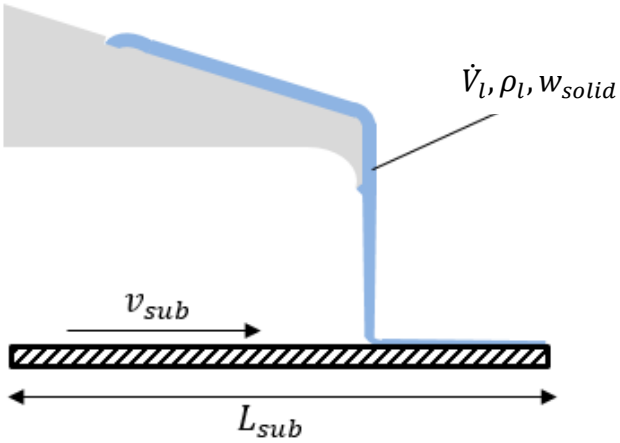

Figure 56 - Sketch for calculation of coated mass during Curtain Coating.

By knowing the coating width, it is possible to determine the deposited solid per unit surface area, called the grammage of coating G_{coat}, as:

$$G_{coat} = \frac{m_{coat}}{W_{coated} L_{sub}} \tag{164}$$

4.2 Drying of Coatings

4.2.1 Net Isosteric Heat of Sorption and Desorption Isotherm

The sorption energy, which has to be added to the heat of vaporization of pure water Δh_{vap} to consider the hygroscopic character of paper materials, is called the net isosteric heat of sorption Δh_{sorp}. It was determined together with the desorption isotherm for untreated ACK 350 cardboard of MM Karton according to the COST-90 procedure [64]. A static-gravimetric method was used, where wet substrate of known initial mass was stored in closed containments above saturated salt solutions of known water activity in the gas phase, and at constant temperatures, until equilibrium was reached (Figure 57). This is a simple and widely used procedure to determine sorption characteristics [65-67]. Five salt solutions were investigated at two different temperatures. From experience it is known that typical mean substrate temperatures during the drying process lie between 25 and 80 °C, with long

residence time around 40 °C. For this reason, desorption isotherm experiments were done at 40 and 60 °C. The salt solutions and the corresponding water activities are given in Table 18.

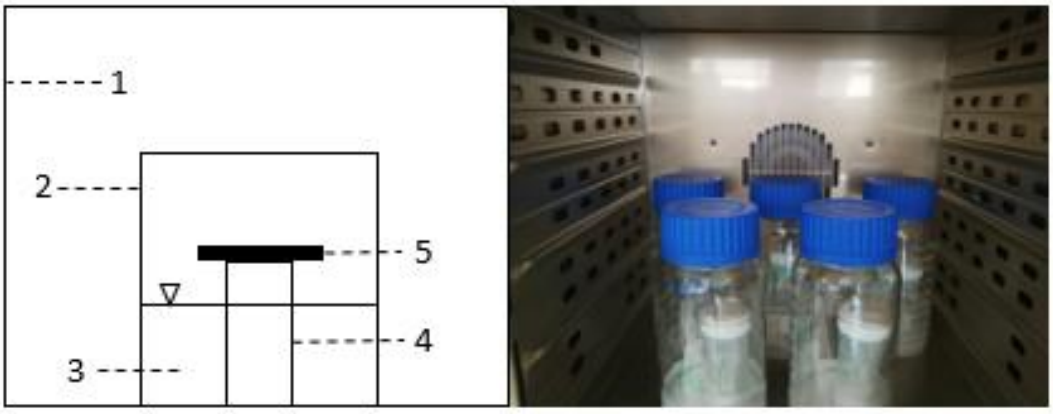

Figure 57 – Set up of sorption experiments with oven (1), closed containment (2), salt solution (3), column (4) and cardboard sample (5).

Table 18 - Equilibrium vapor activities for the used saturated salt solutions [68]

Saturated Salt Solution	Water Activity at 40 °C	Water Activity at 60 °C
NaOH	0.0626	0.0362
$MgCl_2$	0.316	0.2926
$Mg(NO_3)_2$	0.4842	0.45*
NaCl	0.7468	0.7441
KCl	0.8232	0.8022

*extrapolated from 50 °C

Water activities are given in reference [68] by Greenspan (1977). Untreated ACK 350 was cut with a hollow punch of 4 cm diameter, wetted with an air-brush pistol with pure water, weighed on an analytical scale and positioned in the corresponding containment. After 144 h, equilibrium was reached for all samples. The samples were weighed again on an analytical scale and dried for 2 h at 140 °C. Subsequently, the dry mass was recorded. Results in tabular form are given in Table 33 and Table 34 in the appendix. Due to the time-consuming procedure, only single measurements were done.

4.2.2 Convection Dryer

The design of a convection dryer was one of the central tasks in this thesis. The mission statement was to integrate a convection dryer into the coating unit which is capable of performing reproducible experiments to investigate the overall drying energy necessary to dry a coated substrate. Naturally, an economic solution should be presented. Further constraints

were given by the limited space available. This means the dryer must not exceed a certain length to comply with security regulations in fire safety.

4.2.2.1 Hot Air Supply

The two reasons for hot air supply were, firstly, ensuring a uniform temperature of the dryer itself and, secondly, providing a certain amount of drying air at the appropriate temperature. For the first task, a combination of a Leister LHS 61L System (16 kW) heater with continuous temperature control via potentiometer and an air exit diameter of 92 mm with a Leister ASO blower, which can supply up to 13500 L air/min for the chosen frequency of 50 Hz at 20 °C and under free outlet conditions, was used [69]. A frequency converter was installed additionally to enable volume flow control. The maximum possible temperature at a given air flow and the characteristic pressure-drop curve of the heater and blower, respectively, are given in Figure 105 [69]. For the second task, the stand-alone device Leister Mistral 6 System (3.4 kW) hot-air blower was used. This tool allows both the control of temperature up to 650 °C, depending on the air flow rate, and the control of the air flow itself. Maximum air flow rate at free outlet conditions is 350 L/min [70]. Unfortunately, no characteristic pressure-drop curve was available. However, Leister provided alternative data of comparable blowers, which can be found in the appendix (Figure 106). The dependency of real volume flow rate to volume flow rate adjustment is linear, as can be seen in the appendix (Figure 107). The outlet diameter is 48 mm [70].

4.2.2.2 Dryer Geometry

Well-defined flow conditions form the basics to ensure a reproducible drying process. Internal flow is less dependent on the ambient conditions and hence was preferred. To assure a well-understood, uniform drying process, the geometry was designed in a way that a uniformly distributed, fully developed and laminar flow moves over the substrate. To integrate the dryer into the coating unit without substantial modifications of the beforementioned, a minimum width of the drying channel W_{dryer} of 65 cm was necessary. A high aspect ratio was chosen to ensure short entrance length for the velocity profile along the dryer height and at the same time to prevent overlapping with boundary layers growing along the side walls (Figure 58). A minimum dryer height of 2 cm was set to ensure some safe distance between the moving transport plate (or rather the moving bottom of the drying chamber) and the fixed upper plate. To choose the appropriate dryer dimensions, especially the maximum velocity and the typical temperature range for drying experiments using the Leister Mistral 6 System are of relevance. To find an optimum height, width and length, optimization steps as presented in Figure 59 were performed.

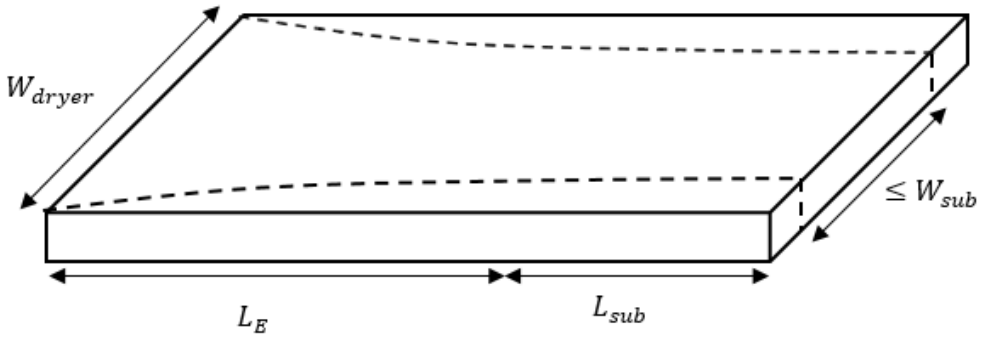

Figure 58 - Dryer geometry with growing boundary layers at the side walls (dashed lines) and short entrance length L_E of velocity profile over the dryer height. At least the planned substrate width W_{sub} must be available between the growing boundary layers at the side walls.

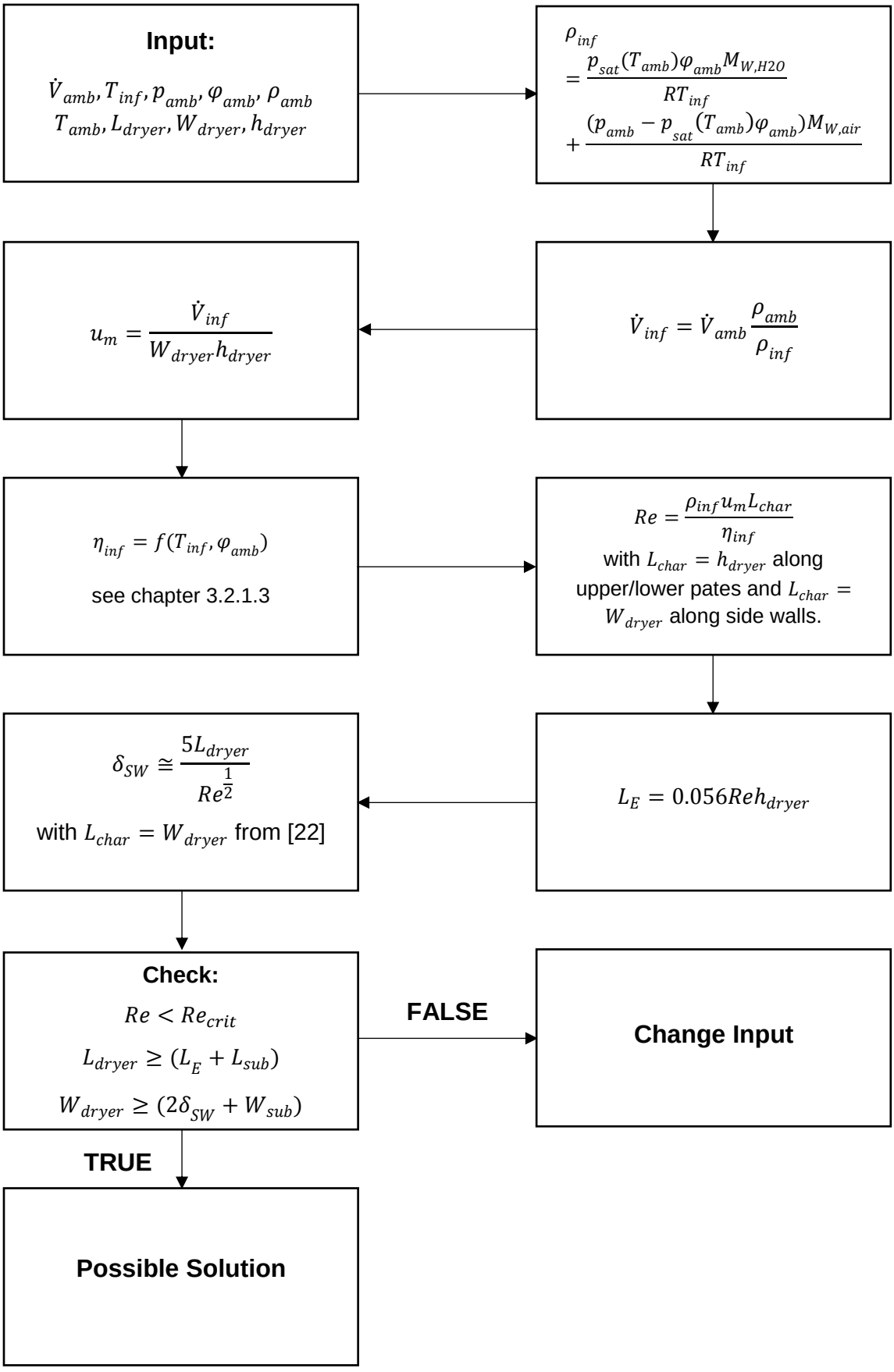

Figure 59 - Optimization procedure for dryer geometry.

The volume flow rate at ambient conditions, $\dot{V}_{amb}$, is fixed by the maximum volume flow rate of the Mistral 6 System (=350 L/min). Typical drying air temperatures T_{inf} were assumed to reach a maximum of 200 °C. The ambient humidity φ_{amb} was set to 0.4, and the pressure p_{amb} was assumed to be constant (also in the dryer) at 101.3 kPa. Saturation pressure, density and viscosity data at ambient temperature were taken from references [35] and [36] as explained in chapter 3.2.1. The critical Reynolds number Re_{crit} for internal flow is generally assumed to be 2100, and the substrate to be dried should have A3 format ($L_{sub} = 0.42\ m;\ W = 0.297\ m$) [22]. The effective substrate width is reduced to the maximum coating width of $W_{sub} = 25$ cm. The optimization procedure explained in Figure 59 led to the conclusion to use the minimum width and height of the dryer, since Reynolds numbers are low anyway and too low Reynolds numbers can lead to long drying times. Results are summarized in Table 19.

Table 19 - Results of geometry optimization of dryer

Parameter	Value
Re	~420
$(L_E + L_{sub})$	(0.47 + 0.42) m
$(2\delta_{SW} + W_{sub})$	(0.13 + 0.297) m

Obviously, exceeding the critical Reynolds number and overlaps with the boundary layers at the side walls are no issue in the proposed geometry. However, the minimum dryer length cannot be calculated from data above because the flow inlet was not designed yet. The inlet design should assure a uniform flow distribution at least over the substrate width. A simple geometry was proposed by ao. Prof. H. Steiner of TU Graz Institute of Fluid Mechanics and Heat Transfer. He argued to use an inlet pipe, positioned at the mid of the dryer width, a few channel diameters downstream from the backside wall, which is orientated perpendicular to the main flow direction (Figure 60). The stagnation of the flow in the region below the pipe and at the backside wall leads to a pressure buildup, which should ultimately produce a uniform flow over the dryer width. The introduced pressure loss for the conditions described above was estimated as shown in chapter 2.2.3. This led to a total pressure loss of

$$\Delta p = \left(\Delta p_{in} + \Delta p_{dryer}\right) = (12 + 1)\ Pa$$

The small pressure loss is a direct consequence of the small Reynolds number in the system. Consequently, the assumption of constant pressure within the dryer is valid, and the volume flow rate of Mistral 6 System does not have to be corrected with the characteristic pressure loss curve. Instead, the volume flow rate for free outlet conditions can be used.

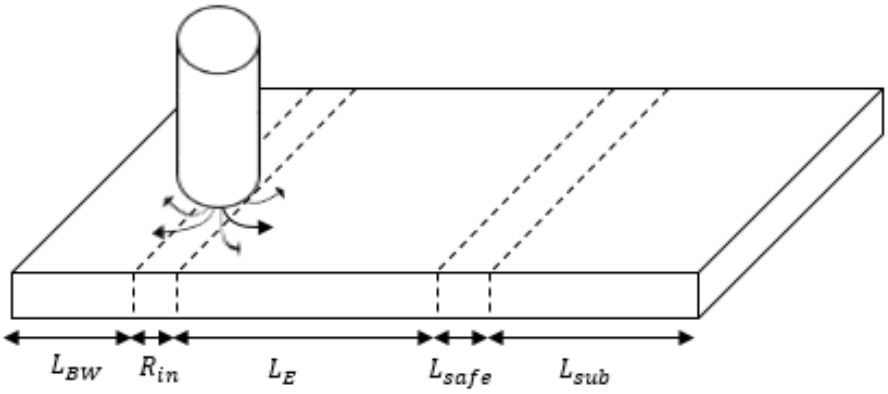

Figure 60 - Inlet geometry proposed by ao. Prof. H. Steiner. Symbols are explained in the text. The curved arrows indicate the air flow.

At this point it was not clear where exactly to position the inlet pipe, and if the small pressure loss can produce uniform flow over the substrate width. For this reason, a CFD simulation was conducted in Ansys Fluent® by ao. Prof. H. Steiner and Dipl.-Ing. H. Hinterbichler at the TU Graz Institute of Fluid Mechanics and Heat Transfer. A geometry of an overall length of $L_{dryer} = 131\ cm$ was proposed. The overall length includes an inlet section with the mentioned pipe mounted a certain distance away from the backside wall L_{BW}. Two different inlet sections were tested, where the overall length was kept at 131 cm. The distance of the inlet pipe from the backside wall was 10 and 22.4 cm, and the inlet radius $R_{in} = 2.4\ cm$ as given for the Leister Mistral 6 System. The inlet section is followed by the entrance region $L_E = 47\ cm$ and a safety margin L_{safe} of around 18 or 30 cm (depending on the position of the inlet pipe). The geometry ends with the drying chamber, with exactly the substrate length $L_{sub} = 42\ cm$. For both designs two inlet velocities were tested. The higher velocity corresponds to the case of a drying temperature T_{inf} of 200 °C and an ambient volume flow rate $\dot{V}_{amb}$ of 350 L/min and is hereafter related to as the maximum inlet velocity case. The lower velocity corresponds to a drying temperature of 100 °C and an ambient volume flow rate of 100 L/min and is hereafter related to as the minimum inlet velocity case. A summary of the conditions is given in Figure 61 and a coordinate system for the problem is introduced in Figure 62. The simulated flow was analyzed according to the following criteria in the substrate region:

- Parabolic shape of the air flow velocity profile
- Uniformity and absolute value of the midplane velocity
- Uniformity and absolute value of the velocity gradient

The parabolic shape of flow profiles is a hint for a fully developed laminar flow, as explained in chapter 2.2.2. Deviations from the parabolic shape are hence expected for positions far

upstream and for high Reynolds numbers. Figure 63 (A) and (B) show the difference between minimum and maximum inlet velocity for the case of $L_{BW} = 10\ cm$ at different positions along the substrate length L_{sub} in the mid of the substrate width W_{sub}. Figure 63 (C) and (D) show the profiles for the maximum inlet velocity cases as above, but at different positions along the width.

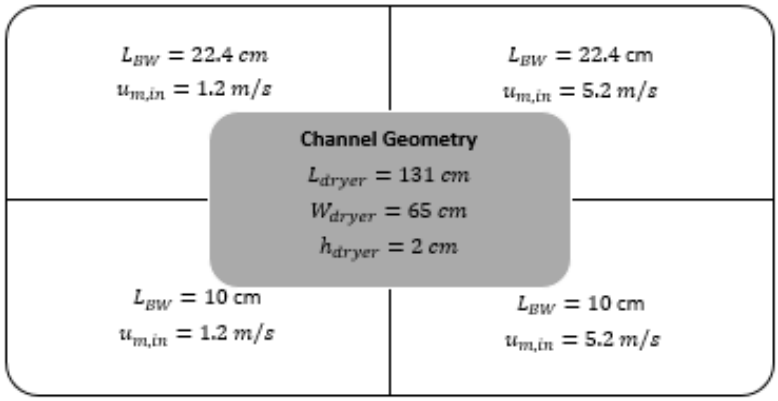

Figure 61 - Conditions for CFD simulation.

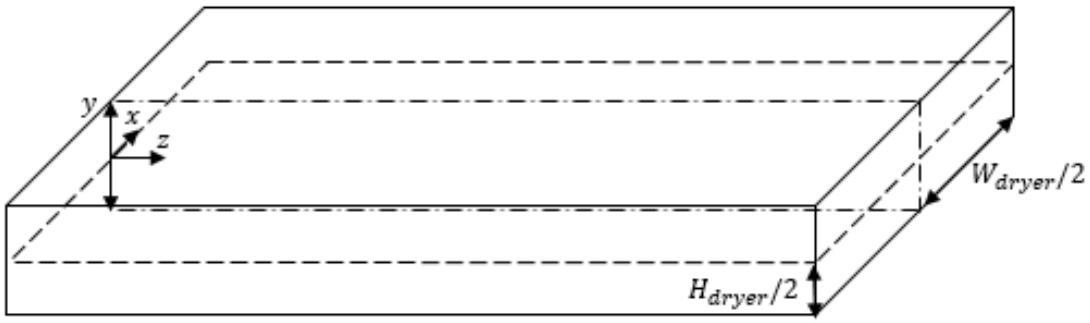

Figure 62 – Drying chamber with the coordinate system. The coordinate system is positioned at the very upstream position of the dryer in the mid along the dryer height and width. The upstream end of the substrate lies at $z = 0$ and the plane at which $y = 0$ is indicated by the dashed line. The plane at which $x = 0$ is indicated by the dash-dotted line.

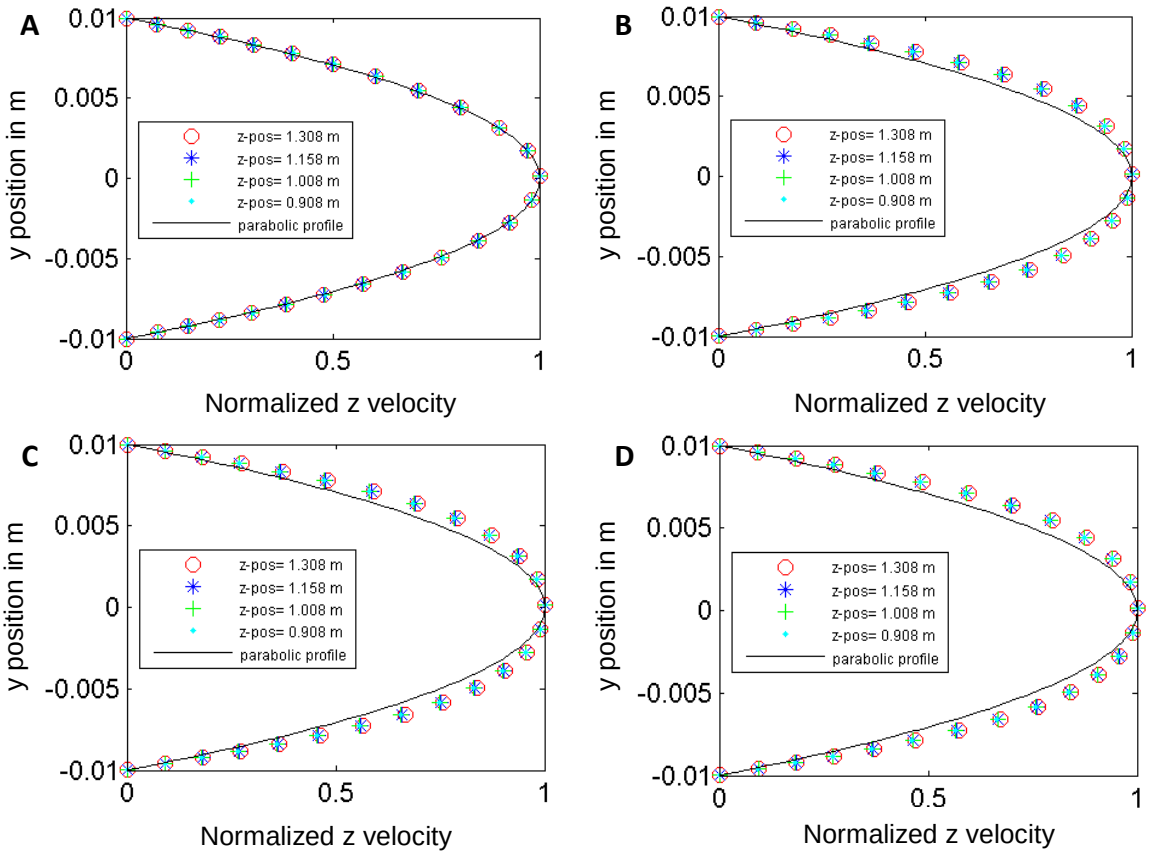

Figure 63 - Predicted velocity profiles for $L_{BW} = 10\ cm$, (A) $u_{min,in}$, width position= mid, (B) $u_{max,in}$, width position= mid (C) $u_{max,in}$, width position= ± 6.25 cm from mid, (D) $u_{max,in}$, width position= ± 12.5 cm from mid.

All velocity profiles are nearly parabolic in shape, though small deviations can be found for the cases of maximum inlet velocity. The same trend is seen for the inlet position at 22.4 cm, as shown in the appendix. The dependency of the profile shape on the position along the substrate width is small, but tends to deviate stronger from the parabolic shape at positions off the midplane. This can be explained by a slightly higher velocity in this region, as can be seen hereafter. A uniform velocity in the main flow direction above the substrate at the plane where $y = 0$ is a hint for well-behaved flow and enables uniform drying (Figure 62). This velocity is called the midplane velocity in the following discussion. As can be seen in Figure 63 above, the midplane velocity is the maximum velocity in the flow profile. To avoid confusion with the maximum inlet velocity, this nomenclature is not used in this chapter. The simulation revealed highest deviation of midplane velocities near the dryer exit. Hence this position is compared for the four cases in Figure 64.

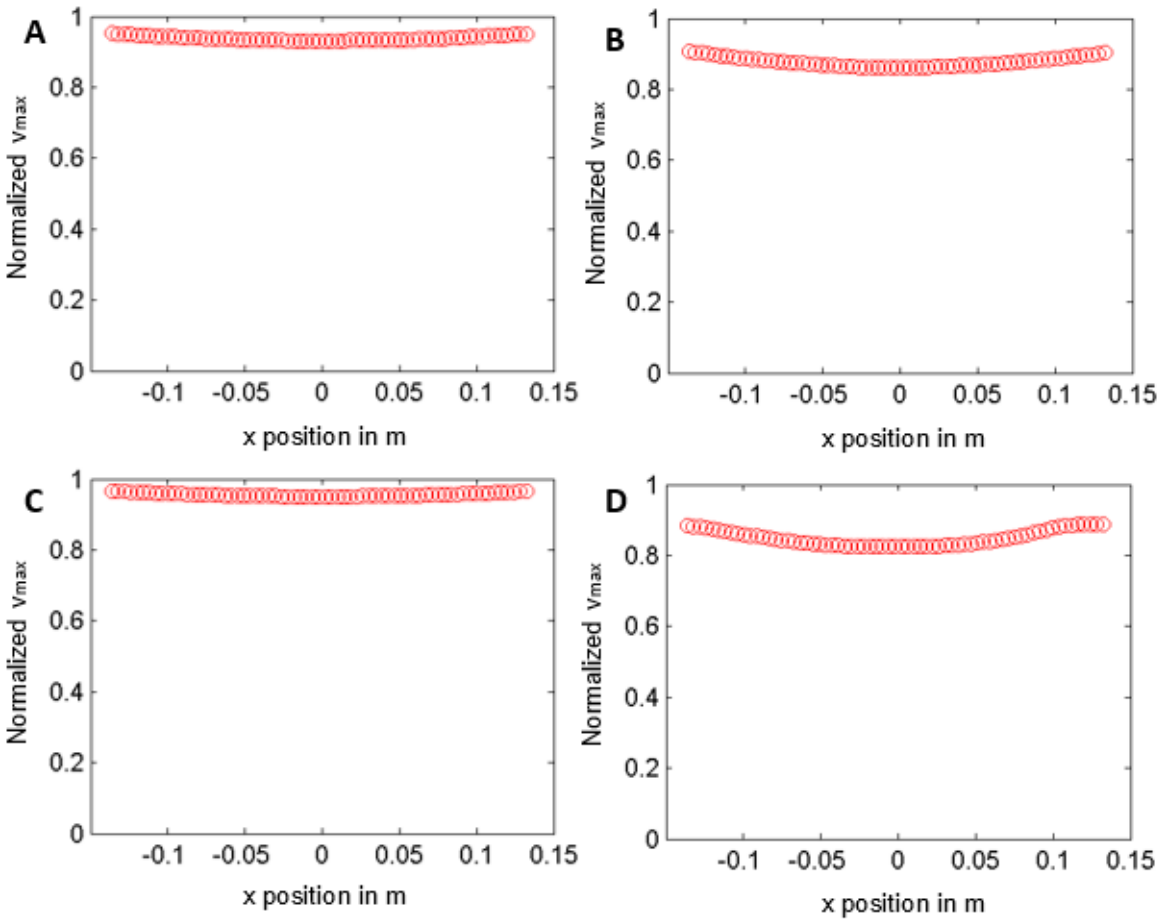

Figure 64 – Predicted midplane velocities at the exit. (A) $L_{BW} = 22.4\ cm$, $u_{min,in}$, (B) $L_{BW} = 22.4\ cm$, $u_{max,in}$,(C) $L_{BW} = 10\ cm$, $u_{min,in}$, (D) $L_{BW} = 10\ cm$, $u_{max,in}$.

The midplane velocity is more uniform for the minimum inlet velocity cases. Deviations smaller than 5 % can be found over the substrate width. For the maximum inlet velocity case, deviations as high as approximately 10 % occur. For the purpose of uniform drying, however, it is assumed that all cases are acceptable. The asymmetry in case (D) may be caused by the turbulence model, used in the CFD simulation. It should be noted that throughout the substrate edges, higher midplane velocities are predicted. This can lead, as mentioned before, to higher deviation from the parabolic profile. A more thorough look on the midplane velocity is given in Figure 65 for the important maximum inlet-velocity cases.

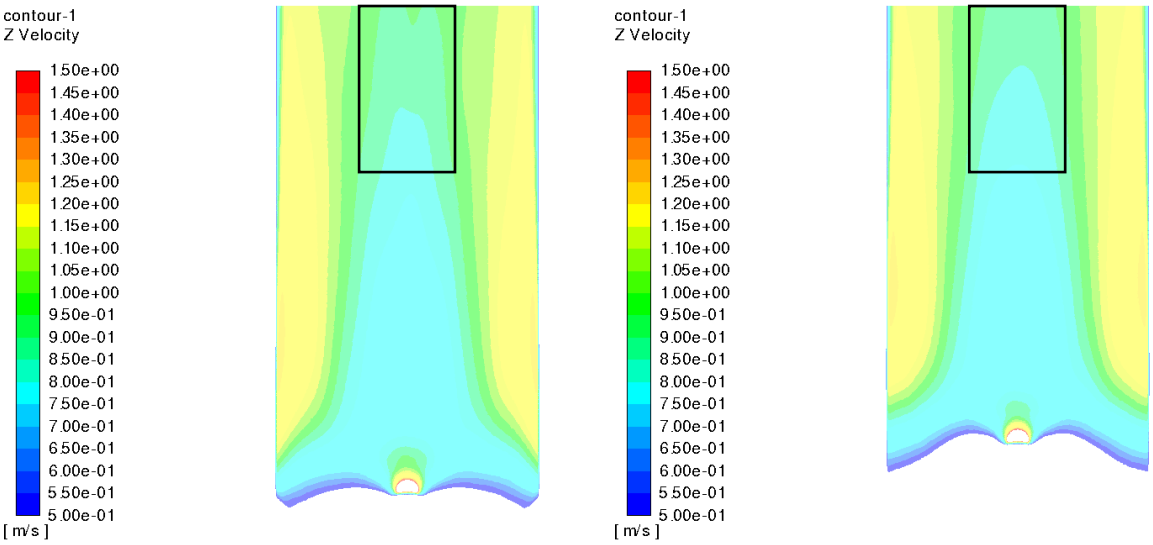

Figure 65 - Predicted midplane velocities in the entire dryer for the maximum inlet velocity case for $L_{BW} = 10\ cm$ (left) and $L_{BW} = 22.4\ cm$ (right). The black framed rectangle shows the substrate position.

The midplane velocity range above the substrate for both maximum inlet velocity cases is approximately between 0.75 and 0.9 m/s. This means a maximum deviation based on the minimum midplane velocity of 20 %. The velocities tend to increase downstream and seem to be slightly higher for the 10 cm inlet position. Again, it is assumed that the deviations are within an acceptable range and none of the inlet designs is clearly advantageous. Another important point for uniform drying is the velocity gradient at the substrate surface. The simulation revealed that the velocity gradients for the minimum inlet velocity cases are in the order of 45 to 50 s^{-1}, which is low and would implicate long drying times. The maximum inlet velocity case is certainly the more interesting one with regard to efficient drying times and is presented in Figure 66. The velocity gradient range at the substrate surface varies for both inlet geometries from 200 to 220 s^{-1}, which is interpreted as acceptable for uniform drying. The case of 22.4 cm inlet position seems to be slightly more uniform, which is an advantage of this geometry. On the other hand, the 10 cm inlet position gives slightly higher velocity gradients at the surface, which is positive with regard to short drying times.

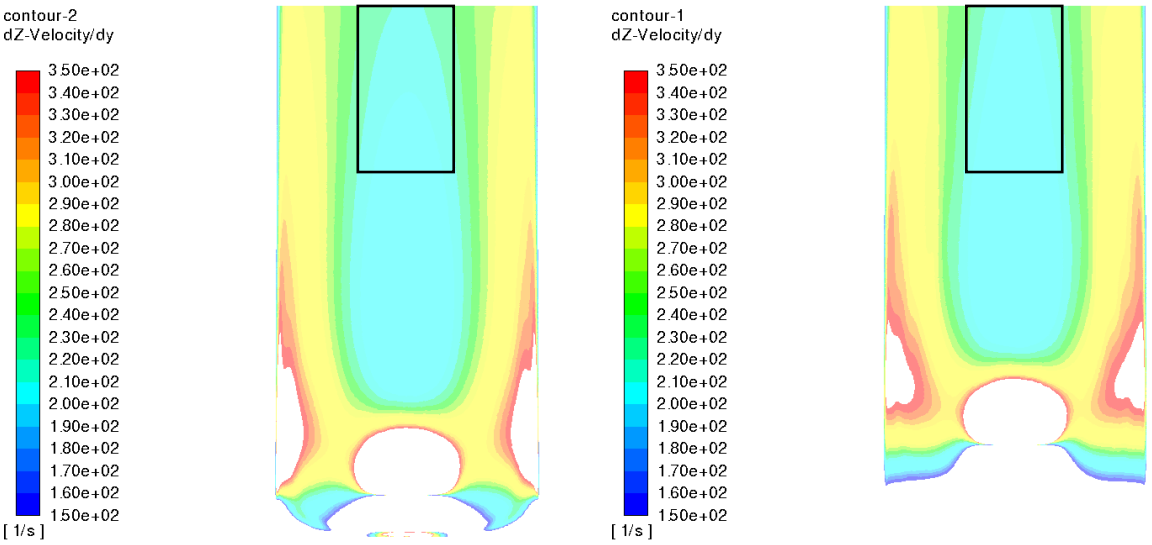

Figure 66 - Predicted velocity gradients at the substrate surface for the maximum inlet-velocity case in the entire dryer with $L_{BW} = 10\ cm$ (left) and $L_{BW} = 22.4\ cm$ (right). The black rectangle shows the substrate position.

To summarize the simulation results, no clearly advantageous inlet geometry could be identified. As expected, the minimum inlet velocity cases lead to a more uniform and fully developed flow, with the severe drawback of low Reynolds numbers and low velocity gradients and, hence, less drying efficiency. The maximum inlet velocity cases lead to acceptable deviations from fully developed, laminar profiles and uniformity. The velocity gradient at the substrate surface is more uniform for the 22.4 cm inlet position, but has slightly higher values for the 10 cm distance. Further simulation results are shown in the appendix (Figure 108 to Figure 123). For the sake of flexibility, both inlet positions were introduced in the dryer design, by two holes in the upper dryer plate and a switchable faceplate with an adapter pipe for the connection with the heat blower. The faceplate is tightened by screws and can be used for both inlet positions, simply by rotation. The bottom of the drying chamber is mobile and not directly connected to the dryer. Instead it is connected to a linear actuator and serves simultaneously as transport plate for the Curtain Coating process. The transport plate was, hence, geometrically adapted to ideally fit into the chamber. For security reasons, a minimum distance of 1 cm between the stiff metal parts of the dryer side walls and the moving transport plate had to be ensured. This would result in a gap between transport plate and side walls and, thereby, a loss of drying air. To avoid losses at these positions, a combination of a strip-brush, mounted on the transport plate side walls, with a U-shaped pocket at the dryer side walls was installed. The strip-brush consists of PEEK (Polyetheretherketone), which withstands working conditions of maximum 280 °C. A sketch demonstrates the principle of the moving bottom and the strip-U-pocket combination (Figure 67). The width of the transport plate is 62 cm, with

1.5 cm PEEK brushes at the plate side walls. The maximum plate thickness is 8 mm, with a sharp edge at the front to 4 mm thickness with an angle of 10° to avoid air current transport to the coating process.

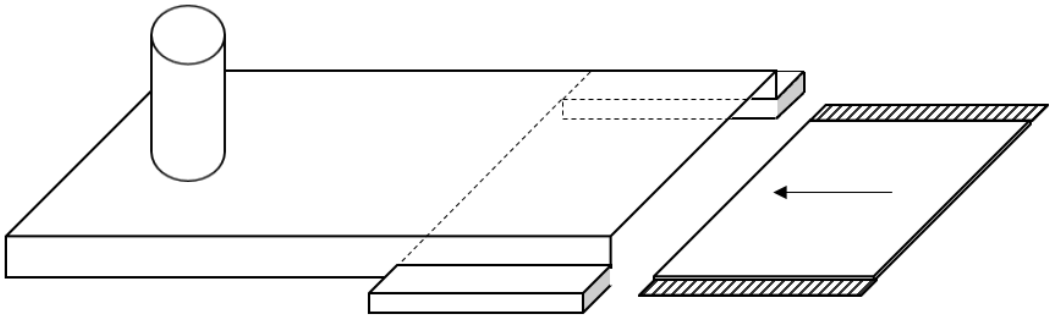

Figure 67 - Dryer geometry with moving bottom of the drying chamber (=transport plate) and U-pocket/strip brush combination to avoid air losses.

The geometry was constructed by the Technical Bureau of MM Karton Frohnleiten with special contributions from Ing. R. Paar and Ing. E. Stadlhofer. As the material for the dryer, a special Fe-Ti alloy was used, which is recommended for high-temperature applications. The thickness of 2 mm is based on a compromise between introduced mass (or rather heat capacity) and mechanical stability. To prevent irregular surface within the dryer, the construction was cambered and screwed at the outside instead of welded. A reinforcing rib is mounted at the top to prevent material distortion by high-temperature stress. An engineering drawing of the dryer is given in Figure 68.

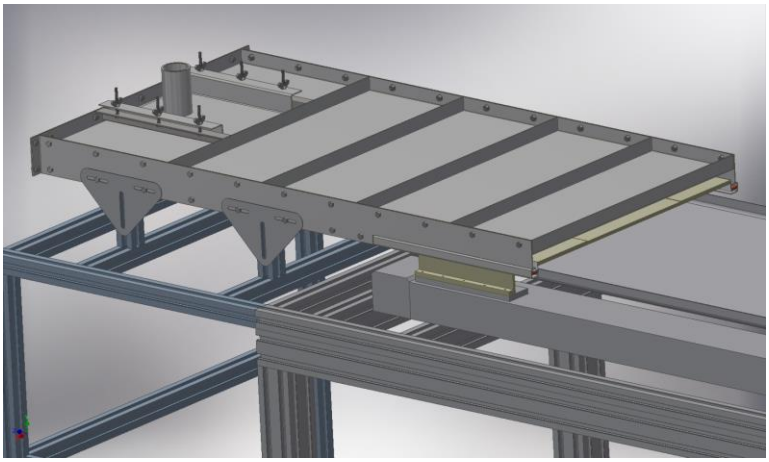

Figure 68 - Engineering drawing of the dryer. The switchable faceplate with the adapter pipe for the use of the 10 cm inlet position is seen. At the flow exit, the U-profile/brush combination can be identified. The transport plate is in the channel.

The transport plate consists of aluminum, because of the too high mass for the linear actuator when using the same material as for the dryer. The lower temperature resistance of aluminum is not a problem, since typical drying air temperatures are around 150 °C, and residence times in the dryer of maximum 5 min are standard. Aluminum has a melting point of 660 °C and is known for low thermal expansion [71]. Furthermore, no mentionable stresses act on the transport plate. This led to the conclusion of applicability of the material. The plate possesses a depression of 2 mm, which runs through the entire plate length, and is shaped according to the A3 format. The depression is used for positioning of insulating materials like cork below the substrate without altering the channel geometry. A picture of the transport plate is given in Figure 69.

Figure 69 - The transport plate with the PEEK brush at the side walls and an insulating plate of cork in the depression for drying experiments is shown.

The entire dryer surface was charged with 10 cm thick glass wool as an insulating layer and an outer shell of aluminum to keep the glass wool at the corresponding positions. A full view sketch of the dryer is given in the appendix (Figure 129).

4.2.2.3 Drying Temperature

The substrate temperature, as well as the temperature of the upper plate in the drying chamber, were measured with PT100 resistance sensors Heraeus M222-70, radially wired. At 0 °C, the resistance of the PT100 is exactly 100 Ω. By increasing the temperature, the electrical resistance is also increased, for example at 100 °C the resistance is 138.51 Ω. The electrical connection was performed with a simple two-wire system, and copper cables of 0.5 mm^2 cross sectional area were used. The maximum cable length is approximately 3 m, where the best part of all cables is at room temperature. Since the resistance of copper cables of this cross-sectional area is only about 36 Ω/km at 20 °C, and the correction factor for temperature does not change the order of magnitude, this additional resistance was neglected [63]. Three resistance sensors were positioned at uniform distances along the upper plate of the drying

chamber in order to measure the plate temperature at different positions along the main flow direction. The first sensor is positioned at the very upstream position (=DF1) of the substrate, the second at the substrate mid (=DF2) and the third near the dryer exit (=DF3). Figure 70 shows the principal set-up.

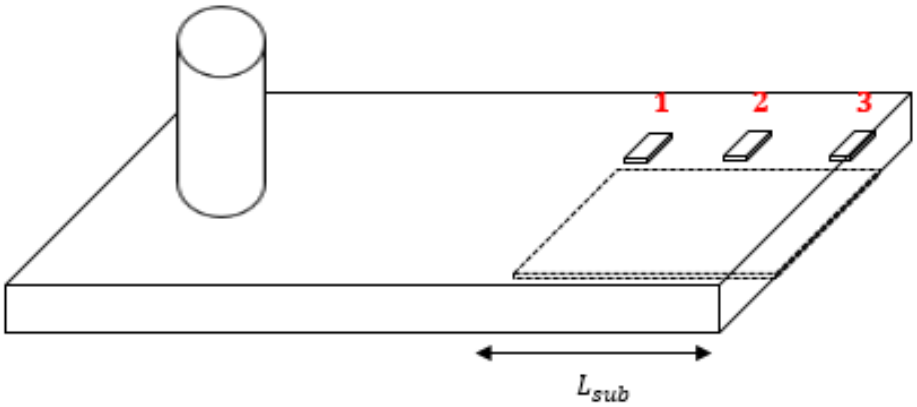

Figure 70 – Set-up for temperature measurement in the drying chamber. The dotted sheet shows a substrate in the chamber. Three resistance sensors were installed at the upper plate.

To record the temperature on the substrate and at the upper plate of the drying chamber, a Yokogawa μR10000 436104 device of the pen-model type was used. Four signal channels can be used in parallel, and the temperature range lies between 0 and 300 °C (0 to 100 % on the plotted chart). The sensitivity of the pens is 0.1 mm on a sheet width of 100 mm. Printing speed can be varied between 1 and 12000 mm/h. In the case of pure water as the coating liquid, 4000 mm/h was used. In all other cases 2000 mm/h was set. The device consists of an input terminal where the connection with the corresponding resistance sensor is provided. Subsequently, two scanners are installed to switch the signal to the correct channel using solid state relays. After each scanner an A/D converter to convert the analog to a digital signal is positioned. This is followed by the CPU, a pen servo to find the right position for the pen and an XY plotter. Furthermore, a display shows the current temperatures of the individual channels and a motor drives the paper feed. A sketch of the set-up is given in Figure 71 [73].

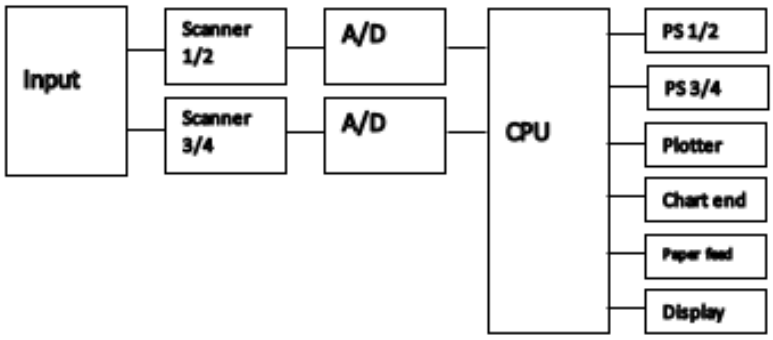

Figure 71 - Set-up of temperature recording system [73].

As mentioned above, four signal channels are available in the recording system. Three channels are occupied by the upper plate temperature sensors installed in the drying chamber. The last channel is used for a mobile temperature measuring element (MTME). The element possesses three PT100 resistance sensors and switches to determine the channel in use. Only one switch can be opened at a time to extract meaningful temperature results from the Yokogawa recording system. The MTME is used to measure substrate temperature during the drying process by positioning of the sensors directly at the substrate surface. A picture of the MTME is given in Figure 72.

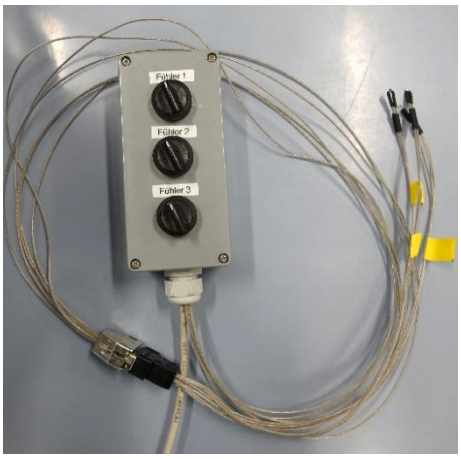

Figure 72 - Mobile temperature measuring element (MTME) with three PT100 sensors, which can be used consecutively.

Wiring and integration was done by the Bureau of Electrical Engineering as well as Process Engineering of Mayr-Melnhof Karton Frohnleiten.

4.2.3 Coating with Air-Brush Pistol

Water was deposited using an air-brush pistol, charged with a slot die. To investigate reproducibility of the method, the following experiment was performed:

The air-brush pistol, containing water at RT, was mounted approximately 60 cm from the coating position at an angle to the horizontal substrate motion of about 60°. An air supplying device was set to a certain air pressure by an adjusting knob, which started the coating flow. The substrate of known mass was moved through the coating position and into the unheated dryer with a velocity of 20 m/min. The substrate was removed, put into a PE-pack of known mass, and the mass was recorded. The procedure was repeated five times. A water load of 24.3 ± 0.4 g/m^2 was found for these conditions (appendix, Table 35). The reproducibility was interpreted as good, and the coated mass can be compared to typical Curtain Coating processes. For this reason, the coating method was used for further drying experiments.

4.2.4 Determination of Dry Mass

Binder drying chambers of type FD53 E2 were used for post-process drying. The reachable temperature range of the drying chamber is 5 to 300 °C, and the heat is delivered by forced convection [74]. Another method for post-process drying is the use of a Mettler Toledo Halogen Moisture Analyzer HB43-S. The temperature setting was 140 °C, with the stop criterion of a drying rate smaller than 1 mg per 50 s, which is recommended for most samples. The sensitivity of the scale is 1 mg, and the permissible mass range of the sample is 0.5 to 54 g. The heat is delivered by an omnidirectional halogen radiator. Analysis of experimental data revealed that, in the case of substrates coated with RS2 Std. and RS3 Std., moisture is reduced inefficiently in the drying chamber or moisture analyzer. The dry substrate mass after coating was therefore determined with the mean dry mass of the uncoated substrate and the solid content of the coated mass $w_{solid}m_{coat}$. The coated mass is determined as explained in 4.1.7.4.The mean dry substrate mass was determined for ACK 350 Std. $m_{sub,dry,uncoated}$ in the moisture analyzer as 327.5 ±0.7 g/m^2 (appendix, Table 36). The dry mass after coating was calculated by:

$$m_{sub,dry} = m_{sub,dry,uncoated} + w_{solid}m_{coat} \quad (165)$$

4.2.5 Substrate Selection

ACK 350 is a frequently used substrate at MM Karton and was set as the standard substrate for all investigations. For the purpose of validation of simulation data, untreated ACK 350 cardboard was used. The uncoated substrate was chosen, since it is very likely that diffusion processes along the substrate thickness can be neglected, which makes the simulation less complex. However, the use of untreated cardboard turned out problematic for the deposition of coating liquids by the Curtain Coating unit. Holes caused by the rough surface were investigated. For investigation of the drying energy of these coating liquids, another substrate, ACK 350 Std., was used, which includes a coating layer that reduces surface roughness. The substrate format was set to 36x20 cm for the following reasons:

- Curtain Coating should always produce a fully coated substrate (effective coating width is ~23 cm).
- Defect area due to fixation of the substrate on the transport plate by adhesive tape should be less than 1% of the overall area.
- Providing enough area for post-drying investigations.
- Avoiding areas with poor boundary conditions in the dryer.

The last point is the main reason why the substrate length was reduced to 36 cm (from originally 42 cm according to the A3 format). From experiments it can be seen that the upper plate temperature at the position near the dryer exit is not constant, but rather decreases after removing the 'Preheating Plate'. This is also observed during the drying process, as can be seen in Figure 73.

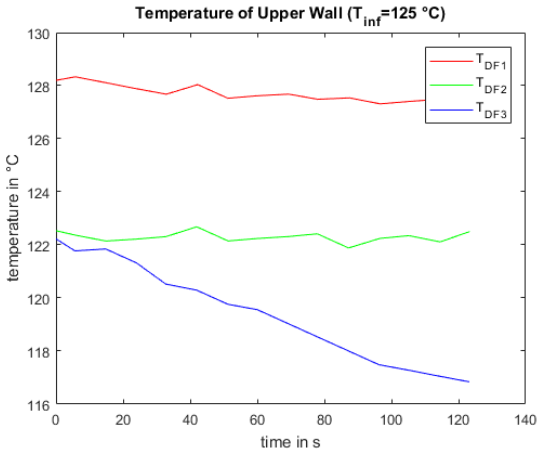

Figure 73 - Temperature trend in the drying chamber during drying process with drying air temperature of 125 °C. With T_{DF1} from sensor 1 (upstream), T_{DF2} from sensor 2 at mid and T_{DF3} from sensor 3 at dryer exit.

4.2.6 Experimental Data Processing

4.2.6.1 Evaluation of the Water Fraction

Calculation of water fraction from experiments is based on the measured masses. By knowing the mass after drying m_{sub} and the dry mass $m_{sub,dry}$, the water fraction after drying is calculated by:

$$w_{sub,H2O} = \frac{(m_{sub} - m_{sub,dry})}{m_{sub}} \tag{166}$$

The same holds for the initial moisture content $w_{sub,H2O,0}$, simply exchanging m_{sub} by the sum of substrate mass before coating $m_{sub,uncoated}$ and the coated mass m_{coat}:

$$w_{sub,H2O,0} = \frac{[(m_{sub,uncoated} + m_{coat}) - m_{sub,dry}]}{(m_{sub,uncoated} + m_{coat})} \tag{167}$$

4.2.6.2 Evaluation of the Substrate Temperature

The substrate temperature is measured in a discontinuous way at three points along the substrate length. One at the very downstream position DF3, one in the mid DF2 and one at the

very upstream position DF1. Experimental data is plotted on an evaluation sheet, which is shown in Figure 74.

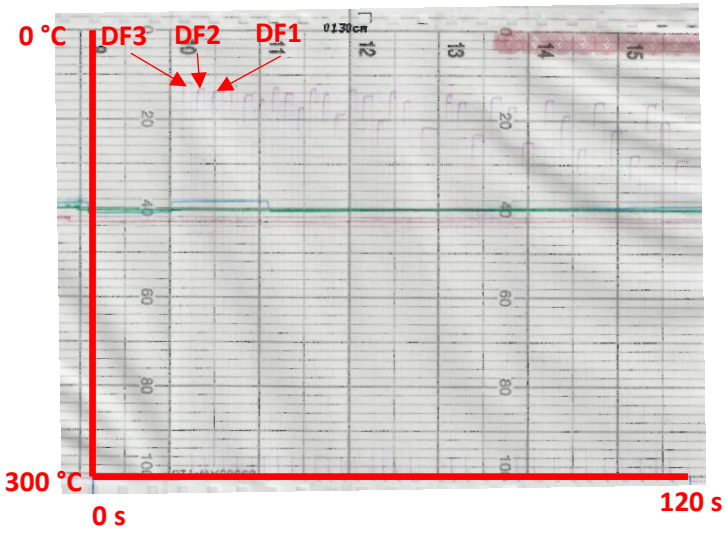

Figure 74 – Plotted evaluation sheet for extracting drying temperatures. The peaks show the measured substrate temperatures in a predefined order, measured with the MTME. The continuous lines are the temperatures of the upper plate.

To estimate the mean temperature from the plot, some steps are necessary. As a first step, the data is digitized, using the Freeware DigitizePlot®. The time dependency of the digitized temperature points at the different positions was found by a polynomial fit (Figure 75 as an example). This resulted in three polynomial functions for the three investigated substrate positions and makes the discontinuous experimental data comparable. The next step was the estimation of a mean substrate temperature for a given drying time, by knowing the temperature at the investigated positions. The method used depends on the required accuracy. For the calculation of drying energies of coating liquids, which is considered as a daily working routine, a simple arithmetic mean can be used. This strategy is supported by the fact that the desired drying energy rate is calculated by $\dot{H}_{drying} = \alpha A_{sub}(T_{inf} - T_{sub})$ with the mean heat transfer coefficient α, investigated in this thesis. Since for typical drying experiments T_{inf} is much higher than T_{sub}, good approximations for the drying energy rate can be found although the mean substrate temperature is determined in this simple way. As an example, consider the drying of a substrate of area $A_{sub} = 0.072\ m^2$. The drying temperature is $T_{inf} = 125\ °C\ (398\ K)$ and the mean heat transfer coefficient is $\alpha = 14\ W/(m^2K)$. The mean substrate temperature was determined using the arithmetic mean at $45\ °C\ (318\ K)$. The real mean substrate temperature is $40\ °C\ (313\ K)$. This gives a drying energy rate from the approximation of $81\ W$ whereas the true value would be $86\ W$. The error is, hence, less than 6 %.

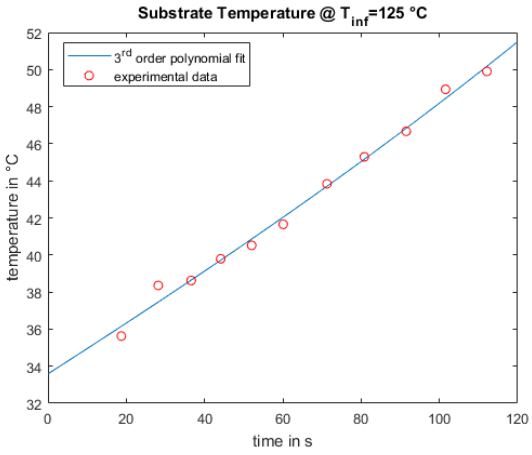

Figure 75 - Example for a polynomial fit of the measured substrate temperature trend.

For the evaluation of the mean heat transfer coefficient itself by comparison with simulation data, higher accuracy is necessary. Inaccurate estimations could lead to a misinterpretation of simulation data, and ultimately to the incorporation of a systematic error for future drying experiments. The experimental temperature points were fitted with three different models that were specifically set up to produce plausible temperature distributions along the substrate length from the known, three, data points.:

- Nusselt-like model
- Sigmoidal model
- Polynomial model

The Nusselt-like model is based on the relation for Nusselt numbers in dynamically developed and thermally developing channel flow with boundary conditions number 2 in Figure 26. Similar trends as shown in Figure 27 are produced by this model. The formula was extracted from the book of Shah and London (1978) [27]. The model is useful if the temperature at the very upstream position is the highest and the other temperatures are similar. Such temperature trends are predicted by the simulation of the drying process. An example for predicted temperature distributions by the simulation are given in Figure 76. The equation for fitting the measured temperature points reads [27]:

$$T_{sub}(x) = \frac{1}{A_{T,Nu}\left(1 - \sum_{n=1}^{3}(B_{T,Nu}/n)e^{-(C_{T,Nu}n)^2 x^*_{E,T}}\right)} \tag{168}$$

with the fitting parameters $A_{T,Nu}$, $B_{T,Nu}$ and $C_{T,Nu}$ and the dimensionless substrate position $x^*_{E,T} = x/L_{E,T}$ with $L_{E,T}$ for $Re = 400$ and $Pr = 0.7$.

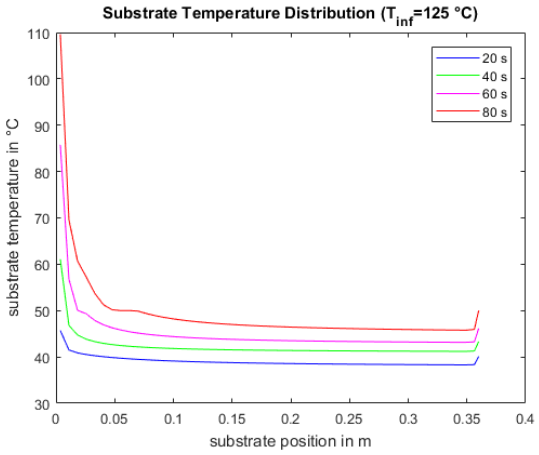

Figure 76 - Typical predicted substrate temperature trends by the simulation.

The model proved to be valid for long drying times and high drying air temperatures, where for lower drying air temperatures the applicability is shifted towards higher drying times.

Experience showed that especially for short drying times the substrate temperatures at the very upstream and the mid positions are similar, and the very downstream position was slightly lower. For this case, the sigmoidal model was introduced, which is based on a Boltzmann equation that is widely known to produce curves of sigmoidal shape:

$$T_{sub}(x) = A_{T,sig}\left(1 - \frac{1}{1 + e^{B_{T,sig}/x^*_{E,T}}}\right) \tag{169}$$

with the fitting parameters $A_{T,sig}$ and $B_{T,sig}$ and the dimensionless substrate position $x^*_{E,T} = x/L_{E,T}$ with $L_{E,T}$ for $Re = 400$ und $Pr = 0.7$. Similar equations as (169) are available in different data processing softwares as for example in Origin to fit sigmoidal curves. The third option is a polynomial fit of order three. The quality of the different fits was evaluated by the parameter Sum of Square Errors SSE_T, which reads:

$$SSE_T = \sum (T_{sub,exp} - T_{sub,fit})^2 \tag{170}$$

The model with the lowest SSE_T value was used with the additional constraint that the polynomial model was only used if the best other model has an SSE_T value higher than 0.1. The estimated mean temperatures, raw data and fit methods used are given in the appendix, Table 38. The arithmetic mean of 100 temperature points equidistantly distributed between the up- and downstream positions of measurement gave the mean temperature data.

5 Experimental Section

5.1 Curtain Coating

The coating liquid was characterized in terms of density, solid content, surface tension and dynamic viscosity as described in 4.1. The container (100 L or 600 L) with the substance was stirred with a ViscoJet® stirrer, and tempered until 40 °C was reached, using electric blankets (~18 h). A high-speed camera was mounted on a swan-neck stand directly on the Curtain Coater, approximately 80 cm from the impingement zone. A substrate was fixed on the transport plate with adhesive tape. The velocity settings for the transport plate were chosen as defined beforehand. The substance was pumped to the coating device with a predefined volume flow rate. The coating process was started. Slow motion video data was optionally recorded with the settings shown in Table 20.

Table 20 - Settings for slow motion video recording

Sony RX100 M4	
Mode	time priority
Framing rate	960 fps
CCD array	1920x1080 Pxls

The substrate was dried in an external drying chamber for 1 min at 110 °C. A picture of the dried substrate was taken. For investigation of the coating window, no videos were recorded.

5.2 Drying of Coatings

5.2.1 Preheating Phase

Uniform boundary conditions in the dryer were established during a preheating phase for the dryer using the LHS 61L heater and the ASO blower of Leister. Preheating times were reduced by the use of a ‘preheating plate' that functions as the bottom of the drying chamber instead of the transport plate. To increase the intensity of heat transfer in the chamber, an additional outflow resistance was installed at the dryer exit. Figure 77 shows the dryer during a preheating phase. The drying air temperature was set to a maximum of 10 °C above the required drying air temperature, and was reduced to the required temperature at least 5 min before termination. A minimum requirement for termination was given, if the upper plate did not deviate more than 5 °C from the desired drying air temperature, and the mean of the three sensors on the upper dryer plate gave approximately (±3 °C) the desired drying air temperature.

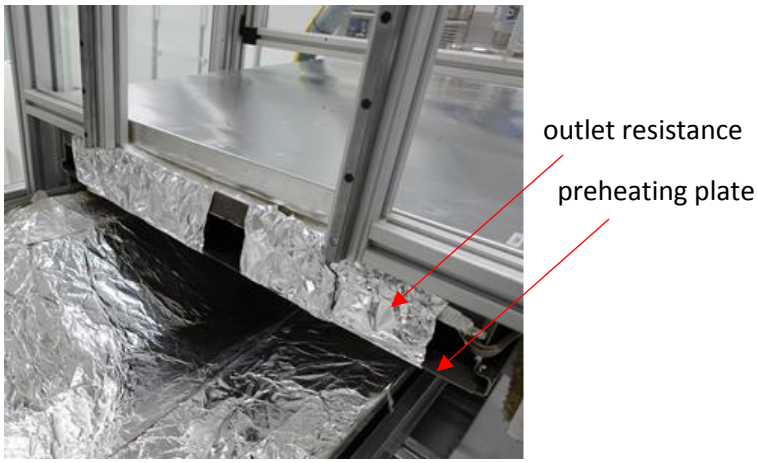

Figure 77 - Dryer outlet with 'preheating plate' and outlet resistance.

5.2.2 Determination of Water Content

5.2.2.1 Drying of Substrates Coated with Pure Water

Ambient relative humidity, temperature and pressure of the air were recorded. Coating was performed with an air-brush pistol at 24 °C liquid and substrate temperature. The air-brush pistol was equipped with a slot die, and mounted approximately 60 cm from the coating position at an angle to the horizontal substrate motion of about 60°. The orientation of the substrate was marked on the surface, and the substrate was fixed using adhesive Alu-tape. For heat supply the Leister Mistral 6 System was used, and the appropriate volume flow rate (=350 L/min) and drying air temperature were set. The preheating plate was removed, and the security locks were activated. An air supplying device was set to a certain air pressure, which started the coating flow. The substrate was moved through the coating position and into the dryer with a velocity of 20 m/min. After a predefined drying time, the substrate was removed from the drying chamber, put into a PE-pack of known mass, and the mass was recorded. The sheet within the PE-pack was cut along the width by a laboratory-guillotine into three plates of approximately the same size. The PE-foil was removed, the individual plates were weighed, and put into an external drying chamber for 20 min at 140 °C. The oven-dry masses of the individual plates were recorded, and the exact dimensions were measured. Due to the marks on the cardboard, every plate relates to a certain position in the dryer.

5.2.2.2 Drying of Substrates Coated with RS2 Std. and RS3_C

Ambient relative humidity, temperature and pressure of the air were recorded. Coating was performed with a Curtain Coating device of the slide-fed type at a temperature of the coating liquid of 40 °C and the substrate temperature of 24 °C. The substrate was fixed on the transport plate using an adhesive Alu-tape. For heat supply the Leister Mistral 6 System was used, and the appropriate volume flow (=350 L/min) and drying air temperature were set. The coating

flow was set to a predefined value by the frequency converter on the supply pump. The preheating plate was removed, and the security locks were activated. The substrate was moved through the coating position and into the dryer with a predefined velocity. After a certain drying time, the substrate was removed from the drying chamber, put into a PE-pack of known mass, and the mass was recorded. The sheet was put into an external drying chamber for 20 min at 140 °C. The oven-dry mass was recorded.

5.2.3 Determination of Substrate Temperature

Ambient relative humidity, temperature and pressure of the air were recorded. The substrate at RT was fixed on the transport plate, and charged with the three resistance sensors of the MTME using an adhesive Alu-tape at the following positions along the substrate length: 1.5, 18 and 34.5 cm (Figure 78). The heat supply was switched to the Leister Mistral 6 System, and the appropriate volume flow (=350 L/min) and air temperature were set. Coating was performed either with an air-brush pistol or with a Curtain Coating device of the slide-fed type according to the procedures explained above. After reaching the drying position, the sensors were connected to the temperature recording device, and the data collection was activated, which gives a dead time of approximately 15 s. The substrate temperature was recorded by switching between the individual sensor channels in a predefined order. After a certain drying time, the MTME was disconnected, and the substrate was removed.

Figure 78 - Substrate with temperature sensors of the MTME at specified positions (left) and correctly fixed sensor with the tip not fully covered by the tape (right).

6 Results and Discussion

6.1 Curtain Coating

6.1.1 Stability Criterion

The stability criterion explained in 2.1.4 based on the Weber number $We > 2$ was checked for suitability (Table 21 and Table 22). The minimum volume flow rate to form a stable curtain was noted. From the known properties, the Weber number could be calculated. It is known that the coating properties for both liquids vary with storage time. A stable curtain was experimentally defined as a falling liquid sheet, which does not break when disturbed by the moving transport plate.

Table 21 - Minimum Weber number for a stable curtain of RS2 Std.

Storage time [d]	Curtain height [cm]	Volume Flow rate [l/min]	We
20	7.5	0.85	2.1
30	7.5	0.91	2.6
1	9.5	0.93	2.8
20	9.5	0.74	2.1
20	9.5	1.05	2.5

Table 22 - Minimum Weber number for a stable curtain of RS3 Std.

Storage time [d]	Curtain height [cm]	Volume Flow rate [l/min]	We
1	7.5	0.91	2.7
8	7.5	0.85	2.4
15	7.5	0.93	2.5
1	9.5	1.21	4.5
8	9.5	0.93	3.1
15	9.5	1.14	3.9

The experiments revealed that the stability criterion is valid in all presented cases, but it is not possible to predict curtain stability based on this criterion because of data scattering. RS2 Std. establishes a stable curtain at slightly lower Weber numbers. The main differences between the coating suspensions, besides the chemical compositions, are the higher apparent viscosity of RS2 Std. (~4 times higher) and the higher undissolved solid load of RS3 Std. (~1.75 times

higher). Especially the high undissolved solid load complicates the flow situation in the liquid sheet [75,76]. It is assumed that this can also influence the curtain stability, and hence alter the criterion, which was derived and tested mainly for polymer solutions (e.g. gelatin solutions) [75,76]. Increasing curtain falling height negatively affects the curtain stability of RS3 Std., where it has minor effects on RS2 Std. Addo-Yobo et al (2010) investigated the effects of particle concentration and size on the stability of liquid sheets. They postulated that the distance from the outlet nozzle to the breaking position of a liquid sheet containing particles is reduced with increasing number and size of particles [75]. Particle size distribution data is not available for the coating liquids, but, as mentioned above, the higher particle concentration of RS3 Std. could also explain the reduced stability of RS3 Std. at increased curtain falling heights. The influence of storage time on curtain stability needs further data, but the results indicate that both, very low and high storage times, are suboptimal for the stability. It must be noted at this point that a curtain at the minimum flow rate tends to show poor coating behavior. If the purpose of a coating experiment lies on the deposition of thin, uniform films, flow rates should be set slightly higher than the minimum flow rate. At the minimum flow rate, the substrate velocity must be decreased substantially to avoid coating defects. This, consequently, results in the deposition of thick films.

6.1.2 Limiting Coating Phenomena

An attempt to identify limiting coating phenomena, as described in [8], failed because of disturbances, which led to wave formation on the curtain during the deposition process. The waves are caused primarily by the collision of the transport plate with the curtain, and secondarily by the air flow dragged along with the plate. The falling liquid sheet is not in steady state and, hence, cannot be directly compared with liquid sheets in standard coating processes, which are in steady state. Frames of video recordings of successful and unsuccessful coating processes for RS2 Std. are shown in Figure 79. Without disturbance, both curtains exhibit flat surfaces (Figure 79 L1 and H1). For the higher volume flow rate, less contraction can be seen downstream of the edge guides because of higher inertia compared to surface tension forces (=higher Weber number). As the transport plate approaches, the surface of the curtain at lower volume flow rate becomes curved in the direction of the substrate transport (L2 in Figure 79), which indicates air currents impinging on the backside of the curtain. No curvature is seen on the adjacent picture to the right (H2). At collision, no substantial changes can be seen in both cases (L3 and H3). In the last frames (L4 and H4), serious differences are obvious. The wavy surface of the low volume flow curtain occupies the entire liquid sheet. The coating deposition is prevented by a thick layer of air between substrate and the coating. The process is not in equilibrium. The surface of the high volume flow process is still flat, and the contact line on the substrate seems to be sharp and undisturbed. Most video

records made for unsatisfactory coating experiments of RS2 Std. showed similar effects, though they were less dramatic normally. The resulting coated substrates are shown in Figure 81. Frames of video recordings of successful and unsuccessful coating processes for RS3 Std. are shown in Figure 80. Without disturbance, both curtains are characterized by flat surfaces (L1 and H1 in Figure 80). As the transport plate approaches, the surface of the curtain of lower volume flow rate becomes slightly curved in the direction of the substrate transport (L2), which indicates air currents impinging on the backside of the curtain. No curvature is seen on the right picture (H2). At collision (L3 and H3), the lower volume flow rate shows that the liquid is pulled along with the substrate. The curtain at higher volume flow rate is still straightly impinging onto the substrate. Marked differences can be seen during the deposition process in the last pictures (L4 and H4). A wavy surface accompanied by a thin air layer between substrate and coating liquid, and a strongly bent curtain is seen for low volume flow rate, where the higher volume flow rate shows still a sharp contact line. Similar phenomena were observed for most unsatisfactory coating experiments with RS3 Std. However, less strong waves on the curtains could also be observed for fully coated substrates. The results of the coating experiments are shown in Figure 82.

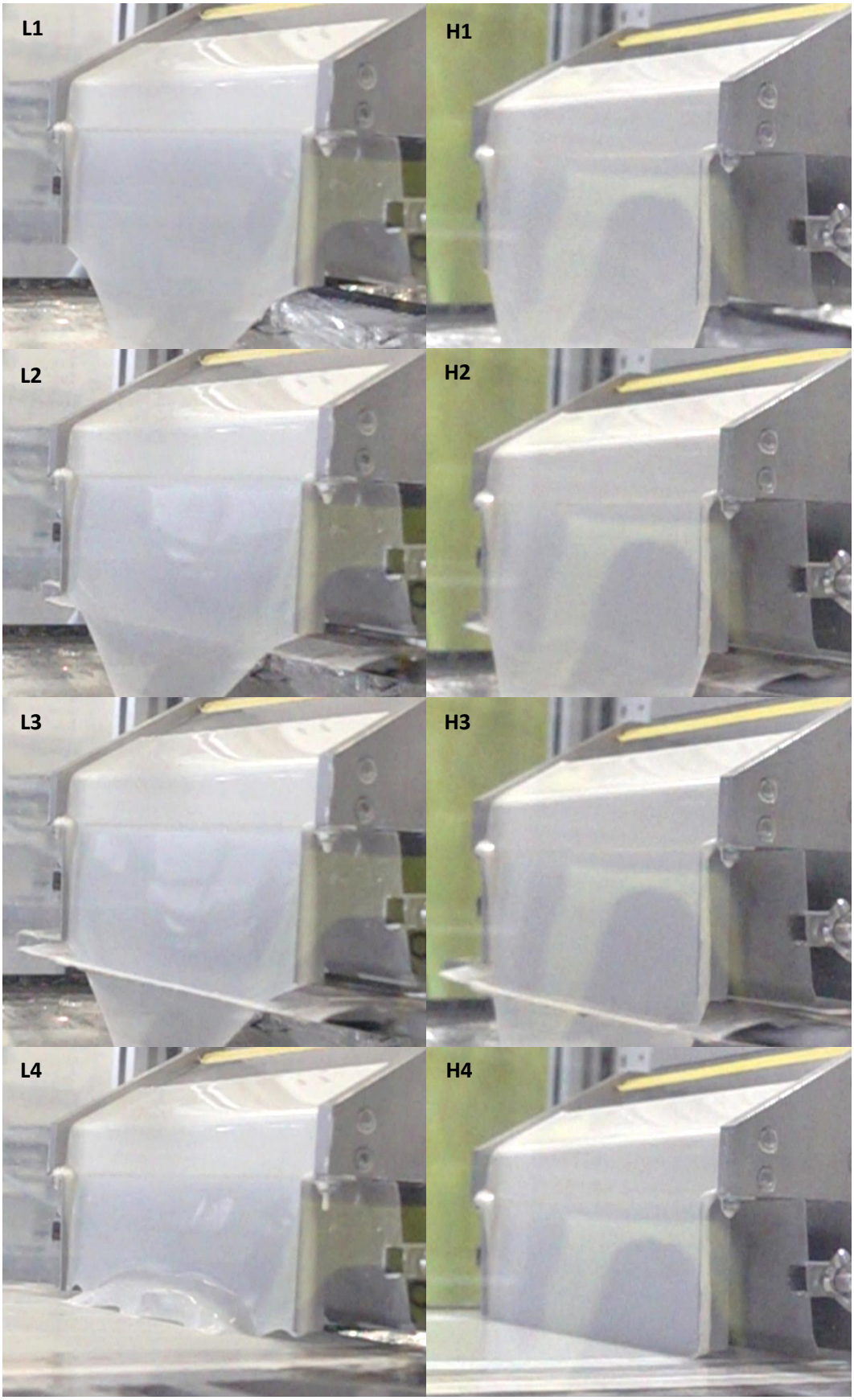

Figure 79 - RS2 Std. video analysis. Left column: $\dot{V}_l = 0.7\ l/min$, $v_{imp} = 1.07\ m/s$, $v_{sub} = 1.8\ m/s$; Right column: $\dot{V}_l = 2.5\ l/min$, $v_{imp} = 1.08\ m/s$, $v_{sub} = 5\ m/s$.

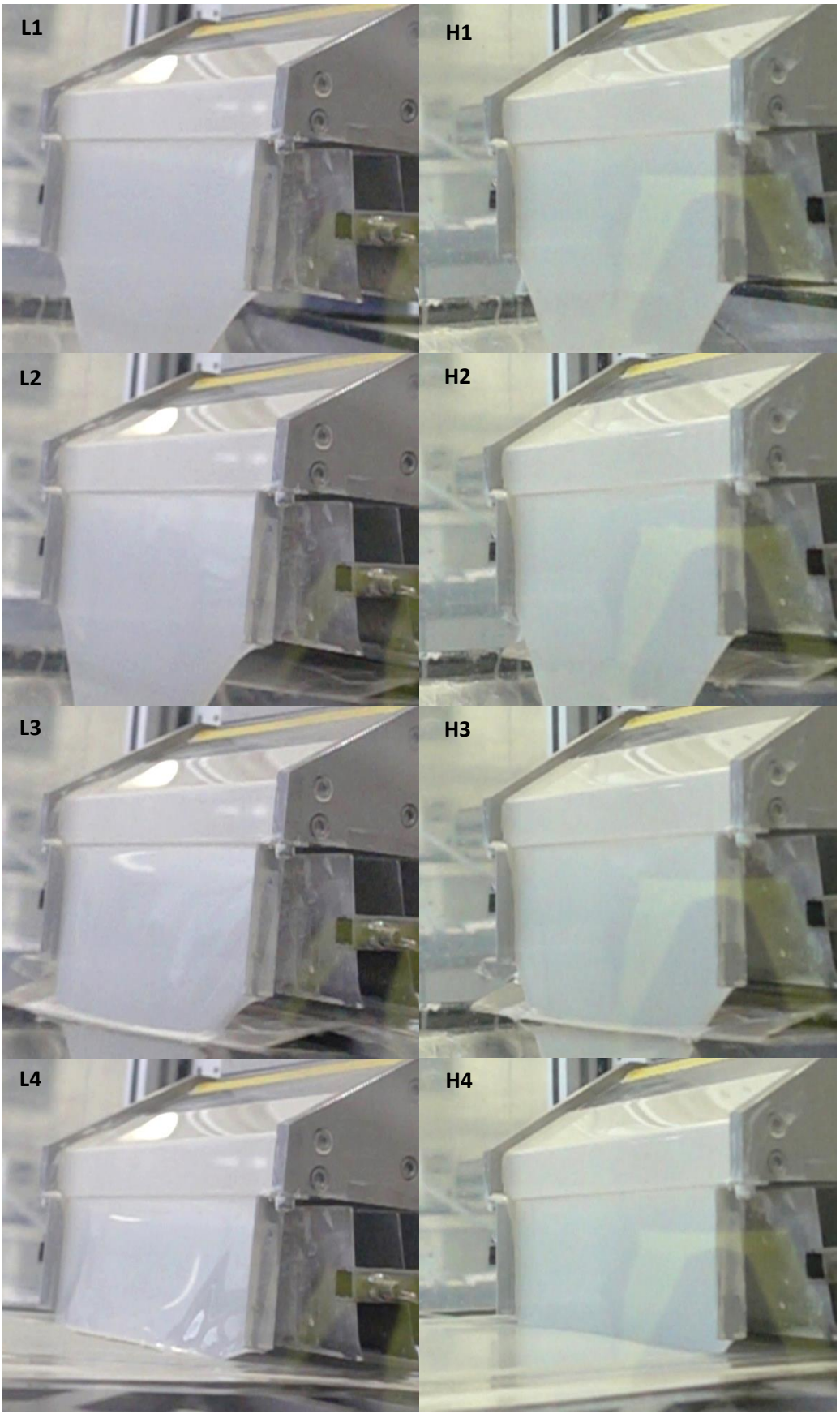

Figure 80 - RS3 Std. video analysis. Left column: $\dot{V}_l = 0.85\ l/min$, $v_{imp} = 1.18\ m/s$, $v_{sub} = 5\ m/s$; Right column: $\dot{V}_l = 1.1\ l/min$, $v_{imp} = 1.18\ m/s$, $v_{sub} = 1.7\ m/s$.

Figure 81 - RS2 Std. Coating result. Left: $\dot{V}_l = 0.70\ l/min$, $v_{imp} = 1.07\ m/s$, $v_{sub} = 1.8\ m/s$; right: $\dot{V}_l = 2.50\ l/min$, $v_{imp} = 1.08\ m/s$, $v_{sub} = 5\ m/s$.

Figure 82 - RS3 Std. Coating results. Left: $\dot{V}_l = 0.85\ l/min$, $v_{imp} = 1.18\ m/s$, $v_{sub} = 5\ m/s$; right: $\dot{V}_l = 1.10\ l/min$, $v_{imp} = 1.18\ m/s$, $v_{sub} = 1.7\ m/s$.

A higher volume flow rate leads to a higher inertial force, which has evidently positive effects on the coatability in the Curtain Coating process. Besides the volume flow rate, fluid inertia can be increased by increasing impingement velocity. This influence is discussed in the following chapter.

6.1.3 Impingement Velocity

The impingement velocity is primarily controlled by the curtain falling height, and high values positively affect the coating process. Preliminary tests indicated that the ideal length should lie between five and fifteen centimeters. Tests with a curtain falling height of five centimeters showed poor behavior during the deposition step. Twelve and fifteen centimeters gave insufficient curtain stability. Therefore, tests were made with edge guides of seven and nine centimeters length. In Figure 83 and Figure 84, the influence of the impingement velocity on coating of RS2 Std. and RS3 Std. curtains is shown.

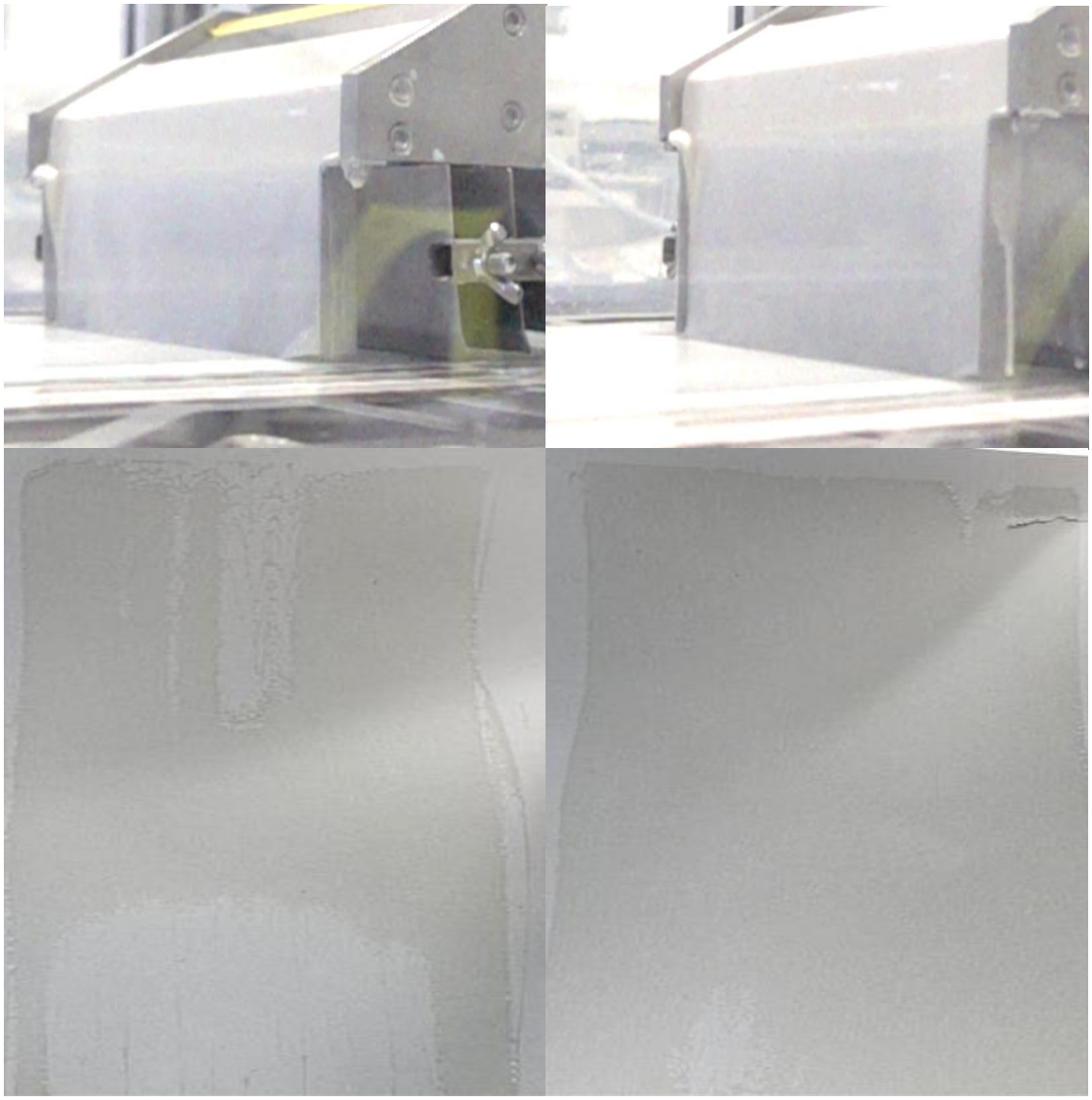

Figure 83 - RS2 Std. impingement velocity effects. Left column: $\dot{V}_l = 1.29\ l/min$, $v_{imp} = 1.07 m/s$, $v_{sub} = 4.2\ m/s$; Right column: $\dot{V}_l = 1.29\ l/min$, $v_{imp} = 1.24\ m/s$, $v_{sub} = 4.2\ m/s$.

The only difference between the right and the left columns in Figure 83 is the curtain falling height and, consequently, the impingement velocity. Viscous drag imparted by the substrate seems to pull the left curtain slightly forward, which is not the case for the curtain on the right. None of the curtains on these photos reveals air impingement. The difference does not look severe during the process, but the corresponding coated substrates below exhibit remarkable differences. Although the picture to the right shows coating failures, the best part is coated, which is not the case for the lower impingement velocity on the left. Similar trends could be seen at $\dot{V}_l = 1.55\ l/min$, $v_{sub} = 5\ m/s$ and $\dot{V}_l = 1.08\ l/min$, $v_{sub} = 2.6\ m/s$ for, where $v_{imp} = 1.07$ and $1.24\ m/s$, respectively (see appendix Figure 125 and Figure 124).

Figure 84 - RS3 Std. impingement velocity effect. Left column: $\dot{V}_l = 0.93\ l/min$, $v_{imp} = 1.18\ m/s$, $v_{sub} = 3.7\ m/s$; Right column: $\dot{V}_l = 0.93\ l/min$, $v_{imp} = 1.33\ m/s$, $v_{sub} = 3.8\ m/s$.

The coating processes illustrated in Figure 84 left and right are the same, except of two points: the left column shows a coating process of lower impingement velocity and a slightly lower velocity of the transport plate. The second point should positively affect coatability for a fixed volume flow rate. However, the curtain on the left shows again more disturbances caused by the collision with the transport plate and air currents. The right curtain with the higher impingement velocity looks flatter, with a sharp contact line. This is also seen from the resulting products, which shows failure for the lower impingement velocity. Similar trends could be seen for comparisons of $\dot{V}_l = 0.86\, l/min,\ v_{sub} = 4.59\, m/s,\ v_{imp} = 1.18\, m/s$ with $\dot{V}_l = 0.81\, l/min,\ v_{sub} = 4.33\, m/s,\ v_{imp} = 1.33\, m/s$ and $\dot{V}_l = 0.91\, l/min,\ v_{sub} = 3.90\, m/s,\ v_{imp} = 1.16\, m/s$ with $\dot{V}_l = 0.91\, l/min,\ v_{sub} = 4.20\, m/s,\ v_{imp} = 1.33\, m/s$ (Figure 127 and Figure 126).

Generally, the larger curtain falling height gave better behavior during the deposition process, while the curtain stability was good enough to reach minimum coated masses with this higher curtain falling height. The edge guides of 9 cm length were set as the standard for all the following experiments. Again, the positive influence of fluid inertia was proven in this section.

6.1.4 Operability Window

The foregoing sections reveal the importance of fluid inertia for successful deposition of thin films with the considered device. The influence of surface tension was investigated separately by Mayr-Melnhof Karton by varying surfactant concentrations for both coatings. It can be shown that too high surface tension forces make the coating process unfeasible. The liquid tends to detach from the edge guides, and contraction occurs far upstream. A stable curtain over the entire edge guide length cannot be established. By increasing the surface tension, the maximum possible curtain falling height is substantially decreased, which leads to low impingement velocity accompanied with the negative effects discussed above. The effects of viscosity and substrate velocity were investigated in the following section, and the applicability of a coating window of the form of Figure 10 was checked. Especially the boundary for successful deposition of low grammage of coating was investigated. For each coating liquid, the Reynolds numbers just inside and just outside the window at two different substrate velocities were recorded. An experiment was assessed as 'coatable' if the substrate is uniformly coated without visual defects. Three different RS2 Std. were tested (Table 4). One was produced as usual, and one with a lower content of solid. This leads to a substantial decrease of viscosity. The liquid produced as usual was stored for 20 days after the experiments. It is known that the viscosity of RS2 Std. increases with increasing storage time. Three different RS3 Std. were tested (Table 8). One was produced as usual, and one was produced with a higher content of solid. This leads to a substantial increase of viscosity. The liquid produced as usual was stored for 20 days after the experiments. It is known that the

viscosity of RS3 Std. decreases with increasing storage time. The boundary of the operability window must lie between points just inside and just outside of the coating window at the same substrate velocity. RS2 Std. was coated at grammages from 4 to 10.25 g/m^2, in steps of 1.25 g/m^2. RS3 Std. was coated at grammages from 6 to 13.5 g/m^2, in steps of 1.75 g/m^2. The grammage is related to the totally dried state of the coating, and was investigated for substrate velocities of 4.25 and 5 m/s. Capillary numbers for RS2 Std. were in the range of 5-25 and for RS3 Std. 2.5-6. Tabular data is given in the appendix, Table 37.

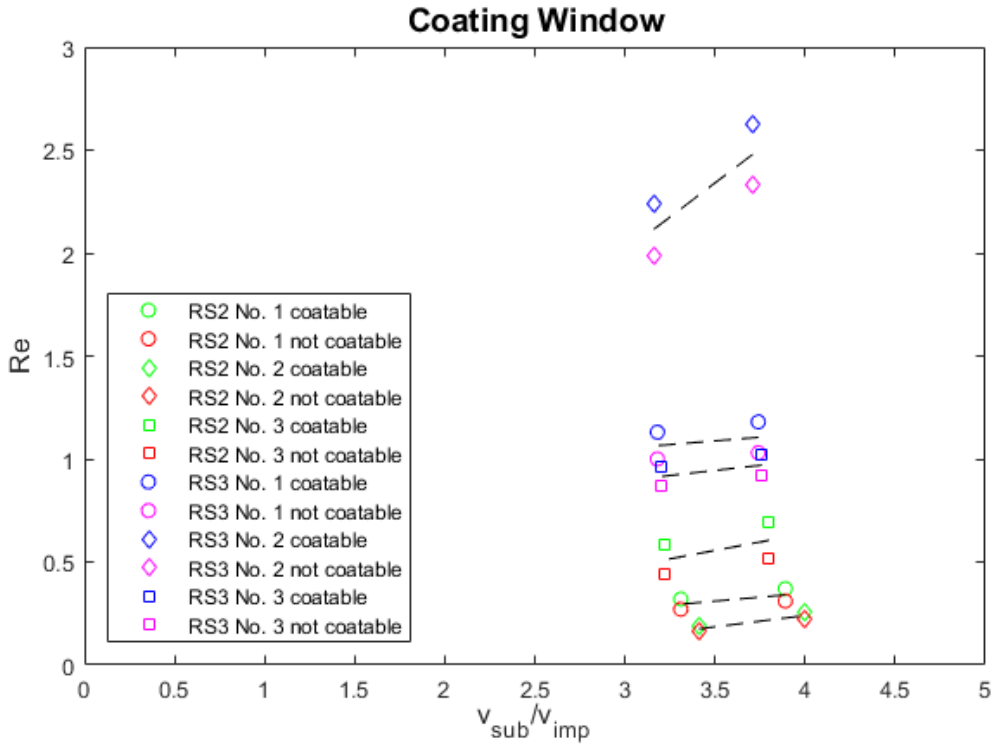

Figure 85 - Coating Window boundary estimation of RS2 Std. and RS3 Std. The dashed lines indicate the boundary positions.

The applicability of the coating window is obviously violated for this device, as seen in Figure 85. The main difference of the used device compared to standard apparatuses is the discontinuous working principle, which accompanies strong disturbances in the curtain. The liquid is not in steady state, which makes characterization impossible in the same way as for steady-state processes. The boundary of the coating window is shifted with varying viscosity of the suspension. From the data above, it can be said that higher viscosity shifts the operability window to lower Reynolds numbers. This agrees with intuition since high viscosity fluids tend to balance disturbances more efficiently. Further analysis, if higher or lower substrate velocities are beneficial, led to ambiguous results, and a clear recommendation cannot be given from the conducted experiments (appendix, Figure 128). The coating window was modified by incorporation of the capillary number. The capillary number shows the influence of surface

tension forces and can furthermore account for the positive effects of viscose forces that were seen in the Coating Window in Figure 85. This led to the modified coating window as shown in Figure 86.

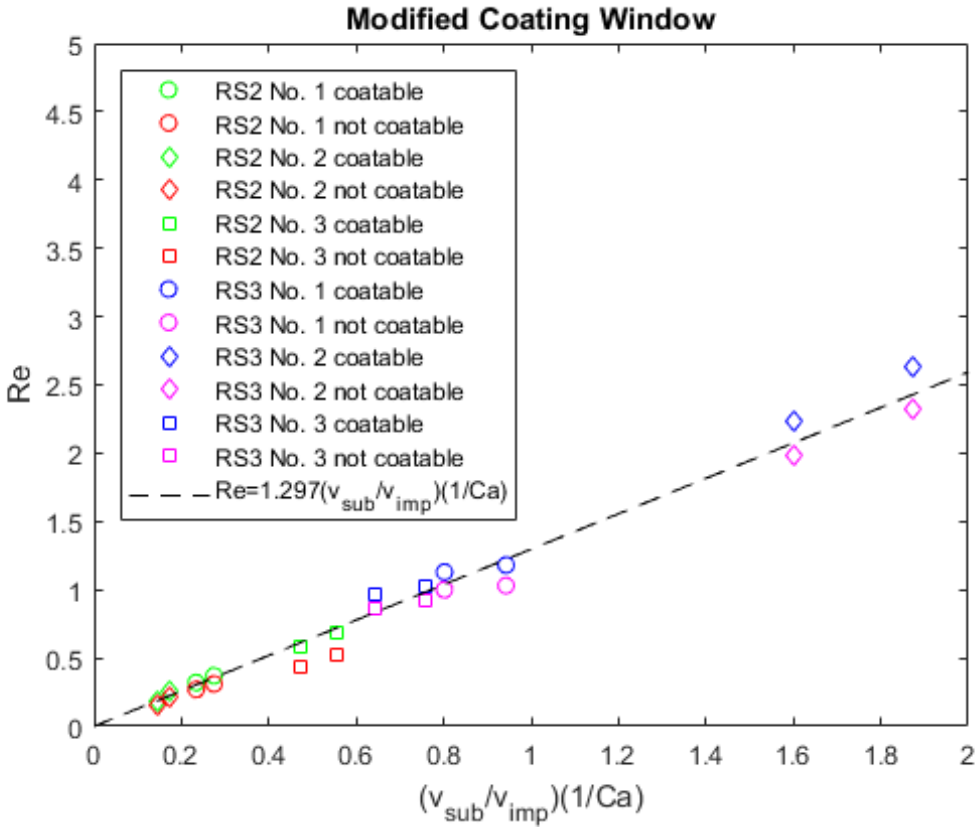

Figure 86 - Modified Coating Window.

The modified coating window gives a linear correlation that agrees well with experimentally determined boundary positions. The equation to find the Reynolds number on the boundary is given by:

$$Re = 1.297 \frac{v_{sub}}{v_{imp}} \frac{1}{Ca} \tag{171}$$

With the Reynolds number Re, the substrate velocity v_{sub}, the impingement velocity v_{imp} and the capillary number Ca. The boundary of the coating window for both coating types (RS2 Std. and RS3 Std.) can be described by the same correlation. This indicates that the boundary of the coating window is independent of the suspension type, in contrast to the results found for the stability criterion as discussed in section 6.1.1. The correlation can be used to predict minimum film thicknesses realizable for coatings of known density, dynamic viscosity and surface tension.

6.2 Drying of Coatings

6.2.1 Substrates Coated with Pure Water

6.2.1.1 Validation of Simulations

Before comparing simulation results to the experiments, results are compared to idealized curves to ensure that results comply with general findings in practice. For this, substrate data of untreated ACK 350 cardboard was used. The simulation conditions are summarized in Table 23.

Table 23 - Simulation conditions for validation

Condition	Value
$w_{sub,H2O}\ (t = 0)$	0.50
$T_{sub}\ (t = 0)$	24 °C
T_{inf}	125 °C
$\dot{V}_{amb}$	350 L/min
φ_{amb}	0.4
L_{sub}	0.36 m
t_{drying}	500 s
Δt	0.5 s
Δx	7.2 mm
Substrate Position	0.18 m

Comparison data for an ideal paper drying processes were extracted from the book of Karlsson (2009) [29]. In most transient drying processes, the focus of interest lies on the temperature and moisture content of the substrate (Figure 87).

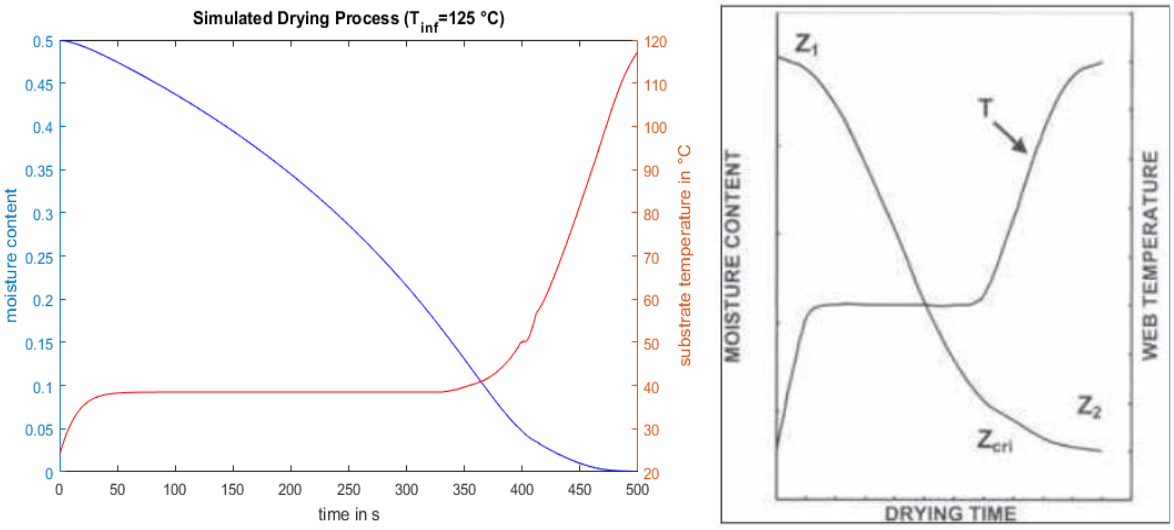

Figure 87 - Predicted (left) and ideal (right) trend of water fraction and substrate temperature during paper drying [29].

Both, the predicted moisture content and the substrate temperature are similar to the ideal curves. Shortly after the start, the moisture content falls slowly and the substrate temperature rises fast. Thereupon, the reduction of moisture content accelerates, where the substrate temperature reaches a plateau at 38.5 °C. At the latest drying stage, the moisture content slowly converges towards zero and the substrate temperature rises steeply. Just before reaching the drying air temperature, the substrate temperature flattens again. In the book of Karlsson (2009) the first phase is called the ‘heat-up phase' [29]. After this, the 'constant rate period' follows. This phase is followed up by the 'falling-rate period'. The names of the latter phases refer to the drying rate, which is another point of central interest (Figure 88) [29].

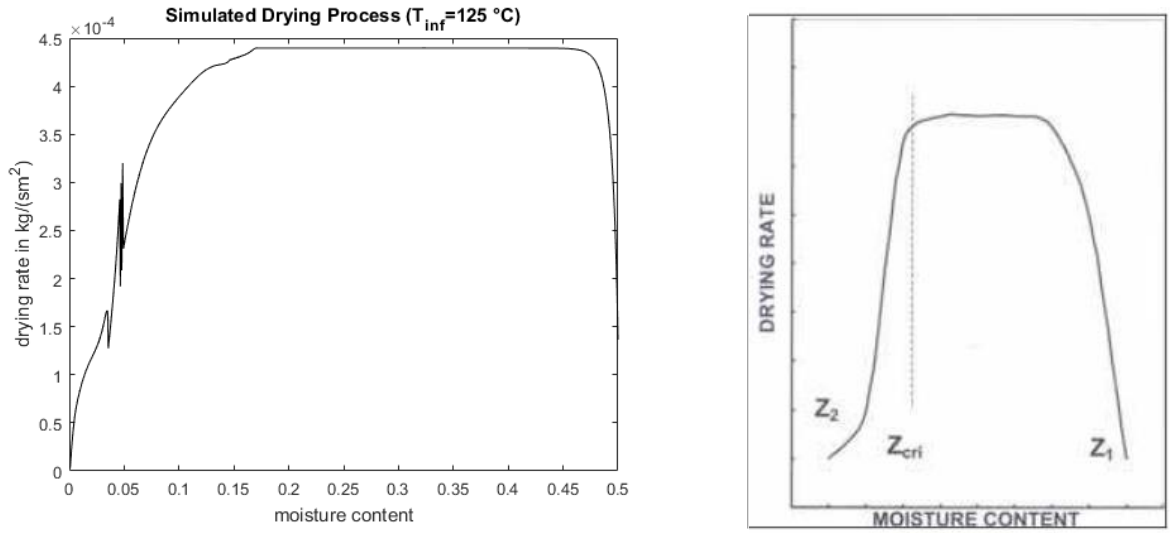

Figure 88 - Predicted (left) and ideal (right) drying rate during paper drying [29].

Again, good agreement is obvious. At the beginning, the drying rate rises fast in both, the predicted and the ideal case. A constant drying rate is followed up. In the ideal diagram, the falling-rate period sets in abruptly, and the drying rate falls drastically. This is not the case for the simulated results. Here, the drying rate gradually decreases before reaching a fast-falling region. Furthermore, no flattening of the predicted curve is observed at low moisture contents. Karlsson (2009) explains the falling-rate period as a result of several processes that are hygroscopic effects, increasing diffusion resistance and a movement of the evaporation front deeper into the substrate [29]. However, only hygroscopic effects are considered in the current simulation, which can lead to deviations in the region of low water contents. A specific point of interest in this thesis is the impact of the modification of Nusselt and Sherwood numbers according to the adapted version of the work of Abramzon and Sirignano (1989) [32]. In the theory, the effect on the dimensionless numbers must be higher for high drying rates. Since

the drying rates discussed in this thesis are rather low, a small effect is expected (Figure 89 and Figure 90).

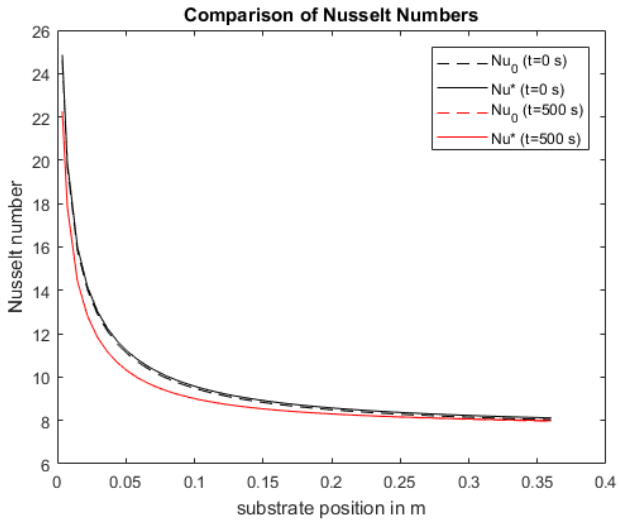

Figure 89 - Effect of Nusselt number modification during drying process.

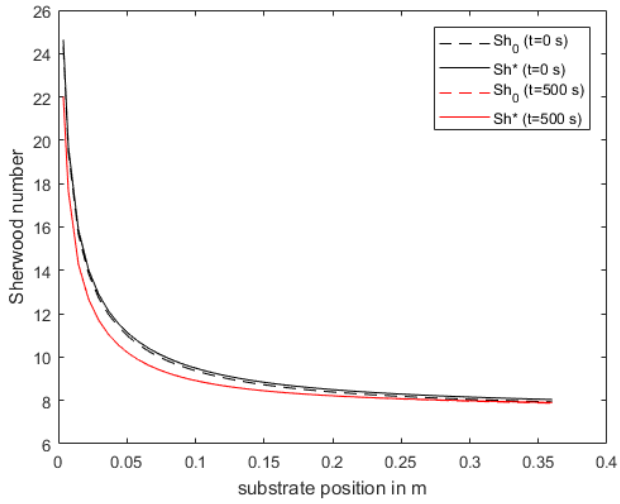

Figure 90 - Effect of Sherwood number modification during drying process.

The curves of modified and standard correlations for the dimensionless transfer coefficients nearly coincide. The impact of the modification is, as expected, low. The simulation assumes a channel flow, where the boundary layer grows at the lower plate (that is the substrate). This means that, at every instant of time, an undisturbed thermal and mass flow must be present outside the boundary layer. Validity of this assumption is checked with the simulation itself, as shown in Figure 92 and Figure 91.

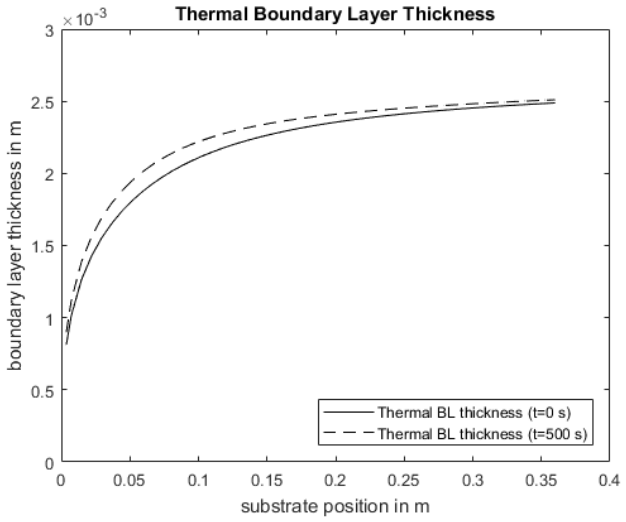

Figure 92 - Thermal boundary layer thickness along substrate length during drying.

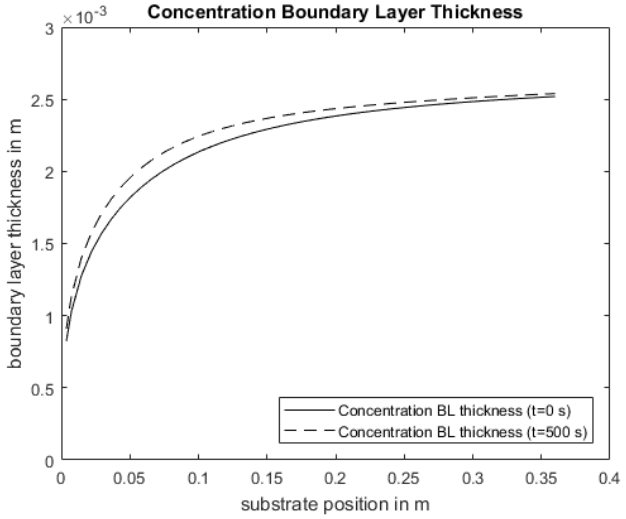

Figure 91 - Concentration boundary layer thickness along substrate during drying.

Both, thermal and concentration boundary layer are less than half the channel height. This suggests that the assumption is correct. Since the boundary layers are less than half the channel height, a possibly growing boundary layer at the upper plate should not influence the assumptions of the simulation.

6.2.1.2 Validation of Drying Experiments

Drying experiments at different drying air temperatures and different drying times were performed. Every experiment was performed three times. This means that overall 36 experiments for evaluation of water fractions for four different drying times and three different drying air temperatures were performed. Subsequently, 9 experiments were performed to

characterize the substrate temperature during the drying process at three different drying air temperatures. Important conditions are summarized in Table 24.

Table 24 - Experimental conditions for drying experiments ($T_{sub,0} = 24\,°C$, $w_{sub,H2O,0} = 0.125$)

Condition	Investigated Points
Drying Air Temperatures [°C]	100, 125, 150
Drying Times [s]	20, 40, 60, 80

The experimental results were assessed in terms of plausibility of the drying trends and reproducibility of the experiments (Figure 93).

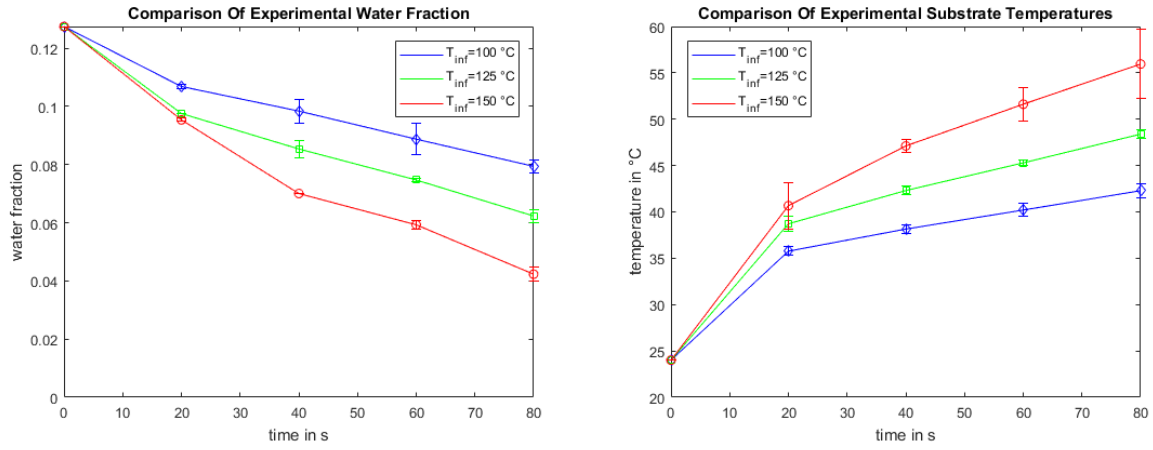

Figure 93 – Experimental drying results for substrates coated with pure water.

Both evaluation criteria show plausible trends. Drying at higher temperatures and for longer drying times leads to lower water fractions and higher substrate temperatures. The sigmoidal shape, as predicted for the water fraction from the ideal drying process, cannot be seen in the drying experiments above. The reason for this could lie in too low drying times. The substrate temperature exhibits the typical flattening curve. The standard deviations seem to be sufficiently low. This suggests good reproducibility of the drying experiments, and confirms both the principal drying procedure and the design of the dryer itself.

6.2.1.3 Comparison of Simulation and Experiments

The drying experiments are compared to the simulation results. Simulation and experimental results in tabular form, as well as raw data, can be found in the appendix (Table 38 to Table 51). Simulation conditions are summarized in Table 25 and a graphical representation of a drying process at a drying air temperature of 125 °C is shown in Figure 94.

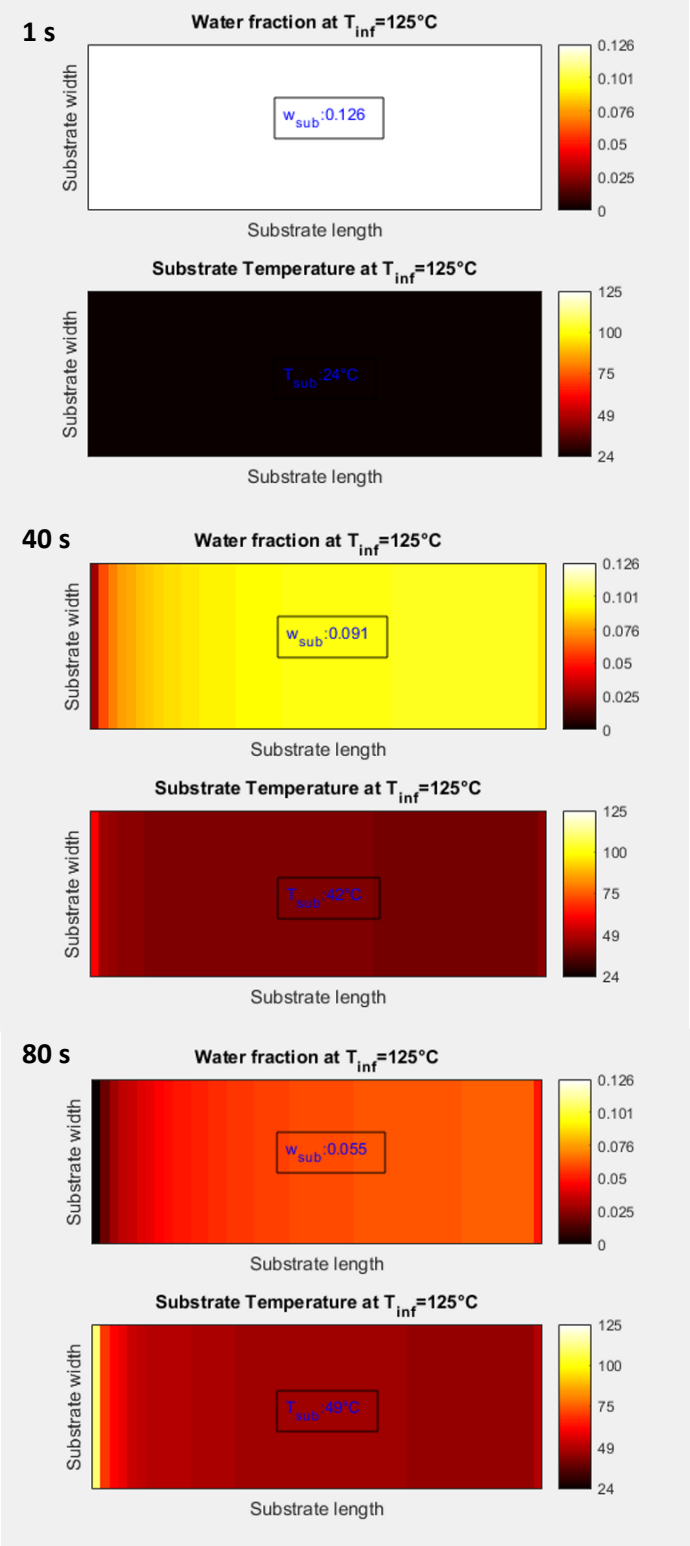

Figure 94 - Water fraction and substrate temperature distribution during a typical drying process at $Tinf = 125\ °C$ predicted by the simulation.

Mean values in the simulation were evaluated by the arithmetic mean for all nodes and by considering the size of the control volume of the node:

$$X_{sub,mean} = \frac{\sum_{i=1}^{n} k_i X_{sub,i}}{\sum_{i=1}^{n} k_i} \tag{172}$$

with $X_{sub,mean}$ as the mean quantity (water fraction or substrate temperature), the number of nodes n, the node i and a factor which accounts for the size of the present control volume k_i. For $i = 1$ and $i = n$, $k_i = 1$ otherwise $k_i = 2$. This accounts for the half-sized control volumes at the substrate edges ($x = 0$ and $x = L_{sub}$).

Table 25 - Simulation conditions for comparison with experiments

Condition	Value		
$\boldsymbol{w_{sub,H2O}}$ $\boldsymbol{(t = 0)}$*	0.1275	0.126	0.124
$\boldsymbol{T_{sub}}$ $\boldsymbol{(t = 0)}$	24 °C	24 °C	24 °C
$\boldsymbol{T_{inf}}$	100 °C	125 °C	150 °C
$\boldsymbol{\dot{V}_{amb}}$	350 L/min		
$\boldsymbol{\varphi_{amb}}$	0.4		
$\boldsymbol{L_{sub}}$	0.36 m		
$\boldsymbol{t_{drying}}$	80 s		
$\boldsymbol{\Delta t}$	0.1 s		
$\boldsymbol{\Delta x}$	0.0072 m		

*based on analysis of experimental results

6.2.1.3.1 Water Fraction

Figure 95 shows the comparison between simulated and measured water fractions. In principle, the mean values for the water fraction of experiments and simulation agree well. Especially the highest drying temperature case (E) shows relatively low deviations. Though, two discrepancies can be identified for all drying temperatures. Firstly, the experimental water fraction at low drying times (up to 20 s) seems to drop much faster than predicted. Interestingly, at least for the lower drying temperatures (A, C), this effect is already balanced at the next evaluation point (40 s). A similar effect can be identified in the article of Wilhelmsson et al. for their investigations of paper drying machines B and C, as labeled in their article [30]. This effect is somewhat counterintuitive, and could be explained by measurement problems (e.g. evaporation losses after finishing the drying step). The second discrepancy occurs after long drying times. Experimental curves tend to flatten more rapidly than predicted, which is clearly more distinct for the lowest drying air temperature (A). A reason for this could be the increasing diffusion resistance, as already discussed in chapter 6.2.1.1, which is not implemented in the simulation. Lower drying air temperature can negatively affect this resistance, since the

diffusion coefficient is a function of temperature. A difference of more than 10 °C of mean substrate temperature is commonly seen between the lowest and the highest considered drying air temperatures and at long drying times. The diffusion coefficient for gases at low pressure can be estimated by $\mathrm{D} \propto T^{1.75}$ [35]. This gives an increase of around 6 % for the diffusion coefficient for a temperature step from 40 to 50 °C. The prediction of water distribution in the substrate is poor at the first sight. A good part of this impression is caused by the large deviation at low drying times (20 s). If one considers the possibility of experimental problems at this point, the prediction quality seems to be more favorable. The principal forecast that water fraction increases with the downstream position is confirmed, although the absolute values, as well as the relative differences between the investigated regions, deviate. A reason for this could lie in the used Nusselt number correlation. A correlation for constant substrate temperature and perfect insulation of the upper plate was used in the simulation. Especially, the constant substrate temperature deviates from the assumption for long drying times. An analysis of the fluid phase and a more detailed investigation of water diffusion in the substrate could help to understand the source of deviation, but is out of the scope of this thesis.

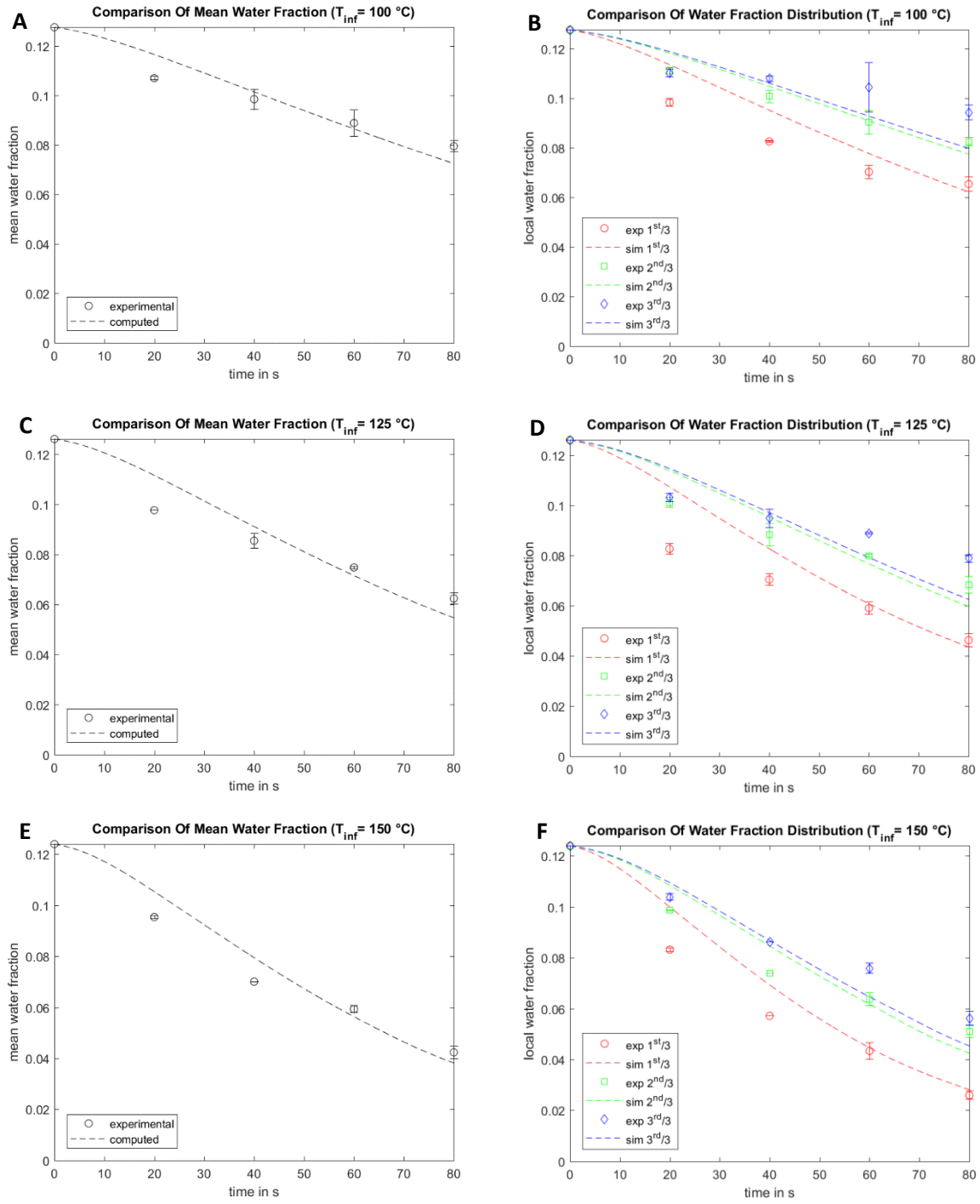

Figure 95 - Comparison of water fraction results. With mean water fraction for 100, 125, 150 °C in A, C, E, respectively and water fraction at first, second and third position for 100, 125, 150 °C in B, D, F, respectively. First, second and third refer to the substrate area, which was cut after drying in three plates of similar areas. The areas are counted in the main flow direction.

6.2.1.3.2 Substrate Temperatures

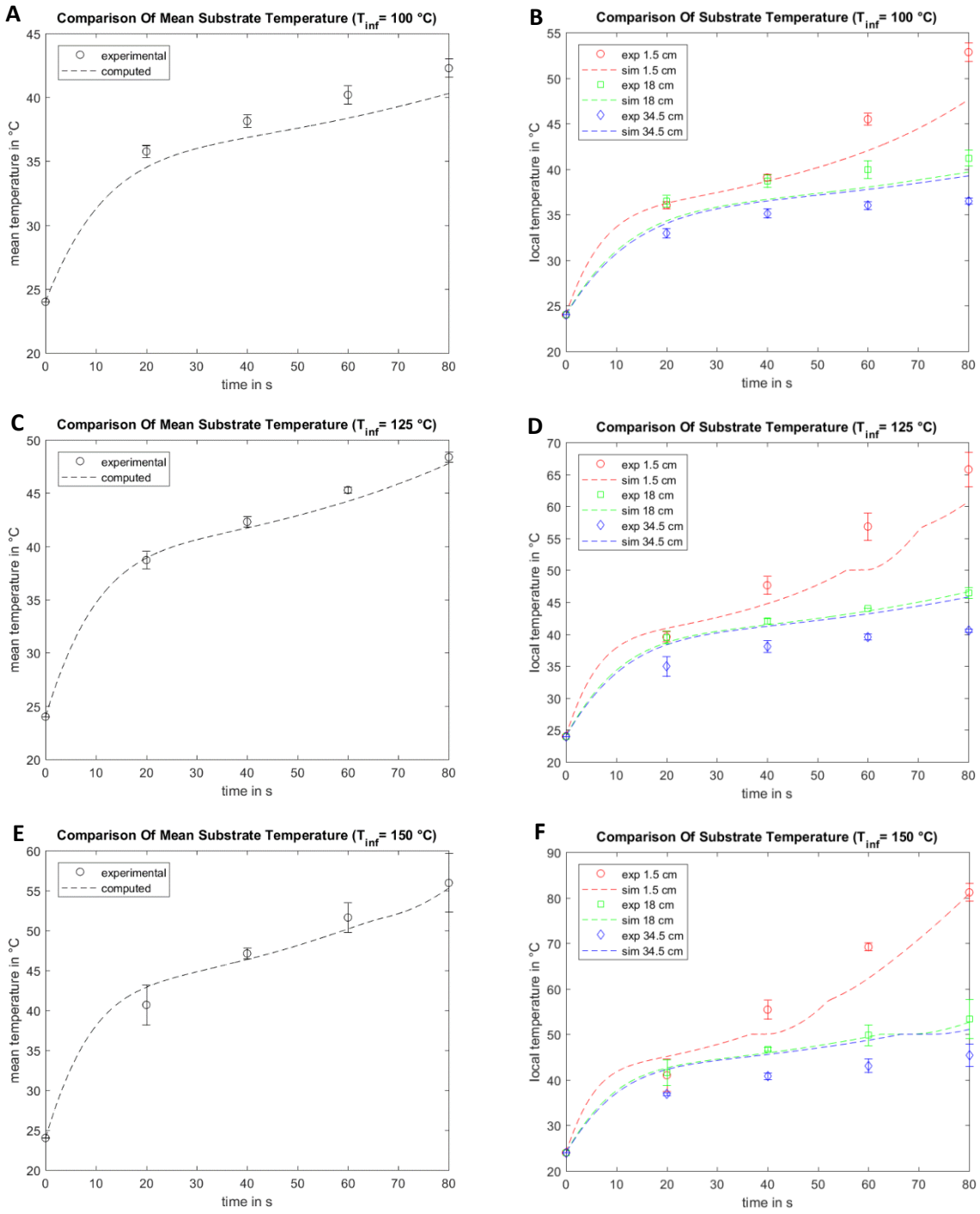

Figure 96 - Comparison of substrate temperature results. With mean substrate temperature for 100, 125, 150 °C in A, C, E, respectively and substrate temperature at position 1.5, 18 and 34.5 cm for 100, 125, 150 °C in B, D, F, respectively. Positions are measured from the very upstream position of the substrate.

Figure 96 shows the comparisons between simulated and measured substrate temperatures. It should be noted that the substrate temperature of the simulation was evaluated in the same

region as the experimental data (between 1.5 and 34.5 cm) from the mean of all nodes in this region (46 nodes). Predicted mean substrate temperatures (A, C, E) agree well with the experimental results. Solely for the case of the drying air temperature of 100 °C (A), the substrate temperatures are consistently underestimated by 2°C at an order of magnitude of 35 °C. Since for all other experiments deviations are smaller than 1 °C, and the shape of the curves agree for any case, an experimental problem could be the reason. From the experimental point of view, an incorrect initial temperature could be a possible cause. The influence of an initial temperature of 30 °C instead of the assumed 24 °C is investigated by the use of the simulation (Figure 97).

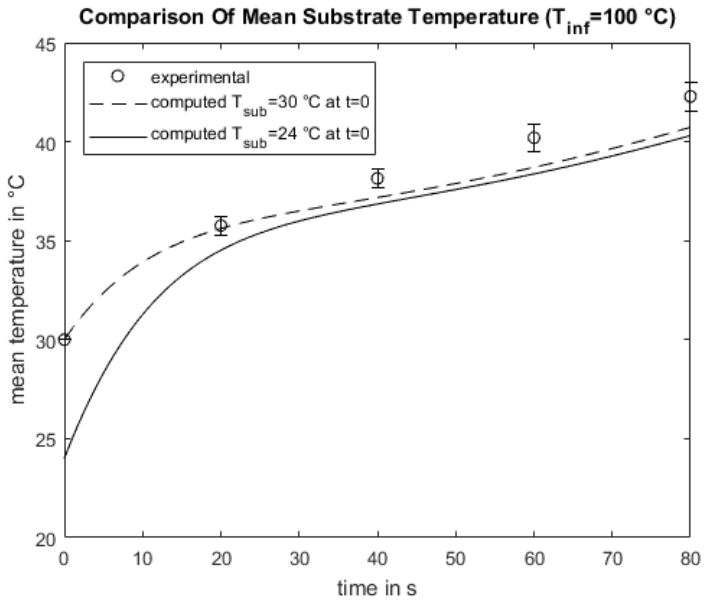

Figure 97 - Predicted impact of higher initial temperature.

The simulation revealed that the increase of initial temperature by 6 °C cannot explain the whole deviation. Analysis of the temperature distribution diagram Figure 96 (B) shows, however, that the sensor at the substrate mid gave temperature data, higher than in the other diagrams (D,F). This is a hint to measurement problems. The temperature distribution in the substrate is fairly well reproduced, though particularly the temperature difference between the position downstream and the mid is underestimated. For sure, this could be a subsequent error from simplifications and poorly investigated diffusion properties already discussed in the water fraction section 6.2.1.3.1.

6.2.1.3.3 Quality of the Simulation

The simulation produced results in good agreement with experimental values, which confirms the used strategy. Deviations were found especially for lower drying temperatures and low water contents, as explained above. A weakness of the simulation is the poor prediction of the

effective water distribution in the substrate, which is not of central interest for this thesis. The focus of interest lies on the prediction of a mean heat transfer coefficient for the considered drying process. Mean temperatures and water contents in the region of interest (down to water fractions of around 0.06) fit very well to the simulated results. Since the energies needed to remove water and rise substrate temperature are well known from literature and experimental data, the simulation is assessed to give excellent results for the prediction of the mean heat transfer coefficient.

6.2.1.4 Evaluation of the Heat Transfer Coefficient

The mean heat transfer coefficient can be extracted from the simulation by:

$$\alpha = \frac{\dot{q}_{conv}}{(T_{inf} - T_{sub})} \tag{173}$$

with the overall heat flux from the drying air $\dot{q}_{conv}$ extracted from the simulation, the drying air temperature T_{inf} and the substrate temperature T_{sub}. The mean heat transfer coefficient was evaluated every 100 ms for a drying time of 80 s and at a drying air temperature of 125 °C (Figure 98).

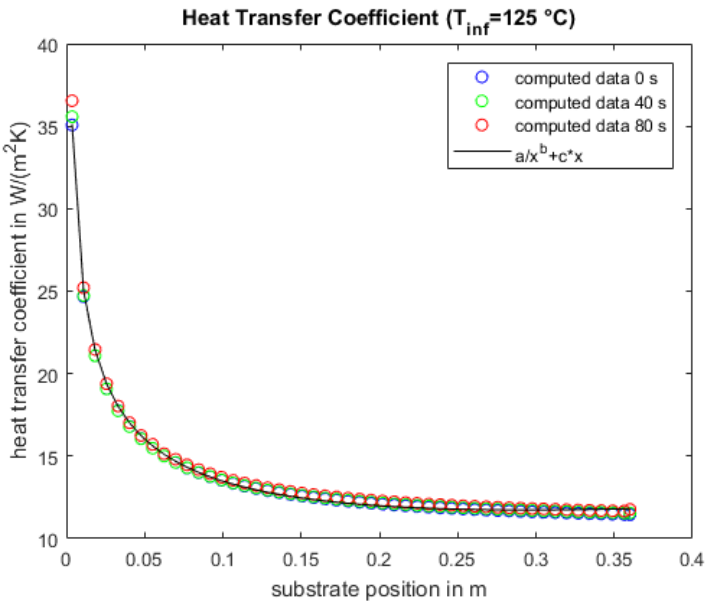

Figure 98 - Heat transfer coefficient at different drying times and positions for drying air temperature of 125 °C.

In Figure 98, it can be seen that the heat transfer coefficient does not vary with drying time, and solely depends on the substrate position. The mean heat transfer coefficient over the substrate length for all investigated drying air temperatures was calculated (Table 26). This was done by integration of the fitting equation shown in Figure 98 that reads:

$$\alpha = \frac{1}{x_e - x_0} \int_{x_0}^{x_e} \left(\frac{a}{x^b} + cx \right) dx \tag{174}$$

with the fitting parameter a, b and c, the upstream edge position of the substrate $x_0 = 0$ and the downstream edge position of the substrate $x_e = L_{sub}$.

Table 26 - Calculated mean heat transfer coefficients over substrate length for air flow of $\dot{V}_{amb} = 350\ l/min$ and different drying air temperatures.

T_{inf} [°C]	α [W/(m²K)]
100	13.59
125	13.86
150	14.25

6.2.2 Substrates Coated with RS2 Std. and RS3_C

6.2.2.1 Drying Experiments

For comparison purposes, the coated mass was set in a way that the initial water content in the substrate before drying is equal for both liquids at 0.113. This led to a grammage of 8.5 g/m² for RS2 Std. and 18.5 g/m² for RS3_C, always related to the fully dried state. The values were oriented at the minimum coating grammage of RS2 Std. to produce fully coated substrates. The following results were gained for different drying times at a drying air temperature of 125 °C (Figure 99). Tabular data is given in the appendix Table 52 to Table 55.

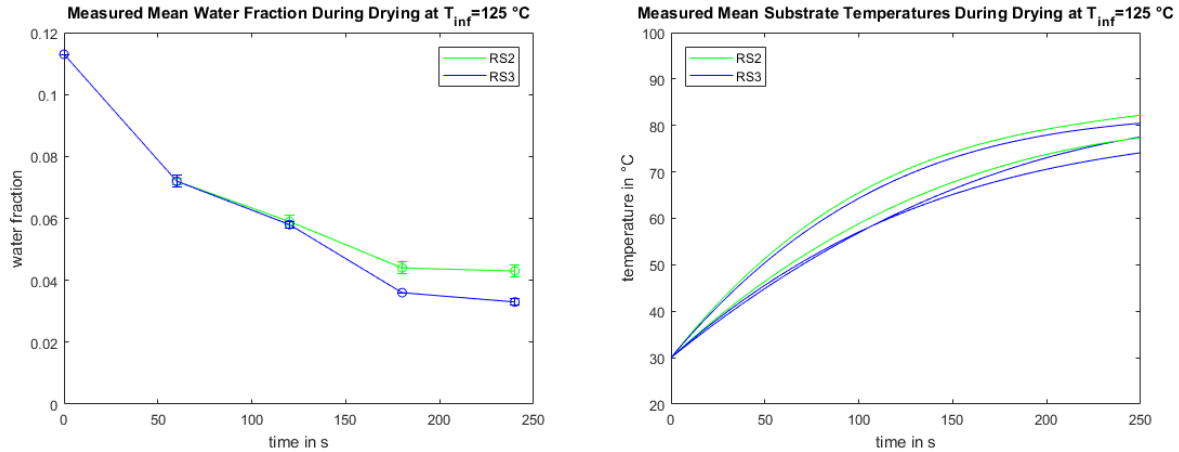

Figure 99 – Measured water fractions (left) and substrate temperatures (right) for RS2 Std. and RS3_C coated substrates. The water fractions are the arithmetic means of three measurements, substrate temperatures are single measurements (for RS2 Std. an outlier was eliminated in which a sensor was not positioned correctly, therefore only two curves are presented).

6.2.2.2 Calculation of the Drying Energy

The consumed drying energy is calculated by the following equation:

$$H_{drying} = \sum_{t=1}^{n} [\alpha A_{sub} (T_{inf} - T_{sub,t}) \Delta t] \quad (175)$$

with the drying energy H_{drying}, the mean heat transfer coefficient for the considered conditions α, the contact area between drying air and substrate A_{sub}, the drying air temperature T_{inf}, the mean substrate temperature at the considered time step $T_{sub,t}$, the time step index t, the number of time steps n and the time step Δt. Finally, the specific drying energy can be found by dividing the drying energy by the removed quantity of water, as presented in Figure 100. Tables of results are given in the appendix Table 52 and Table 53.

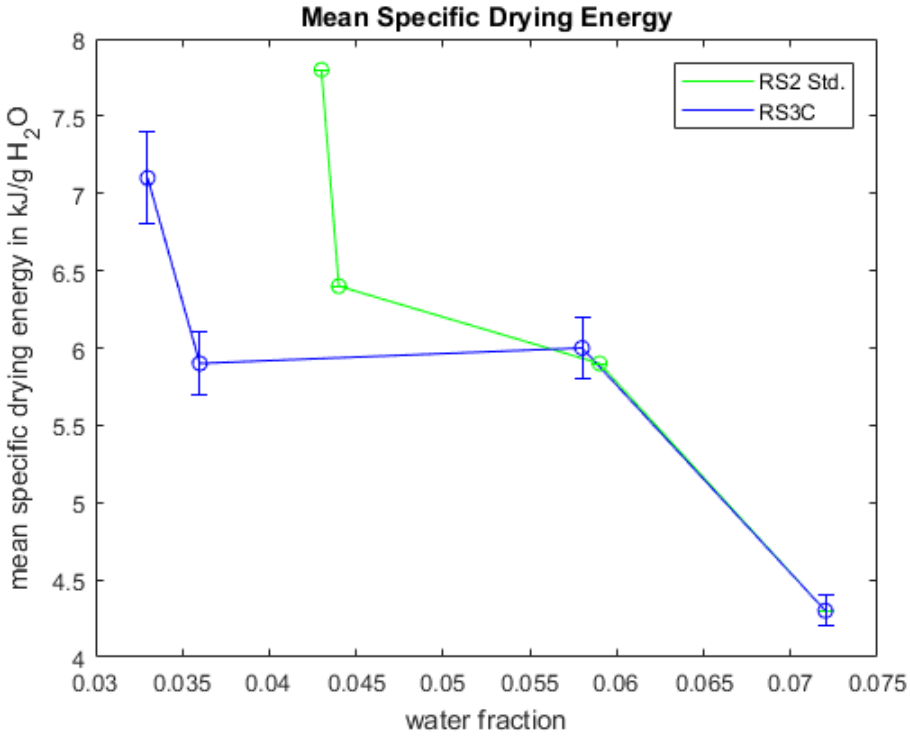

Figure 100 - Calculated specific drying energies for RS2 Std.- (8.5 g/m²) and RS3_C- (18.5 g/m²) coated ACK 350 Std.

Drying of RS2 Std. and RS3_C coated substrates down to water fractions of 0.072 led to similar energy consumptions. For both coatings, approximately 4.3 kJ/g removed H_2O were found. The drying characteristics seem to be quite similar down to water fractions of about 0.058. After this, the curves diverge. The energy consumption of RS2 Std. rises much faster, which could be explained by the barrier properties of the partly dried suspension. It is obvious that decreasing the water fraction of RS2 Std. coated substrates to values lower than 0.043 is hardly possible at the current conditions. The energy consumption of RS3_C coated

substrates, on the other hand, steeply rises at much lower water contents, although much more solid was deposited on these substrates (see coating grammages). The absolute values of the specific drying energies are hard to compare to literature data, because values depend on the nature of the coatings, the final water content, and on the substrate type. However, Karlsson (2009) gives values of 2.8-5 kJ/g H_2O as the energy consumption for drying of coated paper materials in impingement dryers [29]. The order of magnitude of the evaluated energies is thereby confirmed.

7 Conclusions and Outlook

Investigations in the field of cardboard coating and drying were performed. A lab-scale Curtain Coating unit was optimized and extended by a convection dryer. The Curtain Coating process was investigated and standard procedures based on dimensionless numbers were applied to characterize the process. A better understanding of the impact of physical material properties on the coating process was developed. Reasons for deviations from continuous processes were found and recommendations for further investigations were given. A convection dryer was designed and installed at the coating unit. A drying process of cardboard, coated with pure water, was modelled and a mean heat transfer coefficient in the dryer was extracted from a simulation. Computed mean water fractions and mean substrate temperatures agree well with experimental data. The specific drying energy for two different coatings on cardboard was calculated using data from an experimental drying procedure. The study provides a basic understanding of the coating process. It enables further investigations to ultimately predict coatability in the Curtain Coating process based on material data and process settings. It provides basic knowledge on the drying process of cardboard and can form the starting point for the set-up of various drying experiments.

7.1 Conclusions Curtain Coating

Stability of the curtain was substantially increased with the proposed edge guide geometry on the Curtain Coating die of the slide-fed type. The volume flow rate needed for stable curtains could be reduced to approximately one third compared to the original geometry. The standard stability criterion $We > 2$ was applicable, but the absolute values of the Weber number to find a stable curtain showed data scattering for the investigated suspensions. It is assumed that the high undissolved solid load complicates the flow situation, especially for RS3 Std. RS2 Std. established stable curtains at lower Weber numbers (~2.5) than RS3 Std. (~3.7). The major limiting phenomena for the deposition process are disturbances of the curtain. This is caused by the collision of the transport plate and air currents with the curtain. If fluid inertia is increased sufficiently, the process is affected positively, and the mentioned disturbances are not observed anymore. The positive effects of fluid inertia could be seen in different experiments. Increasing volume flow rate and increasing impingement velocity both led to better coatability. The standard operability window, which was developed for continuous Curtain Coating processes, is not applicable. Increasing viscosity seems to shift the coatability window to lower Reynolds numbers. The standard operability window was modified by incorporation of the capillary number. By this, a modified coating window was found, which gives a linear

correlation to predict the boundary of coatability based on physical properties. The modified coating window agrees well with experimental data.

7.2 Outlook Curtain Coating

Further modifications of the coating device are not necessary, since typical coating grammages of the full-scale plant can be reproduced. First tests with multilayer curtains also led to satisfactory results in terms of coatability. For better understanding of the current process and the impact of the undissolved solids on curtain stability, experiments with well investigated coating solutions could be planned. An extensively studied Curtain Coating liquid would be aqueous gelatin solution. The impact of the undissolved solid load on the stability of the liquid sheet should be evaluated and incorporated into the stability criterion to enable the prediction of curtain stability based on physical properties.

7.3 Conclusions Drying of Coatings

Mean water fractions and mean substrate temperatures of wet cardboard predicted by a simulation agrees well with mean values from experiments. This confirms the assumptions for the flow situation during the dryer design and the experimentally determined sorption characteristics. The installed convection dryer yields highly reproducible results, which is a positive indication for the developed drying strategy and the dryer design itself. Deviation of predicted results from drying experiments of wetted substrates were mainly seen for the effective temperature, and water fraction distributions within the substrate. A possible reason for this is the used correlation for the Nusselt number, which is not strictly valid for the entire drying time. Another reason could lie in the poor knowledge of moisture diffusion in the plane of the cardboard sheet. At low water contents, the water fraction is slightly overestimated, which could be due to not included effects, like the increase of diffusion resistance with decreasing water content. The mean heat transfer coefficient extracted from simulation data showed reasonable trends. Based on the good agreement of mean water fractions and substrate temperatures of experiment and simulation, the heat transfer coefficient is able to give good approximations for specific drying energies of different substrates and coatings. The investigation of specific drying energies of a substrate with different coatings gave reasonable results.

7.4 Outlook Drying of Coatings

To clarify the origin of deviations between predicted and measured temperature and water fraction distributions, the simulation could be extended by an analysis of the drying air flow and diffusion effects in the plane of the cardboard. This would certainly lead to a more profound understanding of the drying process, and improved data for the heat transfer coefficient and diffusion properties of the deposited coatings could be obtained.

References

[1] d'Errico, F., Dayet Bouillot, L., García-Diez, M., Pitarch Martí, A., Garrido Pimentel, D. and Zilhão, J. (2016). The technology of the earliest European cave paintings: El Castillo Cave, Spain. *Journal of Archaeological Science*, 70, pp.48-65.

[2] Lacovara, P. (2016). *The world of Ancient Egypt*. Greenwood Press, Santa Barbara, p.3.

[3] Lambourne, R. (1999). *Paint and surface coatings*. 2nd ed. Woodhead Publishing, Cambridge, pp.1-3.

[4] Kistler, S.F. and Schweizer, P.M. (1997). Coating science and technology: an overview. In: S.F. Kistler and P.M. Schweizer, *Liquid Film Coating - scientific principles and their technological implications*, 1st ed. Springer, Glasgow, pp.3-15.

[5] Landau, L. and Levich, B. (1942). Dragging of a Liquid by a Moving Plate. *Acta Physicochim. URSS*, 17, pp.42-54. In: Pelcé, P. (1988), *Dynamics of Curved Fronts*, Academic Press Inc., San Diego, pp. 141-154.

[6] Moore, E. and Cramer, J. (2018). *World's Top Ten Paints Companies 2016 Annual Report*. [online] Wpcia.org. Available at: http://www.wpcia.org/news/2016.html [Accessed 20 Jan. 2018].

[7] Fenn, J. (2007). History of Vacuum Roll Coating. In: Mattox, D.M. and Harwood, V. (2007). *50 years of vacuum coating technology and the growth of the Society of Vacuum Coaters*, Society of Vacuum Coaters. [online] Academia.edu. Available at: http://www.academia.edu/4463008/History_of_Vacuum_Roll_Coating [Accessed 20 Jan. 2018].

[8] Miyamoto, K. and Katagiri, Y. (1997). Curtain coating. In: S.F. Kistler and P.M. Schweizer, *Liquid Film Coating - scientific principles and their technological implications*, 1st ed. Springer, Glasgow, pp.463-494.

[9] Taylor, L.H. (1903). *Maschine zur Herstellung von aus Nährstoffen bestehenden Formstücken mit allseitig geschlossenem Überzug, wie Konfekt, Pastetchen o. dgl*., German Patent, DE145517.

[10] Hughes, D.J. (1968). *Method for simultaneously applying a plurality of coated layers by forming a stable multilayer free-falling vertical curtain*. US Patent, 3508947.

[11] Gardón, J. L. F. (2005), *Annual Report*, Rapid Alert System for Food and Feed.

[12] Weinstein, S.J. and Palmer, H.J. (1997). Capillary hydrodynamics and interfacial phenomena. In: S.F. Kistler and P.M. Schweizer, *Liquid Film Coating - scientific principles and their technological implications*, 1st ed. Springer, Glasgow, pp.19-62.

[13] Chhabbra, R.B. and Richardson, J.F. (1999). *Non-Newtonian Flow in Process Industries: Fundamentals and Engineering Applications*, 2nd *ed.,* Elsevier Ltd., Oxford, pp. 9.

[14] Ade, F. (1976). *Gleitflächenbeschichtungsvorrichtung*. US Patent, 4041897.

[15] Fahrni, F. and Zimmermann, A. (1978). *Coating device*. US Patent, 4109611.

[16] Nishida, S., Katagiri, Y. and Suga, Y. (1994). *Curtain Coating method with reduced neck-in*. US Patent, 5304402A.

[17] Greiller, J.F. (1975), *Apparatus for production of photographic elements*. US Patent, 3867901 A.

[18] Conroy, J.E., Ruschak, K.J. and Devine, W.D. (1995), *Edge guide lubricating fluid delivery apparatus*. US Patent, 5382292.

[19] Reiter, T.C. (1989), *Curtain Coating Method and Apparatus*. US Patent, 4830887.

[20] Kistler, S.F. and Scriven, L.E. (1984). Coating flow theory by finite element and asymptotic analysis of the Navier-Stokes system. *Int. J. Numer. Methods Fluids*, 4, 207-229.

[21] Brown, D.R. (1961). A study of the behaviour of a thin sheet of moving liquid. *J. Fluid Mech.,* 10, pp. 297-305.

[22] Steiner, H. (2014). *Transport Processes I*. Lecture Notes.

[23] Baehr, H. and Stephan, K. (2011). *Wärme- und Stoffübertragung*. Springer, Berlin, pp. 394.

[24] Idel'chik, I.E. (1966). *Handbook of Hydraulic Resistance*, Israel Program of Scientific Translation Ltd., Jerusalem, pp. 67.

[25] Idel'chik, I.E. (1966). *Handbook of Hydraulic Resistance*, Israel Program of Scientific Translation Ltd., Jerusalem, pp. 450-451.

[26] Brenn, G. (2014). *Transport Processes II*. Lecture Notes.

[27] Shah, R.K. and London, A.L. (1978). Supplement 1, Laminar flow in forced convection ducts. In: T.F. Irvine and J.P. Hartnett, *Advances in Heat Transfer*. Academic Press Inc., London, pp.153-195.

[28] Incropera, F.P. and DeWitt, D.P., (1996) *Fundamentals of Heat and Mass Transfer,* 4th ed. John Wiley and Sons, New York, pp. 321-325.

[29] Karlsson, M. (2010). *Papermaking, part 2, Drying*, 2nd ed. Paperi ja Puu Oy, Helsinki, pp.14-77.

[30] Wilhelmsson, B., Stenström, S., Nilsson, L., Krook, R., Persson, H. and Wimmerstedt, R. (1996). Modeling multicylinder paper drying - validation of a new simulation program. *TAPPI Journal*, 79, pp. 157-167.

[31] Krischer, O. and Kast, W. (1979). *Die wissenschaftlichen Grundlagen der Trocknungstechnik, 1. Auflage*. Springer, Berlin, pp. 54.

[32] Abramzon, B. and Sirignano, W.A. (1989). Droplet vaporization model for spray combustion calculations, *Int. J. Heat Mass Transfer* 32, pp. 1605-1618.

[33] Incropera, F.P. and DeWitt, D.P., (1996) *Fundamentals of Heat and Mass Transfer,* 4th ed. John Wiley and Sons, New York, pp. 256-263.

[34] Tsilingiris, P.T. (2008). Thermophysical and transport properties of humid air at temperature range between 0 and 100 °C. *Energy Conversion and Management*, 49, pp. 1098–1110.

[35] Poling, B.E., Prausnitz J.M and O'Connell, J.P. (2001), *The Properties of Gases and Liquids*, 5th *ed*. McGraw-Hill, New York.

[36] engineeringtoolbox.com. (2018). *Engineering ToolBox*. [online] Available at: https://www.engineeringtoolbox.com/material-properties-t_24.html [Accessed 1 Nov. 2017].

[37] Krischer, O. and Kast, W. (1979). *Die wissenschaftlichen Grundlagen der Trocknungstechnik, 1. Auflage*. Springer, Berlin, pp. 271-275.

[38] Hashemi, S.J., Comes, V.G., Crotogino, R.H. and Douglas, W.J.M. (1997). In-Plane Diffusivity of Moisture in Paper. *Drying Technology – An Intern. Journal*, 15, pp. 265-294.

[39] Van der Wel, G.K. and Adan O.C.G. (1999). Moisture in organic coatings – a review. *Progress in Organic Coatings*, 37*,* pp. 1-14.

[40] Vieira, M.G.A. and Rocha, S.C.S. (2008). Mathematical modeling of handmade recycled paper drying kinetics and sorption isotherms. *Braz. J. Chem. Eng.,* 25, pp. 299-312.

[41] Ramarao, B.V. (1998), Moisture sorption and transport processes in paper materials, *Stud. Surf. Sci. Catal.*, 120, pp. 531-560.

[42] Rhim, J.W. and Lee, J.H. (2009). Thermodynamic Analysis of Water Vapor Sorption Isotherms and Mechanical Properties of Selected Paper-Based Food Packaging Materials. *J. Food Sci.*, 74**,** pp. 502-511.

[43] Menkov, N.D. (2000). Moisture sorption isotherms of chickpea seeds at several temperatures. *J. Food Eng*., 45, pp. 189-194.

[44] Staudt, P.B., Tessaro, I.C., Marczak, L.D.F., Soares, R. de P. and Cardozo, M. (2013). A new method for predicting sorption isotherms at different temperatures: Extension to the GAB model. *J. Food Eng.*, 118, pp. 247–255.

[45] Quirijns, E.J., van Boxtel, A.J.B., van Loon, W.K.P. and van Straaten, G. (2005). Sorption isotherms, GAB parameters and isosteric heat of sorption. *J. Sci. Food Agric.*, 85*,* pp. 1805-1814.

[46] IKA® (2010). Process reactor *Standard Production Plant 50:* User's guide, Staufen.

[47] Mettler Toledo (2010**)**. Precision balance *XS204:* User's guide, Greifensee.

[48] Kern (2010). Laboratory scale *572:* User's guide, Balingen.

[49] Mezger, T. G. (2012). *Das Rheologie Handbuch, 4. Auflage*, Vincentz Network Verlag, Hannover, pp. 238-240.

[50] Chhabbra, R.B. and Richardson, J.F. (1999). *Non-Newtonian Flow in Process Industries: Fundamentals and Engineering Applications*, 2nd *ed.* Elsevier Ltd., Oxford, pp. 56-75.

[51] Slatter*,* P. (2015). The rheometry of free surface flows. *J. Non Newton. Fluid Mech.*, *222*, pp. 248-252.

[52] Hens, J. and Van Abbenyen, W. (1997). Slide Coating. In: S.F. Kistler and P.M. Schweizer, *Liquid Film Coating - scientific principles and their technological implications*, 1st ed. Springer, Glasgow, pp.427-462.

[53] Dullaert, K. and Mewis J. (2005). Stress jumps on weakly flocculated dispersions: Steady state and transient results. *J. Colloid. Interface Sci.*, 287*,* pp. 542-551.

[54] Ewoldt, H., Johnston, M.T. and Caretta L.M. (2015). Experimental challenges of shear rheology: how to avoid bad data. In: S. Spagnolie, *Complex Fluids in Biological Systems*, Springer, New York.

[55] SITA, (2016), *Bubble pressure tensiometer pro line t15:* User's guide, Dresden.

[56] Randall Schunk, P. and Scriven, L.E. (1997). Surfactant effects in coating processes. In: S.F. Kistler and P.M. Schweizer, *Liquid Film Coating - scientific principles and their technological implications*, 1st ed. Springer, Glasgow, pp.495-536.

[57] Tricot, Y.-M. (1997). Surfactants: static and dynamic surface tension. In: S.F. Kistler and P.M. Schweizer, *Liquid Film Coating - scientific principles and their technological implications*, 1st ed. Springer, Glasgow, pp.99-136.

[58] Christov, N. C., Danov, K. D., Kralchevsky, P. A., Ananthapadmanabhan, K. P. and Lips, A. (2006). Maximum Bubble Pressure Method: Universal Surface Age and Transport Mechanism in Surfactant Solutions*. Langmuir*, 22, pp. 7528-7542.

[59] Mettler Toledo (2009), *Halogen Moisture Analyzer HB43-S:* User's guide, Greifensee.

[60] Netzsch, (2007), P*rogressing cavity pump NM021BY02S12B:* User's guide, Selb.

[61] Scherzinger, (2007), *Gear pump 4030-710-B-DM-75-2:* User's guide, Furtwangen*.*

[62] Krohne, (2016), *Magnetic-inductive flowmeter OPTIFLUX 4000 and IFC 300:* User's guide, Duisburg.

[63] Sony, (2015), *Compact camera RX100 M4:* User's guide, China.

[64] Wolf, W., Spiess, W.E.L. and Jung, G. (1985). Standardization of Isotherm Measurements. In: Simatos, D. and Multon J.L. *Properties of Water in Foods*, Martinus Nijhoff Publishers, Dordrecht, pp. 661-679.

[65] Wang, N. and Brennan*,* J.G. (1991). Moisture sorption isotherm characteristics of potatoes at four temperatures. *J. Food Eng.*, 14, pp. 269-287.

[66] Mohamed, L.A., Kouhila, M., Jamali, A., Lahsasni, S. and Mahrouz, M. (2005). Moisture sorption isotherms and heat of sorption of bitter orange leaves. *J. Food Eng.*, 67, pp. 491–498.

[67] Kaymak-Ertekin, F., Gedik*,* A. (2004). Sorption isotherms and isosteric heat of sorption for grapes, apricots, apples and potatoes. *Lebensm.-Wiss. u.-Technol.,* 37, pp. 429–438.

[68] Greenspan L. (1977). Humidity Fixed Points of Binary Saturated Aqueous Solutions. *J. Res. Natl. Bur. Stand.*, 81 A(1), pp. 89.

[69] Leister, (2017), *Air Blower and Heater ASO and LHS 61L:* General Catalogue for Process Heat*,* Kaegiswil.

[70] Leister, (2017), *Heatblower Mistral 6 System:* User's guide, Kaegiswil.

[71] Holleman, A.F, Wiberg, E. and Wiberg, N. (2007). *Lehrbuch der Anorganischen Chemie*, *102. Auflage*, Walter De Gruyter & Co, Berlin.

[72] Locke, D. (2008). *Guide to the Wiring Regulations, 17th Edition IEEE Wiring Regulation (BS 7671: 2008)*, John Wiley & Sons Ltd., Hoboken, Appendix 4.

[73] Yokogawa, (2017), *Recorder µR10000:* User's guide. Netherlands.

[74] Binder, (2010), *Drying chamber FD53 E2:* User's guide*.* Tuttlingen*.*

[75] Addo-Yobo, F.O., Pitt, M. J. and Obiri, H. A. (2011). The effects of particle size on the mechanisms of atomization of suspensions using hydraulic spray nozzles. *AIChE J.*, 57, pp. 2007-2024.

[76] Sauret, A., Troger, A. and Jop, P. (2017). An experimental study on particle effects in liquid sheets. pp.3–6. [online] epj-conferences.org. Available at: https://www.epj-conferences.org/articles/epjconf/pdf/2017/09/epjconf162002.pdf [Accessed 01 Mar. 2018].

Appendix

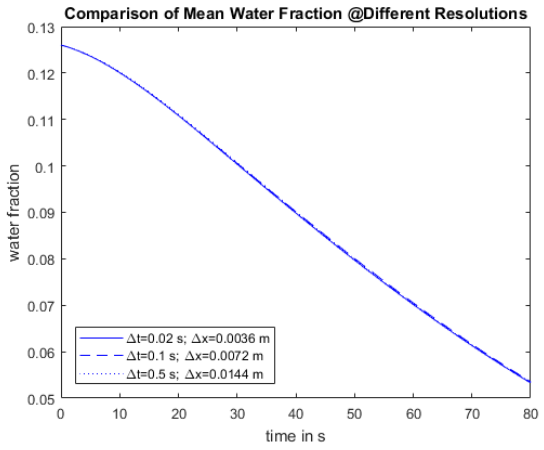

Figure 101 - Influence of grid resolution on simulation results. Mean Water Fraction.

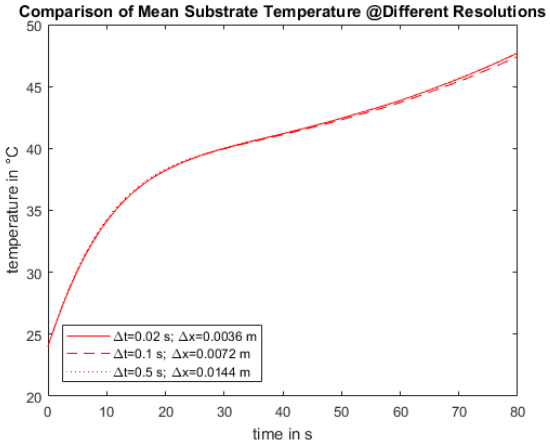

Figure 102 - Influence of grid resolution on simulation results. Mean Substrate Temperature.

Table 27 – Ostwald-De Waele Parameter of RS2 Std. with coefficient of determination.

n_O	K_O	R^2
0.974	0.469	0.9999
0.973	0.608	0.9999
0.975	0.461	0.9999

Table 28 – Ostwald-De Waele Parameter of RS3 Std. with coefficient of determination.

n_O	K_O	R^2
0.741	0.578	0.9906
0.749	0.270	0.9833
0.774	0.594	0.9836

Table 29 – Influence of high shear step on RS2 Std.: Upstream shear rate of 100 s^{-1}; High shear step for 1 s; after 2 s at 40 s^{-1} viscosity was compared. Shear rate and duration are in conjunction with typical flow conditions for Curtain Coating.

High Shear Rate [s^{-1}]	η @ 100 s^{-1} [mPas]	η @ 40 s^{-1} ; 2 s [mPas]
0	403	414
500	400	433
1000	398	449
2000	370	424

Table 30 - Influence of high shear step on RS3 Std.: Upstream shear rate of 100 s^{-1}; High shear step for 1 s; After 1.5 s at 70 s^{-1} viscosity was compared. Shear rate and duration are in conjunction with typical flow conditions for Curtain Coating.

High Shear Rate [s^{-1}]	η @ 100 s^{-1} [mPas]	η @ 70s^{-1} ; 1.5 s [mPas]
0	175	194
500	166	190
1000	165	187
2000	162	173

Table 31 - Production of salt solutions.

Salt Solution	Mass Salt Added [g]
10 mM NaCl	0.584
100 mM NaCl	5.840
5 mM NaBr	0.514
100 mM NaBr	10.289

Calibration Assessment of SITA

Name			Data				Knock-Out-Criteria			Additional Criteria	
Tenside	Salt Solution	Additional Info	Aparatus Constant λ	Abs. Deviation of λ given by confidence interv.	Rel. Deviation of λ given by confidence interv.	Correlation Coefficient (=R)	Residue trend	rel. Deviation by confidence interval>=20%	R<0.98	R<0.99	nearly normal distributed residues
3mM_DTAB	5mM_NaBr	-	6,251	0,6896	11,03	0,9964	n	n	n	n	j
0_5mM_SDS	100mM_NaCl	-	6,895	0,6951	10,08	0,9981	n	n	n	n	n
0_75mM_SDS	100mM_NaCl	-	5,675	0,4915	8,66	0,9981	n	n	n	n	n
1mM_DTAB	5mM_NaBr	PEEK	5,139	0,4935	9,60	0,9971	n	n	n	n	j
1mM_SDS	10mM_NaCl	-	4,075	0,2618	6,42	0,9989	n	n	n	n	n
0_5mM_SDS	10mM_NaCl	-	4,3595	0,3953	9,07	0,9984	n	n	n	n	j
0_2mM_SDS	100mM_NaCl	-	5,2972	0,6567	12,40	0,9984	n	n	n	n	j
2mM_SDS	10mM_NaCl	-	4,2272	0,1463	3,46	0,9996	n	n	n	n	j
1mM_SDS	100mM_NaCl	-	5,5985	0,3468	6,19	0,9989	n	n	n	n	n
3mM_DTAB	100mM_NaBr	-	5,2594	0,2681	5,10	0,9991	n	n	n	n	j
3mM_SDS	10mM_NaCl	-	4,75	0,1506	3,17	0,9997	n	n	n	n	j
4mM_DTAB	100mM_NaBr	-	6,2776	0,5589	8,90	0,9973	n	n	n	n	n
2mM_DTAB	5mM_NaBr	PEEK	7,0078	0,7609	10,86	0,9963	n	n	n	n	j
2mM_DTAB	100mM_NaBr	-	5,2191	0,2559	4,90	0,9992	n	n	n	n	j
			mean	**5,4**							
			stddev	**0,89**							

Figure 103 – Data of all solutions to evaluate the apparatus constant for the SITA bubble pressure tensiometer.

Table 32- Production of surfactant solutions.

Surfactant Concentration [mM]	Mass Surfactant Added [mg]
SDS in 10 mM NaCl	
0.1	5.8*
0.5	14.4
1	28.6
2	57.7
3	86.4
SDS in 100 mM NaCl	
0.2	5.8
0.5	14.5
0.75	21.6
1	28.5
DTAB in 5 mM NaBr	
1	31.3
2	61.7
3	92.5
5	154.8
7	216.0
10	308.4
12	370.1
DTAB in 100 mM NaBr	
2	61.7
3	92.6
4	123.5

* 200 mL salt solution was used to increase the necessary mass of surfactant. SDS (Sigma Aldrich; 74255-250G; 25.01.2017); DTAB (Sigma Aldrich; D8638-25G; 25.01.2017); NaBr (Sigma Aldrich; 71329-250G; 25.01.2017); NaCl (Sigma Aldrich; S7653-250 G).

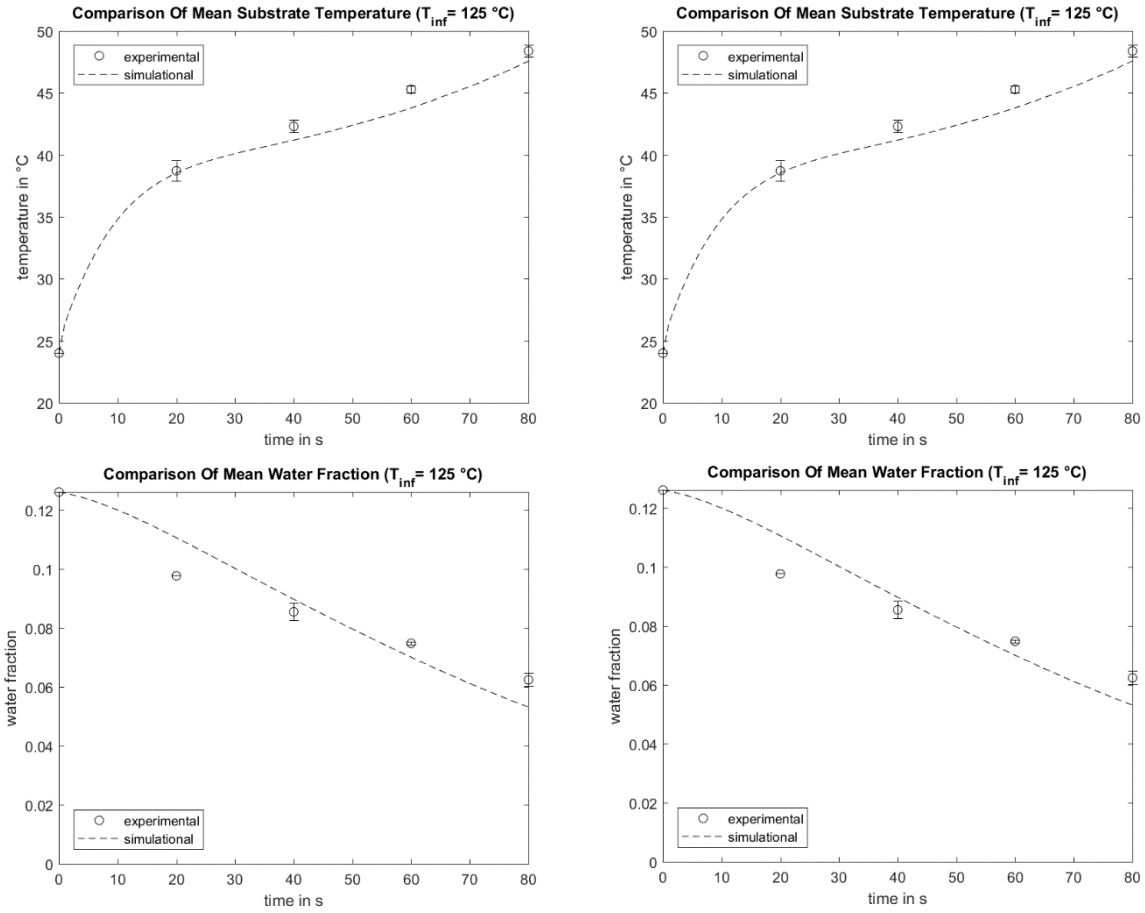

Figure 104 - Simulation results for T_{inf}=125 °C with different planar diffusion coefficients. Left column shows results where the planar diffusion coefficient of water in the substrate was divided by 10 after calculation as described in the Materials section. At the right column, it was multiplied by 10.

Table 33 – Desorption results of untreated ACK 350 at 40 °C.

	NaOH*	$MgCl_2$*	$Mg(NO_3)_2$*	NaCl*	KCl*
H_2O activity [-]	0.0626	0.316	0.4842	0.7468	0.8232
Dry Mass [g]	0.3986	0.3910	0.3792	0.3966	0.3909
Water Load [-]	0.0517	0.0647	0.0680	0.1087	0.1294

*NaOH (Sigma Aldrich, 71690-1KG, 18.06.2017); $MgCl_2$*$6H_2O$ (Sigma Aldrich, M9272-100G, 18.06.2017); $Mg(NO_3)_2$*$6H_2O$ (Sigma Aldrich; 237175-1KG; 18.06.2017); NaCl (Sigma Aldrich; S7653-250G; 25.01.2017); KCl (Sigma Aldrich; P5405-1KG; 18.06.2017);

Table 34 - Desorption results of untreated ACK 350 at 60 °C.

	NaOH*	$MgCl_2$*	$Mg(NO_3)_2$*	NaCl*	KCl*
H_2O activity [-]	0.0362	0.2926	0.45*	0.7441	0.8022
Dry Mass [g]	0.3928	0.3999	3.3948	0.4020	0.3971
Water Load [-]	0.0517	0.0647	0.0680	0.1087	0.1294

*for details on the chemicals see Table 34

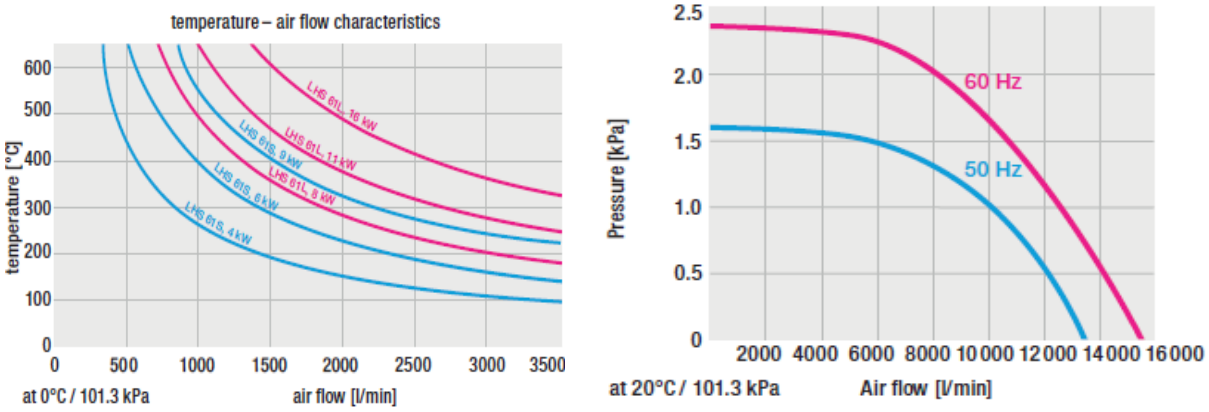

Figure 105 - Achievable temperature for LHS 61L (left), characteristic pressure drop curve for ASO blower (right).

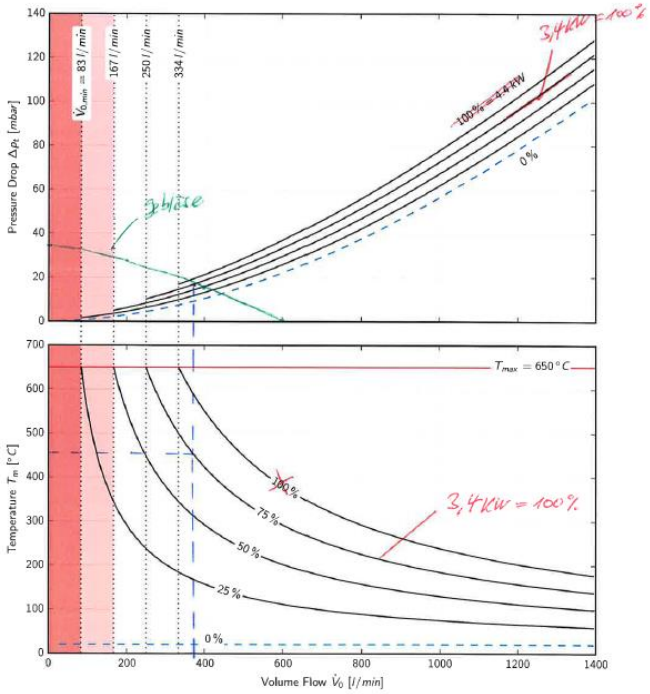

Figure 106 - Achievable temperature and characteristic pressure drop curve for comparable system to Leister Mistral 6 System. Kindly made available by Leister Process Heat.

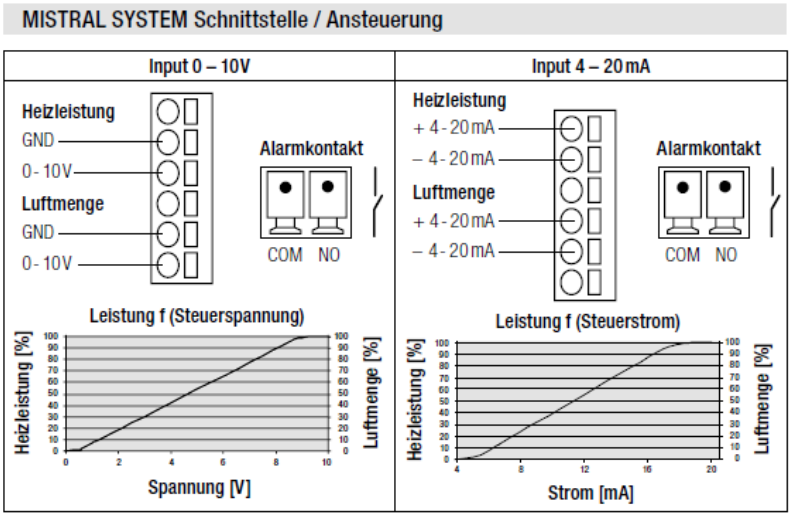

Figure 107 - Dependency of temperature and volume flow on power settings of Leister Mistral 6 System.

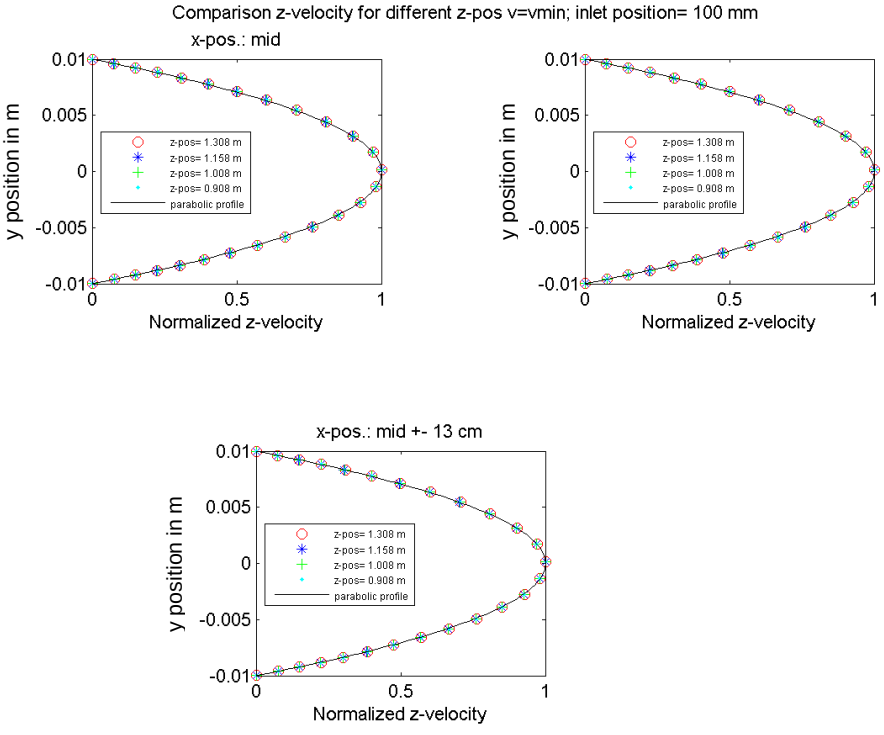

Figure 108 – Predicted velocity profiles along substrate width for inlet position L_{BW}=10 cm and v_{min}.

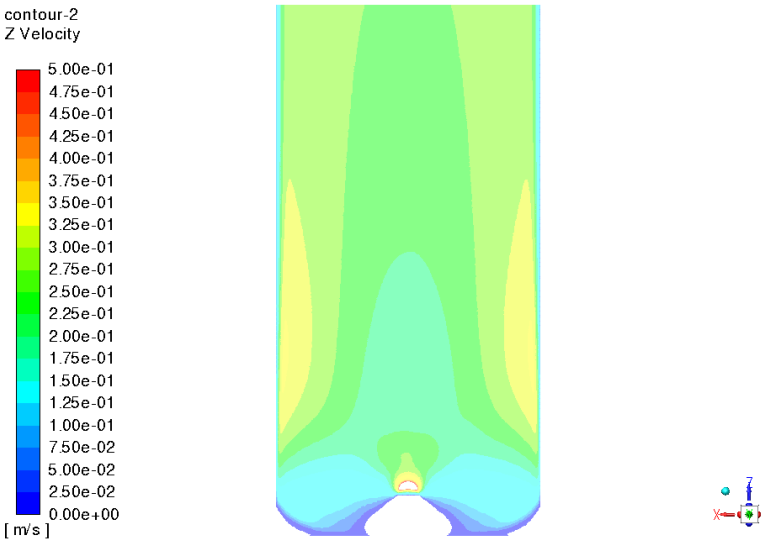

Figure 109 - Predicted midplane velocities for inlet position L_{BW}=10 cm and v_{min}.

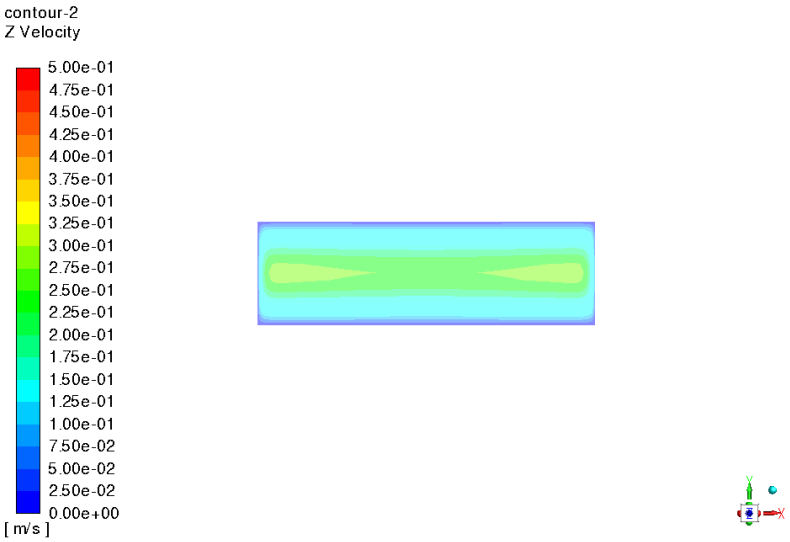

Figure 110 - Predicted velocity distribution at exit for inlet position L_{BW}=10 cm and v_{min}.

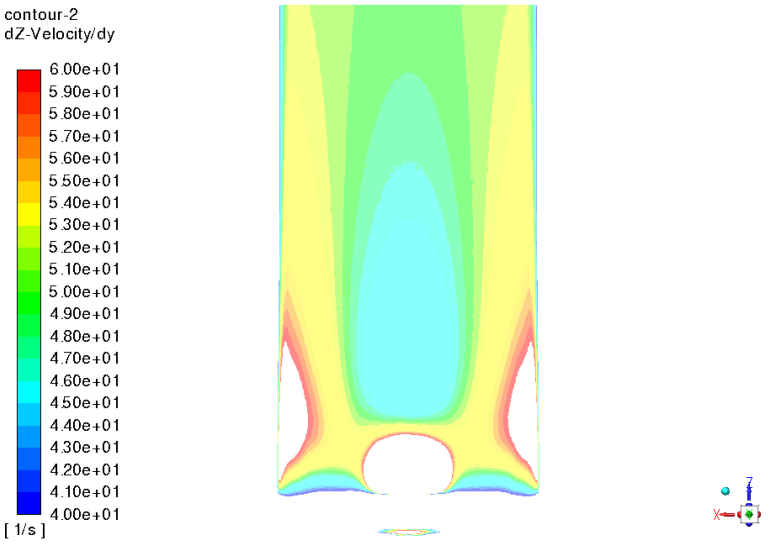

Figure 111 - Predicted velocity gradients at dryer bottom for inlet position L_{BW}=10 cm and v_{min}.

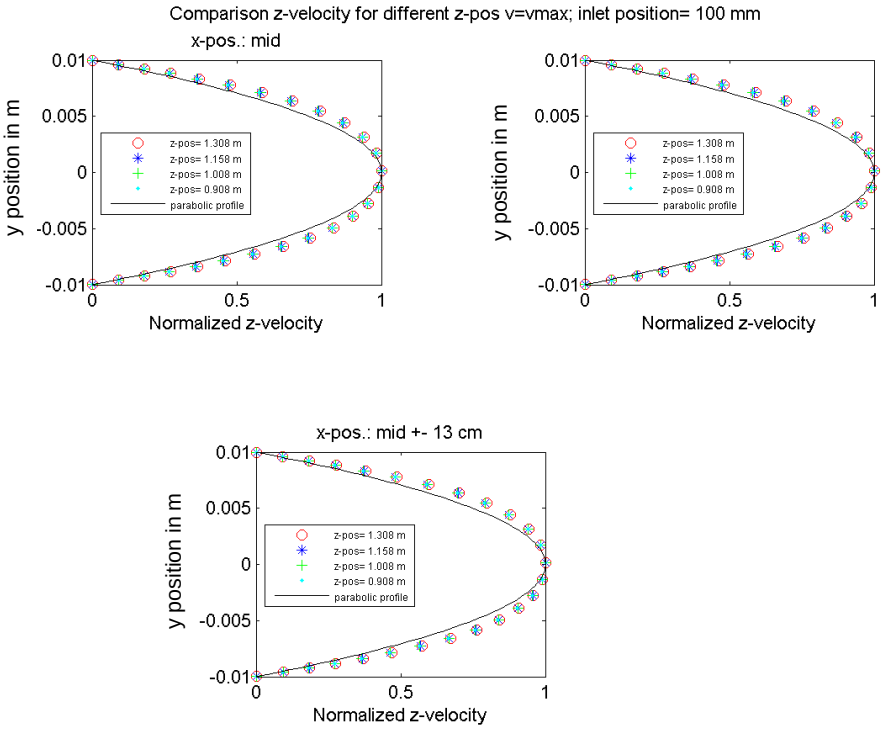

Figure 112 - Predicted velocity profiles along substrate width for inlet position L_{BW}=10 cm and v_{max}.

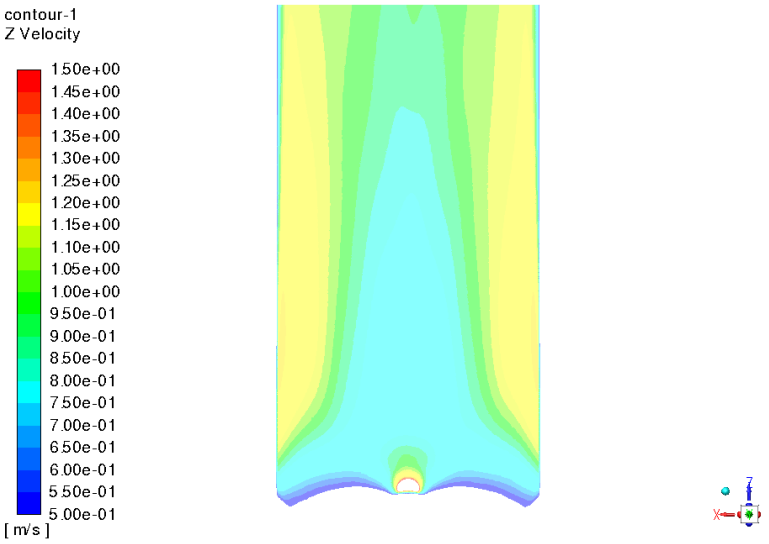

Figure 113 - Predicted midplane velocities for inlet position L_{BW}=10 cm and v_{max}.

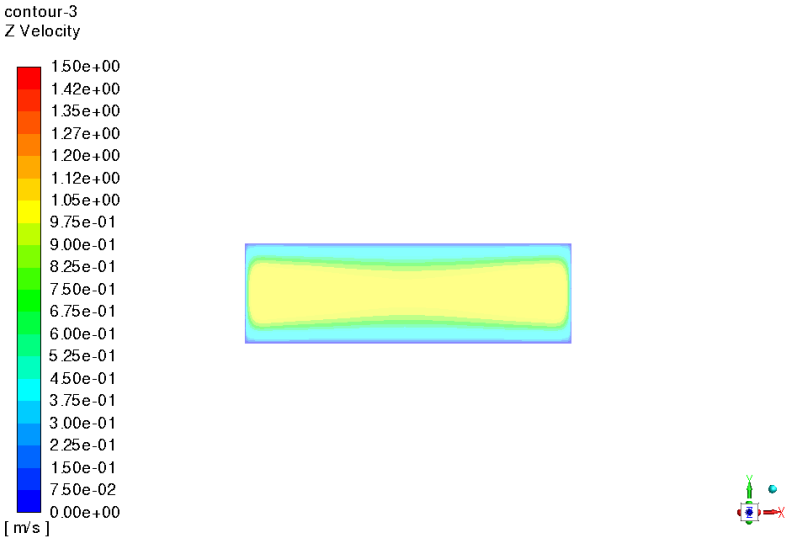

Figure 114 - Predicted velocity distribution at exit for inlet position L_{BW}=10 cm and v_{max}.

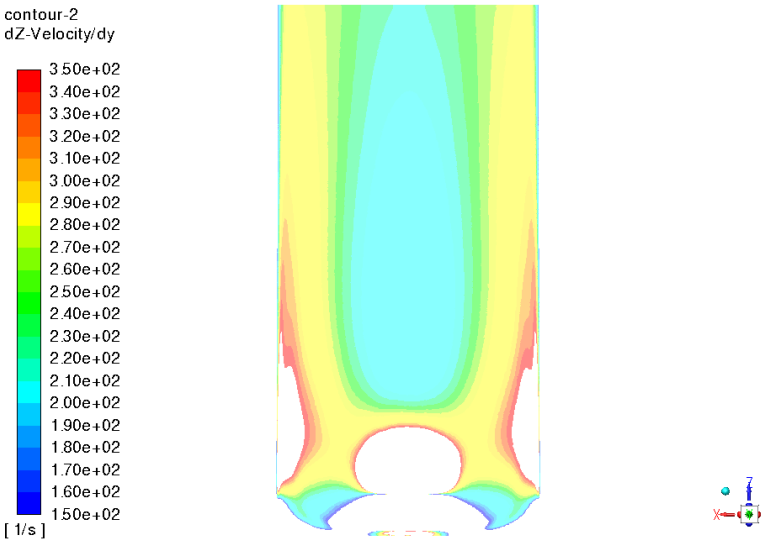

Figure 115 - Predicted velocity gradients at dryer bottom for inlet position L_{BW}=10 cm and v_{max}.

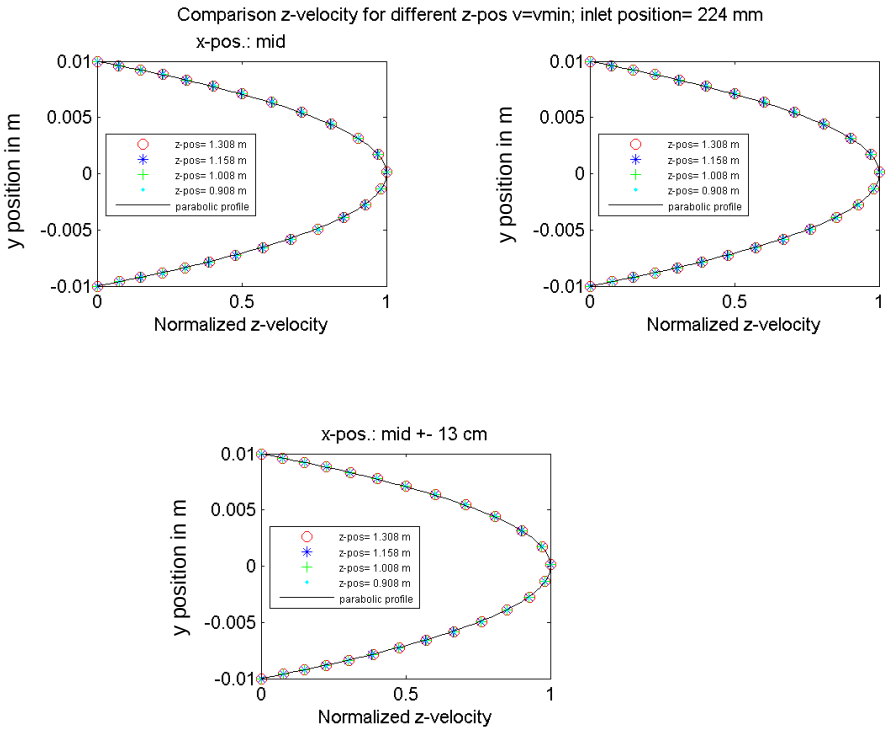

Figure 116 - Predicted velocity profiles along substrate width for inlet position L_{BW}=22.4 cm and v_{min}.

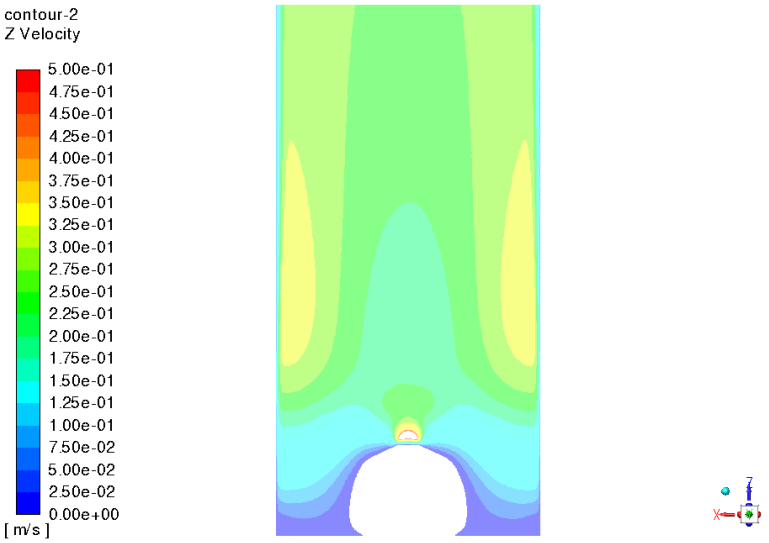

Figure 117 - Predicted midplane velocities for inlet position L_{BW}=22.4 cm and v_{min}.

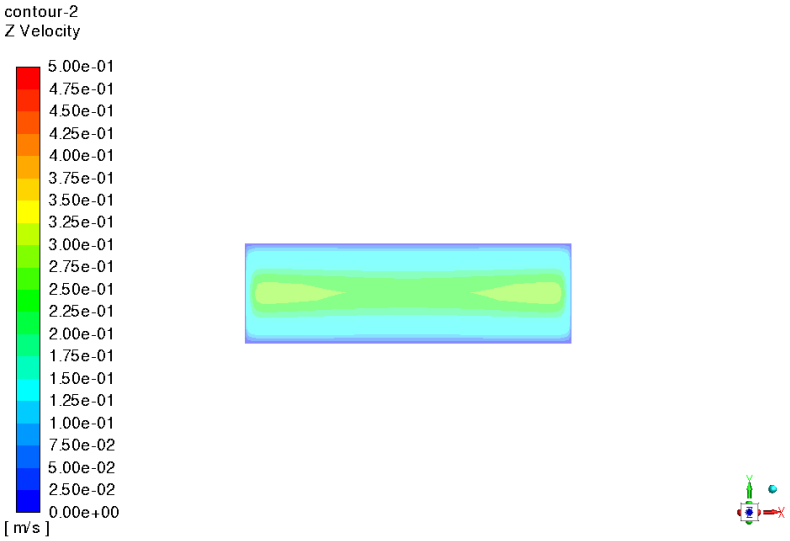

Figure 118 - Predicted velocity distribution at exit for inlet position L_{BW}=22.4 cm and v_{min}.

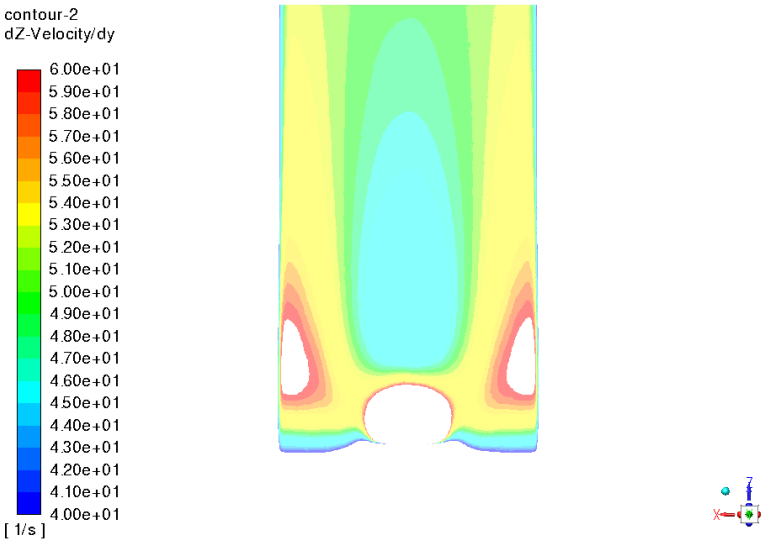

Figure 119 - Predicted velocity gradients at dryer bottom for inlet position L_{BW}=22.4 cm and v_{min}.

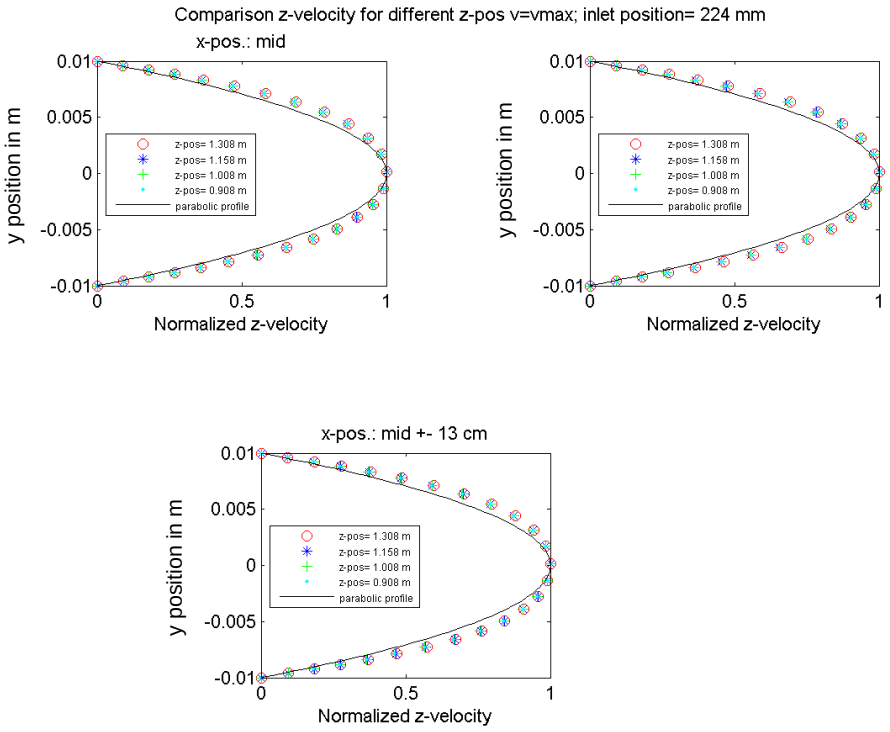

Figure 120 - Predicted velocity profiles along substrate width for inlet position L_{BW}=22.4 cm and v_{max}.

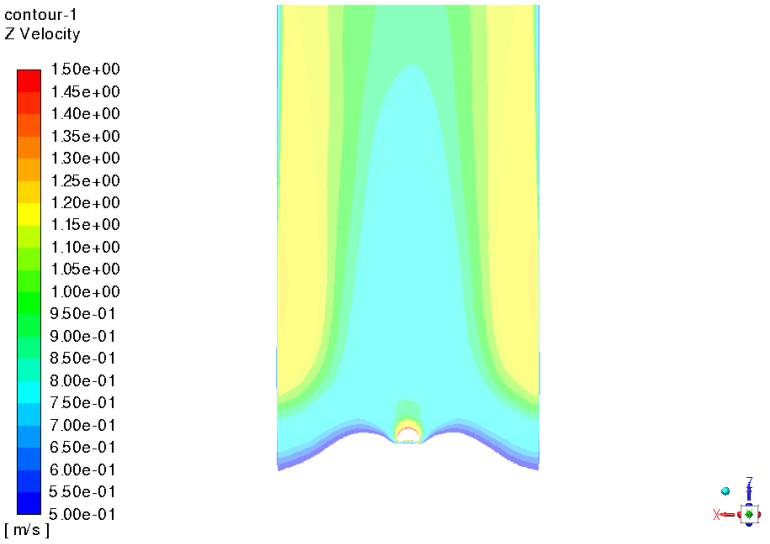

Figure 121 - Predicted midplane velocities for inlet position L_{BW}=22.4 cm and v_{min}.

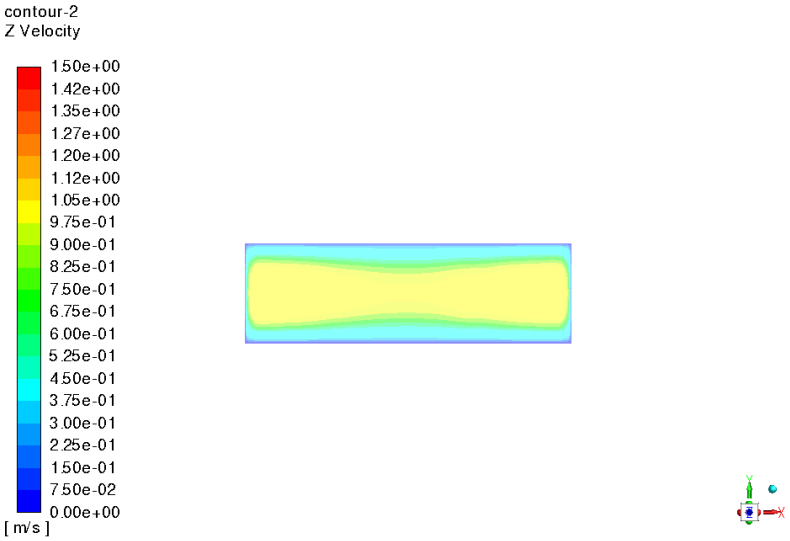

Figure 122 - Predicted velocity distribution at exit for inlet position L_{BW}=22.4 cm and v_{max}.

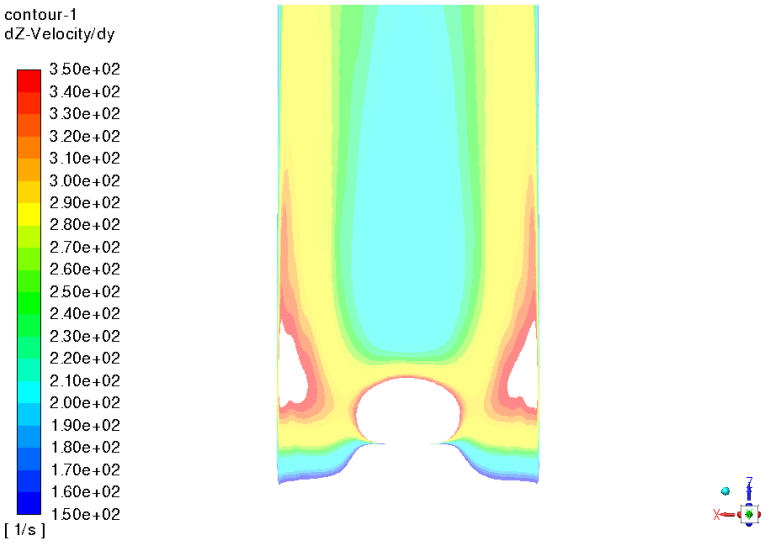

Figure 123 - Predicted midplane velocities for inlet position L_{BW}=22.4 cm and v_{max}.

Table 35 – Air-Brush Pistol reproducibility.

Number	Grammage H_2O [g/m^2]
1	23.8
2	24.2
3	24.4
4	25.0
5	24.0
mean	**24.3 ±0.4**

Table 36 - ACK 350 Std. measured dry mass.

Number	Grammage H_2O [g/m^2]
1	327.7
2	327.5
3	327.1
4	327.0
5	328.2
6	326.2
7	328.5
mean	**327.5 ±0.7**

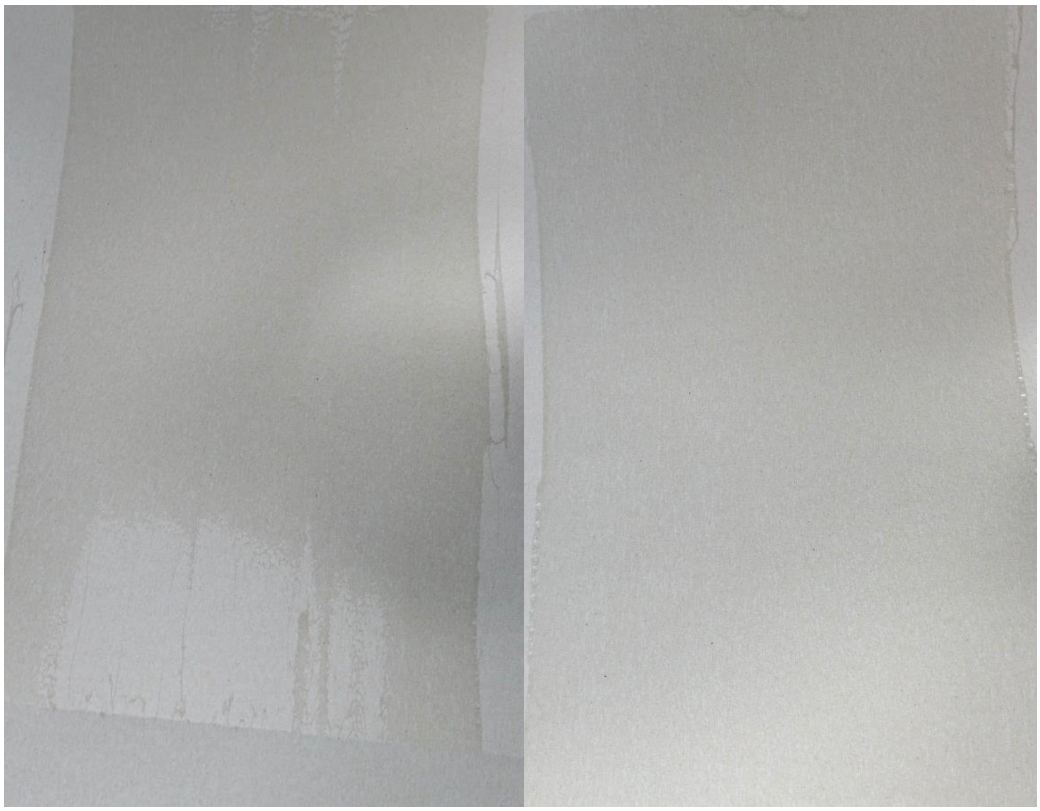

Figure 125 - RS2 coated substrate. $\dot{V}_l = 1.55\ l/min$, $v_{sub} = 5\ m/s$, $v_{imp} = 1.07$ (left) and $1.24\ m/s$ (right).

Figure 124 - RS2 Std. coated substrate. $\dot{V}_l = 1.08\ l/min$, $v_{sub} = 2.6\ m/s$, $v_{imp} = 1.07$ (left) and $1.24\ m/s$ (right).

Figure 126 - RS3 Std. coated substrate. $\dot{V}_l = 0.86\ l/min$, $v_{sub} = 4.59\ m/s$, $v_{imp} = 1.18\ m/s$ (left) and $\dot{V}_l = 0.81\ l/min$, $v_{sub} = 4.33\ m/s$, $v_{imp} = 1.33\ m/s$ (right).

Figure 127 - RS3 Std. coated substrate. $\dot{V}_l = 0.91\ l/min$, $v_{sub} = 3.90\ m/s$, $v_{imp} = 1.16\ m/s$ (left) and $\dot{V}_l = 0.91\ l/min$, $v_{sub} = 4.20\ m/s$, $v_{imp} = 1.33\ m/s$ (right).

Table 37 - Applicability of coating window.

Coating Liquid	Quality	Coated Mass [g/m²]	Mass Flow Rate [g/min]	Re	v_{sub}/v_{imp}
RS2 Std. 1	uncoated	6.5	27.69	0.31	3.89
RS2 Std. 1	coated	7.75	33.01	0.37	3.89
RS2 Std. 1	uncoated	6.5	23.53	0.27	3.31
RS2 Std. 1	coated	7.75	28.06	0.32	3.31
RS2 Std. 2	uncoated	7.75	33.51	0.22	4.00
RS2 Std. 2	coated	9	38.91	0.26	4.00
RS2 Std. 2	uncoated	6.5	23.91	0.16	3.41
RS2 Std. 2	coated	7.75	28.51	0.19	3.41
RS2 Std. 3	uncoated	4	21.70	0.52	3.80
RS2 Std. 3	coated	5.25	28.48	0.69	3.80
RS2 Std. 3	uncoated	4	18.4	0.44	3.23
RS2 Std. 3	coated	5.25	24.21	0.58	3.23
RS3 Std. 1	uncoated	8.5	24.43	1.03	3.74
RS3 Std. 1	coated	9.75	28.03	1.18	3.74
RS3 Std. 1	uncoated	9.75	23.82	1.00	3.18
RS3 Std. 1	coated	11	26.88	1.13	3.18
RS3 Std. 2	uncoated	9.75	27.49	2.33	3.71
RS3 Std. 2	coated	11	31.01	2.64	3.71
RS3 Std. 2	uncoated	9.75	23.36	1.99	3.16
RS3 Std. 2	coated	11	26.36	2.24	3.16
RS3 Std. 3	uncoated	11	32.49	0.92	3.76
RS3 Std. 3	coated	12.25	36.18	1.02	3.76
RS3 Std. 3	uncoated	12.25	30.75	0.87	3.20
RS3 Std. 3	coated	13.5	30.34	0.96	3.20

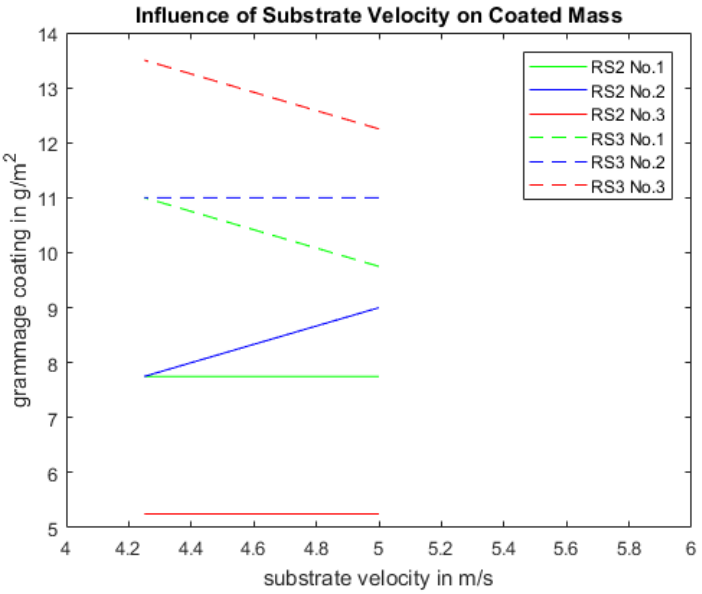

Figure 128 - Influence of substrate velocity on minimum reachable coated mass of RS2 Std. and RS3 Std.

Table 38 - Fitted untreated ACK 350 temperature during drying of pure water coated substrates.

T_{inf} [°C]	t_{drying} [s]	Repetition	T_{sub} [°C] @1.5 cm	T_{sub} [°C] @18 cm	T_{sub} [°C] @34.5 cm	T_{sub} [°C] mean	Fit-Method
100	20	1	36.6	36.0	32.3	35.3	sigmoidal
100	20	2	35.8	36.1	33.1	35.5	polynomial
100	20	3	35.7	37.4	33.5	36.4	polynomial
100	40	1	39.5	37.7	34.5	37.5	polynomial
100	40	2	39.0	39.3	35.4	38.6	polynomial
100	40	3	38.7	39.0	35.6	38.4	polynomial
100	60	1	46.0	38.7	35.4	39.3	Nu-like
100	60	2	45.9	41.1	36.2	41.1	polynomial
100	60	3	44.6	40.1	36.4	40.2	Nu-like
100	80	1	53.4	40.0	36.0	41.4	Nu-like
100	80	2	53.8	42.2	36.6	43.2	Nu-like
100	80	3	51.4	41.5	36.8	42.3	Nu-like
125	20	1	40.5	38.1	32.7	37.6	sigmoidal
125	20	2	39.6	40.5	36.2	39.6	polynomial
125	20	3	38.5	39.8	35.9	38.9	polynomial
125	40	1	49.0	42.1	36.8	42.3	Nu-like
125	40	2	48.3	42.6	39.0	42.9	Nu-like
125	40	3	45.7	41.5	38.5	41.7	Nu-like
125	60	1	58.3	44.0	38.9	45.4	Nu-like
125	60	2	58.4	44.1	40.1	45.6	Nu-like
125	60	3	53.8	44.0	39.7	44.9	Nu-like
125	80	1	67.3	45.4	40.2	47.7	Nu-like
125	80	2	68.1	46.5	40.8	48.8	Nu-like
125	80	3	62.0	47.4	40.6	48.6	Nu-like
150	20	1	41.5	41.4	36.8	40.6	polynomial
150	20	2	36.4	38.2	36.5	37.6	polynomial
150	20	3	45.1	45.1	37.3	43.8	polynomial
150	40	1	53.8	46.3	40.1	46.5	polynomial
150	40	2	54.1	46.7	40.6	46.8	Nu-like
150	40	3	58.4	47.1	41.8	48.1	Nu-like
150	60	1	68.1	47.2	41.5	49.4	Nu-like
150	60	2	70.1	52.8	42.5	53.9	Nu-like
150	60	3	69.4	49.4	45.2	51.5	Nu-like
150	80	1	81.5	47.9	42.9	51.2	Nu-like
150	80	2	70.1	52.8	42.5	60.3	polynomial
150	80	3	78.7	53.8	48.8	56.4	Nu-like

Table 39 – Measured water fractions of untreated ACK 350 during drying coated with pure water. Outlier were identified (red) if measured overall and local masses do not fit.

T_{inf} [°C]	t_{drying} [s]	Repetition	sample	$w_{sub,H2O}$ [kg/kg]
100	20	1	overall	0.106
100	20	1	1st/3	0.100
100	20	1	2nd/3	0.112
100	20	1	3rd/3	0.109
100	20	2	overall	0.107
100	20	2	1st/3	0.098
100	20	2	2nd/3	0.109
100	20	2	3rd/3	0.109
100	20	3	overall	0.108
100	20	3	1st/3	0.097
100	20	3	2nd/3	0.112
100	20	3	3rd/3	0.112
100	40	1	overall	0.096
100	40	1	1st/3	0.082
100	40	1	2nd/3	0.100
100	40	1	3rd/3	0.109
100	40	2	overall	0.101
100	40	2	1st/3	0.083
100	40	2	2nd/3	0.104
100	40	2	3rd/3	0.108
100	40	3	overall	0.105
100	40	3	1st/3	0.083
100	40	3	2nd/3	0.098
100	40	3	3rd/3	0.107
100	60	1	overall	0.082
100	60	1	1st/3	0.067
100	60	1	2nd/3	0.084
100	60	1	3rd/3	0.094
100	60	2	overall	0.095
100	60	2	1st/3	0.074
100	60	2	2nd/3	0.093
100	60	2	3rd/3	0.118
100	60	3	overall	0.089
100	60	3	1st/3	0.070
100	60	3	2nd/3	0.094
100	60	3	3rd/3	0.101
100	80	1	overall	0.082

100	80	1	1st/3	0.069
100	80	1	2nd/3	0.085
100	80	1	3rd/3	0.098
100	80	2	overall	0.080
100	80	2	1st/3	0.062
100	80	2	2nd/3	0.081
100	80	2	3rd/3	0.093
100	80	3	overall	0.077
100	80	3	1st/3	0.065
100	80	3	2nd/3	0.081
100	80	3	3rd/3	0.091
125	20	1	overall	0.099
125	20	1	1st/3	0.085
125	20	1	2nd/3	0.104
125	20	1	3rd/3	0.102
125	20	2	overall	0.097
125	20	2	1st/3	0.084
125	20	2	2nd/3	0.101
125	20	2	3rd/3	0.105
125	20	3	overall	0.105
125	20	3	1st/3	0.080
125	20	3	2nd/3	0.099
125	20	3	3rd/3	0.102
125	40	1	overall	0.082
125	40	1	1st/3	0.067
125	40	1	2nd/3	0.084
125	40	1	3rd/3	0.090
125	40	2	overall	0.086
125	40	2	1st/3	0.071
125	40	2	2nd/3	0.087
125	40	2	3rd/3	0.098
125	40	3	overall	0.089
125	40	3	1st/3	0.073
125	40	3	2nd/3	0.094
125	40	3	3rd/3	0.097
125	60	1	overall	0.074
125	60	1	1st/3	0.056
125	60	1	2nd/3	0.080
125	60	1	3rd/3	0.089
125	60	2	overall	0.075
125	60	2	1st/3	0.061

125	60	2	2nd/3	0.080
125	60	2	3rd/3	0.089
125	60	3	overall	0.075
125	60	3	1st/3	0.060
125	60	3	2nd/3	0.079
125	60	3	3rd/3	0.089
125	80	1	overall	0.065
125	80	1	1st/3	0.049
125	80	1	2nd/3	0.071
125	80	1	3rd/3	0.079
125	80	2	overall	0.062
125	80	2	1st/3	0.047
125	80	2	2nd/3	0.070
125	80	2	3rd/3	0.080
125	80	3	overall	0.060
125	80	3	1st/3	0.043
125	80	3	2nd/3	0.064
125	80	3	3rd/3	0.077
150	20	1	overall	0.096
150	20	1	1st/3	0.082
150	20	1	2nd/3	0.098
150	20	1	3rd/3	0.106
150	20	2	overall	0.095
150	20	2	1st/3	0.083
150	20	2	2nd/3	0.099
150	20	2	3rd/3	0.103
150	20	3	overall	0.095
150	20	3	1st/3	0.084
150	20	3	2nd/3	0.099
150	20	3	3rd/3	0.102
150	40	1	overall	0.050
150	40	1	1st/3	0.058
150	40	1	2nd/3	0.074
150	40	1	3rd/3	0.089
150	40	2	overall	0.071
150	40	2	1st/3	0.056
150	40	2	2nd/3	0.076
150	40	2	3rd/3	0.085
150	40	3	overall	0.069
150	40	3	1st/3	0.057
150	40	3	2nd/3	0.071

150	40	3	3rd/3	0.085
150	60	1	overall	0.057
150	60	1	1st/3	0.039
150	60	1	2nd/3	0.062
150	60	1	3rd/3	0.073
150	60	2	overall	0.061
150	60	2	1st/3	0.045
150	60	2	2nd/3	0.067
150	60	2	3rd/3	0.078
150	60	3	overall	0.060
150	60	3	1st/3	0.047
150	60	3	2nd/3	0.062
150	60	3	3rd/3	0.077
150	80	1	overall	0.044
150	80	1	1st/3	0.025
150	80	1	2nd/3	0.053
150	80	1	3rd/3	0.058
150	80	2	overall	0.039
150	80	2	1st/3	0.025
150	80	2	2nd/3	0.048
150	80	2	3rd/3	0.052
150	80	3	overall	0.044
150	80	3	1st/3	0.028
150	80	3	2nd/3	0.053
150	80	3	3rd/3	0.058

Table 40 - Comparison experiments/simulation mean water fraction @ T_{inf}=100 °C.

t_{drying} [s]	$w_{sub,H2O,exp}$ [kg/kg]	$w_{sub,H2O,sim}$ [kg/kg]
20	0.107± 0.001	0.116
40	0.098 ± 0.004	0. 101
60	0.089 ± 0.005	0.086
80	0.079 ± 0.002	0.072

Table 41 - Comparison experiments/simulation local water fraction @ T_{inf}=100 °C.

t_{drying} [s]	$w_{sub,H2O,exp}$ [kg/kg]	$w_{sub,H2O,sim}$ [kg/kg]]	$w_{sub,H2O,exp}$ [kg/kg]	$w_{sub,H2O,sim}$ [kg/kg]]	$w_{sub,H2O,exp}$ [kg/kg]	$w_{sub,H2O,sim}$ [kg/kg]]
	1st/3		2nd/3		3rd/3	
20	0.098 ±0.002	0.113	0.111 ±0.001	0.118	0.111 ±0.001	0.119
40	0.083 ±0.001	0.095	0.101 ±0.002	0.105	0.108 ±0.001	0.106
60	0.070 ±0.003	0.078	0.090 ±0.005	0.091	0.104±0.001	0.093
80	0.065 ±0.003	0.062	0.082 ±0.002	0.077	0.094 ±0.003	0.080

Table 42 - Comparison experiments/simulation mean water fraction @ T_{inf}=125 °C.

t_{drying} [s]	$w_{sub,H2O,exp}$ [kg/kg]	$w_{sub,H2O,sim}$ [kg/kg]
20	0.098*	0.111
40	0.085 ± 0.003	0.091
60	0.075 ± 0.001	0.071
80	0.062 ± 0.002	0.055

* outlier was identified

Table 43 - Comparison experiments/simulation local water fraction @ T_{inf}=125 °C.

t_{drying} [s]	$w_{sub,H2O,exp}$ [kg/kg]	$w_{sub,H2O,sim}$ [kg/kg]]	$w_{sub,H2O,exp}$ [kg/kg]	$w_{sub,H2O,sim}$ [kg/kg]]	$w_{sub,H2O,exp}$ [kg/kg]	$w_{sub,H2O,sim}$ [kg/kg]]
	1st/3		2nd/3		3rd/3	
20	0.084*	0.107	0.102*	0.115	0.104*	0.115
40	0.070 ±0.002	0.083	0.088 ±0.004	0.095	0.095 ±0.004	0.097
60	0.059 ±0.002	0.061	0.080 ±0.002	0.077	0.089 ±0.002	0.079
80	0.046 ±0.003	0.044	0.068 ±0.003	0.060	0.079 ±0.001	0.063

* outlier was identified

Table 44 - Comparison experiments/simulation mean water fraction @ T_{inf}=150 °C.

t_{drying} [s]	$w_{sub,H2O,exp}$ [kg/kg]	$w_{sub,H2O,sim}$ [kg/kg]
20	0.095 ± 0.001	0.105
40	0.070*	0.079
60	0.059 ± 0.001	0.056
80	0.042 ± 0.002	0.038

Table 45 - Comparison experiments/simulation local water fraction @ T_{inf}=150 °C.

t_{drying}	$w_{sub,H2O,exp}$ [kg/kg]	$w_{sub,H2O,sim}$ [kg/kg]]	$w_{sub,H2O,exp}$ [kg/kg]	$w_{sub,H2O,sim}$ [kg/kg]]	$w_{sub,H2O,exp}$ [kg/kg]	$w_{sub,H2O,sim}$ [kg/kg]]
[s]	1st/3		2nd/3		3rd/3	
20	0.083 ±0.001	0.100	0.099 ±0.001	0.108	0.104 ±0.001	0.110
40	0.057*	0.069	0.074*	0.085	0.086*	0.087
60	0.043 ±0.003	0.045	0.064 ±0.003	0.062	0.076 ±0.002	0.065
80	0.026 ±0.002	0.028	0.051 ±0.002	0.042	0.056 ±0.003	0.045

* outlier was identified

Table 46 - Comparison experiments/simulation mean substrate temperature @ T_{inf}=100 °C.

t_{drying} [s]	$T_{sub,exp}$ [°C]	$T_{sub,sim}$ [°C]
20	35.8 ± 0.5	34.5
40	38.1 ± 0.5	36.9
60	40.2 ± 0.7	38.4
80	42.3 ± 0.7	40.3

Table 47 - Comparison experiments/simulation local substrate temperatures @ T_{inf}=100 °C.

t_{drying}	$T_{sub,exp}$ [°C]	$T_{sub,sim}$ [°C]	$T_{sub,exp}$ [°C]	$T_{sub,sim}$ [°C]	$T_{sub,exp}$ [°C]	$T_{sub,sim}$ [°C]
[s]	@ 1.5 cm		@ 18 cm		@ 34.5 cm	
20	36.0 ±0.4	36.2	36.5 ±0.6	34.3	33.0 ±0.5	34.0
40	39.1 ±0.3	38.7	38.7 ±0.7	36.7	35.1 ±0.5	36.5
60	45.5 ±0.6	42.0	40.0 ±1.0	38.0	36.0 ±0.4	37.8
80	52.9 ±1.0	47.6	41.2 ±0.9	39.7	36.5 ±0.3	38.3

Table 48 - Comparison experiments/simulation mean substrate temperature @ T_{inf}=125 °C.

t_{drying} [s]	$T_{sub,exp}$ [°C]	$T_{sub,sim}$ [°C]
20	38.7 ± 1.0	38.9
40	42.3 ± 0.6	41.7
60	45.3 ± 0.3	44.2
80	48.4 ± 0.6	47.8

Table 49 - Comparison experiments/simulation local substrate temperatures @ T_{inf}=125 °C.

t_{drying}	$T_{sub,exp}$ [°C]	$T_{sub,sim}$ [°C]	$T_{sub,exp}$ [°C]	$T_{sub,sim}$ [°C]	$T_{sub,exp}$ [°C]	$T_{sub,sim}$ [°C]
[s]	@ 1.5 cm		@ 18 cm		@ 34.5 cm	
20	39.6 ±0.8	40.9	39.5 ±1.0	38.7	34.9 ±1.6	38.3
40	47.6 ±1.4	44.8	42.0 ±0.4	41.5	38.1 ±0.9	41.2
60	56.8 ±2.2	50.1	44.0 ±0.1	43.6	39.6 ±0.5	43.2
80	65.8 ±2.7	60.7	46.4 ±0.8	46.6	40.5 ±0.3	45.8

Table 50 - Comparison experiments/simulation mean substrate temperature @ T_{inf}=150 °C.

t_{drying} [s]	$T_{sub,exp}$ [°C]	$T_{sub,sim}$ [°C]
20	40.7 ±2.5	42.9
40	47.1 ±0.7	46.4
60	51.6 ±1.9	50.2
80	56.0 ±3.7	55.3

Table 51 - Comparison experiments/simulation local substrate temperatures @ T_{inf}=150 °C.

t_{drying}	$T_{sub,exp}$ [°C]	$T_{sub,sim}$ [°C]	$T_{sub,exp}$ [°C]	$T_{sub,sim}$ [°C]	$T_{sub,exp}$ [°C]	$T_{sub,sim}$ [°C]
[s]	@ 1.5 cm		@ 18 cm		@ 34.5 cm	
20	41.0 ±3.6	45.1	41.6 ±2.8	42.6	36.9 ±0.4	42.3
40	55.4 ±2.1	50.1	46.7 ±0.3	45.9	40.8 ±0.7	45.6
60	69.2 ±0.8	62.3	49.8 ±2.3	49.5	43.1 ±1.5	48.7
80	81.2 ±1.9	80.9	53.4 ±4.3	52.7	45.4 ±2.5	51.1

Table 52 - Water fractions during drying at T_{inf}=125 °C of RS2 Std. (8.5 g/m^2) coated ACK 350 Std.

t_{drying} [s]	Repetition	$w_{sub,H2O}$ [kg/kg]
60	1	0.073
60	2	0.071
60	3	0.072
120	1	0.057
120	2	0.058
120	3	0.061
180	1	0.043
180	2	0.047
180	3	0.043
240	1	0.043
240	2	0.041
240	3	0.046

Table 53 - Water fractions during drying at T_{inf}=125 °C of RS3_C (18.5 g/m^2) coated ACK 350 Std.

t_{drying} [s]	Repetition	$w_{sub,H2O}$ [kg/kg]
60	1	0.074
60	2	0.072
60	3	0.070
120	1	0.057
120	2	0.057
120	3	0.059
180	1	0.040
180	2	0.051*
180	3	0.033
240	1	0.033
240	2	0.031
240	3	0.034

* air bubbles in coating

Table 54 - Substrate temperatures for RS2 Std. (8.5 g/m^2) at ACK 350 Std. The third repetition was excluded, since one sensor had poor contact with the substrate.

t_{drying} [s]	Position	T_{sub} [°C] Rep. 1	T_{sub} [°C] Rep. 2
0	1.5 cm	30	30
0	18 cm	30	30
0	34.5 cm	30	30
0	mean	30	30
20	1.5 cm	44.5	38.4
20	18 cm	38.8	39.1
20	34.5 cm	35.4	33.6
20	mean	39.6	37.0
40	1.5 cm	55.7	45.7
40	18 cm	46.9	46.8
40	34.5 cm	40.7	37.5
40	mean	47.8	43.3
60	1.5 cm	64.1	52.1
60	18 cm	54.2	53.5
60	34.5 cm	46.0	41.6
60	mean	54.7	49.1
80	1.5 cm	70.1	57.7
80	18 cm	60.7	59.1
80	34.5 cm	51.0	45.7
80	mean	60.6	54.2
100	1.5 cm	74.2	62.5
100	18 cm	66.3	63.8
100	34.5 cm	55.9	49.8
100	mean	65.4	58.7
120	1.5 cm	76.7	66.7
120	18 cm	71.0	67.8
120	34.5 cm	60.5	53.6
120	mean	69.4	62.7
140	1.5 cm	78.1	70.4
140	18 cm	74.8	71.3
140	34.5 cm	64.9	57.0
140	mean	72.6	66.3
160	1.5 cm	78.9	73.6
160	18 cm	77.7	74.3
160	34.5 cm	68.9	60.0
160	mean	75.2	69.3
180	1.5 cm	79.5	76.5

180	18 cm	79.6	77.1
180	34.5 cm	72.5	62.2
180	mean	77.2	71.9
200	1.5 cm	80.3	79.1
200	18 cm	80.4	79.6
200	34.5 cm	75.6	63.6
200	mean	78.8	74.1
220	1.5 cm	81.7	81.5
220	18 cm	80.2	82.3
220	34.5 cm	78.3	64.1
220	mean	80.1	75.9
240	1.5 cm	84.2	83.9
240	18 cm	78.9	85.0
240	34.5 cm	80.5	63.4
240	mean	81.2	77.4

Table 55 - Substrate temperatures for RS3_C (18.5 g/m^2) at ACK 350 Std.

t_{drying} [s]	Position	T_{sub} [°C] Rep. 1	T_{sub} [°C] Rep. 2	T_{sub} [°C] Rep. 3
0	1.5 cm	30	30	30
0	18 cm	30	30	30
0	34.5 cm	30	30	30
0	mean	30	30	30
20	1.5 cm	39.6	43.4	40.2
20	18 cm	37.0	38.8	35.9
20	34.5 cm	34.1	34.8	32.7
20	mean	36.9	39.0	36.3
40	1.5 cm	47.5	54.4	48.6
40	18 cm	43.6	46.9	41.9
40	34.5 cm	37.9	39.3	35.7
40	mean	43.0	46.9	42.1
60	1.5 cm	54.2	63.1	55.5
60	18 cm	49.6	54.1	47.9
60	34.5 cm	41.6	43.7	38.9
60	mean	48.4	53.6	47.4
80	1.5 cm	59.6	69.8	61.1
80	18 cm	55.1	60.5	53.7
80	34.5 cm	45.0	47.8	42.2
80	mean	53.2	59.4	52.3
100	1.5 cm	64.0	74.8	65.5

100	18 cm	60.1	66.2	59.3
100	34.5 cm	48.3	51.6	45.6
100	mean	57.5	64.2	56.8
120	1.5 cm	67.6	78.3	68.9
120	18 cm	64.5	71.1	64.6
120	34.5 cm	51.5	55.1	48.8
120	mean	61.2	68.2	60.8
140	1.5 cm	70.7	80.4	71.6
140	18 cm	68.5	75.2	69.5
140	34.5 cm	54.5	58.3	51.9
140	mean	64.6	71.3	64.4
160	1.5 cm	73.3	81.5	73.7
160	18 cm	71.9	78.6	73.9
160	34.5 cm	57.4	61.1	54.7
160	mean	67.5	73.8	67.4
180	1.5 cm	75.7	81.9	75.4
180	18 cm	74.8	81.2	77.6
180	34.5 cm	60.3	63.6	57.2
180	mean	70.2	75.5	70.1
200	1.5 cm	78.0	81.6	77.0
200	18 cm	77.0	83.0	80.7
200	34.5 cm	63.0	65.6	59.2
200	mean	72.7	76.8	72.3
220	1.5 cm	80.5	81.1	78.5
220	18 cm	78.7	84.1	82.9
220	34.5 cm	65.8	67.2	60.6
220	mean	75.0	77.5	74.0
240	1.5 cm	83.4	80.4	80.2
240	18 cm	79.8	84.5	84.3
240	34.5 cm	68.5	68.3	61.3
240	mean	77.2	77.7	75.3

Table 56 – Specific drying energy of RS2 Std. (8.5 g/m^2) on ACK 350 Std. with initial water fraction of 0.113.

$w_{sub,H2O}$ [kg/kg]	H_{drying} [kJ/g H_2O evaporated]
0.072	4.3
0.059	5.9
0.044	6.4
0.043	7.8

Table 57 - Specific drying energy of RS3 Std. (18.5 g/m^2) on ACK 350 Std. with initial water fraction of 0.113.

$w_{sub,H2O}$ [kg/kg]	H_{drying} [kJ/g H_2O evaporated]
0.072	4.3 ± 0.1
0.058	6.0 ± 0.2
0.036	5.9 ± 0.2
0.033	7.1 ± 0.3

Figure 129 - Full view of dryer inclusive coating pan.